Construction and Modification of Cobalt Active Sites for Efficient Photocatalytic Hydrogen Generation

(コバルト活性部位の構築と修飾による効率的な光触媒水素生成に関する研究)

Xiaohui REN

Graduate School of Chemical Sciences and Engineering

Hokkaido University

2021

Contents

Contents **I**

Abstract **1**

Chapter 1 Introduction **4**

1.1 Semiconductor-based photocatalytic hydrogen generation 4

1.2 The photocatalytic H_2 generation over CdS 9

1.3 General concept of cobalt-based cocatalysts for H_2 evolution 12

1.4 Previous researches over CdS and cobalt-based cocatalysts 15

1.4.1 Cobalt 16

1.4.2 Cobalt oxides 16

1.4.3 Cobalt phosphides 17

1.4.4 Other cobalt-based cocatalyst 22

1.5 Modifications of cobalt active sites toward improved catalytic performance 23

1.5.1 Optimal loading amount 23

1.5.2 Decrease the size of cocatalyst 24

1.5.3 Coordination environment 25

1.6 Thesis motivations and organization 27

References 30

Chapter 2 Single cobalt atom anchored black phosphorous nanosheets as an effective cocatalyst promotes photocatalysis **40**

2.1 Introduction 40

2.2 Experimental section 42

2.2.1 Materials preparation 42

2.2.2 Material characterization 42

2.2.3 Photocatalytic H_2 evolution activity measurements 44

2.3 Results and discussion 45

2.3.1 Synthesis and characterization of few-layer BP nanosheets 45

Content

2.3.2 Characterization of modified photoanodes 55

2.3.3 Photocatalytic H_2 evolution performance on CdS-BP-Co materials. 58

2.4 Conclusions 68

References 68

Chapter 3 Metal dopants mediated interfacial engineering of ultrafine CoP nanoparticles for promoting photocatalytic H_2 evolution 75

3.1 Introduction 75

3.2 Experimental section 76

3.2.1 Material preparation 76

3.2.2 Material characterization 77

3.2.3 Photochemical measurements 78

3.3 Results and discussion 79

3.3.1 Synthesis and structural characterizations of Ca-modified CoP@CdS 79

3.3.2 Structural characterizations of Ca-modified CoP@CdS 80

3.3.3 Photocatalytic H_2 generation performance 92

3.3.4 DFT calculation and mechanism analysis 95

3.4 Conclusions 101

References 101

Chapter 4 Rational construction of dual cobalt active species encapsulated by ultrathin carbon matrix from MOF for boosting photocatalytic H_2 generation 106

4.1 Introduction 106

4.2 Experimental section 108

4.2.1 Materials preparation 108

4.2.2 Material characterization 108

4.2.3 Photocatalytic performance measurement 109

4.2.4 Calculation methods. 110

4.3 Results and discussion 110

4.3.1 Synthesis of CdS-Co-CoO_x@C 110

2.3.2 Characterization of Co-MOF decomposed Co@C 116

Content

4.3.3 Photocatalytic H_2 generation performance 122

4.3.4 Research on catalytic mechanism 128

4.4 Conclusions 131

References 131

Chapter 5 Conclusions and future prospects 138

5.1 General conclusions 138

5.2 Future prospects 140

Acknowledgement 142

Abstract

Semiconductor-based photocatalysis that directly converts solar energy into hydrogen (H_2) has been recognized as an essential technology in “Green Chemistry”. In a highly efficient photocatalyst system, the utilization of cocatalyst is necessary to boost photogenerated electron-hole pair separation and to provide sufficient active sites for surface chemical reactions. Of particular interest, cobalt and cobalt species have been endowed with competitive advantages over noble metals as the cocatalysts for photocatalytic H_2 generation. However, traditional cobalt-based cocatalysts still encounter great challenges such as low active sites utilization efficiency and poor chemical stability. To overcome the aforementioned drawbacks, it is highly desirable to have rational design on the active sites of cobalt-based cocatalyst. Thus, the object of this thesis is to realize controllable growth and distribution of cobalt-based cocatalysts as well as to modify the cobalt active sites with improved efficiency and stability for photocatalytic H_2 generation. By taking CdS as benchmark semiconductor, the relations between interfacial charge transfer behavior and coordination environment of cobalt active sites have been studied, which can provide basic understanding about the mechanism of modifications over cocatalyst/semiconductor system to achieve high activity.

In chapter 1, a general background about semiconductor-based photocatalytic H_2 generation and the concept of cobalt-based cocatalysts were introduced. Then, the key factors on modifying cobalt active sites toward improved catalytic performance, including loading amount, size effect, and coordination environment were discussed. In the end, the ongoing researches beyond CdS and cobalt-based cocatalysts were summarized.

In chapter 2, in order to maximizing the size effect and enlarging surface exposed area of cobalt-based active sites, two-dimensional black phosphorous (BP) has been chosen as the substrate for dispersing single-atom cobalt active sites. Owing to the intrinsic lone pair electrons, cobalt ions can be stably anchored on the surface of BP nanosheets through Co-P coordination. In-depth structural examination revealed that one isolated Co atom is coordinated with one or two phosphorous atoms as well as four oxygen atoms by forming Co-P(O) species in BP-Co atomic structure. An evidential improvement of photocatalytic reduction capability has been realized due to the interaction between Co and P, while 18-fold enhancement can be achieved on CdS

when taking BP-Co as a noble-metal-free cocatalyst for H_2 evolution (the average H_2 production rate is 345.4 μmol h^{-1}). This strategy can open up new opportunities for constructing atomically active sites in low-dimensional nanostructure.

In chapter 3, a novel and facile preparation strategy has been developed to fabricate ultrafine CoP nanoparticles on the surface of CdS. By utilizing organophosphorus compound triphenylphosphine (PPh_3) as phosphorous source, the as-fabricated CoP nanoparticles were intrinsically encapsulated by carbon layer and applied as cocatalyst into photocatalytic H_2 evolution. This synthesis strategy does not require flammable compounds (e.g. PH_3 or H_2, etc.) or corrosive conditions, which makes it much safer and easier to manipulate comparing to conventional methods. It was found that Ca^{2+} as an alkaline earth metal ion may easily substitute the Cd^{2+} lattice sites of CdS. Specially, intimate contact between CdS and CoP can be realized owing to the ascending reducibility of CdS after Ca^{2+} modification. Meanwhile, the Ca^{2+} dopants can act as surface trapping sites on CdS, leading to strong trap-state emission together with long-lived charge carriers. Benefitted from fast interfacial charge transfer and effective photogenerated electron-hole separation, the photocatalytic H_2 generation rate of Ca-modified CdS-CoP can reach up to the highest value (about 2441.5 μmol h^{-1} with turnover frequency as high as 703.2 h^{-1}) under optimal conditions. This finding simplifies the fabrication procedure for constructing and modifying cobalt active sites with efficient photocatalytic H_2 generation performance.

In chapter 4, the spatially separated Co and CoO_x dual cocatalyst encapsulated in carbon substrate was constructed by annealing ultrathin two-dimensional (2D) Co-based MOF (Co-MOF) nanosheets on the surface of CdS. The cooperation between Co (reduction cocatalyst) and CoO_x (oxidation cocatalyst and hole acceptor) has been regarded to play an important role for high-efficient photocatalytic H_2 evolution. In addition, the intimate contact between CdS and cobalt active species in carbon matrix that formed after calcination could also enable fast charge transfer for efficient catalytic reactions. As a result, an approximate 12.5-fold enhancement of H_2 generation performance from 0.161 mmol h^{-1} of CdS to 1.997 mmol h^{-1} of the newly formed CdS-Co-CoO_x@C with the apparent quantum efficiency of 43.7% at 420 nm has been achieved. The fundamental roles of 2D-MOF derived carbon matrix toward rational construction of dual cobalt active species were visualized by combining a series of in-situ and ex-situ temperature-dependent analytic strategies. This study provides comprehensive understanding on the structural variation of 2D-MOF nanostructure

during pyrolysis, offering a meaningful way for controllable designation on dual cobalt-based cocatalyst towards efficient photocatalytic applications.

In chapter 5, an overall summary of this dissertation work was presented. This thesis carried out a systematic study on the construction and modification of cobalt active sites for photocatalytic H_2 generation under visible light irradiation. The thesis reveals that both surface chemistry and electronic properties of cobalt-based cocatalysts can be altered through rational design and modification. Three feasible strategies were found to be crucial for the significant improvement on photocatalytic H_2 generation performance: 1) construction of spatially separated cobalt active sites with optimized structure for improving active sites utilization efficiency; 2) modification of interfacial charge transfer behavior between semiconductor and cocatalyst for promoting photogenerated electron-hole pair separation; and 3) engineering the coordination environment of cobalt active sites for lowering energy barrier in surface reactions. The relevant findings in this study deepen the understanding on rational design of cobalt-based cocatalysts, which provides new insights toward construction and modification of cobalt active sites for photocatalytic H_2 generation.

Chapter 1 Introduction

1.1 Semiconductor-based photocatalytic hydrogen generation

The growing demands on energy resources, environmental pollution and climate change have become the world main challenges and concerns in recent years. In this regards, renewable energy that derived from earth's natural sources/processes tends to be an ideal alternative for replacing traditional fossil fuels. Rapid developments of renewable energy and related technologies are now beginning to reshape the structure of world energy markets. Currently, the consumption of renewable energy (3.2 EJ) accounting for over 40% of the growth in primary energy in 2019 at global level.[1] The renewable energy has the potential to create opportunities and accelerate the emerging trends and to shift the world onto a more sustainable pathway.

Hydrogen is known as the clean and sustainable energy carrier form which plays an essential role in low-carbon economy system. In the past decades, the developments of hydrogen energy system as well as applications of hydrogen in different fields have attracted worldwide interests (Figure 1.1).[2-4] The importance of hydrogen as a renewable energy resources arises due to the excellent energy storage capacity (33.33 kWh kg^{-1}), which is far exceeds that of gasoline or other forms of fossil fuel such as diesel (11.9 kWh kg^{-1}) and petrol (11.6 kWh kg^{-1}).[5] Hydrogen can be produced through a diversity of technologies including chemical, biological, electrolytic, photolytic, and thermochemical processes.[6] In general, global hydrogen production is extensively based on fossil resources (natural gas reforming and gasification of coal), although those processes involve CO_2 production and will have a great contribution to the greenhouse effect. Other technologies such as water electrolysis, biomass gasification, and photoelectrocatalysis are either expensive at large scale or still in developing stage. Therefore, searching for substantial and cost-effective alternatives excluding the production of any greenhouse gases is the key element.

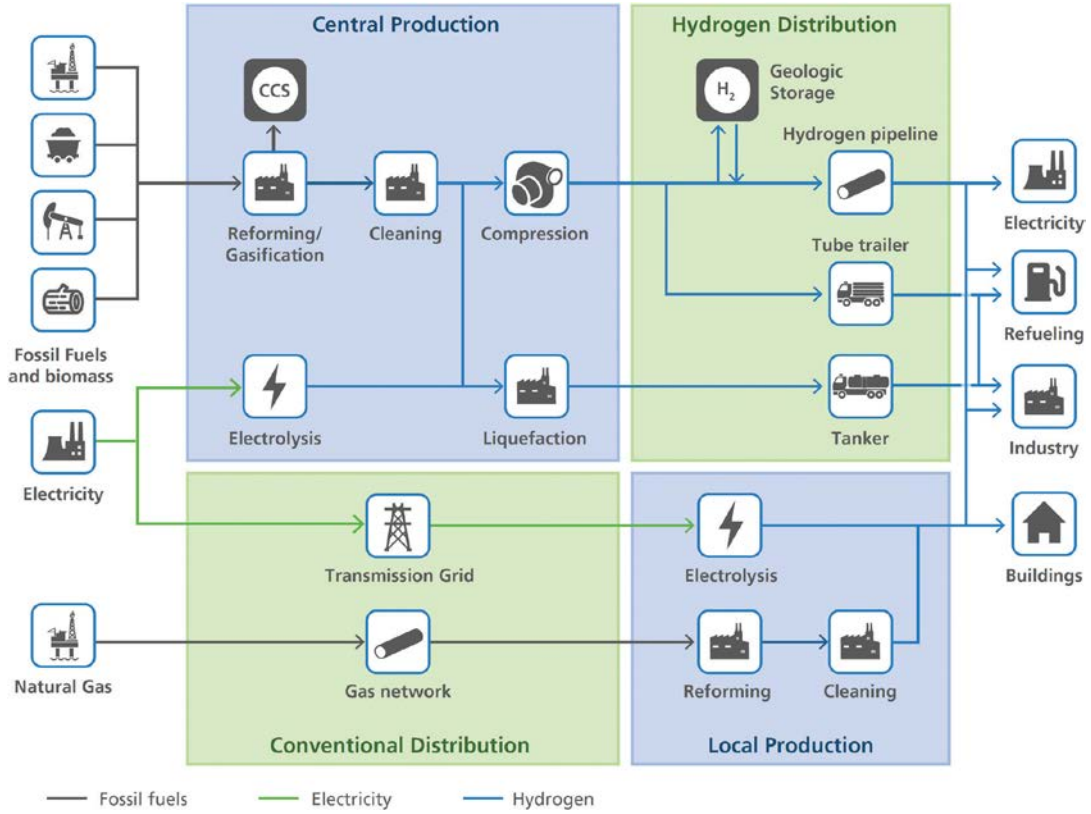

Figure 1.1 The overview of key hydrogen production and usage pathways in the current energy economy systems.[4]

Sunlight has been regarded as the most abundant and freely available eco-friendly energy source. The amount of solar irradiation that received by earth surface is $3x10^{24}$ J per year, which is 10^4 times higher than annual world consumption rate. As one of the most powerful technologies in "Green Chemistry", photocatalysis that can directly utilize solar energy for driving many catalytic processes such as water splitting, CO_2 reduction, organic compounds degradation and N_2 photofixation has shown great potential.[7-9] In 1972, a pioneering work by Fujishima and Honda reported an intriguing phenomenon that water can be successfully decomposed into H_2 and O_2 under light irradiation by utilizing photocatalytic materials.[10] In this way, solar energy can be converted into H_2 in an environmental-friendly approach without the production of any harmful byproducts, which paves the way for exploring water as future energy source.[11] Considering all the environmental and economic aspects, photocatalytic water splitting from renewable water and solar energy can be regarded as a promising protocol to overcome the global challenges in energy and climate change.

Chapter 1

Photocatalysis is a photon-driven catalytic reaction process with multiple elementary steps. Generally, the semiconductor-based photocatalytic reaction can be mainly divided into three critical steps: (i) light absorption and generation of charge carriers (electrons and holes), (ii) photogenerated charges separation and transfer, and (iii) surface chemical reactions. Starting from the photo adsorption of semiconductor, both electrons and holes will be excited under light irradiation. Then, photogenerated electrons and holes will independently diffuse to the surface of the semiconductor. Finally, the electrons or holes will participate into hydrogen and oxygen evolution reactions. Meanwhile, photocatalytic reactions can be classified into the following two categories: "downhill" reactions and "uphill" reactions. In "downhill" reactions, the photon energy that absorbed by photocatalyst is used for driving thermodynamically favored reactions (such as the decomposition of organic compounds). As for "uphill" reactions, the photon energy is more likely to be converted into chemical energy.[12] Basically, the overall water splitting is composed of two half-reactions, which are H_2 evolution reaction (HER) and O_2 evolution reaction (OER). Thermodynamically, the evolution of H_2 and O_2 via water splitting is a typical "uphill reaction" which requires large positive change of Gibbs free energy (ΔG = +237 kJ mol^{-1}).

The fundamental mechanism of semiconductor-based photocatalytic water splitting has been illustrated in Figure 1.2. Starting from the photo adsorption of semiconductor, electrons (e^-) and holes (h^+) can be generated after the semiconductor absorbing photon energy ($h\nu$) higher than or equal to its bandgap (E_g).[13] When semiconductor adsorbs photons with the energy $h\nu \geq E_g$, electrons in the filled valence band (VB) of semiconductor will be excited to the empty conduction band (CB), leaving holes in the VB. For semiconductor-based photocatalysts, the generation of the electron-hole pair can be written as follows:

$$\text{Semiconductor} + h\nu \rightarrow e^-_{CB} + h^+_{VB} \qquad (h\nu \geq E_g)$$

The generation and recombination of electrons and holes will happen simultaneously on the surface and in the bulk of semiconductor, while the separated electrons or holes which successfully migrate to the surface active sites would have the capacity of reducing and oxidizing identical pre-adsorbed chemicals through surface active sites. In this stage, the defect sites of semiconductor usually serve as recombination centers and result into decreased photocatalytic efficiency.

Moreover, the redox capability of photocatalysts is determined by the band positions of the edges of CB/VB, which means that the reduction and oxidation reactions can happen only when the bandgap and band position are both satisfied. From the viewpoint of thermodynamics, the top edge of VB need to be more positive than O_2/H_2O oxidation potential (1.23 V vs. SHE; 0.82 V vs. NHE, pH=7) whilst bottom edge of CB need to be more negative than H^+/H_2 reduction potential (0 V vs. SHE; -0.41 V vs. NHE, pH=7) in order to expedite both forms of overall photocatalytic water splitting. Thus, the bandgap of semiconductor should be more than 1.23 eV in order to meet the requirement of minimum energy input for water splitting under light irradiation. In addition, due to the energy losses, kinetic overpotentials are needed to drive the HER (ΔE_H in Figure 1.2) and the OER (ΔE_O in Figure 1.2), and thus the E_g of ideal semiconductor-based photocatalysts should basically lie in the range of 1.5 to 2.5 eV.[14]

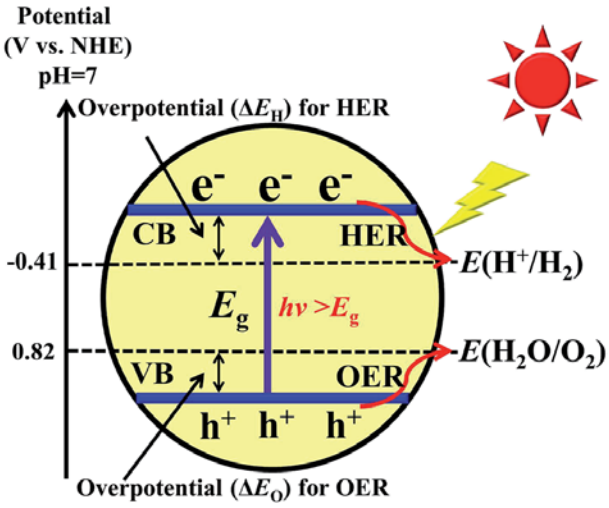

Figure 1.2 Mechanism of semiconductor-based photocatalytic water splitting.[13]

The key for achieving efficient photocatalytic reactions is the constantly utilization of photogenerated electrons and holes in surface active centers.[15] For a long time, the light harvesting, generation and separation of electron-hole pairs as well as the catalytic performance of the specific reactions have been regarded as three major concerns which greatly influence photo-to-chemical energy conversion in photocatalysis. Multi-faceted strategies on improving photocatalytic water splitting performance have been developed due to the fact that majority of semiconductor-based photocatalysts suffer from low photo-to-chemical energy conversion efficiency.[16-19] In order to achieve broadband light absorption and highly efficient charge separation, integrated photocatalyst system based on Type-II heterojunction and Z-scheme heterojunction (as illustrated in Figure 1.3) are two most reported models to harvest solar energy for direct e^- and h^+ generation in the opposite

direction with efficient charge transport and separation. However, Type-II heterojunction can hardly achieve the real overall water splitting reactions due to undesirable surface back reactions. Alternatively, the Z-scheme system with separated of H_2 and O_2 evolution active sites is able to drill H_2 and O_2 from water, although the internal electric field will deplete most of photogenerated electrons and holes.

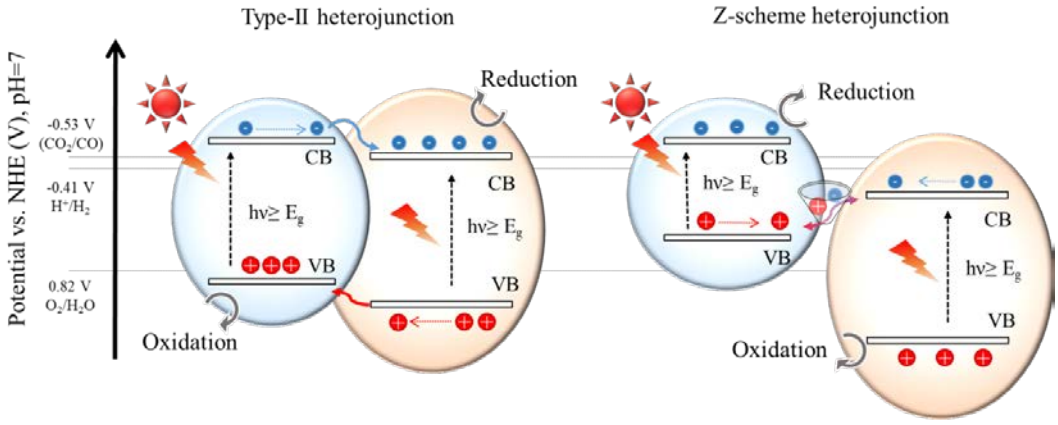

Figure 1.3 Schematic illustrations of type-II heterojunction and Z-scheme heterojunction.

Another general concept that has been widely accepted is to adopt two different materials which can work altogether in one integrated photocatalyst system: a semiconductor with promising solar energy absorption ability, and a cocatalyst providing sufficient active sites for catalytic reactions (Figure 1.4).[20] The synergistic effects between photocatalyst and cocatalyst can help to boost photogenerated electron-hole pair separation and promote surface chemical reactions.[21] In other words, the photocatalysts are likely to be designed with wide range of light absorption covering from ultraviolet (UV) to visible region with moderate bandgap position for thermodynamic requirement. The utilization of cocatalyst is necessary to boost photogenerated electron-hole pair separation and provide sufficient active sites for surface chemical reactions. As the redox active sites, the cocatalyst with larger work function and lower Fermi level can capture photoexcited electrons. Meanwhile, cocatalysts with moderate reactant adsorption and desorption energy is kinetic favorable to photocatalytic reactions. Apart from that, the cocatalyst can also improve the stability of photocatalyst. Up to now, the concerns on searching of cost-efficient, environmental-friendly, stable cocatalysts are indispensable for achieving high photocatalytic performance.

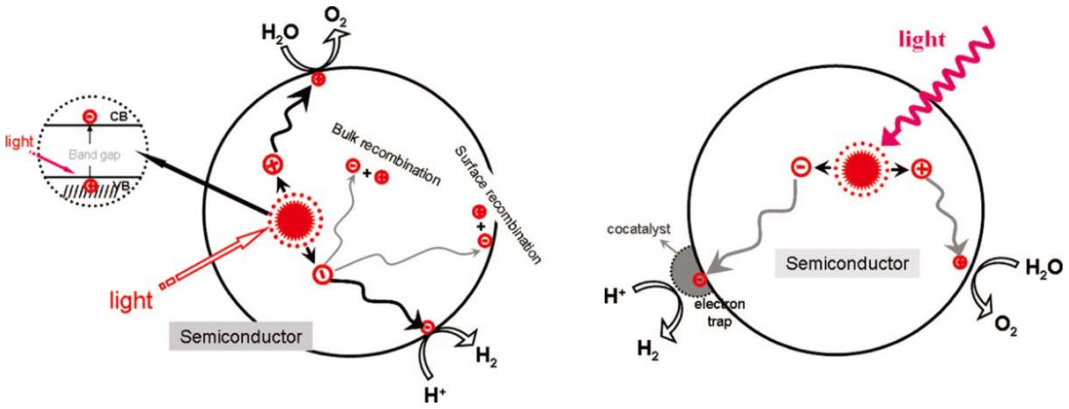

Figure 1.4 The schematic comparison between (a) traditional and (b) cooperative photocatalysis.[20]

Although the semiconductor photocatalysts is capable of overall water splitting in thermodynamics, the photocatalytic water splitting for directly H_2 and O_2 evolution is difficult to occur kinetically owing to the sluggish four-electrons/holes transfer process. For a better investigation into the underlying mechanism of photocatalysis which can guide the exploration of high efficient photocatalysts, an additional electron donor/acceptor is usually provided to scavenge h^+ in the VB or e^- in the CB to close the redox cycling reactions. Over the past 40 years, a lot of concerns in photocatalysis are focused on H_2 and O_2 evolution half reactions. The standard equation and reduction potential of H_2 and O_2 evolution half reactions are illustrated below:

$4H^+ + 4e^- \rightarrow 2H_2$ (E_0 = 0 V vs. SHE, pH = 0)

$2H_2O \rightarrow 4H^+ + 4e^- + O_2$ (E_0 = +1.23 V vs. SHE, pH = 0)

In these H_2 half reaction systems, the oxidation side was replaced by appropriate sacrificial reductants (such as methanol, ethanol, ascorbic acid, lactic acid, and Na_2S/Na_2SO_3); Meanwhile, for O_2 half reaction systems, the common used sacrificial oxidants are $AgNO_3$, CCl_4, $Na_2S_2O_8$, and Fe^{2+}/Fe^{3+}. For contributing the developments of efficient photocatalysts for water splitting, it is important to explore the cocatalysts for the half reactions.

1.2 The photocatalytic H_2 generation over CdS

In a photocatalytic water splitting reaction, photocatalyst plays a crucial role. Until now, large-band-gap semiconductors such as TiO_2, $SrTiO_3$, ZnO, and etc. have been widely studied as the photocatalyst for water splitting due to its environmentally friendly and cost-

effective advantages.[22] However, the low absorption and photo activity in the visible region greatly limit its application scope. Recent advances in CdS and CdS-based photocatalysts provide us new hot topics and insights into photocatalytic H_2 production. The features including strong visible-light absorption, excellent carrier mobility, and efficient surface active sites have been noticed, which make it capable to act in visible-light response photocatalyst system for multiply reactions.

Generally, CdS exists in two main crystal structural polytypes: cubic structure and hexagonal structure as illustrated in Figure 1.5.[23, 24] The differences between cubic and hexagonal structures derive from the lattice parameters and electronic band structures. The optical bandgap values for hexagonal and cubic CdS are calculated to be 2.4 eV and 2.3 eV, respectively. In the band structure of both cubic and hexagonal CdS, S 3p orbitals contribute to the top of the VB, while Cd 5s and 5p orbitals contribute to the bottom of the CB. The lower position of the CB is dominated by Cd 3d orbitals which possesses strong reduction ability for H^+ to H_2. The pioneer work in 1981 reported by James R. Darwent and George Porter demonstrates the photocatalytic H_2 generation from H_2O by employing CdS as the photocatalyst under visible light irradiation.[25] Owing to the high chemical and thermal stability, appropriate band structure, and wide optical absorption range, hexagonal CdS has been regarded as one of the most prominent visible-light-responsive photocatalyst which would provide better H_2 production performance and higher photo-efficiency comparing to cubic CdS.

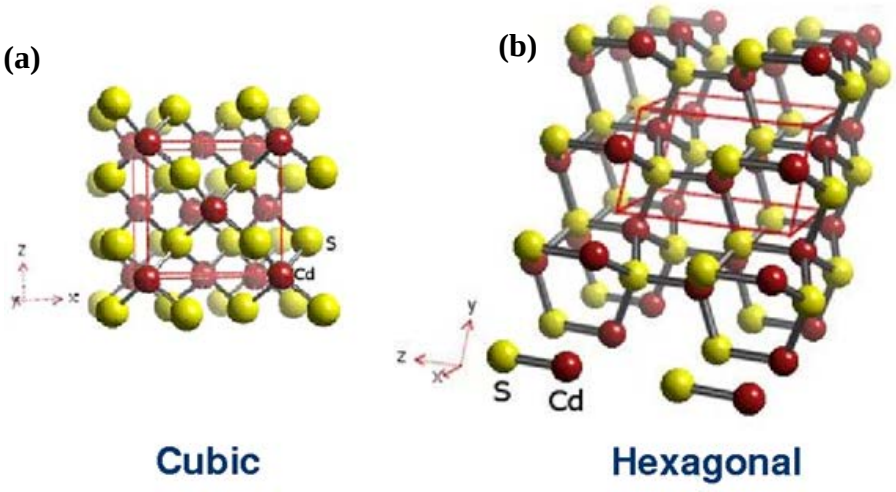

Figure 1.5 Crystal structures of CdS: (a) sphalerite (cubic) structure and (b) wurtzite (hexagonal) structure.[24]

It is known that bare CdS usually exhibits poor H_2 production photocatalytic activity than expected owing to the rapid recombination of photogenerated charge carriers consisting of bulk recombination and surface recombination. Loading of Pt as cocatalyst on the surface of CdS can significantly hinder the recombination of photogenerated carriers and improve the photocatalytic performance. The modification of CdS by loading Pt nanoparticles is able to boost photogenerated charge transfer and accelerate the H_2 evolution reaction, thereby increasing the photocatalytic H_2 production performance about 20 times higher than that of bare CdS. Although Pt nanoparticles are excellent cocatalyst for H_2 evolution, they suffer from high cost and low abundance which largely restrict their practical applications. Therefore, in the present stage, more attentions from researchers are focused onto the developments of cost-effective transition metals and their compounds as cocatalysts for improving the visible-light photocatalytic H_2 production.

However, photocorrosion under light illumination is a common phenomenon during the photocatalytic process with CdS photocatalysts, which makes it difficult for CdS or CdS-based photocatalysts to be widely applied in the industrial field.[26] This has attracted extensive attention and interest from researchers in recent years in an effort to effectively avoid the photocorrosion of CdS photocatalysts. Previous studies demonstrated that CdS seriously suffers from photocorrosion mainly because that the self-oxidation of S^{2-} anions in CdS is much easier than oxidation of water. When sulfur ions combined with photogenerated holes and are oxidized into sulfur, the photocatalytic properties of CdS and CdS-based photocatalysts become highly unstable and the catalytic performance of CdS photocatalysts is reduced. Moreover, the defects that produced on CdS surface due to photocorrosion will lead to photogenerated electron-hole recombination and cause redox reactions on the CdS surface under aerobic conditions. The photocorrosion mechanism of CdS has been proposed in Figure 1.6. In detail, electron-hole pairs that generated upon light illumination ($h\nu > E_g$) can either recombine or migrate to the surface of CdS. As a competition process of photocatalytic oxidation, the self-oxidation process of CdS is thermodynamic enabled by depleting photogenerated h^+ through the interaction with adsorbed SH^- groups. This process may give rise to SH• species, which can be finally transformed into cadmium sulfate in the presence of O_2 and H_2O through various S^{IV} intermediates, such as $SO_2^{\bullet-}$ and HSO_3^- /SO_3^{2-}.[26]

The photocorrosion of CdS can be relieved but not inhibited even with the assistance of sacrificial reductants. In order to improve the photocatalytic stability of CdS-based photocatalysts for practical and large-scale photocatalytic H_2 generation, loading suitable dual cocatalysts on CdS and constructing heterojunctions can accelerate the photogenerated charge carrier transfer and migration which inhibits the photocorrosion process to some extent. However, exploring novel strategies to further improve the stability of CdS-based photocatalysts is a key and urgent challenge for developing highly efficient photocatalysts for H_2 production.

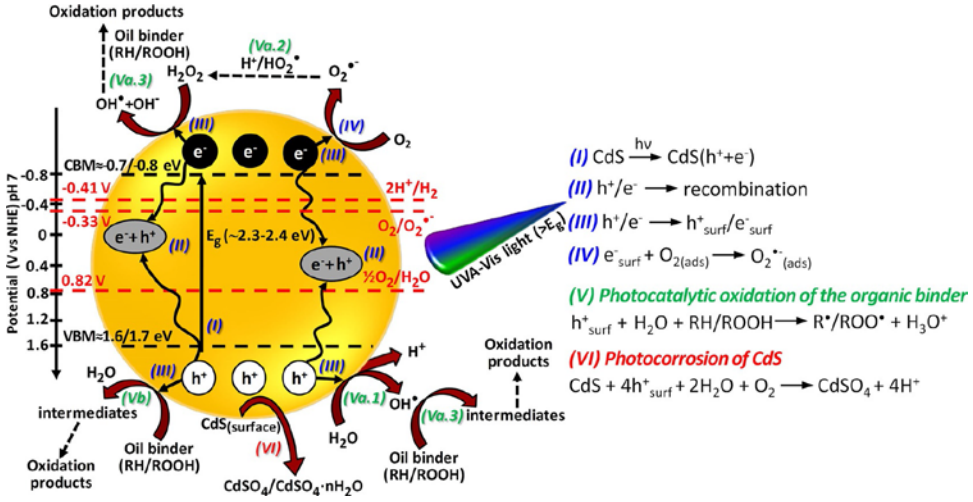

Figure 1.6 Proposed mechanism for the photocorrosion of CdS-based pigments and photocatalytic oxidation process of the oil binder over CdS-based particles.[26]

1.3 General concept of cobalt-based cocatalysts for H_2 evolution

A cocatalyst is usually recognized as an intrinsically inactive material which can improve the activity, stability and selectivity of semiconductor photocatalysts toward catalytic reactions. In photocatalytic water splitting, the cocatalysts play two major roles in facilitating the photocatalytic performance (Figure 1.7): i) extracting and trapping the photogenerated charge carriers to suppress the recombination of electrons and holes in photocatalysts; ii) providing more reaction active sites by supplying the trapped charge carriers for the activation of reactant molecules or redox reactions.

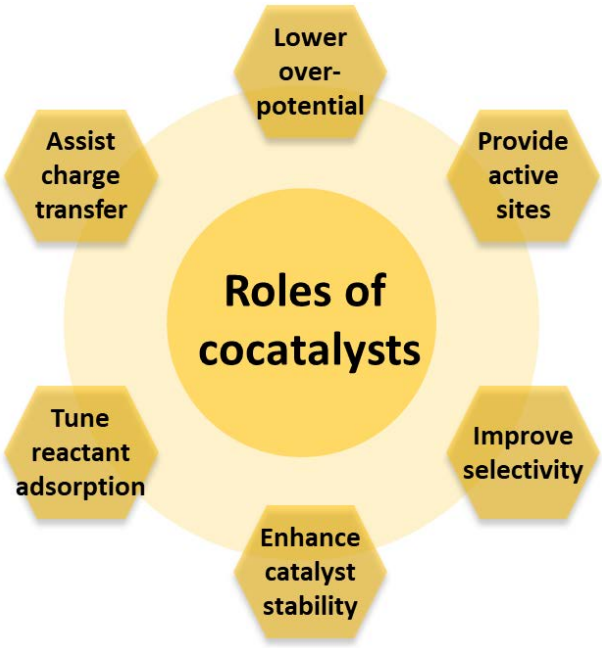

Figure 1.7 Roles of cocatalysts in semiconductor-based photocatalytic system.

Currently, most of the developed photocatalyst systems utilize noble-metal-based cocatalysts to achieve high photocatalytic activity. Regarding to photocatalytic H_2 evolution, Ru, Rh, Pd, Pt, Au and Ag have been extensively investigated as efficient cocatalysts. Among them, Pt is the most effective cocatalyst due to its largest work function and lowest overpotential for H_2 evolution. The highest photocatalytic activities for H_2 production using visible-light irradiation are from photocatalysts loaded with Pt as the cocatalyst. Unfortunately, noble-metal based cocatalysts are too scarce and expensive to be used for large-scale energy production. Therefore, the development of noble-metal free cocatalysts with high efficiency and low-cost features is highly desirable.

During the past decades, many kinds of earth-abundant transitional metal elements, such as Co, Ni and Cu, have been participated to construct cocatalysts for assisting photocatalytic photocatalytic H_2 production.[27] For example, the loading of metals on semiconductors results in the formation of a Schottky barrier at the metal/semiconductor interface. On the other hand, these metals (i.e. Co, Ni and Cu) are capable of catalyzing the proton reduction to H_2 molecules. Therefore, an enhanced photocatalytic H_2 production activity could be observed when these metals are loaded as cocatalysts on semiconductors. Transition metal oxides and hydroxides (NiO, NiO_x, CoO, CoO_x, CuO and Cu_2O) are well-known as noble-metal-free cocatalysts for photocatalytic H_2 production. Transition metal sulfides and carbides (FeS, CoS, NiS, NiS_2, CuS, MoS_2,

MoS_3 and WS_2) have been reported as excellent candidates for cost-effective cocatalysts, aiming to substitute for noble metals in photocatalytic H_2 evolution. Recently, transition metal phosphides (TMPs) and metal phosphorus trichalcogenides (MPTs) have been widely studied as noble metal-free cocatalysts owing to the excellent conductivity and good chemical stability.[28] Until now, most of TMPs (M= Ni, Co, Fe, Mo, Mn, Cu, etc.) are applied as cocatalysts for preventing electron-hole recombination.

To our notice, cobalt-based cocatalysts are promising candidates in the photocatalysis due to their outstanding catalytic performance and low-cost. The advantages such as diverse properties, fine conductivity, excellent chemical and thermal stability, and abundant adsorption sites and catalytic reaction centers endow cobalt-based cocatalysts with great potential for using cobalt-based cocatalysts to promote photocatalytic H_2 generation can be explained as the following three aspects:

a) To boost charge separation and transfer efficiency: During the first stage of photocatalysis when charge carriers are excited in semiconductor after light absorption, the simultaneously recombination of photogenerated electrons and holes will lead to severe energy loss in the form of phonons or photons. The intimate contact between cocatalyst and semiconductor results into the construction of heterojunction. This heterojunction is capable of assisting interfacial charge transfer, promoting charge separation and transport from semiconductor (photocatalyst) to cocatalyst. Besides that, the heterojunction with a short distance between the semiconductor and cocatalyst can reduce the necessary charge transfer distance, effectively inhibiting the bulk recombination and enhancing the overall efficiency.

b) To increase active sites: After the excited charge carriers have reached to the surface of semiconductor, the amount of active sites has become the main bottlenecks since excessive charge carrier will recombine before participating in chemical reactions due to the slow kinetics for water splitting. In this consideration, the loading of cocatalysts as additional active sites on the surface of semiconductor is necessary for promoting photocatalytic reactions by trapping charge carriers and lowering the activation energy. Depending on the composition and structure of cocatalysts, different roles in accelerating the surface chemical reactions can be realized. For overall water splitting, the activation energy should include two half reactions: water reduction and

oxidation. Since the water oxidation for O_2 generation involves four holes transfer process, this half reaction is kinetically unfavorable and has been regarded as the greatest challenging step in the photocatalytic water splitting. Thus, the utilization of cocatalysts with low O_2 evolution overpotential could notably boost the overall efficiency of photocatalytic water splitting. In recent years, several cost-effective cobalt-based cocatalysts, such as CoO_x, Co_3O_4, Co-Pi have received much attention due to their outstanding performance for O_2 evolution. Taking cobalt oxide (CoO) as an example, the valence state of Co recycles from +2 to +4 for collecting photogenerated holes and backs to +2 again after oxidizing water into O_2.

c) To decrease the adsorption and desorption free energy: The process of surface catalysis on the cocatalysts can be divided into three steps. (1) Reactants are adsorbed on the surface of the cocatalysts, which is related to the surface structure and inherent attributes of the cocatalysts. (2) The cocatalysts capture photoexcited charge carriers to reduce, or oxide reactant adsorbed on its surface. (3) The resultant products are desorbed from the surface of the cocatalysts to generate free product molecules. Therefore, in the early stage of catalytic reactions, it is expected that reactants can easily be absorbed on the surface of cocatalysts. While in the latter stage of catalytic reaction, it is expected that the adsorption capability of cocatalysts for resultant products is relatively small so that the resultant products can be quickly desorbed for the formation of the next resultant molecules. Meanwhile, the adsorption sites of reactants are related to the location of the active sites in theory. Therefore, the adsorption free energy (ΔG_{H^*}) are commonly employed as evaluation criteria for the difficulty of the catalytic reaction. Some cobalt-based cocatalysts exhibit low ΔG_{H^*}, which indicates that these cobalt-based cocatalysts are appropriate for photocatalytic H_2 production.

1.4 Previous researches over CdS and cobalt-based cocatalysts

With the growing abilities on the atomic designation of metal nanostructure, earth-abundant transition metals and its clusters have been endowed with competitive advantages over noble metals for achieving efficient H_2 evolution.[29, 30] As an important non-precious transition metal, cobalt with less 3d-orbital occupancy has already demonstrated its promising advantages in energy conversion and storage, especially for

H_2 evolution.[31] Of particular interest, cobalt could form a series of compounds with high stability and metallic nature due to its multiple valence states. Especially, some Co species (such as Co_3O_4, CoO and CoP) have semiconductor properties, which means they could be good candidates for the construction of heterojunction structures on the surface of CdS.[32] To improve the understanding on the roles of cobalt-based cocatalysts in the CdS photocatalytic H_2 production system, I would like to introduce the present investigations on various cobalt-based cocatalysts and their roles on improve the photocatalytic H_2 evolution of CdS.

1.4.1 Cobalt

The work function of metallic Co (5.0 eV) is close to the value of Au (5.31 - 5.47 eV) and Pd (5.22 – 5.60 eV).[33] Therefore, Co as cocatalyst is able to contribute to the migration of photo-excited carriers as well as separation of electrons and holes. Meanwhile, owing to the low ΔG_{H^*} on Co surface, the electrons on the Co surface can easily reduce the H^+ to H_2 and improve photocatalytic H_2 generation in consequence. Those features provide the possibility for the utilization of low-cost Co as an alternative for noble metals in photocatalytic H_2 production.[34] Non-noble metal Co can be loaded on CdS via in-situ photo-deposition method. In 2017, Jiang et al. reported the in-situ anchoring of cobalt nanoparticles on CdS prepared by mixing a certain amount of $CoCl_2$ and CdS in benzyl alcohol solution and then irradiating under visible light. The Co nanoparticles with the average size <2 nm and CdS can integrated as a highly efficient catalyst towards H_2 evolution with the rate of ~848 μmol h^{-1} has been achieved.[35] Another work by Wei Chen, the authors loaded Co particles (diameter about 5 nm) on the surface of CdS by photo-deposition. The loading of Co can realize effectively separation of photo-excited electrons and holes. The highest photocatalytic H_2 evolution rate of Co/CdS (1.0 wt% Co) reaches up to 1299 μmol h^{-1} under visible light irradiation, which is 17 times of that of pure CdS.[34] However, the effort of Co^0 on CdS has not yet been fully understood because Co nanoparticles are extremely unstable and will be easily oxidized to CoO when exposed in atmosphere environment.

1.4.2 Cobalt oxides

Cobalt oxides such as CoO, Co_3O_4, and CoO_x (CoO and Co_3O_4) can be utilized as cocatalysts for photocatalytic H_2 generation. Recent advances have reported the ability of CoO_x (CoO and Co_3O_4) for capturing hole in a time frame of few picoseconds and

also actively partaking in the photocatalytic reaction as oxidation cocatalyst.[36-38] The most common method utilized to prepare cobalt oxides is the annealing treatment. It is usually necessary to prepare a cobalt-based precursor in advance, followed by annealing at a desired temperature and time.[39] Liu et al. established an efficient photocatalytic system by in-situ crafting CoO_x layer onto the negatively charged surface of CdS to form a core-shell structure. After impregnation-calcination, an intimate interface can be formed between the CdS and CoO_x, which offers identical charge transfer channels to enable fast carriers transportation and bring great improvement on the separation of photogenerated electrons and holes. In consequence, 43-folds enhancement on the H_2 production rate has been achieved on CdS/CoO_x compared to the pristine CdS.[37] In addition, Moniruddin et al. have prepared CdS/CoO_x/Co-metal ternary heterostructure where Co metal and CoO_x were used as photogenerated electron- and hole-capturing cocatalysts, respectively. The synergistic charge separation benefits the H_2 evolution over CdS.[40] Recently, Wang et al. proposed a CoO_x/N, S-doped carbon/CdS ternary heterostructure which derived from ZIF-67 template. The ultrafine CoO_x cooperated with N, S-doped carbon matrixes could provide a sufficient number of reaction sites and demonstrate excellent cocatalystic ability on CdS. The optimized CoO_x/N, S-doped carbon/CdS sample exhibits enhanced photocatalytic H_2 production rate of 40.1 mmol g^{-1} h^{-1} under visible light irradiation with the sacrificial agent lactic acid, which is 57 times higher than that of bare CdS and is comparable to that of Pt-deposited CdS.[41] The authors found the strong interaction of CoO_x with carbon can accelerate the transport of photogenerated electrons between CdS and CoO_x at the interface, and enhance the photocatalytic H_2 production in consequence.

1.4.3 Cobalt phosphides

It was suggested that the P atoms play a positive role for photocatalytic H_2 evolution.[42-44] Cobalt phosphides including Co_2P, CoP, CoP_2, and CoP_3 were found to demonstrate distinct water splitting abilities. The H_2 generation performance of CoP was slightly higher than that of Co_2P with the same morphologically and similar Co-P bond lengths.[45] In addition, the performance can be further improved in the situation of CoP_2 and CoP_3.[46-49] It is noted that the negatively charged P atoms can trap the positively charged H_2, acting as active sites on catalyst surfaces and achieving highly efficient water reduction. [50] However, higher P content commonly will induce a lower conductivity to TMPs because electronegative P can strongly restrict the electron

delocalization in metal, further delay the conductivity and result in drawbacks toward H_2 generation reactions.[51] Therefore, the effects of activity and conductivity derived from different P contents in TMPs play the important roles to the final photocatalytic activity.

Lu et al. demonstrated that the photocatalytic H_2 evolution reaction rate was highly dependent on Co surface state. The (112) facet Co_2P loaded on graphene demonstrated beneficial Co_2P-H species formation and low H_2 adsorption free energies (ΔG_H).[52] The Co_2P-CdS was prepared via in-situ hydrothermal method as illustrated in Figure 1.8a. Sample with a loading ratio of 1.2 mol% Co_2P gave greatly improved H_2 production rate, and the value can reach to 0.356 mmol h^{-1} after further introducing K_2HPO_4 to facilitate proton transport as hydrogen-chains.[53] Furthermore, the influence of oxygen incorporation levels were investigated by controlling phosphorization time during hydrothermal synthesis when $Co(CH_3COO)_2$ and Na_2HPO_2 were adopted as starting materials. Benefitted from the intimate interaction between CdS nanorods and oxygen-incorporation Co_2P (o-Co_2P) (Figure 1.8b), 5 wt% o-Co_2P/CdS demonstrated enhanced photocatalytic H_2 production rate of 184.48 mmol h^{-1} g^{-1} (Figure 1.8c) and AQE about 22.17% at 420 nm.[54] The Fu's group found that mono-dispersed Co_2P NPs can be used as novel cocatalysts for photocatalytic H_2 production with CdS nanorods in DL-mandelic acid. During the photocatalytic reactions, DL-mandelic acid as the electron donor was oxidized to benzoylformic acid on CdS nanorods, which provided a green and economical way to synthesize benzoylformic acid from DL-mandelic acid.[55]

Recent studies on the high electrochemical activity of CoP triggered the exploration of its capacity towards photocatalytic reaction.[56] Dandelion-flower-like CoP modified CdS-reduced graphene oxide-MoS_2 (CdS-rGO-MoS_2) nanocomposites achieved an efficient H_2 evolution ability with rate of 8.39 mmol h^{-1} g^{-1} and apparent quantum efficiency of 22.5%.[57] In this multi-components structure, rGO framework was favor to the conduction of photogenerated electrons from CdS to MoS_2 and CoP active sites due to lower Fermi energy level. The efficient electron transfer property has prolonged the lifetime of the charge carriers, enabling photogenerated electrons to reduce adsorbed H^+ into H_2. In-situ synthesis of CoP nanoparticles on the surface of CdS nanorods through gas-solid reaction with NaH_2PO_2 under 300 °C has been reported, the obtained 1wt% CoP-CdS hybrid showed excellent photocatalytic activity (13785 μmol h^{-1} g^{-1}) owing to the faster electrons transfer in the intimate interface between CdS and CoP.[58] With the

help of the carbon layer, the CdS@C-CoP composites exhibited further improvement on both photocatalytic performance and stability under visible light irradiation.[59] Besides that, CoP_x-CdS core-shell heterostructure in Figure 1.8d showed enhanced photocatalytic H_2 production under visible light. The H_2 evolution rate of the optimal sample can reach up to 500000 μmol h^{-1} g^{-1} in Na_2S/Na_2SO_3 solution with the AQE reaching 35% (Figure 1.8e). A total of 35 mmol H_2 was produced within 70 hours of irradiation which corresponds to the turnover numbers (TONs) 630000 per mole of cobalt and TOF of 9000 h^{-1}.[60] Similarly, Dong et al. denoted a stable photocatalytic activity of CoP_x-CdS in Na_2S/Na_2SO_3 solution for about 504 mmol h^{-1} g^{-1}, which was higher than the results of noble metal Pt of 0.5 wt% (225 mmol h^{-1} g^{-1}), and 3.3 wt% Pt/CdS (167 mmol h^{-1} g^{-1}) under the same condition.[61]

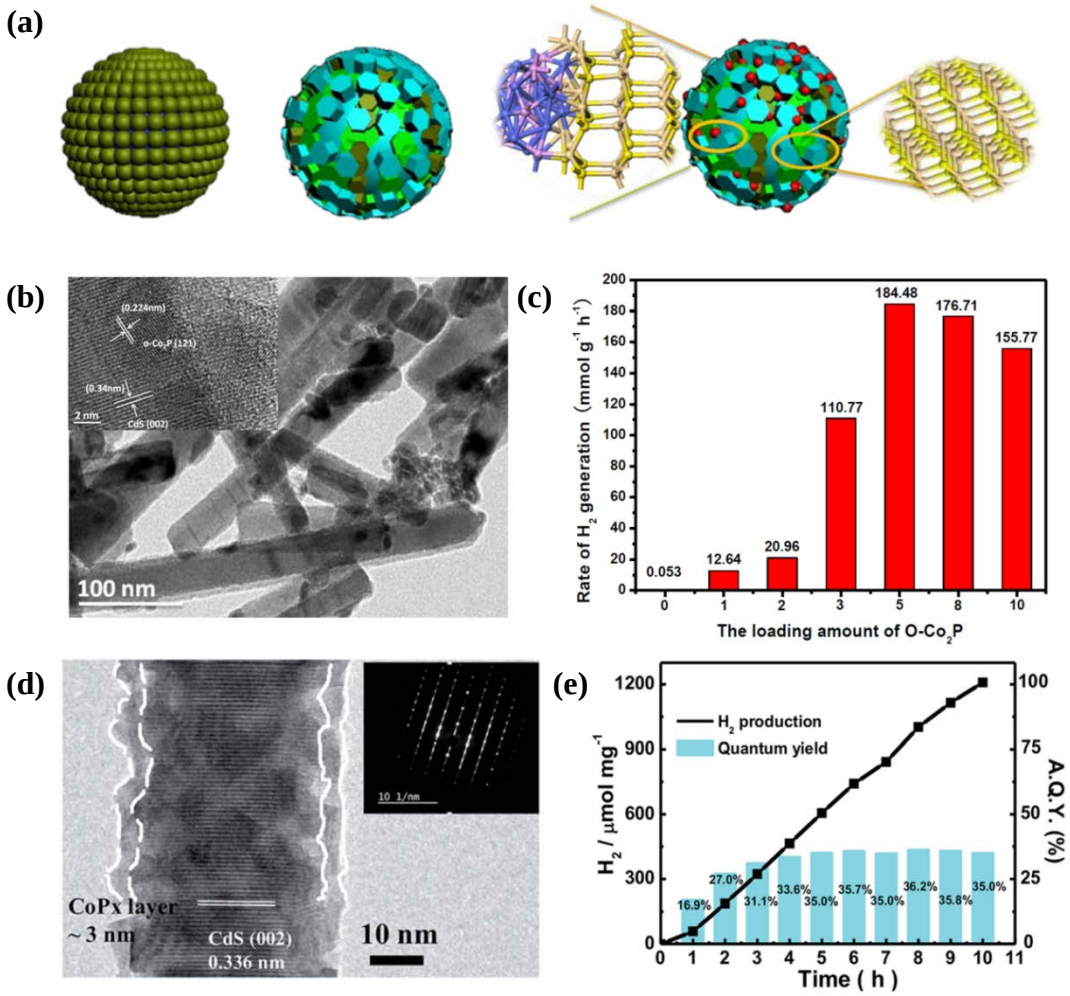

Figure 1.8 (a) Schematic illustration for the synthesis of CdS-Co_2P sub-microspheres.[53] (b) SEM image of CdS/o-Co_2P-5wt% sample (inset: related HRTEM image). (c) Comparison of the photocatalytic H_2 evolution over different o-Co_2P contents.[54] (d) HRTEM image of CoP_x/CdS_2. (e) Time-course H_2 evolution over CoP_x/CdS.[60]

The CoP integrated with CdS revealed good activity for photocatalytic arylalcohols oxidization. Hydroxyl free radicals (as proven from Figure 1.9a) were generated from water and served as the driving species for the reaction, which resulted into 88.0% conversion with 109.1 μmol H_2 evolution for 5 wt% CoP/CdS (Figure 1.9b).[62] Piao et al. shared the possibility of using ultra-small CoP nanoparticle (Figure 1.9c) as an efficient catalyst to promote formic acid photocatalytic decomposition into CO_2 and H_2. An excellent H_2 production up to 182±12.5 μmol h^{-1} g^{-1} can be achieved without any additives (Figure 1.9d). During the reaction, the DMPO-OH signal could be detected, which indicated that H_2O may provide part of H^+ and •OH radicals to participate into the reaction. The H^+ from HCOOH and H_2O was the source of H_2 generation, and •OH radicals produced form H_2O in associated with the photogenerated holes on the VB band of CdS will oxidize $COOH^-$ anion to generate CO_2 in the same time (Figure 1.9e).[63] In Table 1.1, I have simply compared the performance over CdS by using cobalt phosphides as cocatalyst. This work proved the feasibility of taking advantages of photocatalysts such as CoP as an alternative for replacing noble metals in some applications for appropriate performance.[64]

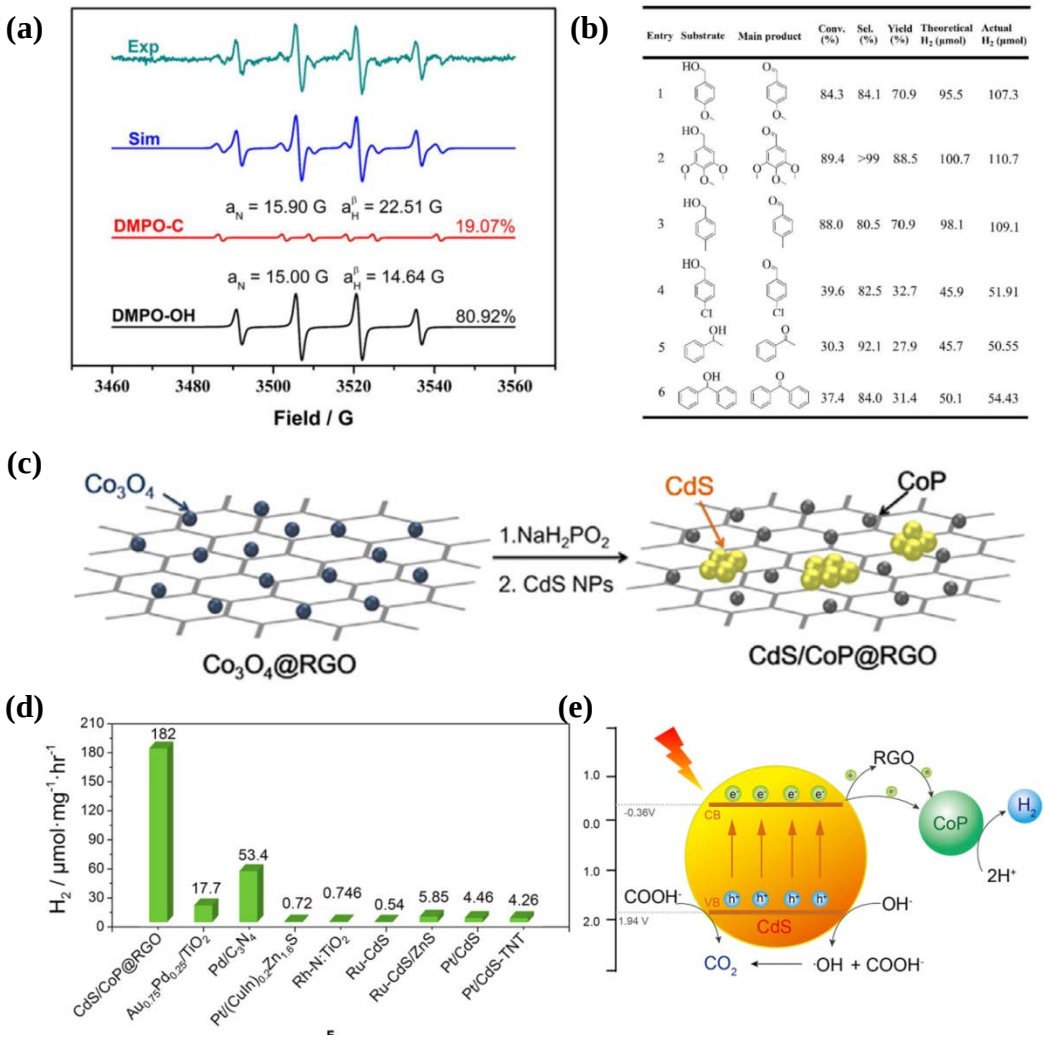

Figure 1.9 (a) ESR experiments for identifying •OH radicals. (b) Production of benzyl alcohols oxidation from different substituents.[62] (c) Synthesis of CdS/CoP@RGO hybrid material. (d) Comparison of CoP@RGO with other cocatalyst and (e) Proposed mechanism for HCOOH dehydrogenation under light irradiation.[63]

Table 1.1 Photocatalytic H_2 generation performance over CdS by using cobalt phosphides as cocatalyst.

Material	Preparation Method	Application	Activity	Ref
Co_2P-CdS	In-situ hydrothermal	Hydrogen evolution (10 volK_2HPO_4 solution)	0.356 μmol h^{-1} AQE = 13.8% (420 nm)	53
o-Co_2P/CdS	Annealing + Phosporization	Hydrogen evolution (13.2 vol% lactic acid solution)	184 mmol h^{-1} g^{-1} AQE = 22.17% (420 nm)	54
Co_2P NPs + CdS NRs	Mixing at high temperature using organic solvent	Hydrogen evolution (0.5 M DL-mandelic acid)	19373 μmol h^{-1} g^{-1} AQE = 6.8% (420 nm)	55
CoP@CdS/RGO-MoS_2	Hydrothermal + Annealing + Phosporization	Hydrogen evolution (20 vol% lactic acid solution)	83907 μmol h^{-1} g^{-1} AQE = 22.5% (425 nm)	57

CoP/CdS NRs	Solvothermal + Annealing + Phosporization	Hydrogen evolution (0.35 M Na_2S/0.25 M Na_2SO_3 solution)	13875 μmol h^{-1} g^{-1} AQE = 11.6% (420 nm)	58
CdS@C-CoP	Annealing+ Phosporization	Hydrogen evolution (0.25 M Na_2S/0.35 M Na_2SO_3)	10089 μmol h^{-1} g^{-1}	59
CoP_x-CdS	Solvothermal	Hydrogen evolution (1.5 M Na_2S/2.1 M Na_2SO_3)	500 μmol h^{-1} mg^{-1} AQE = 35% (450 nm)	60
Co_xP/CdS NRs	Solvothermal + Photochemical	Hydrogen evolution (1.25 M Na_2S/1.75 M Na_2SO_3)	504 mmol h^{-1} g^{-1}	61
CoP/CdS composite	Phosphorization + Hydrothermal	Hydrogen evolution and photooxidation of arylalcohols	88% conversion and 109.1 μmol H_2 in 5 h	62
CdS/CoP@RGO	Annealing + Phosphorization + Mixing	Formic acid dehydrogenation	182 μmol h^{-1} mg^{-1} Selectivity > 99.5% AQE = 32% (420 nm)	63

1.4.4 Other cobalt-based cocatalyst

In addition to Co, cobalt oxides, and cobalt phosphides, other cobalt-based compounds such as Co_8S_9[65], $Co(OH)_2$[66], Co_3N[67], and Co-complex[68] have been proved to be effective cocatalysts for promoting the H_2 evolution activity. Zhang et al. reported that Co_8S_9/CdS nano-composites worked as a redox-mediator-free Z-scheme system can effectively separatethe photoexcited charge carries and achieve enhanced photocatalytic activity.[65] Zhou et al. prepared $Co(OH)_2$ modified CdS and reported that photoexcited electrons in the CB of CdS can effectively transfer to $Co(OH)_2$ and reduce partial Co^{2+} to Co^{+} and Co^{0}, thus accelerating the separation of charg ecarriers of CdS and leading to enhanced photocatalytic H_2 evolution (14.43 mmol h^{-1} g^{-1} for 6.5 mol% $Co(OH)_2$).[66] A similar phenomenon was also observed by Zhang et al., where the H_2 generation rate can reach up to 61 μmol h^{-1} g^{-1}.[69] Cobalt nitride (Co_3N) composed of noble-metal-free elements has been regarded as a metallic interstitial compound. The nitrogen atoms inserted into the interstices of the metal-based framework do not eliminate the metallic properties but influence the electronic properties of the metal by increasing the density of electrons on the surface, which make the compound suitable for the hydrogen production reaction. The loading of Co_3N on CdS can restrain the recombination of photogenerated charge carriers, resulting in enhanced photocatalytic activity for H_2 evolution to 137.33 μmol h^{-1} g^{-1} under visible light irradiation ($\lambda > 420$ nm) with the apparent quantum yield (AQY) of 14.9% at 450.[67]

Recently, our group has developed a novel and facile strategy for anchoring well-dispersed metal species on CdS surface as a model photocatalyst for H_2 generation. The heterogeneous photocatalysts were fabricated through the controlled decarboxylation of

the ethylenediaminetetraacetate (EDTA) ligands in mixtures of Co-EDTA complexes together with CdS under argon atmosphere. The resulting thin amorphous layer which contains Co species was uniformly wrapped on the surface of CdS nanoparticles, achieving a high activity of 3.1 mmol h^{-1} (turnover frequency of 626 h^{-1} and AQE of 56.2% at 420 nm).[70] The superior photocatalytic H_2 evolution performance may derive from "carboxylic acid-metal-H" intermediate with favorable thermodynamics and kinetics advantages to maximize the catalytic efficiency of Co active sites.

1.5 Modifications of cobalt active sites toward improved catalytic performance

Many factors can affect the capability of cobalt-based cocatalysts toward photocatalytic H_2 evolution, such as the loading amount, size and coordination environment. Understand the basic conceptions about the modifications on these factors over cocatalyst/semiconductor system are important in order to achieve high activity.

1.5.1 Optimal loading amount

The volcano type trend between the loading amount of a given cocatalyst and the photocatalytic activity has been demonstrated in Figure 1.10.[29] Initially, the introduction of a cocatalyst onto a semiconductor could gradually enhance the photocatalytic water splitting activity by facilitating charge collection and gas evolution reactions. When the loading amount of a cocatalyst on a semiconductor reaches the optimal value, this cocatalyst/semiconductor system achieves the highest activity. However, further loading of the cocatalyst will drastically decrease the photocatalytic activity. This decrease is caused by the following factors: (i) high cocatalyst loading amount that could result in covering the surface active sites of the semiconductor and hindering its contact with sacrificial reagents or water molecules; (ii) excessive loading of cocatalysts on the surface of semiconductors that could shield the incident light, and thus prevent the light absorption and generation of photogenerated electrons and holes inside the semiconductor; (iii) large particle size deteriorates the catalytic properties of cocatalysts or leads to the disappearance of surface effects; and (iv) cocatalysts at high loading amount could act as charge recombination centers, resulting in the decrease of the photocatalytic activity.

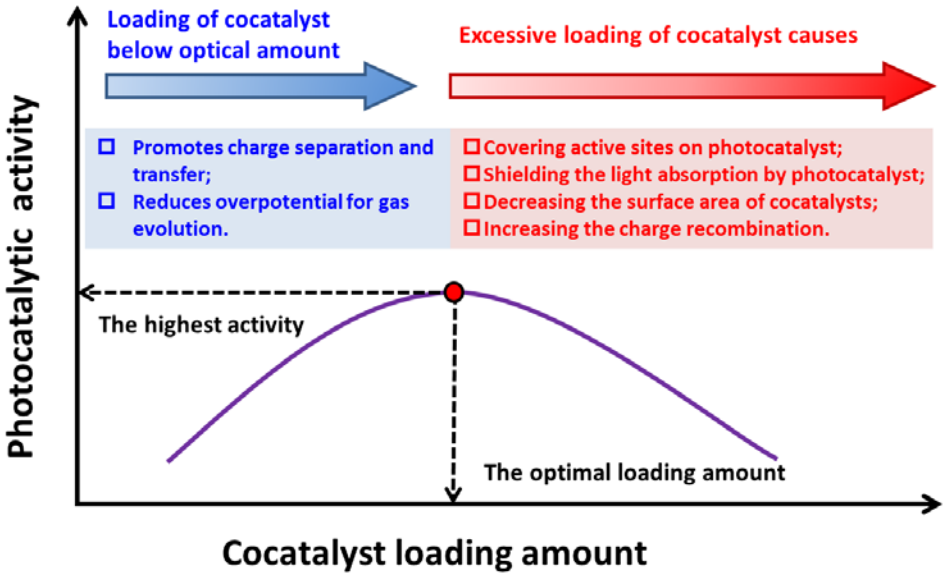

Figure 1.10 The volcano-type relationship between the loading amount of a cocatalyst and the photocatalytic activity of the cocatalyst-loaded semiconductor photocatalyst.[29]

1.5.2 Decrease the size of cocatalyst

When the loading amount of cobalt active sites on semiconductors keep the same, the apparent catalytic activity would be influenced by the size of the cobalt-based cocatalysts. Normally, cobalt-based cocatalysts with smaller size have a larger surface area and more active sites, which result in higher catalytic activity. In addition, cocatalysts with decreased size may exhibit lower barriers for interfacial charge transfer between semiconductors and cocatalysts, thus the charge carriers are less likely to recombine in the bulk of small-sized cocatalysts than in the large-sized ones. As such, the cocatalysts can offer great potential for achieving superior catalytic activity comparable to noble metals. Currently, single-atom catalysts have attracted extensive attention as a new scientific frontier, effectively bridging the fields of heterogeneous and homogeneous catalysis (Figure 1.11).[71] Different from nanoparticles and nanocluster, atomically dispersed cobalt active sites display distinctly different catalytic behavior together with maximizing efficiency owing to the strong size effect and enlarged surface exposed area.[72] It was reported that only small amount of single-atom metals loaded on C_3N_4 are necessary to induce a dramatically improvement of photocatalytic performance.[73] The high effectivity can be contributed to lower recombination rate of photoinduced charge carriers, prolonged lifetime of

photogenerated electrons in addition to favorable surface trap states because of the existence of single-atom metals.

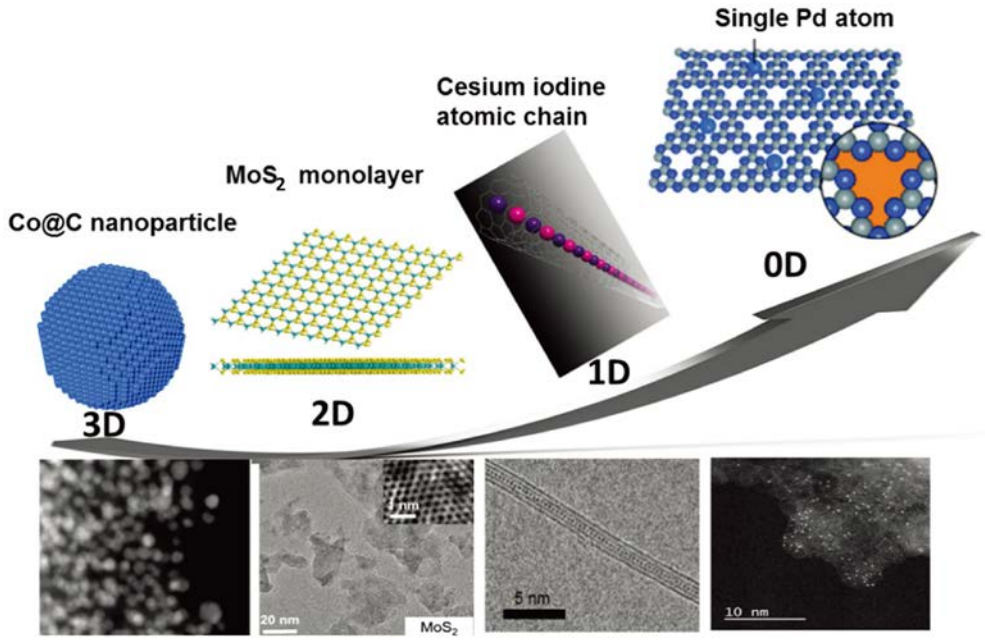

Figure 1.11 Schematic description of research progress for nanoparticle, layered 2D materials, single-atom chains, as well as single-atoms.[71]

Despite numerous merits of single-atom metals, it has been well documented that the surface free energy of metals increases significantly with decreasing particle size, and the tendency of aggregation or sintering during synthetic procedures is usually unavoidable during fabrication processes.[74] Until now, several attempts successfully make an optimization to achieve stable single-atoms dispersion as well as high photocatalytic activity[75-77], while the strategy that applies coordinatively unsaturated material as supporting platform is considered to be the most feasible way in current situation. Previous studies demonstrate that the well-recognized loading amount of single-atoms by conventional synthetic approaches is less than 1.5 wt%. Hence, further developments on design and fabrication of small size/single-atom and high dispersed Co active sites on semiconductors are highly desirable for enhancing photocatalytic H_2 production efficiency.

1.5.3 Coordination environment

Atomic Co^{2+} can incorporate with negatively charged components (such as N, O, P) or redox-active complexes with strong and robust interaction. The developed cobalt-based

cocatalysts which contain atomically dispersed Co^{2+} are suitable models for the investigation of the reaction kinetics of the active site in atomic level. Recently, cobalt-based complexes containing Co_1-N_4 square planar-like structure have been explored as effective H_2 evolution catalysts. Theoretical calculations indicate that H atoms are preferably adsorbed on N atoms which are neighboring the Co atom directly. Meanwhile, the four N atoms around Co possess an evident increase of charge density, suggesting that photoelectrons can easily transfer from electron-donating N to Co atom via Co-N bond upon photoexcitation. Consequently, the photogenerated e^- can participate in the H^+ reduction reaction more productively at Co sites.[78] By changing the coordination environment of the Co atoms, Co_1-P_4 can be obtained through a facile phosphidation under PH_3 atmosphere (Figure 1.12a). As reported by Liu et al., the Co_1-P_4 sites devote to achieve high catalytic ability and efficient charge separation.[79] Importantly, the cobalt-containing species can be well isolated to achieve atomic dispersion owing to the strong confinement effect of the g-C_3N_4 as confirmed by atomic-resolution high-angle-annular-dark-field scanning transmission electron microscopy (HAADF-STEM) (Figure 1.12b-e). The existence of Co_1-P_4 sites can assist efficient electron-hole separation and accelerated photoexciton dissociation at the interface of Co_1-P_4/g-C_3N_4 (Figure 1.12f and 1.12g). Besides that, Co is known to demonstrate multiple oxidation states with both high and low spin electronic configuration, which enable multiple coordination geometries depending on its surrounding ligands.[80] Therefore, many cobalt-based macrocycles such as Co(II) tetraazo-macrocycles, cobalt porphyrins, and cobaloximes are often targeted for catalyst development because of their typically high metal binding affinity and consequently high stability under catalytic conditions. In this regards, the modifications on the coordination environment of cobalt sites can greatly alter the chemical and physical properties and bring great enhancement to catalytic performance.

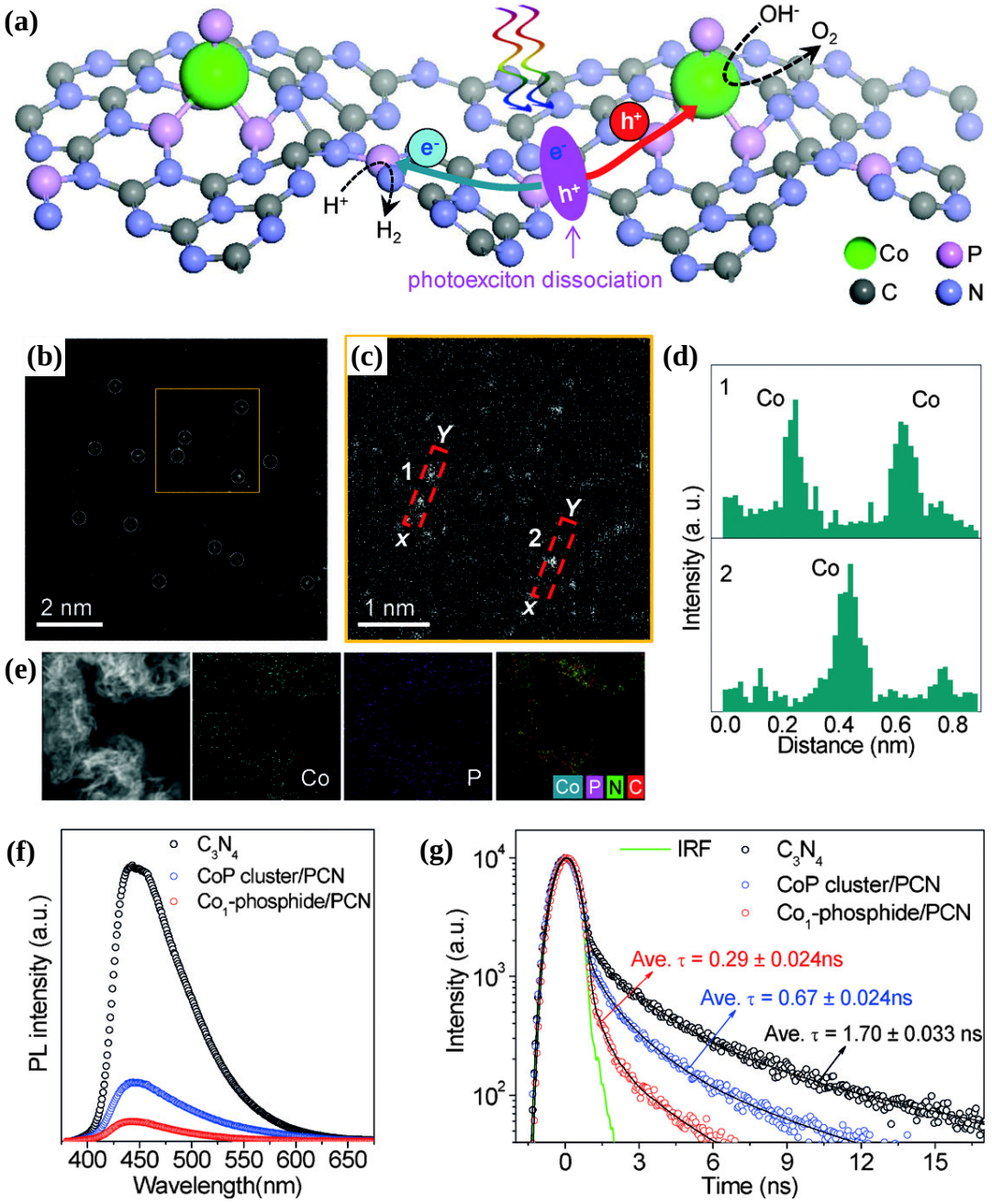

Figure 1.12 (a) Schematic illustration of the photocatalytic H_2 evolution on the Co_1-P_4/g-C_3N_4, in which the photogenerated carriers are spatially separated and transferred to active sites. (b) and (c) HAADF-STEM image, (d) Intensity profiles, and (e) Elemental mapping of Co_1-P_4/g-C_3N_4. (f) Steady-state fluorescence spectra at 298 K. (g) Corresponding time-resolved fluorescence kinetics.[33-35]

1.6 Thesis motivations and organization

The development of efficient and stable photocatalysts which enable H_2 generation from water are highly desired for the use of renewable solar light and water as a

valuable and environment-friendly approach. On the basis of the above-mentioned overview, the efficiency of photocatalytic reaction system can be controlled by three critical factors: light absorption, photogenerated charges separation, and surface chemical reactions. Accordingly, I have provided my strategies for constructing a robust and efficient photocatalytic system for H_2 generation: (i) Utilizing CdS as the photocatalyst can provide desirable photogenerated electrons for H_2 production under visible-light irradiation; (ii) Rational construction of suitable cobalt-based cocatalysts with more active sites and lowering the reaction barrier for enhancing H_2 production; (iii) Modifying the interface between CdS and cobalt-based cocatalysts for charge modulation as well as photogenerated charge separation.

In this dissertation, I am focusing on the rational construction and modification of cobalt active sites on CdS nanoparticles in order to achieve efficient photocatalytic H_2 generation. First, Co single active sites coordinated on BP nanosheets have been applied in photocatalytic H_2 evolution as a novel cocatalyst. The atomically dispersed cobalt active sites and improved electron-hole separation efficiency through additional Co-P(O) charge transfer channel greatly improve the photocatalytic performance of CdS. Then, I have proposed a novel and convenient preparation strategy to fabricate ultrafine CoP nanoparticles by utilizing triphenylphosphine (PPh_3) as phosphorous source and applied into photocatalytic H_2 evolution. By analyzing the interaction between surface dopants on CdS and CoP species, the basic roles of phosphorus toward the modification of cobalt active sites have been elucidated. Finally, carbon matrix encapsulated dual cobalt active species (Co and CoO_x) on the surface of CdS have been developed for high-efficient photocatalytic H_2 evolution under visible-light irradiation. The cooperation between Co (reduction cocatalyst) and CoO_x (oxidation cocatalyst and hole acceptor) has been regarded to play an important role for high-efficient photocatalytic H_2 evolution. In addition, the intimate contact between CdS and cobalt active species in carbon matrix that formed after calcination could also enable fast charge transfer for efficient photocatalytic reactions. Thus, the object of this thesis is to realize controllable growth and distribution of cobalt-based cocatalysts as well as modify the cobalt active sites with improved efficiency and stability for photocatalytic H_2 generation. This dissertation is divided into five chapters. A summary of the remaining four chapters is described as below:

Chapter 2 Single cobalt atom anchored black phosphorous nanosheets as an effective cocatalyst promotes photocatalysis

Downsizing the cocatalyst to clusters or even single atoms has been regarded as an effective strategy to maximizing the atom utilization efficiency of active sites. However, the surface free energy of metals increases significantly with decreasing particle size, promoting the aggregation of small clusters. It is believed that the coordinatively unsaturated materials which strongly interact with the metal species can be used as supporting platform to stabilize the dispersion of isolated metal sites and achieve higher performance. In this chapter, two-dimensional black phosphorous (BP) has been chosen as the substrate for dispersing single-atom cobalt active sites, and a novel nanostructure that cobalt atomically dispersed on two-dimensional BP nanosheets were designed as cocatalyst for improving photocatalytic H_2 evolution. Owing to the intrinsic lone pair electrons, cobalt ions can be stably anchored on the surface of BP nanosheets through Co-P coordination. It was expected that the coordination of Co and P could form new charge transfer channel for prolonging the charge carrier lifetime and improving photocatalytic reduction capability. Therefore, the integration of atomically dispersed metal Co with BP nanosheets substrate as a noble-metal-free cocatalyst can be expected for improving photocatalytic H_2 evolution over CdS under visible light irradiation.

Chapter 3 Metal dopants mediated interfacial engineering of ultrafine CoP nanoparticles for promoting photocatalytic H_2 evolution

Due to the inefficient charge transfer through the interface of semiconductor and cocatalyst, the photocatalytic water splitting efficiency is still far from expectation even with the assistance of cocatalysts. In this consideration, effective interfacial engineering of cocatalyst could be the same important as the development of novel noble-metal-free cocatalyst for H_2 evolution. In this chapter, a novel and facile preparation strategy has been developed to fabricate ultrafine CoP nanoparticles on the surface of CdS. By utilizing organophosphorus compound triphenylphosphine (PPh_3) as phosphorous source, the as-fabricated CoP nanoparticles were intrinsically encapsulated by carbon layer and applied as cocatalyst into photocatalytic H_2 evolution. This synthesis strategy does not require flammable compounds (e.g. PH_3 or H_2, etc.) or corrosive conditions, which makes it much safer and easier to manipulate comparing to conventional methods. Specially, an intimate contact between CdS and CoP can be realized owing to the ascending reducibility of CdS after Ca^{2+} modification. It was believed that fast charge

injection from Ca-modified CdS to CoP active sites would be realized through the newly formed charge transfer channel. Moreover, a reduced Gibbs free energy for H* adsorption ($|\Delta G_{H^*}|$) was found after Ca^{2+} modification. It was expected that Ca^{2+} dopants as surface trapping sites on CdS may lead to strong trap-state emission together with fast charge transfer at the interface of CdS and CoP for improving photocatalytic H_2 generation.

Chapter 4 Rational construction of dual cobalt active species encapsulated by ultrathin carbon matrix from MOF for boosting photocatalytic H_2 generation

After understanding the important roles of active sites and interfacial charge transfer behaviors for catalytic H_2 production, it is highly desired to develop feasible strategies for rational construction of cobalt active sites with uniform dispersion and modification of charge transfer behaviors at the interface of CdS and cobalt-based cocatalysts simultaneously. In this chapter, the spatially separated Co and CoO_x dual cocatalyst encapsulated in carbon substrate was constructed by annealing ultrathin two-dimensional (2D) Co-based MOF (Co-MOF) nanosheets on the surface of CdS. The fundamental roles of 2D-MOF derived carbon matrix toward rational construction of dual cobalt active species were visualized by combining a series of in-situ and ex-situ temperature-dependent analytic strategies. The cooperation between Co (reduction cocatalyst) and CoO_x (oxidation cocatalyst and hole acceptor) has been expected to play a beneficial role for improving photocatalytic H_2 evolution performance. In addition, the intimate contact between CdS and cobalt active species in carbon matrix that formed after calcination could also enable fast charge transfer for efficient catalytic reactions. Thus, controllable designation on dual cobalt-based cocatalyst and modulation on interfacial coordination environment may contribute to desired photocatalytic performance as a result.

Chapter 5 General conclusions and future prospects

This chapter presents an overall summary and conclusion of this dissertation and gives the prospects for future work.

References

1. Li, L.; Lin, J.; Wu, N.; Xie, S.; Meng, C.; Zheng, Y.; Wang, X.; Zhao, Y., Review and outlook on the international renewable energy development. *Energy and Built Environment* **2020**.

2. Abe, J. O.; Popoola, A. P. I.; Ajenifuja, E.; Popoola, O. M., Hydrogen energy, economy and storage: Review and recommendation. *International Journal of Hydrogen Energy* **2019,** *44* (29), 15072-15086.

3. Quarton, C. J.; Tlili, O.; Welder, L.; Mansilla, C.; Blanco, H.; Heinrichs, H.; Leaver, J.; Samsatli, N. J.; Lucchese, P.; Robinius, M.; Samsatli, S., The curious case of the conflicting roles of hydrogen in global energy scenarios. *Sustainable Energy & Fuels* **2020,** *4* (1), 80-95.

4. Staffell, I.; Scamman, D.; Velazquez Abad, A.; Balcombe, P.; Dodds, P. E.; Ekins, P.; Shah, N.; Ward, K. R., The role of hydrogen and fuel cells in the global energy system. *Energy & Environmental Science* **2019,** *12* (2), 463-491.

5. Ganguly, P.; Harb, M.; Cao, Z.; Cavallo, L.; Breen, A.; Dervin, S.; Dionysiou, D. D.; Pillai, S. C., 2D Nanomaterials for Photocatalytic Hydrogen Production. *ACS Energy Letters* **2019,** *4* (7), 1687-1709.

6. Nikolaidis, P.; Poullikkas, A., A comparative overview of hydrogen production processes. *Renewable and Sustainable Energy Reviews* **2017,** *67*, 597-611.

7. Tong, H.; Ouyang, S.; Bi, Y.; Umezawa, N.; Oshikiri, M.; Ye, J., Nano-photocatalytic materials: possibilities and challenges. *Advanced Materials* **2012,** *24* (2), 229-51.

8. Meng, X.; Liu, L.; Ouyang, S.; Xu, H.; Wang, D.; Zhao, N.; Ye, J., Nanometals for solar-to-chemical energy conversion: from semiconductor-based photocatalysis to plasmon-mediated photocatalysis and photo-thermocatalysis. *Advanced Materials* **2016,** *28* (32), 6781-6803.

9. Li, H.; Tu, W.; Zhou, Y.; Zou, Z., Z-Scheme photocatalytic systems for promoting photocatalytic performance: recent progress and future challenges. *Advanced Science* **2016,** *3* (11), 1500389.

10. Fujishima, A.; Honda, K., Electrochemical Photolysis of Water at a Semiconductor Electrode. *Nature* **1972,** *238* (5358), 37-38.

11. Sun, B.; Zhou, W.; Li, H.; Ren, L.; Qiao, P.; Li, W.; Fu, H., Synthesis of Particulate Hierarchical Tandem Heterojunctions toward Optimized Photocatalytic Hydrogen Production. *Advanced Materials* **2018,** *30* (43), 1804282.

12. Guo, Q.; Zhou, C.; Ma, Z.; Yang, X., Fundamentals of TiO_2 Photocatalysis: Concepts, Mechanisms, and Challenges. *Advanced Materials* **2019,** *31* (50), 1901997.

13. Li, X.; Yu, J.; Low, J.; Fang, Y.; Xiao, J.; Chen, X., Engineering heterogeneous semiconductors for solar water splitting. *Journal of Materials Chemistry A* **2015,** *3* (6), 2485-2534.

14. Chen, Z.; Jaramillo, T. F.; Deutsch, T. G.; Kleiman-Shwarsctein, A.; Forman, A. J.; Gaillard, N.; Garland, R.; Takanabe, K.; Heske, C.; Sunkara, M.; McFarland, E. W.; Domen, K.; Miller, E. L.; Turner, J. A.; Dinh, H. N., Accelerating materials development for photoelectrochemical hydrogen production: Standards for methods, definitions, and reporting protocols. *Journal of Materials Research* **2010,** *25* (1), 3-16.

15. Jin, E.; Lan, Z.; Jiang, Q.; Geng, K.; Li, G.; Wang, X.; Jiang, D., 2D sp^2 Carbon-Conjugated Covalent Organic Frameworks for Photocatalytic Hydrogen Production from Water. *Chem* **2019,** *5* (6), 1632-1647.

16. Nakata, K.; Fujishima, A., TiO_2 photocatalysis: Design and applications. *Journal of Photochemistry and Photobiology C: Photochemistry Reviews* **2012,** *13* (3), 169-189.

17. Yu, B.; Zhou, Y.; Li, P.; Tu, W.; Li, P.; Tang, L.; Ye, J.; Zou, Z., Photocatalytic reduction of CO_2 over Ag/TiO_2 nanocomposites prepared with a simple and rapid silver mirror method. *Nanoscale* **2016,** *8* (23), 11870-11874.

18. Qi, K.; Cheng, B.; Yu, J.; Ho, W., A review on TiO_2-based Z-scheme photocatalysts. *Chinese Journal of Catalysis* **2017,** *38* (12), 1936-1955.

19. Liu, G.; Sheng, Y.; Ager, J. W.; Kraft, M.; Xu, R., Research advances towards large-scale solar hydrogen production from water. *EnergyChem* **2019,** *1* (2), 100014.

20. Chen, X.; Shen, S.; Guo, L.; Mao, S. S., Semiconductor-based Photocatalytic Hydrogen Generation. *Chemical reviews* **2010,** *110* (11), 6503-6570.

21. Luo, C.; Ren, X.; Dai, Z.; Zhang, Y.; Qi, X.; Pan, C., Present perspectives of advanced characterization techniques in TiO_2-based photocatalysts. *ACS Applied Materials & Interfaces* **2017,** *9* (28), 23265-23286.

22. Serpone, N.; Emeline, A. V., Semiconductor Photocatalysis — Past, Present, and Future Outlook. *The Journal of Physical Chemistry Letters* **2012,** *3* (5), 673-677.

23. Yuan, Y.-J.; Chen, D.; Yu, Z.-T.; Zou, Z.-G., Cadmium sulfide-based nanomaterials for photocatalytic hydrogen production. *Journal of Materials Chemistry A* **2018,** *6* (25), 11606-11630.

24. Silva, L. A.; Ryu, S. Y.; Choi, J.; Choi, W.; Hoffmann, M. R., Photocatalytic Hydrogen Production with Visible Light over Pt-Interlinked Hybrid Composites of Cubic-Phase and Hexagonal-Phase CdS. *The Journal of Physical Chemistry C* **2008,** *112* (32), 12069-12073.

25. Darwent, J. R.; Porter, G., Photochemical hydrogen production using cadmium sulphide suspensions in aerated water. *Journal of the Chemical Society, Chemical Communications* **1981,** (4), 145-146.

26. Monico, L.; Chieli, A.; De Meyer, S.; Cotte, M.; de Nolf, W.; Falkenberg, G.; Janssens, K.; Romani, A.; Miliani, C., Role of the Relative Humidity and the Cd/Zn Stoichiometry in the Photooxidation Process of Cadmium Yellows ($CdS/Cd_{1-x}Zn_xS$) in Oil Paintings. *Chemistry – A European Journal* **2018,** *24* (45), 11584-11593.

27. Wang, Z.; Fan, J.; Cheng, B.; Yu, J.; Xu, J., Nickel-based cocatalysts for photocatalysis: Hydrogen evolution, overall water splitting and CO_2 reduction. *Materials Today Physics* **2020,** *15*, 100279.

28. Sabatier, P., Hydrogénations et déshydrogénations par catalyse. *Berichte der deutschen chemischen Gesellschaft* **1911,** *44* (3), 1984-2001.

29. Ran, J.; Zhang, J.; Yu, J.; Jaroniec, M.; Qiao, S. Z., Earth-abundant cocatalysts for semiconductor-based photocatalytic water splitting. *Chemical Society Reviews* **2014,** *43* (22), 7787-7812.

30. Twilton, J.; Le, C. C.; Zhang, P.; Shaw, M. H.; Evans, R. W.; MacMillan, D. W. C., The merger of transition metal and photocatalysis. *Nature Reviews Chemistry* **2017,** *1* (7), 0052.

31. Fei, H.; Dong, J.; Arellano-Jiménez, M. J.; Ye, G.; Kim, N. D.; Samuel, E. L. G.; Peng, Z.; Zhu, Z.; Qin, F.; Bao, J.; Yacaman, M. J.; Ajayan, P. M.; Chen, D.; Tour, J. M., Atomic cobalt on nitrogen-doped graphene for hydrogen generation. *Nature Communications* **2015,** *6*, 8668.

32. Lang, D.; Cheng, F.; Xiang, Q., Enhancement of photocatalytic H_2 production activity of CdS nanorods by cobalt-based cocatalyst modification. *Catalysis Science & Technology* **2016,** *6* (16), 6207-6216.

33. Haynes, W. M., *CRC handbook of chemistry and physics*. CRC press: 2014.

34. Chen, W.; Wang, Y.; Liu, M.; Gao, L.; Mao, L.; Fan, Z.; Shangguan, W., In situ photodeposition of cobalt on CdS nanorod for promoting photocatalytic hydrogen production under visible light irradiation. *Applied Surface Science* **2018,** *444*, 485-490.

35. Jiang, D.; Chen, X.; Zhang, Z.; Zhang, L.; Wang, Y.; Sun, Z.; Irfan, R. M.; Du, P., Highly efficient simultaneous hydrogen evolution and benzaldehyde production using cadmium sulfide nanorods decorated with small cobalt nanoparticles under visible light. *Journal of Catalysis* **2018,** *357*, 147-153.

36. Zhu, Y.; Wan, T.; Wen, X.; Chu, D.; Jiang, Y., Tunable Type I and II heterojunction of CoO_x nanoparticles confined in g-C_3N_4 nanotubes for photocatalytic hydrogen production. *Applied Catalysis B: Environmental* **2019,** *244*, 814-822.

37. Liu, Y.; Ding, S.; Shi, Y.; Liu, X.; Wu, Z.; Jiang, Q.; Zhou, T.; Liu, N.; Hu, J., Construction of CdS/CoO_x core-shell nanorods for efficient photocatalytic H_2 evolution. *Applied Catalysis B: Environmental* **2018,** *234*, 109-116.

38. Zhang, J.; Yu, Z.; Gao, Z.; Ge, H.; Zhao, S.; Chen, C.; Chen, S.; Tong, X.; Wang, M.; Zheng, Z.; Qin, Y., Porous TiO_2 Nanotubes with Spatially Separated Platinum and CoO_x Cocatalysts Produced by Atomic Layer Deposition for Photocatalytic Hydrogen Production. *Angewandte Chemie International Edition* **2017,** *56* (3), 816-820.

39. Zhang, W.; Cui, L.; Liu, J., Recent advances in cobalt-based electrocatalysts for hydrogen and oxygen evolution reactions. *Journal of Alloys and Compounds* **2020,** *821*, 153542.

40. Moniruddin, M.; Oppong, E.; Stewart, D.; McCleese, C.; Roy, A.; Warzywoda, J.; Nuraje, N., Designing CdS-Based Ternary Heterostructures Consisting of Co-Metal and CoOx Cocatalysts for Photocatalytic H2 Evolution under Visible Light. *Inorganic chemistry* **2019,** *58* (18), 12325-12333.

41. Wang, J.; Xu, Q.; Liu, M.; Wang, K.; Wang, Z.; Qu, P., The synergetic effect of N, S-codoped carbon and CoO_x nanodots derived from ZIF-67 as a highly efficient cocatalyst over CdS nanorods. *Sustainable Energy & Fuels* **2020,** *4* (4), 1954-1962.

42. Xiao, P.; Sk, M. A.; Thia, L.; Ge, X.; Lim, R. J.; Wang, J.-Y.; Lim, K. H.; Wang, X., Molybdenum phosphide as an efficient electrocatalyst for the hydrogen evolution reaction. *Energy & Environmental Science* **2014,** *7* (8), 2624-2629.

43. Wang, J.; Yang, W.; Liu, J., CoP_2 nanoparticles on reduced graphene oxide sheets as a super-efficient bifunctional electrocatalyst for full water splitting. *Journal of Materials Chemistry A* **2016,** *4* (13), 4686-4690.

44. Pan, Y.; Liu, Y.; Zhao, J.; Yang, K.; Liang, J.; Liu, D.; Hu, W.; Liu, D.; Liu, Y.; Liu, C., Monodispersed nickel phosphide nanocrystals with different phases: synthesis, characterization and electrocatalytic properties for hydrogen evolution. *Journal of Materials Chemistry A* **2015,** *3* (4), 1656-1665.

45. Callejas, J. F.; Read, C. G.; Popczun, E. J.; McEnaney, J. M.; Schaak, R. E., Nanostructured Co_2P electrocatalyst for the hydrogen evolution reaction and direct comparison with morphologically equivalent CoP. *Chemistry of Materials* **2015,** *27* (10), 3769-3774.

46. Wu, T.; Pi, M.; Zhang, D.; Chen, S., 3D structured porous CoP_3 nanoneedle arrays as an efficient bifunctional electrocatalyst for the evolution reaction of hydrogen and oxygen. *Journal of Materials Chemistry A* **2016,** *4* (38), 14539-14544.

47. Wang, J.; Liu, Z.; Zheng, Y.; Cui, L.; Yang, W.; Liu, J., Recent advances in cobalt phosphide based materials for energy-related applications. *Journal of Materials Chemistry A* **2017,** *5* (44), 22913-22932.

48. Wu, T.; Pi, M.; Wang, X.; Zhang, D.; Chen, S., Three-dimensional metal–organic framework derived porous CoP_3 concave polyhedrons as superior bifunctional electrocatalysts for the evolution of hydrogen and oxygen. *Physical Chemistry Chemical Physics***2017,** *19* (3), 2104-2110.

49. Shi, Y.; Zhang, B., Recent advances in transition metal phosphide nanomaterials: synthesis and applications in hydrogen evolution reaction. *Chemical Society Reviews* **2016,** *45* (6), 1529-1541.

50. Zhang, J.; Tian, B.; Wang, L.; Xing, M.; Lei, J., Transition Metal Phosphide As Cocatalysts for Semiconductor-Based Photocatalytic Hydrogen Evolution Reaction. In *Photocatalysis*, Springer: 2018; pp 375-402.

51. Carenco, S.; Portehault, D.; Boissiere, C.; Mezailles, N.; Sanchez, C., Nanoscaled metal borides and phosphides: recent developments and perspectives. *Chemical Reviews* **2013,** *113* (10), 7981-8065.

52. Tian, B.; Li, Z.; Zhen, W.; Lu, G., Uniformly sized (112) facet Co_2P on graphene for highly effective photocatalytic hydrogen evolution. *The Journal of Physical Chemistry C* **2016,** *120* (12), 6409-6415.

53. Li, S.; Wang, L.; Liu, S.; Xu, B.; Xiao, N.; Gao, Y.; Song, W.; Ge, L.; Liu, J., In situ synthesis of strongly coupled Co_2P-CdS nanohybrids: an effective strategy to regulate photocatalytic hydrogen evolution activity. *ACS Sustainable Chemistry & Engineering* **2018,** *6* (8), 9940-9950.

54. Chao, Y.; Zheng, J.; Zhang, H.; Li, F.; Yan, F.; Tan, Y.; Zhu, Z., Oxygen-incorporation in Co_2P as a non-noble metal cocatalyst to enhance photocatalysis for reducing water to H_2 under visible light. *Chemical Engineering Journal* **2018,** *346*, 281-288.

55. Cao, S.; Chen, Y.; Hou, C.-C.; Lv, X.-J.; Fu, W.-F., Cobalt phosphide as a highly active non-precious metal cocatalyst for photocatalytic hydrogen production under visible light irradiation. *Journal of Materials Chemistry A* **2015,** *3* (11), 6096-6101.

56. Yang, H.; Zhang, Y.; Hu, F.; Wang, Q., Urchin-like CoP nanocrystals as hydrogen evolution reaction and oxygen reduction reaction dual-electrocatalyst with superior stability. *Nano Letter* **2015,** *15* (11), 7616-7620.

57. Reddy, D. A.; Choi, J.; Lee, S.; Kim, Y.; Hong, S.; Kumar, D. P.; Kim, T. K., Hierarchical dandelion-flower-like cobalt-phosphide modified CdS/reduced graphene oxide-MoS_2 nanocomposites as a noble-metal-free catalyst for efficient hydrogen evolution from water. *Catalysis Science & Technology* **2016,** *6* (16), 6197-6206.

58. Wang, J.; Wang, P.; Wang, C.; Ao, Y., In-situ synthesis of well dispersed CoP nanoparticles modified CdS nanorods composite with boosted performance for photocatalytic hydrogen evolution. *International Journal of Hydrogen Energy* **2018,** *43* (32), 14934-14943.

59. Wang, P.; Wu, T.; Ao, Y.; Wang, C., Fabrication of noble-metal-free CdS nanorods-carbon layer-cobalt phosphide multiple heterojunctions for efficient and robust photocatalyst hydrogen evolution under visible light irradiation. *Renewable Energy* **2019,** *131*, 180-186.

60. Sun, Z.; Lv, B.; Li, J.; Xiao, M.; Wang, X.; Du, P., Core–shell amorphous cobalt phosphide/cadmium sulfide semiconductor nanorods for exceptional photocatalytic

hydrogen production under visible light. *Journal of Materials Chemistry A* **2016,** *4* (5), 1598-1602.

61. Dong, Y.; Kong, L.; Wang, G.; Jiang, P.; Zhao, N.; Zhang, H., Photochemical synthesis of Co_xP as cocatalyst for boosting photocatalytic H_2 production via spatial charge separation. *Applied Catalysis B: Environmental* **2017,** *211*, 245-251.

62. Xu, Y.; Zeng, L.-Z.; Fu, Z.-C.; Li, C.; Yang, Z.; Chen, Y.; Fu, W.-F., Photocatalytic oxidation of arylalcohols to aromatic aldehydes promoted by hydroxyl radicals over a CoP/CdS photocatalyst in water with hydrogen evolution. *Catalysis Science & Technology* **2018,** *8* (10), 2540-2545.

63. Cao, S.; Chen, Y.; Wang, H.; Chen, J.; Shi, X.; Li, H.; Cheng, P.; Liu, X.; Liu, M.; Piao, L., Ultrasmall CoP Nanoparticles as Efficient Cocatalysts for Photocatalytic Formic Acid Dehydrogenation. *Joule* **2018,** *2* (3), 549-557.

64. Cargnello, M., Formic Acid Dehydrogenation: Phosphides Strike Again. *Joule* **2018,** *2* (3), 379-380.

65. Qiu, B.; Zhu, Q.; Du, M.; Fan, L.; Xing, M.; Zhang, J., Efficient Solar Light Harvesting CdS/Co9S8 Hollow Cubes for Z-Scheme Photocatalytic Water Splitting. *Angewandte Chemie International Edition* **2017,** *56* (10), 2684-2688.

66. Zhou, X.; Jin, J.; Zhu, X.; Huang, J.; Yu, J.; Wong, W.-Y.; Wong, W.-K., New Co(OH)2/CdS nanowires for efficient visible light photocatalytic hydrogen production. *Journal of Materials Chemistry A* **2016,** *4* (14), 5282-5287.

67. Chen, H.; Jiang, D.; Sun, Z.; Irfan, R. M.; Zhang, L.; Du, P., Cobalt nitride as an efficient cocatalyst on CdS nanorods for enhanced photocatalytic hydrogen production in water. *Catalysis Science & Technology* **2017,** *7* (7), 1515-1522.

68. Xu, Y.; Ye, Y.; Liu, T.; Wang, X.; Zhang, B.; Wang, M.; Han, H.; Li, C., Unraveling a Single-Step Simultaneous Two-Electron Transfer Process from Semiconductor to Molecular Catalyst in a CoP_y/CdS Hybrid System for Photocatalytic H_2 Evolution under Strong Alkaline Conditions. *Journal of the American Chemical Society* **2016,** *138* (34), 10726-10729.

69. Zhang, L. J.; Zheng, R.; Li, S.; Liu, B. K.; Wang, D. J.; Wang, L. L.; Xie, T. F., Enhanced Photocatalytic H_2 Generation on Cadmium Sulfide Nanorods with Cobalt Hydroxide as Cocatalyst and Insights into Their Photogenerated Charge Transfer Properties. *ACS Applied Materials & Interfaces* **2014,** *6* (16), 13406-13412.

70. Zhao, G.; Sun, Y.; Zhou, W.; Wang, X.; Chang, K.; Liu, G.; Liu, H.; Kako, T.; Ye, J., Superior Photocatalytic H_2 Production with Cocatalytic Co/Ni Species Anchored on Sulfide Semiconductor. *Advanced Materials* **2017,** *29* (40), 1703258.

71. Zhang, H.; Liu, G.; Shi, L.; Ye, J., Single-Atom Catalysts: Emerging Multifunctional Materials in Heterogeneous Catalysis. *Advanced Energy Materials* **2018,** *8* (1), 1701343.

72. Zhang, H.; Liu, G.; Shi, L.; Ye, J., Single-atom catalysts: emerging multifunctional materials in heterogeneous catalysis. *Advanced Energy Materials* **2018,** *8* (1), 1701343.

73. Gao, G.; Jiao, Y.; Waclawik, E. R.; Du, A., Single atom (Pd/Pt) supported on graphitic carbon nitride as an efficient photocatalyst for visible-light reduction of carbon dioxide. *Journal of the American Chemical Society* **2016,** *138* (19), 6292-6297.

74. Yang, X.-F.; Wang, A.; Qiao, B.; Li, J.; Liu, J.; Zhang, T., Single-Atom Catalysts: A New Frontier in Heterogeneous Catalysis. *Accounts of Chemical Research* **2013,** *46* (8), 1740-1748.

75. Moliner, M.; Gabay, J. E.; Kliewer, C. E.; Carr, R. T.; Guzman, J.; Casty, G. L.; Serna, P.; Corma, A., Reversible Transformation of Pt Nanoparticles into Single Atoms inside High-Silica Chabazite Zeolite. *Journal of the American Chemical Society* **2016,** *138* (48), 15743-15750.

76. Fang, X.; Shang, Q.; Wang, Y.; Jiao, L.; Yao, T.; Li, Y.; Zhang, Q.; Luo, Y.; Jiang, H. L., Single Pt atoms confined into a metal-organic framework for efficient photocatalysis. *Advanced Materials* **2018,** *30* (7), 1705112.

77. Jiang, K.; Siahrostami, S.; Zheng, T.; Hu, Y.; Hwang, S.; Stavitski, E.; Peng, Y.; Dynes, J.; Gangisetty, M.; Su, D.; Attenkofer, K.; Wang, H., Isolated Ni single atoms in graphene nanosheets for high-performance CO_2 reduction. *Energy & Environmental Science* **2018,** *11* (4), 893-903.

78. Cao, Y.; Chen, S.; Luo, Q.; Yan, H.; Lin, Y.; Liu, W.; Cao, L.; Lu, J.; Yang, J.; Yao, T.; Wei, S., Atomic-Level Insight into Optimizing the Hydrogen Evolution Pathway over a Co_1-N_4 Single-Site Photocatalyst. *Angewandte Chemie International Edition* **2017,** *56* (40), 12191-12196.

79. Liu, W.; Cao, L.; Cheng, W.; Cao, Y.; Liu, X.; Zhang, W.; Mou, X.; Jin, L.; Zheng, X.; Che, W.; Liu, Q.; Yao, T.; Wei, S., Single-Site Active Cobalt-Based

Photocatalyst with a Long Carrier Lifetime for Spontaneous Overall Water Splitting. *Angewandte Chemie International Edition* **2017,** *56* (32), 9312-9317.

80. Kohler, L.; Niklas, J.; Johnson, R. C.; Zeller, M.; Poluektov, O. G.; Mulfort, K. L., Molecular Cobalt Catalysts for H_2 Generation with Redox Activity and Proton Relays in the Second Coordination Sphere. *Inorganic chemistry* **2019,** *58* (2), 1697-1709.

Chapter 2 Single cobalt atom anchored black phosphorous nanosheets as an effective cocatalyst promotes photocatalysis

2.1 Introduction

Photocatalytic reaction that can directly drill solar power is essential for next-generation portable and renewable energy applications.[1-3] To develop a high-efficient photocatalytic system, both photogenerated electron-hole pair separation efficiency and activation energy barrier on catalyst surface should be carefully taken into consideration.[4] Toward this end, cocatalysts with the abilities to retard charge carriers recombination and promote surface reactions are commonly used in various photocatalytic reactions such as water splitting, CO_2 reduction, etc.[5-8] Up to now, the searching for efficient cocatalysts becomes the utmost priority. Noble metals have been extensively investigated and metal Pt shows more favorite performance than other metals owing to its optimized work function and overpotential for H_2 evolution.[9] Unfortunately, considering the rarity and expensive cost of noble metals, the exploration of earth-abundant materials as the cocatalyst becomes indispensable.

To date, earth-abundant transition metals such as Co, Ni, Cu and their cluster show promising cocatalytic performance in various photocatalytic reactions.[10-15] Differing from other non-noble metals, Co possesses less 3d-orbital electrons and emerges as a promising catalyst for energy conversion and storage especially for H_2 evolution.[16] The existed cobalt can incorporate with semiconductor, by collecting electrons and providing effective active sites to enhance the ultimate photocatalytic performance in thermodynamics and kinetics aspects during catalytic process.[17] Recent advances indicate atomically dispersed metals (noted as single-atom metal) demonstrate remarkable catalytic activity owing to the strong size effect and enlarged surface exposed area.[18, 19] It was reported that only small amount of single-atom metals loaded on C_3N_4 are necessary to induce a dramatically improvement of photocatalytic performance.[20] The high effectivity can be contributed to longer lifetime of photogenerated electrons in addition to favorable surface trap states because of the existence of single-atom metals.

Despite numerous merits of single-atom metals, the tendency of aggregation is usually unavoidable during fabrication processes.[21] Currently, several attempts

successfully make an optimization to achieve stable single-atoms dispersion as well as high photocatalytic activity[22-24], while the strategy that applies coordinatively unsaturated material as supporting platform is considered to be the most feasible way in current situation. Recently, newly developed graphene-like semiconductor black phosphorous (BP) has gained considerable interests for photo-related applications.[25-27] In the atomic structure of BP, only three of the five electrons in the outermost orbital are covalently bonded to each other, leaving the lone pair electrons to interact with metal ions. Apart from that, the relatively high carrier mobility in association with tunable direct bandgap together make it a promising substrate for stable catalyst dispersing.[28, 29] Recent progress achieved by Bai and co-workers provided solid evidence on BP/Pt heterostructure for demonstrating enhanced stability as well as accelerated charge separation under the influence of strong BP-Pt interaction.[30] Meanwhile, Yuan et al. indicated the important role of Co-P bonds to facilitate charge-carrier transfer for efficient H_2 production.[31] Thereby, the adoption of BP nanosheets as the support material is deemed to trigger high stability and efficient electron-hole separation for atomically dispersed metals, prolonging the charge carrier lifetime and improving the photocatalytic reduction efficiency in consequence. In this regard, the integration of atomically dispersed metal Co with BP nanosheets substrate can be expected for realizing excellent photocatalytic activity. However, no related work has been reported as we known.

Herein, I prepared coordinated Co on BP nanosheets (BP-Co) as a cocatalyst and applied it into photocatalytic H_2 evolution and CO_2 reduction. The H_2 production performance evaluation reveals that BP-Co can dramatically improve the photocatalytic performance of CdS, reaching an attractive H_2 production rate of 345.4 μmol h^{-1} (18 times higher than that of pure CdS). Apart from that, BP-Co can also be used as an effective cocatalyst to promote photocatalytic CO_2 reduction in the presence of photosensitizer $[Ru(2, 2'\text{-bipyridy})_3]Cl_2$ ([Ru]). The CO evolution rate reaches up to 88.6 μmol h^{-1}, superior to those results obtained from the state-of-the-art cocatalysts. The enhanced photocatalytic reduction performance can be attributed into the atomically dispersed cobalt active sites and improved electron-hole separation efficiency through additional Co-P(O) charge transfer channel. By disclosing the ability of BP nanosheets for atomically dispersed cobalt anchoring, our results will provide a meaningful way for designing advanced BP based materials for efficient photocatalysis.

2.2 Experimental section

2.2.1 Materials preparation

Preparation of few-layer BP nanosheets. Few-layer BP nanosheets were obtained by using liquid exfoliation method. In detail, 0.5 g bulk BP was used as received and grinded in an agate mortar with the help of NMP. Then, a small portion of the pre-treated BP solution was transferred into a conical tube (50 mL) with totally 35 mL NMP added. The exfoliation processes are carried out in the micro-tip probe ultrasonication (Branson Sonifier advanced 250) with output power level 5 and duty cycle 50% at a temperature below 25 °C. After 3 hours' sonic exfoliation, the dispersion contains BP nanosheets can be harvested after several times centrifugation at 18000 rpm in order to remove the residual bulk BP. After that, the powder of BP nanosheets was retrieved after washing for three times using acetone and ethanol, and drying under 120 °C overnight for further characterizations.

Fabrication of BP-Co materials. In a typical experiment, the obtained BP nanosheets were mixed with $CoCl{\cdot}6H_2O$ directly. After grinding the aforementioned materials in an agate mortar for 15 minutes, the BP-Co precursor will be collected and transferred into a porcelain boat and located at the heating center of the quartz tube furnace. Before heating, the sealed quartz tube was pumped with argon gas for approximately 30 minutes to evacuate oxygen and air as much as possible. After the argon gas washing was finished, the furnace was heated to 300 °C with heat speed 5 °C min^{-1} and maintain at this temperature for calcination for 2 hours. The final sample named as BP-Co was collected after it cooling down to room temperature and washed by Ethanol and deionized water for 3 times.

2.2.2 Material characterization

The atomic structural information of the sample was determined by X-ray diffraction (XRD, PANalytical X'Pert PRO). Raman spectra were collected by engaging the Raman microscope (NRS-1000, Japan) with 532 nm excitation at room temperature. The surface morphologies of the samples were performed on the field emission scanning electron microscopy (FE-SEM, JSM-6701F). High resolution scanning TEM (STEM) images, and STEM-energy dispersive X-ray spectroscopy (EDX) images were obtained using a JEOL ARM-200CF operated at 200 kV with an X-ray collection angle of ~1 sr. The EDX elemental map was obtained using NSS 3.3.94 Noran System Seven

software, in which principal component analysis can be performed to identify regions with a similar composition within a map. Atomic force microscopy (AFM) measurements were employed on (Nanocute H, Japan) to acquire the thickness of 2D BP nanosheets. UV-Vis absorption spectra were recorded by Ultraviolet-visible spectroscopy (UV-vis, UV-2600 Shimadzu Corp., Japan), the bandgap can be calculated according to transformed Kubelka-Munk function. Zeta-potential analysis was conducted on Zetasizer Nano ZS 90 (Malvern, UK). The surface chemical analysis was conducted on X-ray photoelectron spectroscopy (XPS, VG-ESCA Mark II). The decay time measurements were performed on a Hamamatsu instrument (Hamamatsu C5680, Japan).

X-ray absorption spectroscopy. Co K-edge X-ray absorption fine structure (XAFS) spectra were measured at 290 K in the transmission mode in the Photon Factory Advanced Ring at the High Energy Accelerator Research Organization on beamline 9C. The storage ring energy was 2.5 GeV, and the ring current was 450 mA. A Si (1 1 1) double-crystal monochromator and Rh-coated focusing bent cylindrical mirror were inserted into the X-ray beam path. The X-ray intensity was suppressed to 67% of the maximum flux using a piezo-translator applied to the crystal to suppress higher harmonics. The slit in front of the I_0 ionization chamber had an opening size of 1.0 mm (vertical) 2.0 mm (horizontal). For comparison, Co metal foil, CoO, and CoP on analytical grade were used as reference materials. The data analysis was carried out for cobalt speciation, including the oxidation state and the chemical environment surrounding the atoms. The X-ray energy was calibrated with reference to the first inflection point in the spectrum of Co foil (7709.5 eV). The disks (Φ = 10 mm) were formed by diluting the CoO (11 mg), BP-Co (10 mg) and CoP (10 mg) with boron nitride (30 mg) and measured at the beamline. X-ray absorption spectra were analyzed using the ATHENA program in IFEFFIT package. Pre-edge background was subtracted by a linear equation that was fitted to the region below the absorption edge, while the post-edge background was also subtracted by fitting a polynomial quadratic function to the EXAFS region. The processed data were normalized by cubic spline method. Extended X-ray absorption fine structure (EXAFS) spectra were analyzed in the conventional procedure with the aid of ATHENA and ARTEMIS program in IFEFFIT package. EXAFS oscillations, $\chi(k)$, were extracted from the spectra in the procedure above and transformed from angular wave number k-space (k^3, k_{min} = 2.3 Å^{-1}, k_{max} = 8.2 Å^{-1}) using a Hanning window to interatomic distance R-space to obtain

the radial structure function (RSF). The EXAFS spectrum for the first shell was extracted by the inverse Fourier Transform of the RSF over the appropriate region, and data fitting was performed using the single scattering EXAFS equation in both *k*- and *R*-space. The amplitude and phase shift functions for Co-O and Co-P shells were extracted using a code ARTEMIS from the EXAFS data measured for CoO and CoP.

Photoelectrochemical (PEC) measurements. The PEC measurements were performed in an integrated functional system equipped with a standard three-electrode system, where working electrode was adopted as photoanode and counter electrode (Platinum wire) was used as cathode. Meanwhile, 0.5 M Na_2SO_4 (pH=7) solution were used as electrolytes, and a Ag/AgCl electrode was adopted as the reference electrode. Electrochemistry workstation CHI660D (CH Instruments, Inc., Shanghai) was used to control the bias potential and record the photocurrent generated. The simulated solar light source was placed 20 cm away from the reaction vessel and the illumination intensity on the photoanode was fixed at 100 mW cm^{-2}. Amperometric i-t curves were evaluated under bias potential 0.5 V. The response time ($t_{res.}$) and recovery time ($t_{rec.}$) can be assigned into the time intervals for the rise and decay of photocurrent from 10 % to 90 % and from 90 % to 10 % of its peak value. The Electrochemical Impedance Spectrum (EIS) measurements were conducted at their open-circuit potential, with the frequency range of 100 kHz to 0.01 Hz and perturbation amplitude of 5 mV. The Mott-Schottky plots were acquired under applied alternating current (AC) frequency is 1000 Hz. All the experiments were carried out at the same condition.

2.2.3 Photocatalytic H_2 evolution activity measurements

Photocatalytic activities were evaluated by the hydrogen evolution from water under visible light irradiation. A 300 W xenon arc lamp equipped with a 420 nm cut-off filter (to remove light with a wavelength lower than 420 nm) was used as the visible light source. Commercial CdS and freshly prepared BP-Co were physically mixing together, and 20 mg of mixed sample was dissolved into 80 mL of 20 vol% lactic acids (electron donor) solution by sonication for 5 minutes, after that the solution was transferred into a quartz glass reaction cell and connect to a gas-closed system with a gas-circulated pump. The produced H_2 was recorded and analyzed by an online gas chromatograph (GC-8A, Shimadzu Corp., Ar carrier, TCD, Japan) with argon as the carrier gas. For evaluating the H_2 production performance of BP-Co, 10 mg of catalyst, 20 mg Eosin Y (EY) and 80 mL of 25 vol% TEOA were added in a quartz glass reaction cell that was connected

to a gas-closed system with a gas-circulated pump. Before the irradiation, the reaction cell was evacuated to remove the air completely. The produced H_2 was analyzed by an online gas chromatograph (GC-8A, Shimadzu Corp., Ar carrier, TCD, Japan) with argon as the carrier gas.

2.3 Results and discussion

2.3.1 Synthesis and characterization of few-layer BP nanosheets

Few-layer BP nanosheets are produced from bulk BP crystal material by a facile liquid exfoliation method in 1-Methyl-2-pyrrolidone (NMP) solution as illustrated in Figure 2.1. X-ray diffraction (XRD) patterns (Figure 2.2) show BP bulk and BP nanosheets can be indexed into orthorhombic BP crystalline structure in consistent with JCPDS No. 73-1358. A new diffraction peak (111) appears in the result of as-prepared BP nanosheets which formerly cannot be found in pristine bulk structure, and the peak intensity ratio between (021) and (040) also changes from (0.496/1) to (1.027/1). These slight deviations possibly resulted from the cleaving along with {010} facets of BP crystal during exfoliation process, as reported previously by other papers.[32] Scanning electron microscopy (SEM) images show the exfoliated few-layer BP nanosheets preserved its layer structure while the thickness and size decrease obviously when compared to that of bulk BP crystals (Figure 2.3). BP crystals that re-stacked by a sequence of layer structures, while BP nanosheets with uniformly distributed lateral dimension after liquid exfoliation can be observed. BP nanosheets are found to show intact lamellar structure after sonication procedures, and the morphology of BP nanosheets can be distinctly distinguished.

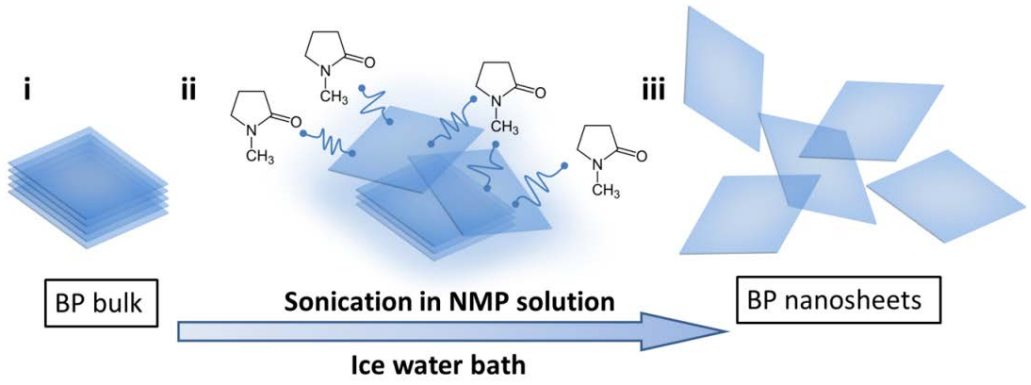

Figure 2.1 Schematic illustration of NMP liquid solution assisted probe sonication exfoliation route in ice water bath to prepare few-layer BP nanosheets.

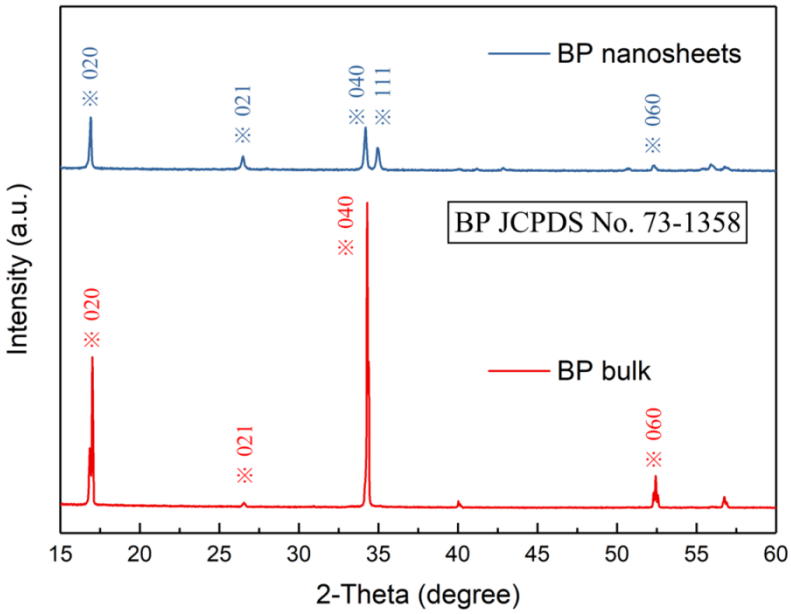

Figure 2.2 XRD patterns of BP bulk and BP nanosheets.

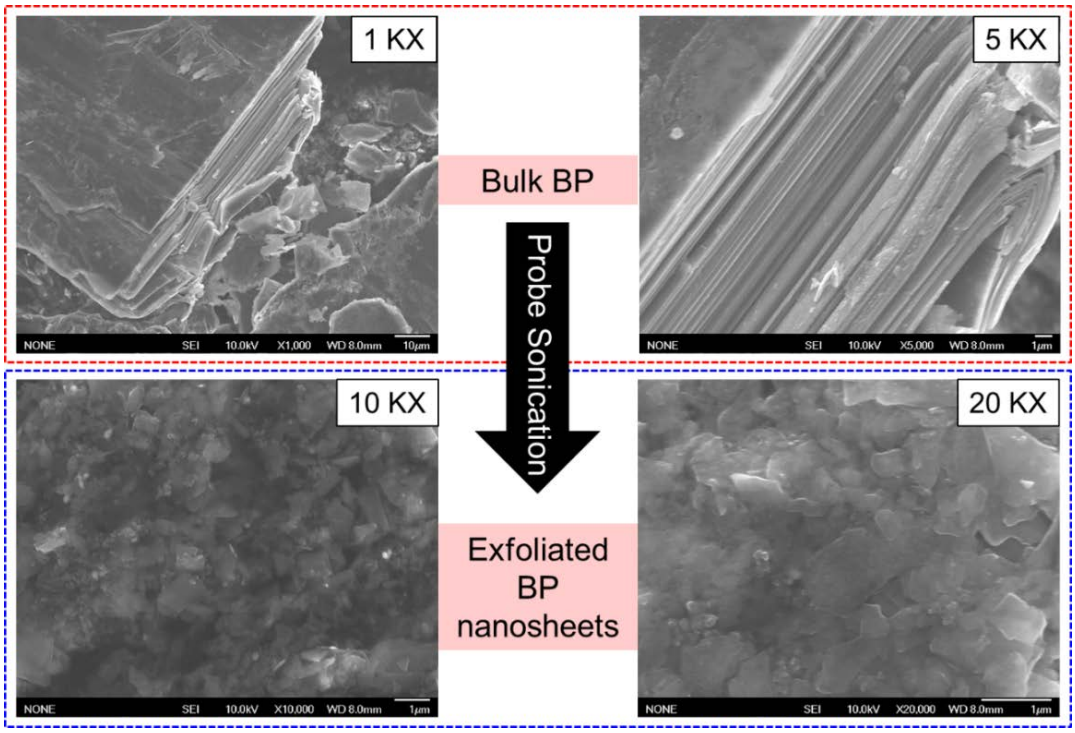

Figure 2.3 SEM images of bulk black phosphorous crystal (left) and as-exfoliated two-dimensional black phosphorous nanosheets (right).

From High-resolution transmission electron microscopy (HRTEM) images (Figure 2.4 and Figure 2.5), the lattice spacing (d-spacing) of 0.33 nm and 0.246 nm corresponds to (021) and (040) plane of few-layer BP nanosheets, respectively.

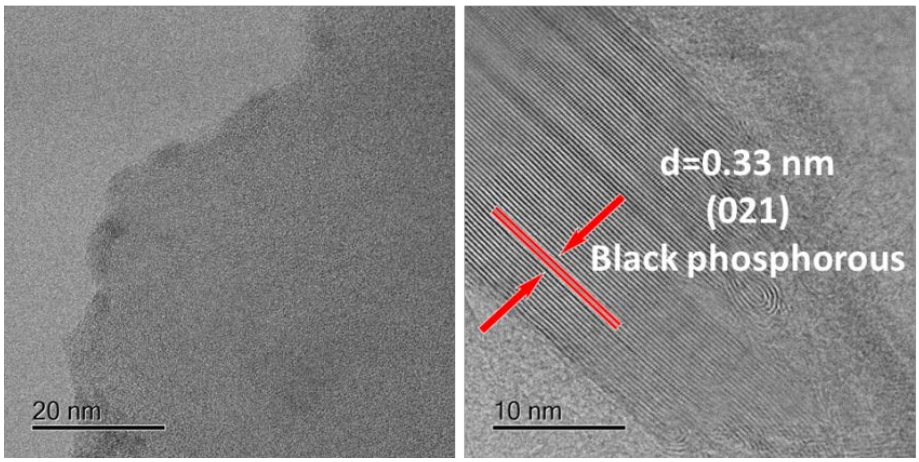

Figure 2.4 TEM and HRTEM images of few-layer BP nanosheets, the lattice spacing (d-spacing) 0.33 nm is corresponding to (021) planes of BP.

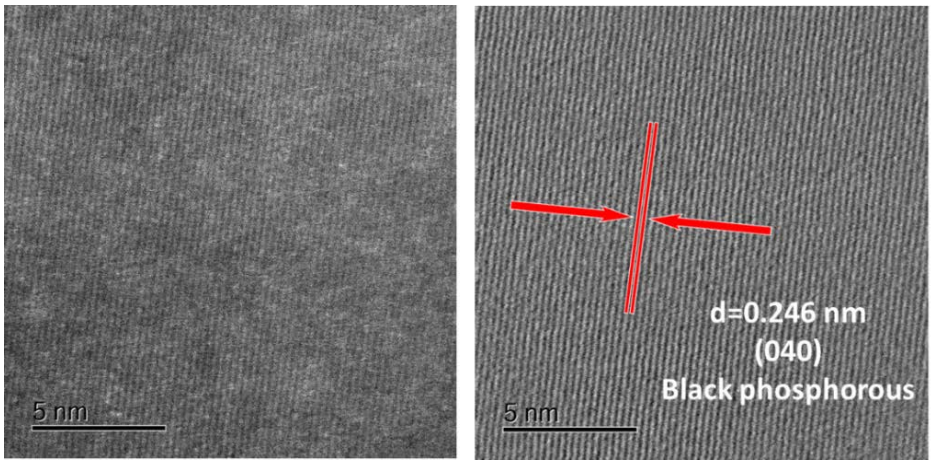

Figure 2.5 Additional TEM and HRTEM images of few-layer BP nanosheets, the lattice spacing (d-spacing) 0.246 nm is corresponding to (040) plane of BP.

In addition, atomic force microscopy (AFM) analyses in Figure 2.6 confirm the lamellar structure which can be observed from TEM measurements. The thickness of as-prepared BP nanosheets ranges from 4 nm to 10 nm, which is corresponding to the value of few-layers BP nanosheets.[33] Average line analysis is preformed based on three-dimensional AFM height image, and the extracted height profile of exfoliated few-layer BP nanosheets is approximately 5 nm, indicating the successful preparation of BP nanosheets.

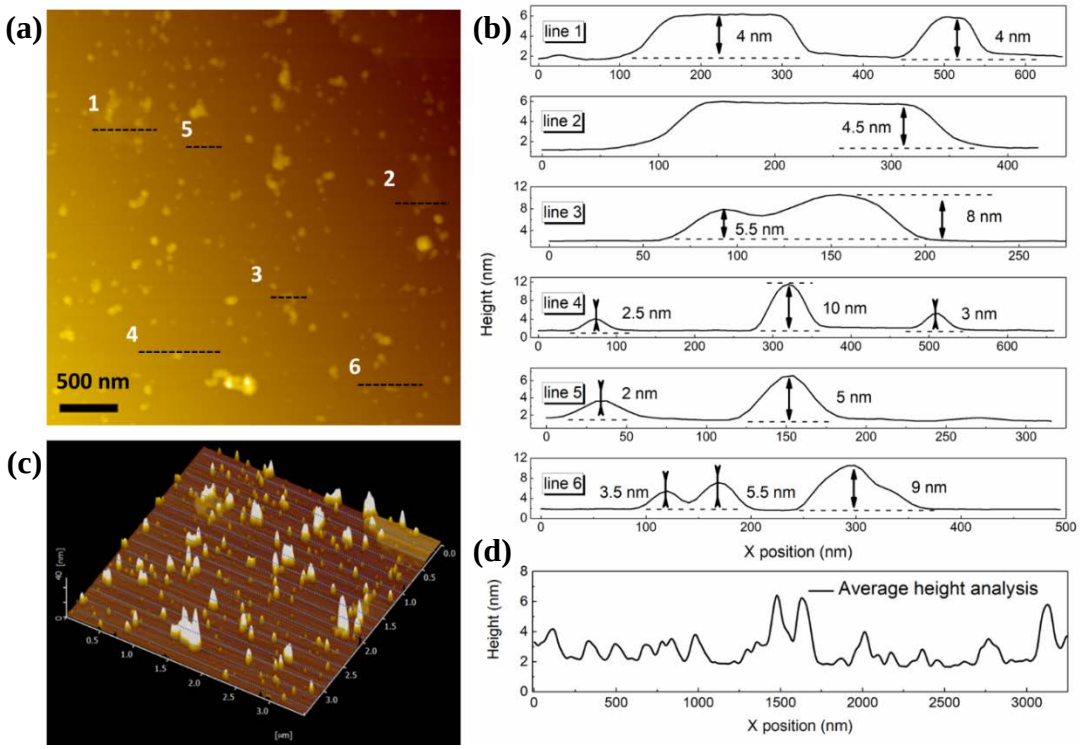

Figure 2.6 (a) Tapping-mode AFM image and (b) the related cross-sectional analysis (line 1 to line 6) of exfoliated BP nanosheets. (c) Average line analysis and (d) the corresponding height profile of exfoliated few-layer BP nanosheets.

Figure 2.7 illustrates the proposed strategy to attach atomically dispersed Co onto the surface of BP nanosheets.

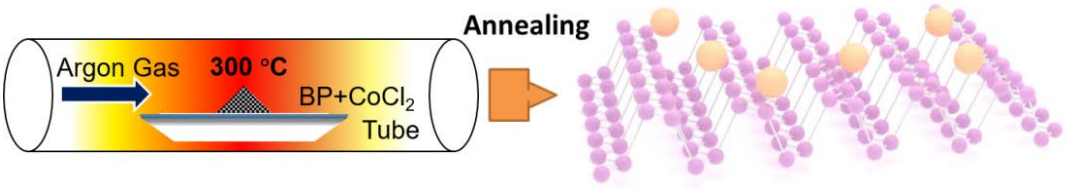

Figure 2.7 proposed strategies to obtain uniform dispersed Co on BP nanosheets substrate and corresponding atomic structure of single atom dispersed BP nanosheets.

To further confirm the interaction between Co and BP, characterizations including TEM, high-angle annular dark-field STEM (HADDF-STEM), AFM and Zeta-potential are investigated (see supporting information **Experimental Section** for detail information). The low resolution TEM image (Figure 2.8a) reveals the typical morphology of layer BP nanosheets. HAADF-STEM image (Figure 2.8b) of BP-Co shows the high density bright dots (highlighted by red circles), which clearly depicts that the Co is atomically dispersed on the surface of BP, while the HRTEM image of

the related area demonstrated in Figure 2.8c indicates good crystallization of BP nanosheets. Besides that, EDX mappings (Figure 2.8d) also indicate the existence of uniformly distributed Co element on BP nanosheets, while unavoidable oxidation and the use of $CoCl_2$ in synthesis processes maybe lead to the appearance of O and Cl elements (Figure 2.9 and Figure 2.10).

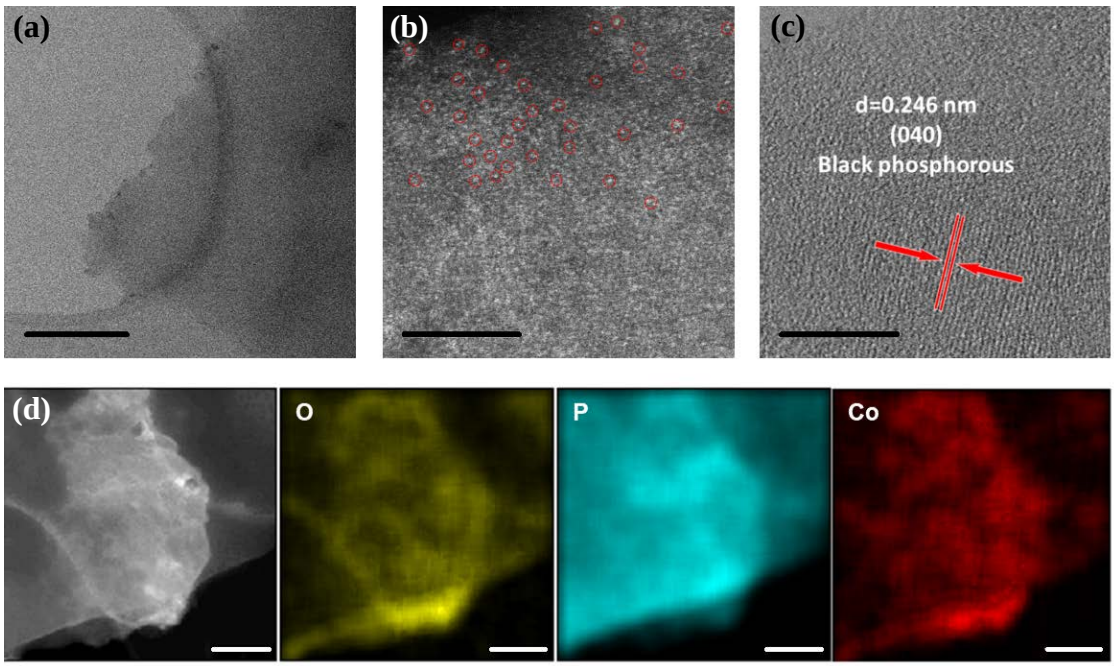

Figure 2.8 (a) Low resolution TEM (scale bar 100 nm), (b) HADDF-STEM (scale bar 5 nm) image (Co atoms are marked using red circles), (c) HRTEM image (scale bar 5 nm) with d-spacing 0.246 nm of BP-Co material. (d) EDS mapping images of as-prepared BP-Co material (scale bar 100 nm).

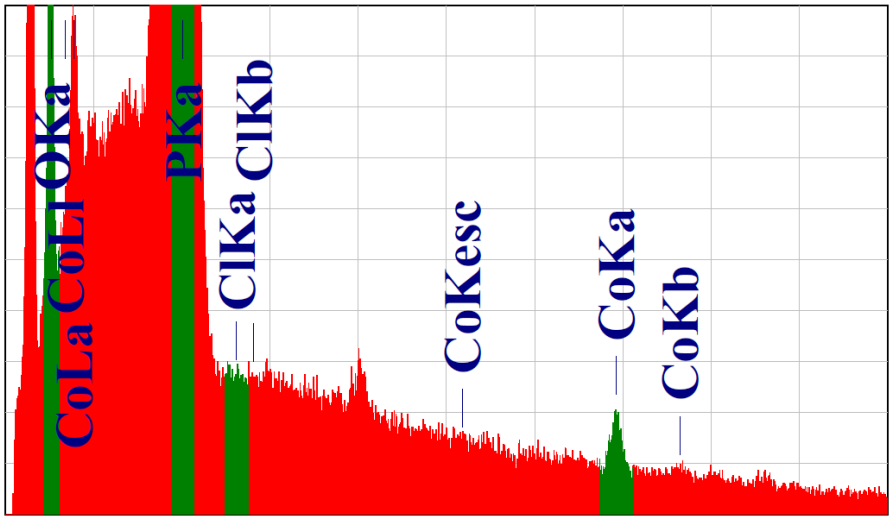

Figure 2.9 Energy-dispersive X-ray spectroscopy of BP-Co.

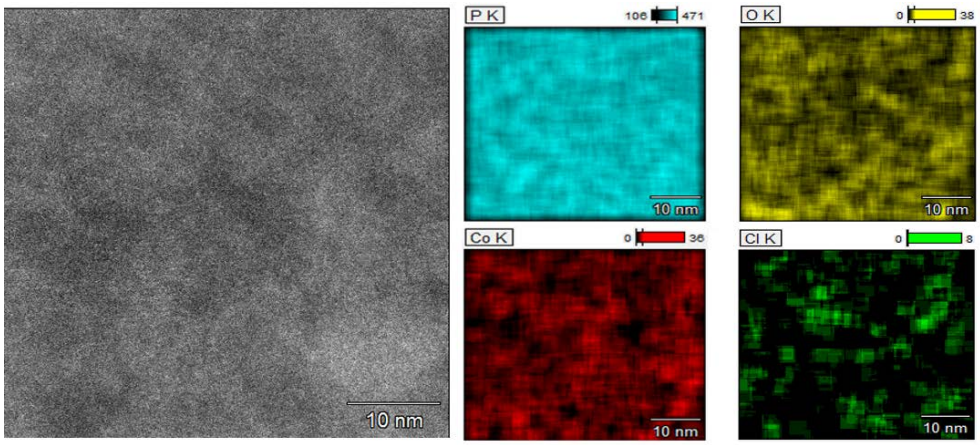

Figure 2.10 TEM image and relevant EDS mapping of elements P, O, Co and Cl from the selected area of BP-Co material.

Both SEM and TEM images show the layer structure of BP nanosheets is preserved after loading with Co, and also a strong interaction between P and Co can prove the successful Co loading on the surface of BP nanosheets. It has been noticed that the layered structure and the lateral size of BP nanosheets remain intact after Co loading from SEM images (Figure 2.11). It is therefore believed that the lone pair electrons in BP atom structure are thermodynamics unstable, preferring to establish stable bond with Co^{2+} spontaneously.

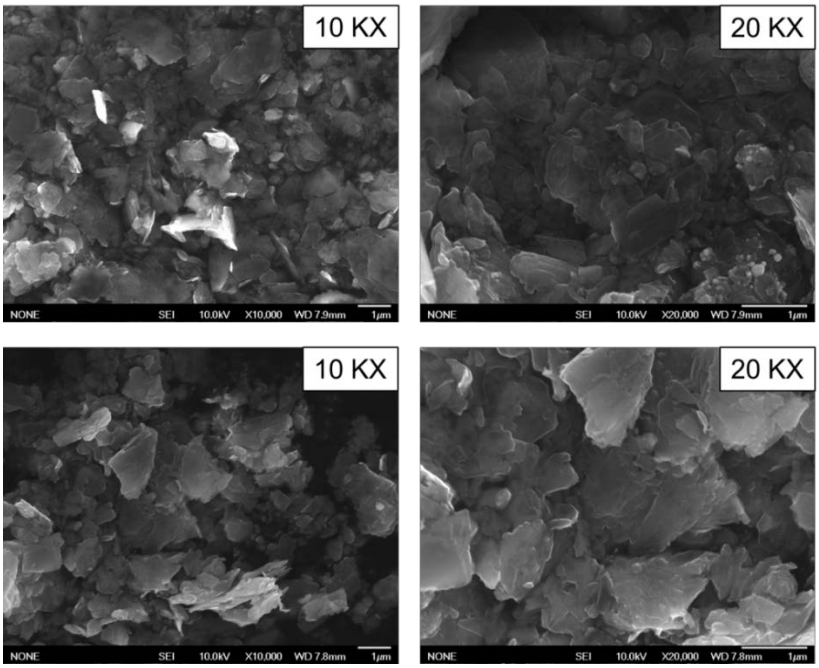

Figure 2.11 Low (left) and high (right) resolution SEM images of BP nanosheets after Co loading.

Meanwhile, the AFM measurement of BP-Co material reveals sheet-like structure and the thickness has nearly no change when compared to that of original BP layers (Figure 2.12a). Zeta-potential measurements in Figure 2.12b indicate the surface charge on BP in solution, and exfoliated BP nanosheets shows the lowest average value of -26.6 mV, suggesting well distribution status than that of bulk BP. Meanwhile, zeta-potential becomes positive after Co modification, and increase from -26.6±0.48 mV for BP nanosheets to +21.9±0.26 mV for BP-Co. Both freshly prepared BP nanosheets and BP-Co materials show well dispersion in water and obvious Tyndall effect. Those results emphasize the successful immobilization of Co onto the negatively charged BP nanosheets.

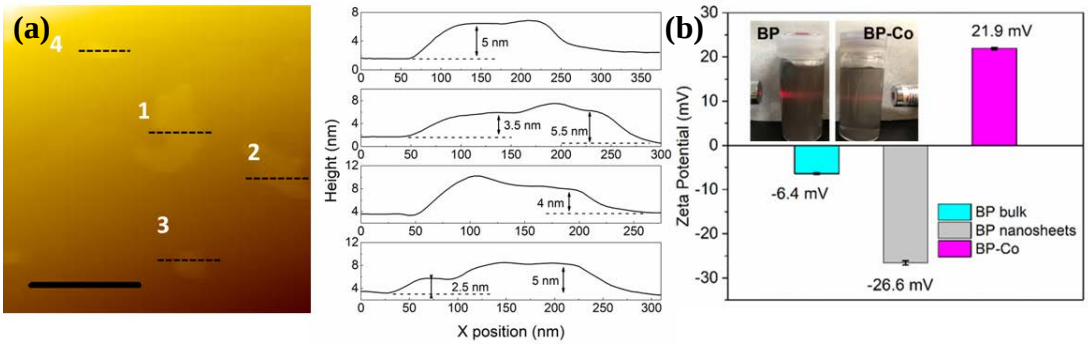

Figure 2.12 (a) Tapping-mode AFM image (scale bar 500 nm) and the related cross-sectional analysis (line 1 to line 4) of BP-Co. (b) Zeta-potential of BP bulk, freshly prepared BP nanosheets and BP-Co tested in ethanol solution. (Inset image: Observation of Tyndall effect of freshly prepared BP nanosheets and BP-Co dispersed in water.)

XRD patterns in Figure 2.13a shows no difference between fresh BP nanosheets and BP-Co, except for the ratio between (040) and (111) peaks appeared at 34.2° and 35° changes little. It is supposed that this phenomenon can reflect the interaction between lone pair electrons on the surface of exposed BP nanosheets and Co ions. Raman spectra of BP nanosheets are shown in Figure 2.13b. BP belongs to the Cmca (No. 64) space group, and in this situation both out-of-plane vibration A_g^1 mode as well as in-plane vibration B_{2g} and A_g^2 modes can be observed through Raman spectra analysis.[34] The position of Raman peaks A_g^1, B_{2g} and A_g^2 of as-exfoliated few-layer BP nanosheets downshift from its bulk counterpart position (Table 2.1) about 0.9 cm^{-1}, 2.1 cm^{-1}, and 3.3 cm^{-1} due to thickness decreasing as previously reported.[35, 36]

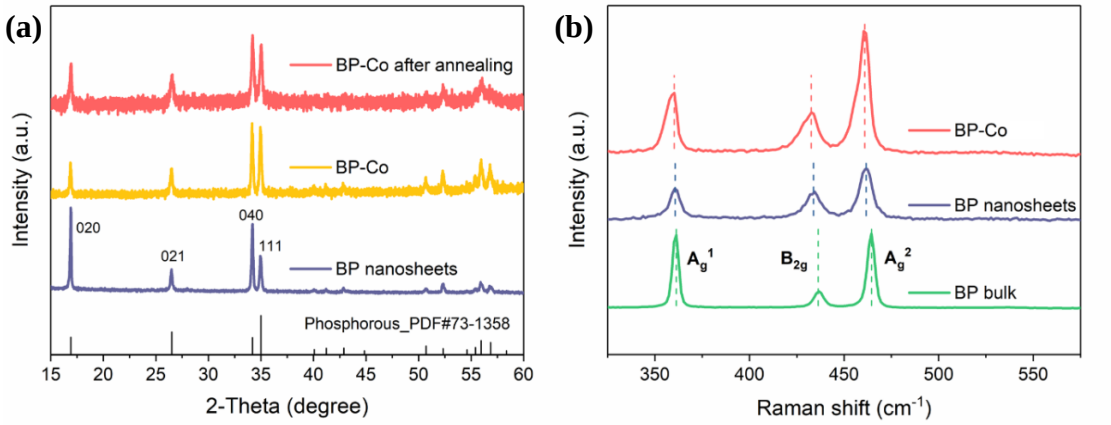

Figure 2.13 (a) XRD analysis of BP nanosheets and BP-Co before and after annealing process. (b) Raman spectra of BP bulk, BP nanosheets and BP-Co.

Table 2.1 Raman peak positions of BP bulk, BP nanosheets and BP-Co

	A_g^1	B_{2g}	A_g^2
BP bulk	361.4 cm^{-1}	436.6 cm^{-1}	464.4 cm^{-1}
BP nanosheets	363.4 cm^{-1}	437.5 cm^{-1}	465.3 cm^{-1}
BP-Co	360.2 cm^{-1}	432.7 cm^{-1}	460.4 cm^{-1}

The light absorption capacities of BP and BP-Co have been determined by UV-Vis-NIR absorption spectra (Figure 2.14), the bandgap of BP and BP-Co can be determined from the threshold value of intrinsic absorption edge (1078 nm for BP and 1512 nm for BP-Co) to be 1.15 eV and 0.82 eV, respectively. A narrowed bandgap from 1.15 eV to 0.82 eV can be observed. The narrowed band gap is believed to be induced by the increased carrier concentration from cobalt ions and the creation of defect levels (or mid-gap state) in the bandgap[37], which acting as trap sites to accommodate the photogenerated electrons and promote charge carrier migration in consequence. The band energy position of BP is determined by Mott-Schottky plot (Figure 2.15), and the flat band potential is determined to be -1.12 V vs. Ag/AgCl (-0.92 V vs. NHE). After coordinated with Co, the flat band potential will further downshift to be -1.01 V vs. Ag/AgCl (-0.81 V vs. NHE).

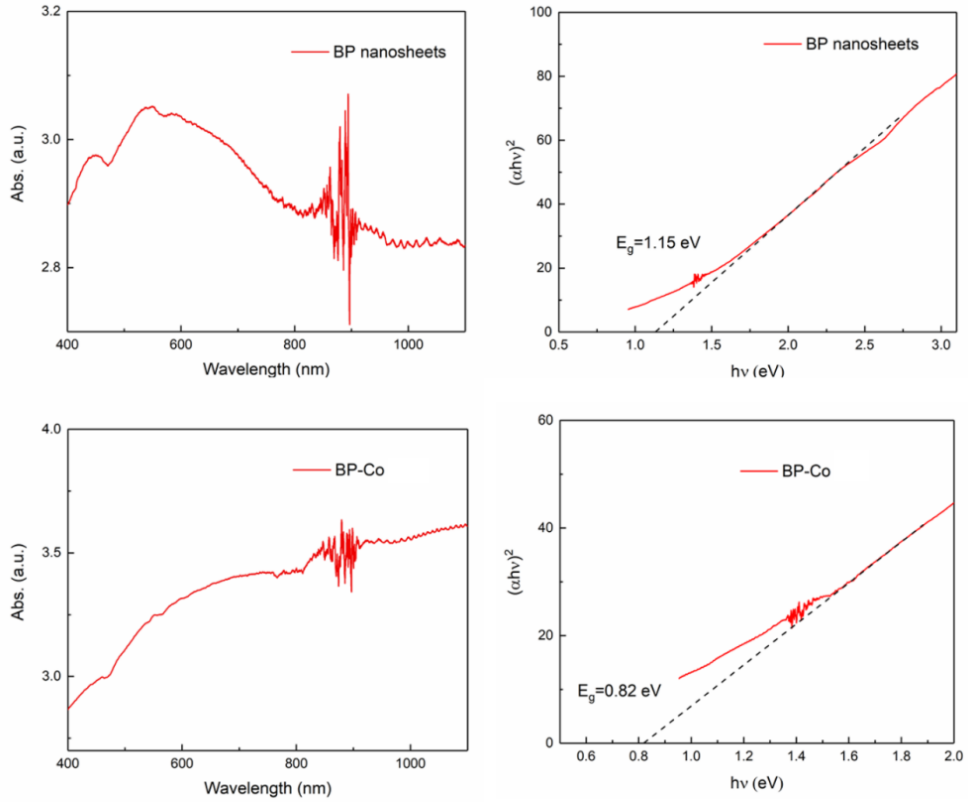

Figure 2.14 Apparent bandgaps of as-exfoliated BP nanosheets and BP-Co determined from UV-Vis absorption spectra.

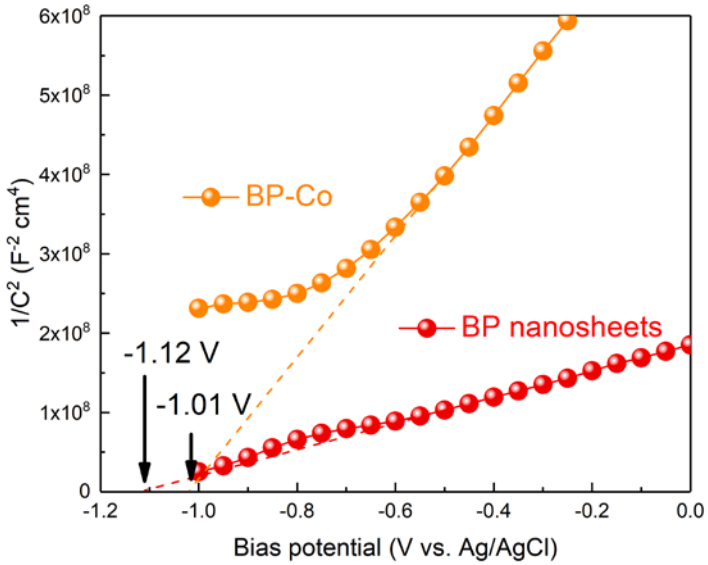

Figure 2.15 Mott-Schottky plot of as-exfoliated BP nanosheets and BP-Co.

Considering the small difference between the flat band potential and conduction band (CB) position for n-type semiconductors, the band positions of BP and BP-Co are estimated (Figure 2.16). It indicates that CB positions of BP and BP-Co are much higher than H_2 production potential (-0.41 V vs. NHE).

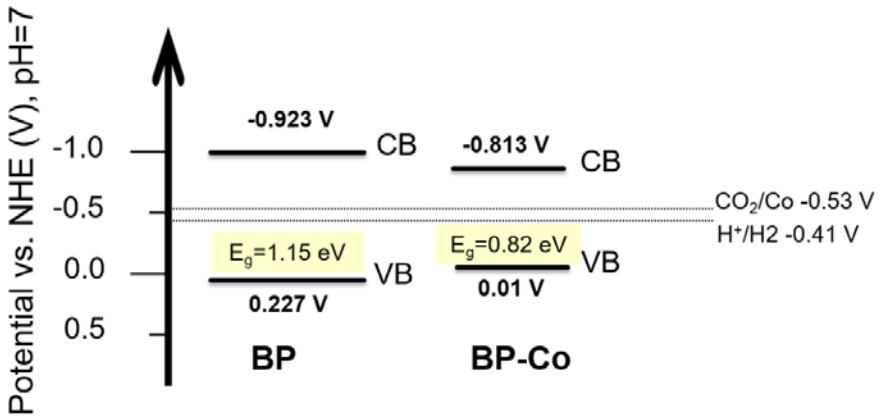

Figure 2.16 Schematic band structure diagram of as-exfoliated BP nanosheets and BP-Co.

Also, the on/off photoresponse behaviors in Figure 2.17 show the photocurrent density of BP-Co is 10 times higher than that of BP nanosheets, and a much longer response time of BP-Co means a longer photogenerated carrier lifetime after Co coordination. EIS investigations (Figure 2.18) also reveal a smaller semicircular radius for BP-Co which represents improved conductivity and lower charge transfer barrier than that of BP nanosheets. Thus, introduce the Co may greatly shorten diffusion distance and realize efficient electron-hole separation to induce favorite photocatalytic reduction kinetics.

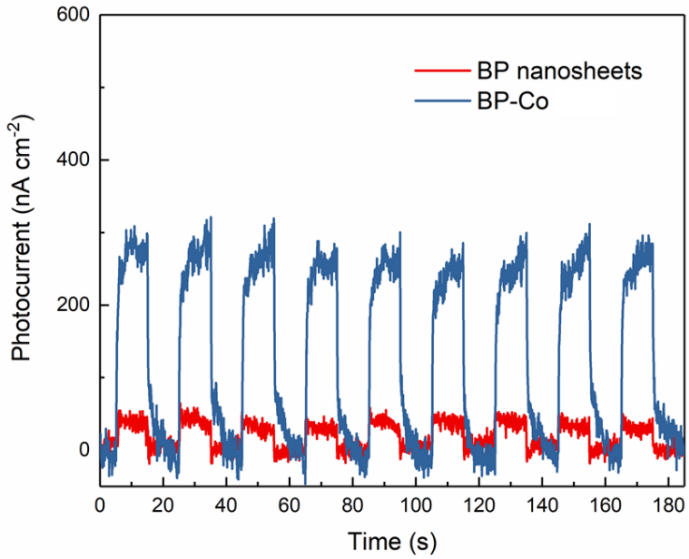

Figure 2.17 Photocurrent response behaviors of as-exfoliated BP nanosheets and BP-Co.

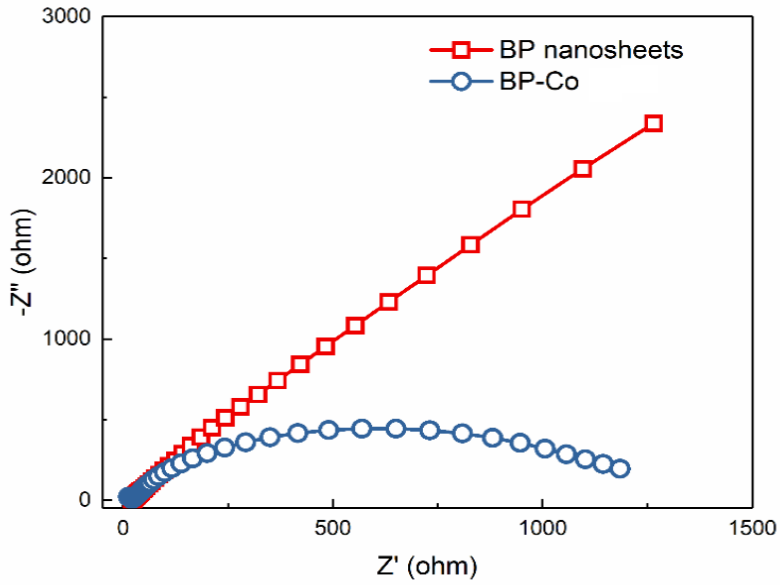

Figure 2.18 EIS plots of as-exfoliated BP nanosheets and BP-Co.

2.3.2 Characterization of modified photoanodes

The chemical states of BP-Co as well as electronic interactions are studied by using X-ray photoelectron spectroscopy (XPS) analysis. For as-prepared BP nanosheets, binding energies at 129.8 eV, 131.0 eV and 133.7 eV can be assigned to P $2p_{3/2}$. P $2p_{1/2}$ and P_xO_y (P-O species) on the surface, respectively.[38] In comparison, the three predominated P 2p peaks (Figure 2.19a) shift to lower binding energies 129.3 eV, 130.6 eV and 133.1 eV, which indicates strong interaction between BP and Co. High resolution core-level Co 2p spectrum (Figure 2.19b) of BP-Co material can be fitted with spin-orbit split $2p_{3/2}$ and $2p_{1/2}$ main peaks and two satellites. The binding energies of 781.7 eV, 786.0 eV, 797.0 eV and 803.4 eV can be attributed into Co^{2+} and Co^{3+} components due to unavoidable surface oxidation, the peak observed lower than 781.7 eV may suggest a new bond Co-P formed due to interaction between Co and P.[39] In all situations, standard C 1s peaks are used for calibration (Figure 2.20 and Figure 2.21).

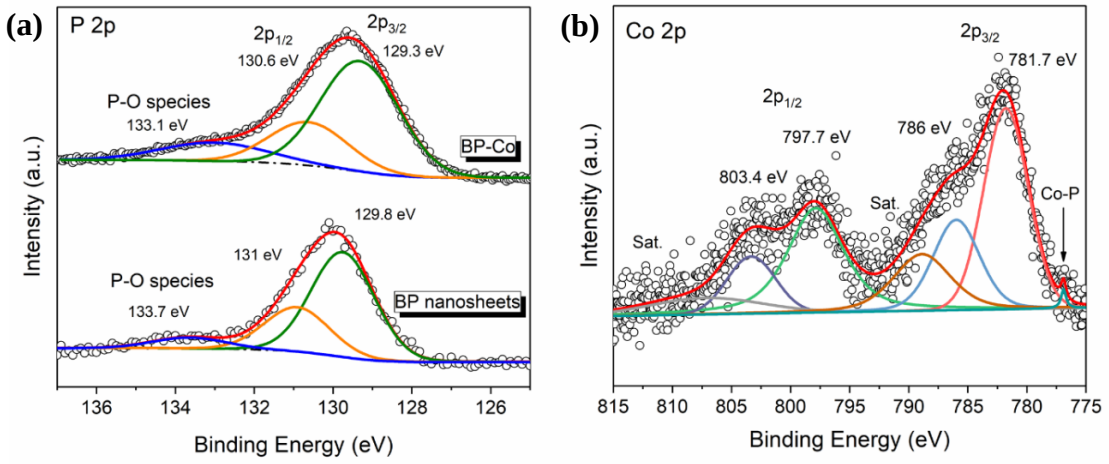

Figure 2.19 (a) P 2p and (b) Co 2p binding energy spectra.

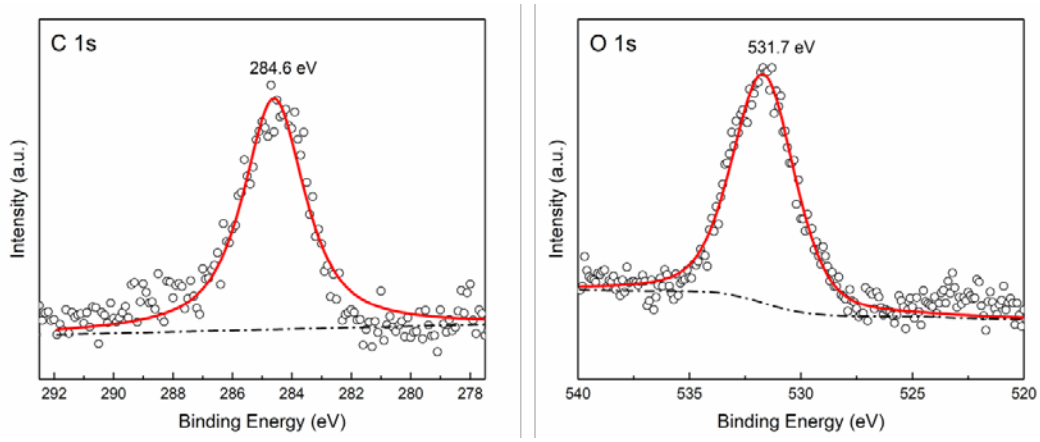

Figure 2.20 Fitting C 1s and O 1s characteristic peaks of BP nanosheets for calibration.

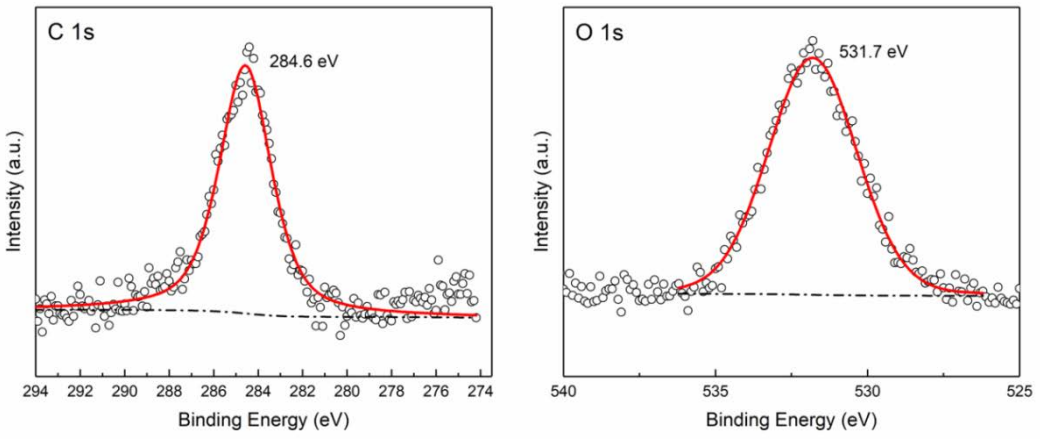

Figure 2.21 Fitting C 1s and O 1s characteristic peaks of BP-Co nanosheets for calibration.

In order to further understand the atomic structure of BP-Co, X-ray absorption near-edge structure (XANES) spectroscopy and Co K-edge extended X-ray absorption fine structure (EXAFS) spectrometry are used to probe the local structure of the Co element

in BP-Co material. The Co K-edge XANES spectra of Co metal foil, CoO, CoP, and BP-Co are demonstrated in Figure 2.22a. Different from the spectra of metallic Co and CoO reference materials, the as-fabricated BP-Co exhibits near edge structure which is very similar to that of CoP reference sample. The EXAFS data of BP-Co was Fourier transformed over R-space range (R range) up to 4.0 Å as shown in Figure 2.22b, the Co metal foil and CoO exhibit typical Co-Co shell peak at 2.2 Å and Co(-O-)Co shell peak at 2.6 Å (both peaks phase shift uncorrected). For BP-Co sample, three peaks appeared in the R range between 0 and 4 Angstrom. While peak position due to Co-O (1.34 Å) and Co-P (1.68 Å) matched well with corresponding peaks of CoO and CoP reference samples, a peak at 2.06 Å does not match the peaks observed for Co metal, CoO, or CoP references and should be related to Co-Cl coordination from surface remained $CoCl_2$.[40-42] Both the XANES and EXAFS information reveal that the Co is coordinated with P after annealing, and no Co-Co peaks are observed which indicates the single-atom status of Co.

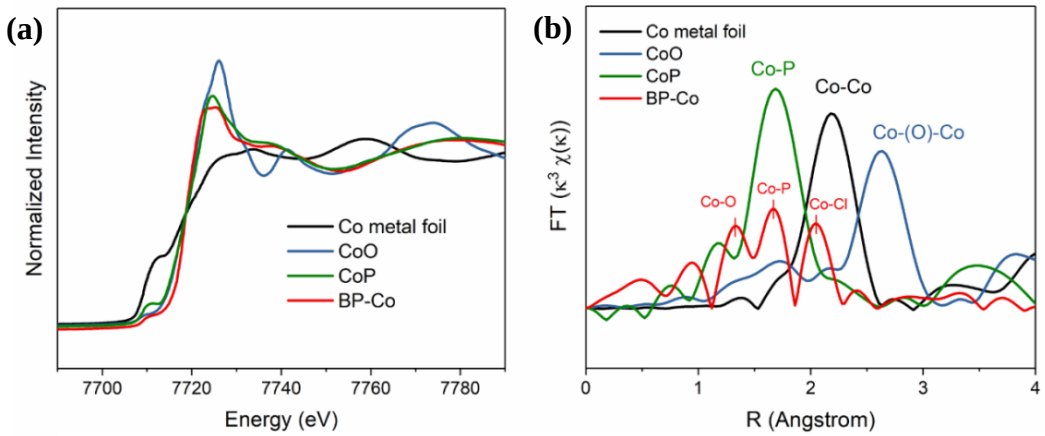

Figure 2.22 (a) Co K-edge XANES spectra and (b) Fourier transform magnitudes of the experimental Co K-edge EXAFS spectra of BP-Co and reference samples.

The coordination number has been extracted from curve fit analyses as shown in Figure 2.23. In detail, the coordination number of cobalt to oxygen is calculated to be 3.9, and the value of cobalt to phosphorous atoms is close to 1.5 (Calculation methods are provided in supporting information). Considering the fact that P-O species existed on the surface of BP nanosheets, it can be predicted that one isolated Co atom is coordinated with one or two phosphorous atoms as well as four oxygen atoms to form Co-P(O) species in BP-Co atomic structure.

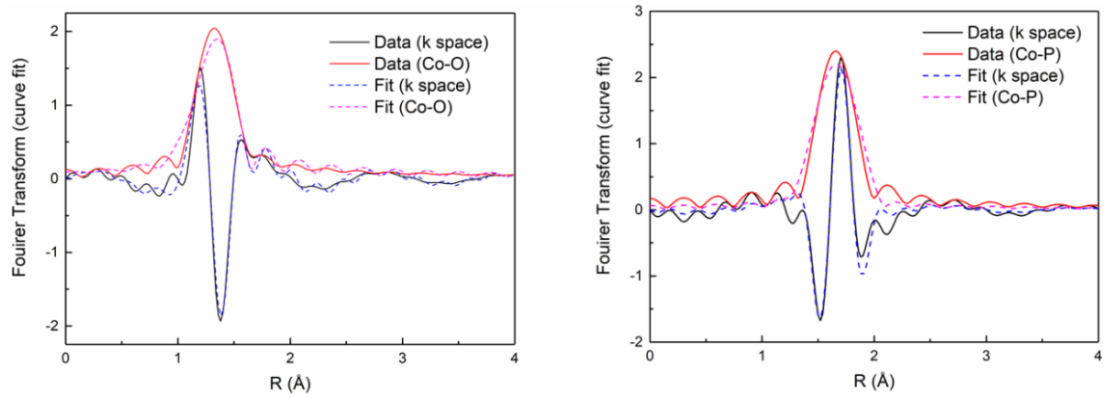

Figure 2.23 The best-fit results in k and R-space for Co-O and Co-P for BP-Co associated Fourier transform k^3-weighted EXAFS spectra.

2.3.3 Photocatalytic H_2 evolution performance on CdS-BP-Co materials.

An evidential improvement of photocatalytic reduction capability has been provided based on our experiments. The as-prepared BP-Co is chosen to combine with CdS for photocatalytic investigations. After combination, the absorption ability of CdS-BP-Co materials has been explored to NIR region, as shown in Figure 2.24.

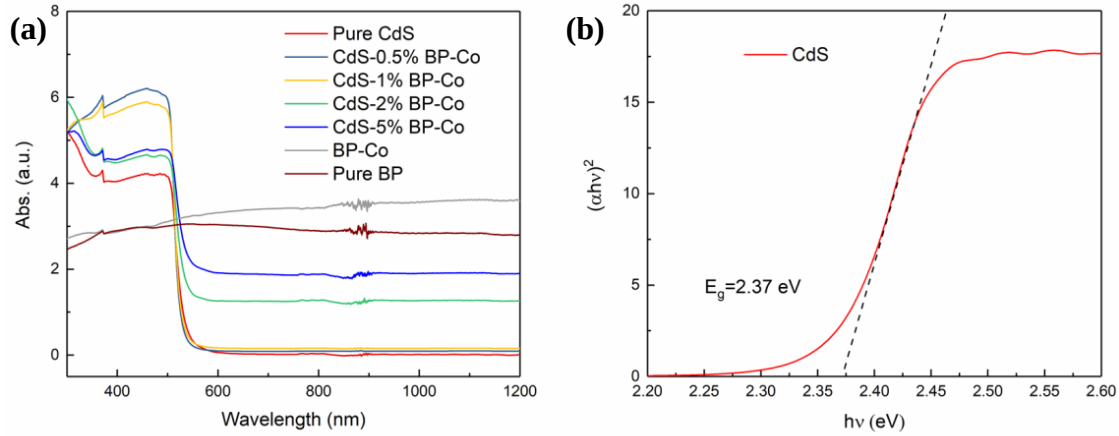

Figure 2.24 (a) UV-Vis diffuse reflectance spectra of pure CdS, CdS with 0.5 wt%-5 wt% BP-Co, BP-Co and pure BP. (b) Intrinsic absorption edge of CdS with the bandgap calculated to be 2.37 eV through transformed Kubelka-Munk function.

As shown in Figure 2.25, pure CdS possesses low photocatalytic H_2 production performance which is only 18.5 μmol h^{-1}. After mechanical mixing CdS with 0.5 wt% BP-Co, 5 times improvement can be achieved. The most optimized ratio between CdS and BP-Co is 1 wt%, and the average H_2 production rate is determined to be 345.4 μmol h^{-1}, which is 18 times higher than that of pure CdS.

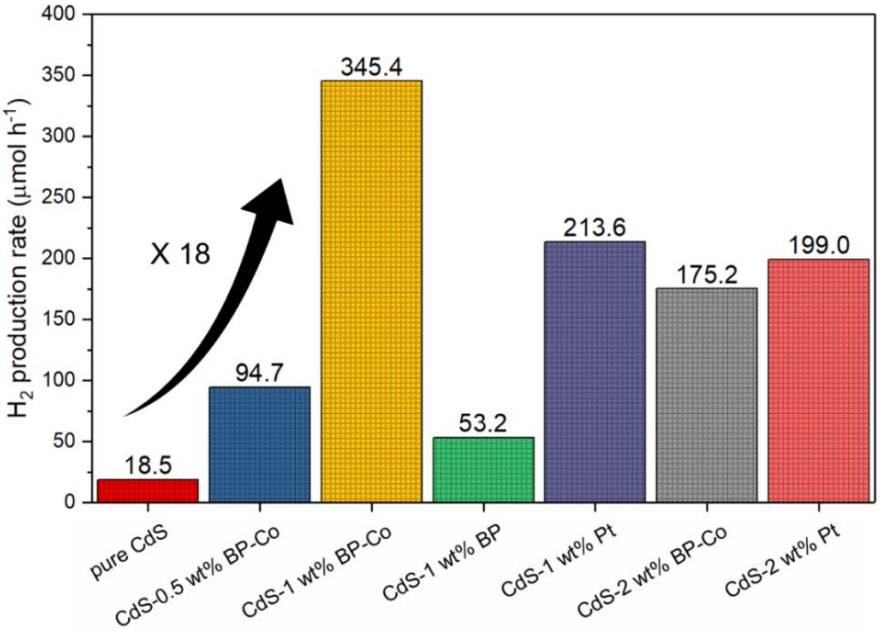

Figure 2.25 Averaged H_2 evolution rate of pure CdS, CdS-0.5 wt% BP-Co, CdS-1 wt% BP-Co, CdS-1 wt% BP, CdS-2 wt% BP-Co, CdS-1 wt% Pt, and CdS-2 wt% Pt. (Catalyst amount: 20 mg).

The H_2 production performance of the optimized CdS-1% BP-Co can retain 90% from the first stage after three cycles (Figure 2.26).

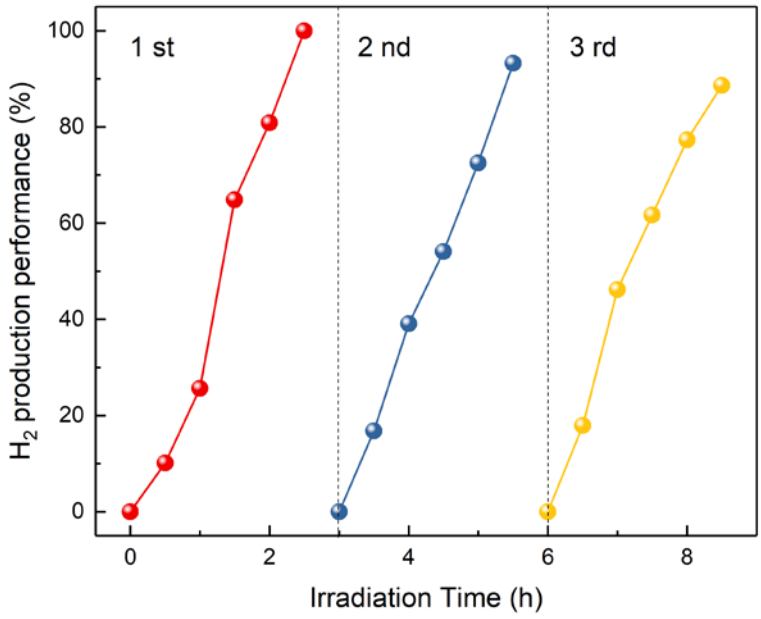

Figure 2.26 Stability test of CdS-1 wt % BP-Co for photocatalytic H_2 production.

The promotion is basically from synergetic effect between BP and Co, for 1 wt% loading of BP will only achieve 3 times enhancement. In Figure 2.25 and Figure 2.26, the H_2 production rate of CdS with 1 wt% BP-Co is even higher than that of Pt at the

same loading amount, and the performance is comparable with other reported BP based material in recent state (Table 2.2).[32, 38, 43] However, no H_2 evolution was observed over bare BP or BP-Co without the assistance of CdS, which I think it is because of the fast electrons and holes recombination in the situation of both BP and BP-Co (Figure 2.27). Our findings not only suggest the importance of BP nanosheets as a substrate for atomic metal loading, but also great potential of BP-Co as substitute for Pt cocatalyst for photocatalytic H_2 evolution.[44-46]

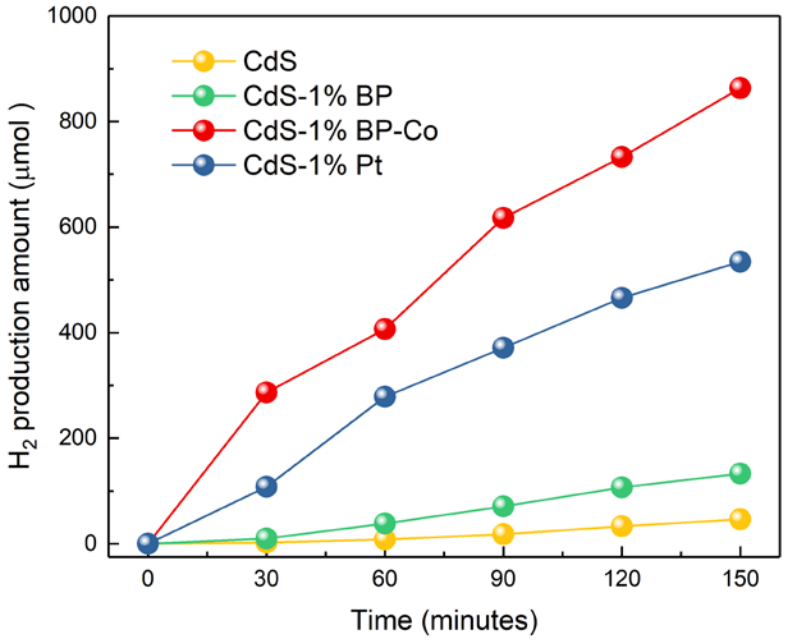

Figure 2.26 Plots of H_2 production amount within 2.5 hours of CdS, CdS-1 wt% BP, CdS-1 wt% BP-Co and CdS-1 wt% Pt.

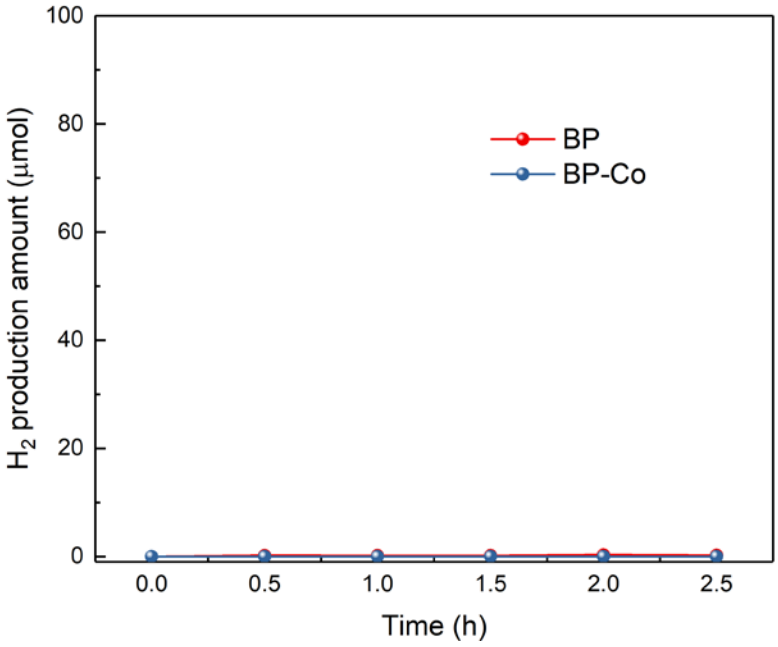

Figure 2.27 H_2 production amount within 2.5 hours of BP and BP-Co.

Table 2.2 Comparison of the photocatalytic H_2 production performance between the present BP-based photocatalysts with rivaling performance in literatures.

Materials	Measurement	H_2 production	Reference
CdS-BP-Co	> 420 nm 20% lactic acid	345.4 μmol h^{-1} 17.27 mmol h^{-1} g^{-1}	**This work**
CdS-BP	> 420 nm 20% lactic acid	53.2 μmol h^{-1} 2.66 mmol h^{-1} g^{-1}	**This work**
C_3N_4-BP	>420 nm 20% methanol	0.427 mmol h^{-1} g^{-1}	JACS, 2017[32]
CdS-BP	> 420 nm 18% lactic acid	11.2 mmol h^{-1} g^{-1}	Angew. Chem., 2017[43]
CdS-BP-MoS_2	> 420 nm 18 % lactic acid	18.1 mmol h^{-1} g^{-1}	Angew. Chem., 2017[43]
BP-CdS-$La_2Ti_2O_7$ ternary composite	>420 nm Na_2S-Na_2SO_3	0.8 mmol h^{-1} g^{-1}	Applied Catalysis B: Environmental, 2019[38]

Based on our experimental results, the mechanism that views BP-Co in both band structure as well as surface interaction has been proposed in Figure 2.28. From the aspects of band structure of CdS-BP-Co, the CB edge of CdS (-1.03 eV vs. NHE) is higher than that of BP nanosheets (-0.92 eV vs. NHE) and BP-Co (-0.81 eV vs. NHE), a thermodynamic driving force will drive photogenerated electrons transfer from excited CdS to BP and Co-P(O) sites in the end. From the aspects of surface interaction, the intimate and large contact interface of CdS, BP and Co-P(O) give a new insight on the enhanced H_2 evolution activities. Generally, two different surface contact modes (face contact and point contact) play different roles in the charge carrier transport and chemical reactions. The face contact between BP nanosheets and CdS particles promotes fast charge transfer, improving electron-hole separation efficiency.[47] Meanwhile, the point contact between CdS and Co-P(O) leads to antenna effect, collecting electrons and lowering the energy barrier of photocatalytic reduction reactions.

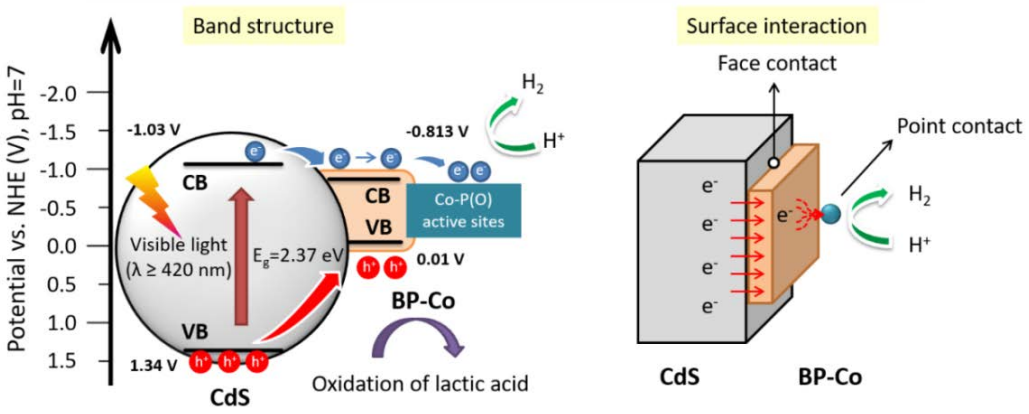

Figure 2.28 Schematic illustrations on the band structure and surface interaction mechanism of photocatalytic reaction on CdS-BP-Co.

The active sites of BP-Co are further revealed by using photosensitizer Eosin Y to exclude the influence from semiconductor CdS. In Figure 2.29, bare BP nanosheets hardly show H_2 production ability. With the contribution from photosensitizer Eosin Y, a great enhancement of water reduction ability (H_2 production about 24.3 μmol h^{-1}) can be achieved by BP nanosheets. The H_2 production as high as 83.4 μmol h^{-1} (8.34 mmol h^{-1} g^{-1}) is achieve by BP-Co.

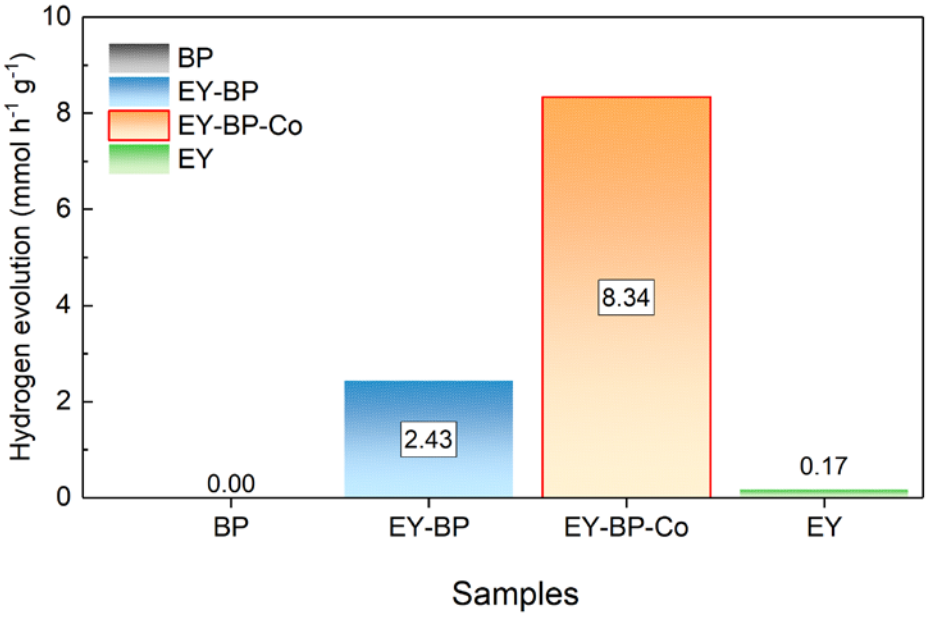

Figure 2.29 Hydrogen evolution performance comparison of BP, EY-BP, EY-BP-Co, and BP-Co EY materials.

I also conduct a series of comparison experiments in proving the importance of BP-Co interaction. Figure 2.30 demonstrates the H_2 production amount within 2 hours of

five different samples based on BP, BP-Co and BP-Co^{2+}. The H_2 production performance of Co^{2+} is negligible, even with the introduction of BP nanosheets, the ultimate H_2 production can only reach one-half of that of BP-Co after annealing.

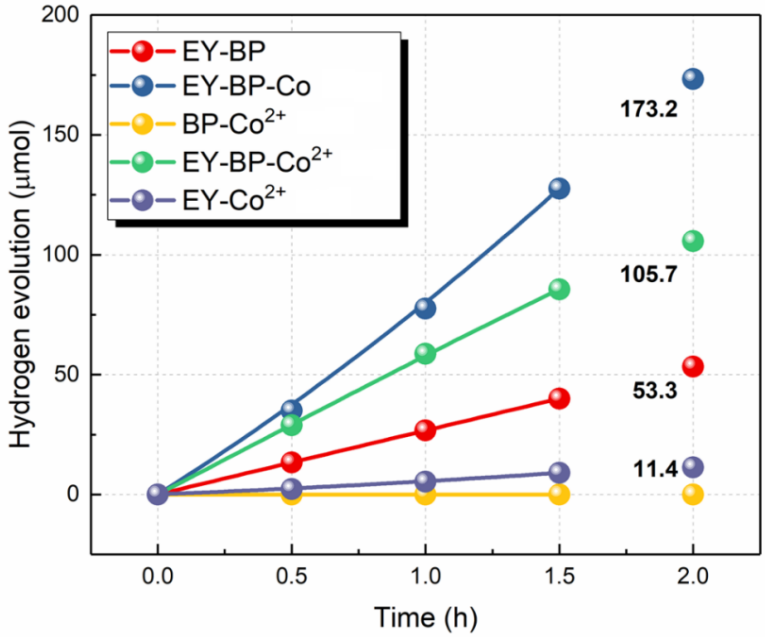

Figure 2.30 H_2 production amount within 2 hours of five different samples based on BP, BP-Co and BP-Co^{2+}. BP-Co^{2+} was prepared by mixing BP with $CoCl{\cdot}6H_2O$ (same Co amount) in ethanol and dried without annealing.

The cycle measurements have been carried out to evaluate the durability of BP photocatalyst. As shown in Figure 2.31, the H_2 production amount depict no distinct decay in the first round, and only a slight reduce on the performance can be find in second and third rounds, which may be induce by decreasing of sacrificial agent and EY. After resupplying the EY, the photocatalytic performance retains after one day, and the activity retain 90 % from its pristine stage even after 1-week duration.

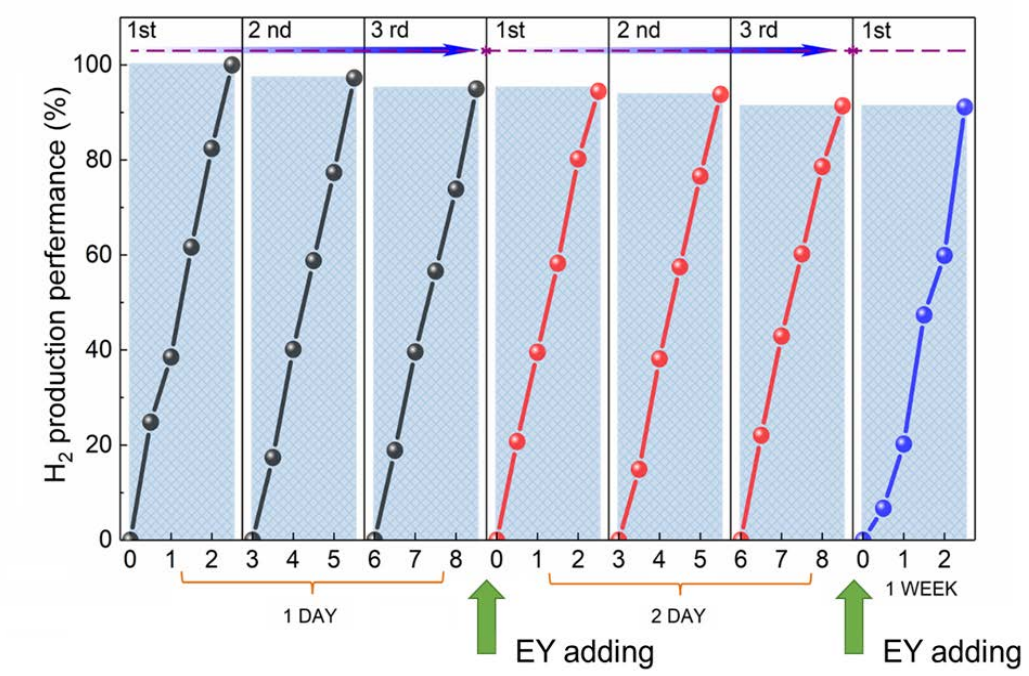

Figure 2.31 Cycling test of H_2 evolution performance over BP-Co.

SEM images (Figure 2.32) demonstrate the lamellar structure of BP nanosheets is preserved after 1-week stability test. The coarse surface of BP-Co is resulted from oxidation, and the small particles which can be observed are P_xO_y species as reported.[48, 49] Meanwhile, no obvious changes can be found in XRD of BP-Co before and after stability test. Therefore, it is reasonable to believe the interaction between Co and P on the surface may slow down the degradation and improve the long-term stability of BP nanosheets.

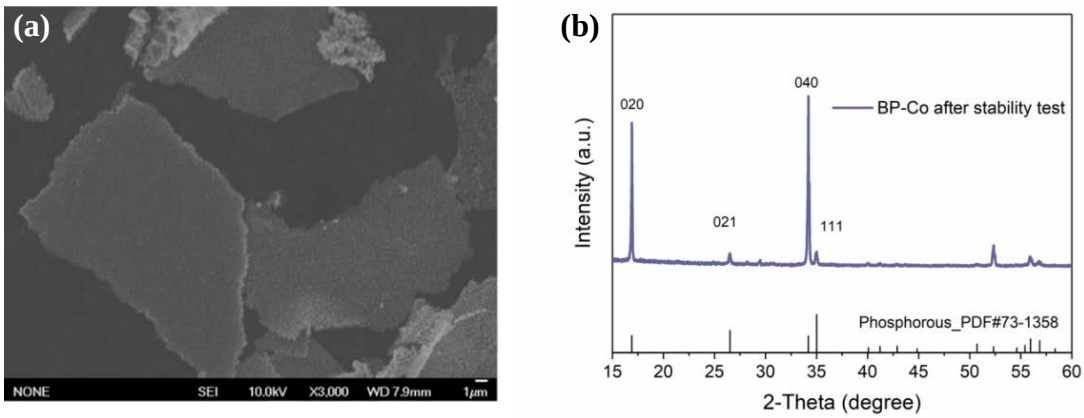

Figure 2.32 SEM images of BP-Co after photocatalytic stability measurement. (b) XRD of BP-Co after stability test.

In addition, time resolved photoluminescence (TRPL) decay spectra (Figure 2.33) indicate a longer carrier lifetime of EY-BP (1139.41 μs) compared to EY (626.36 μs).

The prolonged photogenerated carrier lifetime is derived from efficient electron transfer from EY to BP, for BP nanosheets have good conductivity and suitable bandgap to help electron-hole separation. As to BP-Co, the loading of Co decrease the lifetime from 1139.41 μs to 656.31 μs, revealing new charge transfer channel to Co-P(O) active sites.

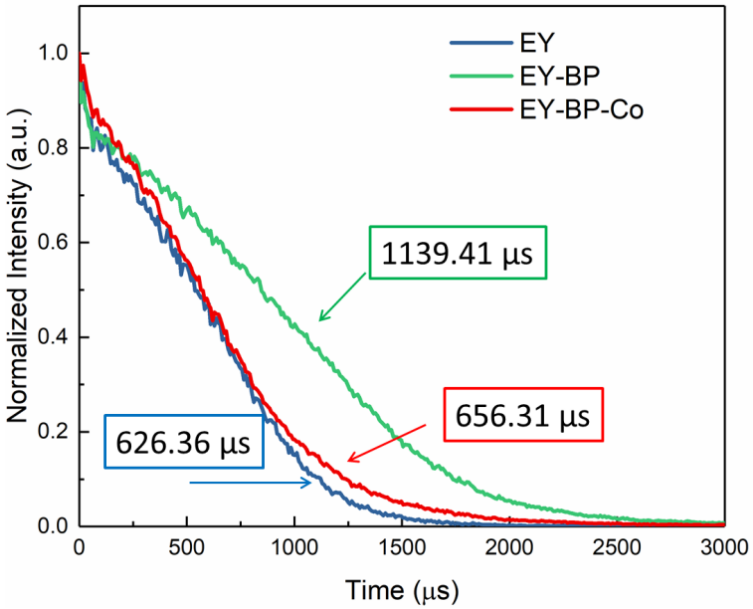

Figure 2.33 Time resolved photoluminescence (TRPL) decay spectra of EY, EY-BP and EY-BP-Co materials.

The mechanism is proposed in Figure 2.34. The Co-P(O) bond formation results into uniform single atom dispersion of Co on BP (BP-Co) and additional charge transfer channel, which are two key reasons for improving the H_2 photocatalytic reaction.

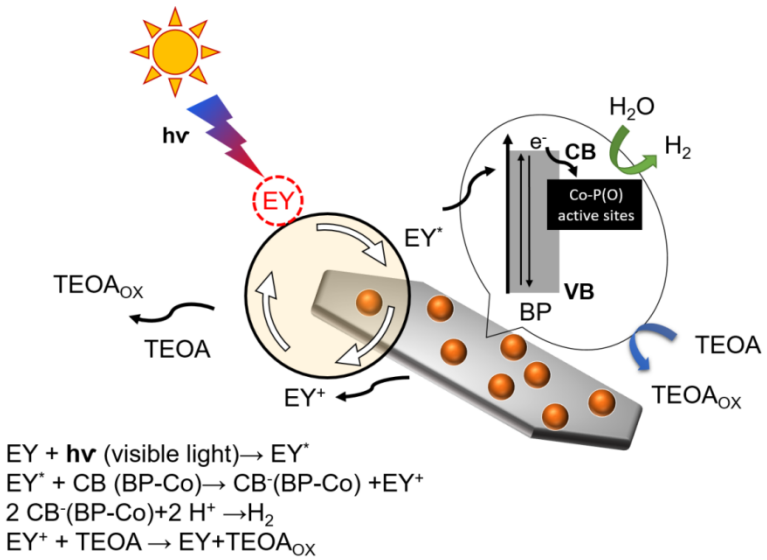

Figure 2.34 The schematic illustration about the mechanism of electron transfer in EY boosted BP-Co materials.

Further investigate on the CO_2 reduction performance (Figure 2.35a) of BP-Co has been carried out in CH_3CN, TEOA and water mixing solution saturated with atmospheric CO_2 in the presence of [Ru] as photosensitizer under visible light ($\lambda > 420$ nm). In detail, bare BP in the presence of [Ru] depicts excellent performance on water reduction to H_2, and nearly no CO can be detected means the CO_2 reduction is much harder kinetically than water reduction for bare BP. After Co loading, the H_2 reduction performance of BP slightly decreases, whereas the CO_2 reduction ability increases dramatically to 88.6 μmol h^{-1}, superior to those obtained with the state-of-the-art noble-metal-free cocatalysts (Table 2.3).[50-55] The CO_2 reduction performance which has been achieved is 88.6 μmol h^{-1} for BP-Co with H_2 production of 61.1 μmol h^{-1} at the same time (Figure 2.35b), and the selectivity of CO is calculated to be 59.2% in consideration of the competition between water and CO_2 reduction. The excellent photocatalytic reduction performance of BP-Co may be triggered by the interaction between Co and P, which has been reported to show electron-rich property for boosting photocatalytic reactions.[56] The electron-rich property of BP-Co may lead to higher surface electron density for promoting photogenerated electrons to participate into the reactions with multiple electrons involved.[57] No CO evolution was observed over bare BP or BP-Co in the absence of [Ru], indicating the cocatalytic effect of BP and BP-Co for photocatalytic CO_2 reduction. Isotope experiments are carried out to validate the source of generated CO by using $^{13}CO_2$ as carbon source to replace $^{12}CO_2$ during our experiments. As shown in Figure 2.35c, the total ion chromatographic peak around 6.2 minutes can be assigned to CO, while O_2 and N_2 are confirmed from air that remain in the sampling needle. The analysis of CO only obtains the m/z= 29 in mass spectra (Figure 2.35c), which is attributed to the ^{13}CO, confirming that the product CO originates from CO_2 reduction. The proposed mechanism for photocatalytic CO_2 reduction over BP-Co has been depicted in Figure 2.35d. The photosensitizer [Ru] is excited under visible light to the [Ru]* state, and transferring generated electrons to the CB and the Co-P(O) active sites of BP-Co. Then, the CO_2 molecules and H^+ are reduced to CO and H_2. The oxidized state of the $[Ru]^+$ receives electrons from sacrificial electron donor TEOA to recover back to [Ru].

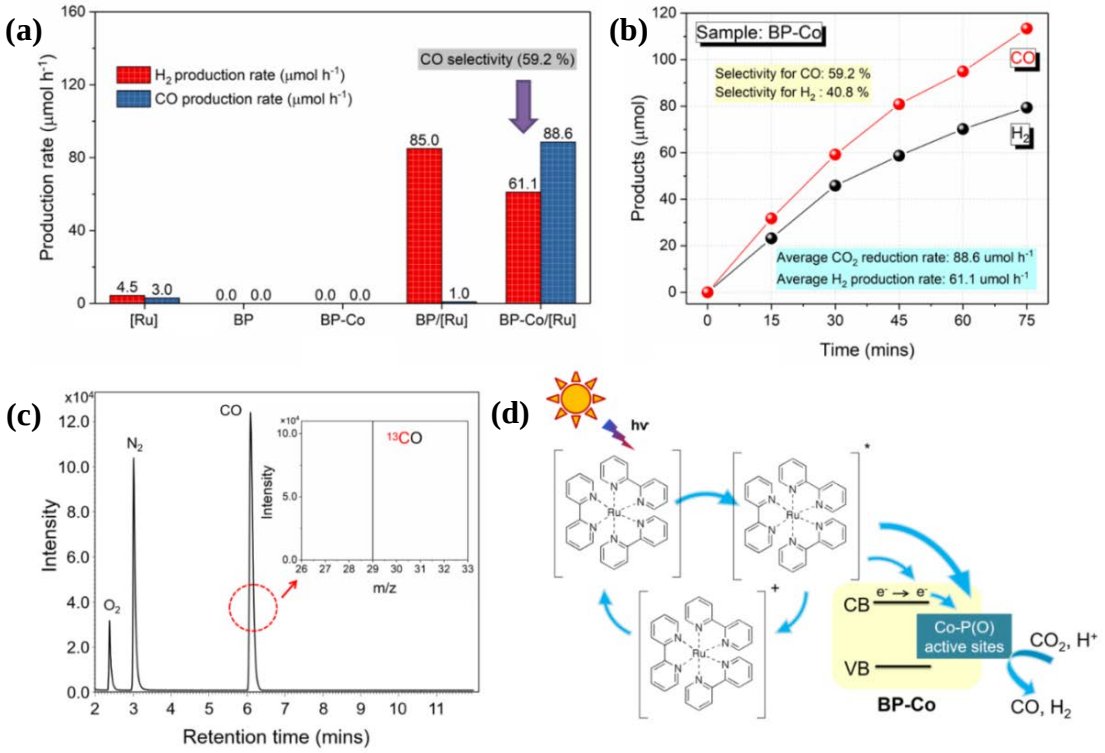

Figure 2.35 (a) Diagram of H_2 generation and CO_2 reduction performance of different catalysts. (b) Time dependent plot of BP-Co for CO_2 photocatalytic reduction with selectivity 59.2% in the presence of [Ru]. (c) GC-mass spectra of ^{13}CO (m/z = 29) produced over BP-Co/[Ru] from the atmosphere of $^{13}CO_2$. (d) The schematic illustration about the mechanism of electron transfer in BP-Co/[Ru] for photocatalytic CO_2 reduction.

Table 2.3 Comparison of the photocatalytic H_2 and CO_2 production performance of BP-Co with the state-of-the-art cocatalysts in the presence of $[Ru(2, 2'\text{-bipyridy})_3]Cl_2$ as photosensitizer.

Materials	H_2 production	CO_2 production	Reference
BP-Co	61.1 μmol h^{-1}	88.6 μmol h^{-1}	**This work**
Co-ZIF-9	59.8 μmol h^{-1}	83.6 μmol h^{-1}	Angew. Chem., 2014[50]
Co_3O_4 Hexagonal Platelets	5.95 μmol h^{-1}	20.03 μmol h^{-1}	Advanced Materials, 2016[51]
Co-C	5.22 μmol h^{-1}	9.36 μmol h^{-1}	Small, 2018[52]
Cu-based BIF-29	7 μmol h^{-1}	33.34 μmol h^{-1}	Angew. Chem., 2019[55]
NiCoOP@ carbon fibers	8.6 μmol h^{-1}	16.6 μmol h^{-1}	Angew. Chem., 2019[54]

2.4 Conclusions

In summary, I have prepared two-dimensional BP-Co nanostructure, where coordinated Co atoms are dispersed on the surface of BP nanosheets. The as-prepared BP-Co can be used as cocatalyst to enhance photocatalytic ability for both H_2 production and CO_2 reduction. I find that BP-Co loaded CdS can deliver much higher H_2 production performance than that of Pt loaded CdS, indicating great potential of BP-Co as substitute for Pt cocatalyst for photocatalytic H_2 evolution. On the other hand, the CO evolution rate as high as 88.6 μmol h^{-1} has been realized from photocatalytic CO_2 reduction over BP-Co in the presence of [Ru], superior to those obtained from the state-of-the-art noble-metal-free cocatalysts. Based on the results of photocatalytic and photoresponse measurements, I attribute the enhancement of photocatalytic reduction to additional charge transfer channel and active sites derived from Co-P(O) bonding which can benefit photocatalytic conversion kinetics for boosting performance. In our work, the Co-P(O) interaction assist stable dispersion of single atom Cobalt on the surface of BP, leading BP-Co nano-materials with good activity as well as promising future in many photo-related applications including hydrogen generation, CO_2 reduction, pollutant degradation and photo-thermal reactions.

References

1. Zou, Z.; Ye, J.; Sayama, K.; Arakawa, H., Direct splitting of water under visible light irradiation with an oxide semiconductor photocatalyst. *Nature* **2001,** *414* (6864), 625-627.

2. Chang, K.; Hai, X.; Ye, J., Transition Metal Disulfides as Noble-Metal-Alternative Co-Catalysts for Solar Hydrogen Production. *Advanced Energy Materials* **2016,** *6* (10), 1502555.

3. Yan, Y.; Chen, J.; Li, N.; Tian, J.; Li, K.; Jiang, J.; Liu, J.; Tian, Q.; Chen, P., Systematic bandgap engineering of graphene quantum dots and applications for photocatalytic water splitting and CO_2 reduction. *ACS Nano* **2018,** *12* (4), 3523-3532.

4. Ran, J.; Jaroniec, M.; Qiao, S. Z., Cocatalysts in semiconductor-based photocatalytic CO_2 reduction: achievements, challenges, and opportunities. *Advanced Materials* **2018,** *30* (7), 1704649.

5. Chang, K.; Mei, Z.; Wang, T.; Kang, Q.; Ouyang, S.; Ye, J., MoS_2/Graphene Cocatalyst for Efficient Photocatalytic H_2 Evolution under Visible Light Irradiation. *ACS Nano* **2014,** *8* (7), 7078-7087.

6. Li, H.; Tu, W.; Zhou, Y.; Zou, Z., Z-Scheme photocatalytic systems for promoting photocatalytic performance: recent progress and future challenges. *Advanced Science* **2016,** *3* (11), 1500389.

7. Meng, X.; Liu, L.; Ouyang, S.; Xu, H.; Wang, D.; Zhao, N.; Ye, J., Nanometals for solar-to-chemical energy conversion: from semiconductor-based photocatalysis to plasmon-mediated photocatalysis and photo-thermocatalysis. *Advanced Materials* **2016,** *28* (32), 6781-6803.

8. Li, Y.; Ouyang, S.; Xu, H.; Hou, W.; Zhao, M.; Chen, H.; Ye, J., Targeted exfoliation and reassembly of polymeric carbon nitride for efficient photocatalysis. *Advanced Functional Materials* **2019,** *29* (27), 1901024.

9. Liu, J.; Li, Y.; Zhou, X.; Jiang, H.; Yang, H. G.; Li, C., Positively charged Pt-based cocatalysts: an orientation for achieving efficient photocatalytic water splitting. *Journal of Materials Chemistry A* **2020,** *8* (1), 17-26.

10. Li, H.; Zhou, Y.; Tu, W.; Ye, J.; Zou, Z., State-of-the-art progress in diverse heterostructured photocatalysts toward promoting photocatalytic performance. *Advanced Functional Materials* **2015,** *25* (7), 998-1013.

11. Twilton, J.; Le, C. C.; Zhang, P.; Shaw, M. H.; Evans, R. W.; MacMillan, D. W. C., The merger of transition metal and photocatalysis. *Nature Reviews Chemistry* **2017,** *1* (7), 0052.

12. Zhao, G.; Zhou, W.; Sun, Y.; Wang, X.; Liu, H.; Meng, X.; Chang, K.; Ye, J., Efficient photocatalytic CO_2 reduction over Co (II) species modified CdS in aqueous solution. *Applied Catalysis B: Environmental* **2018,** *226*, 252-257.

13. Li, Y.; Hao, J.; Song, H.; Zhang, F.; Bai, X.; Meng, X.; Zhang, H.; Wang, S.; Hu, Y.; Ye, J., Selective light absorber-assisted single nickel atom catalysts for ambient sunlight-driven CO_2 methanation. *Nature Communications* **2019,** *10* (1), 2359.

14. Zhang, X.; Fu, A.; Chen, X.; Liu, L.; Ren, L.; Tong, L.; Ye, J., Highly efficient Cu induced photocatalysis for visible-light hydrogen evolution. *Catalysis Today* **2019,** *335*, 166-172.

15. Zhang, H.; Dong, Y.; Zhao, S.; Wang, G.; Jiang, P.; Zhong, J.; Zhu, Y., Photochemical preparation of atomically dispersed nickel on cadmium sulfide for

superior photocatalytic hydrogen evolution. *Applied Catalysis B: Environmental* **2020,** *261*, 118233.

16. Fei, H.; Dong, J.; Arellano-Jiménez, M. J.; Ye, G.; Kim, N. D.; Samuel, E. L. G.; Peng, Z.; Zhu, Z.; Qin, F.; Bao, J.; Yacaman, M. J.; Ajayan, P. M.; Chen, D.; Tour, J. M., Atomic cobalt on nitrogen-doped graphene for hydrogen generation. *Nature Communications* **2015,** *6*, 8668.

17. Zhao, G.; Sun, Y.; Zhou, W.; Wang, X.; Chang, K.; Liu, G.; Liu, H.; Kako, T.; Ye, J., Superior photocatalytic H_2 production with cocatalytic Co/Ni species anchored on sulfide semiconductor. *Advanced Materials* **2017,** *29* (40), 1703258.

18. Zhang, H.; Liu, G.; Shi, L.; Ye, J., Single-atom catalysts: emerging multifunctional materials in heterogeneous catalysis. *Advanced Energy Materials* **2018,** *8* (1), 1701343.

19. Zhao, Q.; Yao, W.; Huang, C.; Wu, Q.; Xu, Q., Effective and Durable Co Single Atomic Cocatalysts for Photocatalytic Hydrogen Production. *ACS Applied Materials & Interfaces* **2017,** *9* (49), 42734-42741.

20. Gao, G.; Jiao, Y.; Waclawik, E. R.; Du, A., Single atom (Pd/Pt) supported on graphitic carbon nitride as an efficient photocatalyst for visible-light reduction of carbon dioxide. *Journal of the American Chemical Society* **2016,** *138* (19), 6292-6297.

21. Yang, X.-F.; Wang, A.; Qiao, B.; Li, J.; Liu, J.; Zhang, T., Single-atom catalysts: a new frontier in heterogeneous catalysis. *Accounts of Chemical Research* **2013,** *46* (8), 1740-1748.

22. Moliner, M.; Gabay, J. E.; Kliewer, C. E.; Carr, R. T.; Guzman, J.; Casty, G. L.; Serna, P.; Corma, A., Reversible transformation of Pt nanoparticles into single atoms inside high-silica chabazite zeolite. *Journal of the American Chemical Society* **2016,** *138* (48), 15743-15750.

23. Fang, X.; Shang, Q.; Wang, Y.; Jiao, L.; Yao, T.; Li, Y.; Zhang, Q.; Luo, Y.; Jiang, H. L., Single Pt atoms confined into a metal-organic framework for efficient photocatalysis. *Advanced Materials* **2018,** *30* (7), 1705112.

24. Jiang, K.; Siahrostami, S.; Zheng, T.; Hu, Y.; Hwang, S.; Stavitski, E.; Peng, Y.; Dynes, J.; Gangisetty, M.; Su, D.; Attenkofer, K.; Wang, H., Isolated Ni single atoms in graphene nanosheets for high-performance CO_2 reduction. *Energy & Environmental Science* **2018,** *11* (4), 893-903.

25. Sakthivel, T.; Huang, X.; Wu, Y.; Rtimi, S., Recent progress in black phosphorus nanostructures as environmental photocatalysts. *Chemical Engineering Journal* **2019,** *379*, 122297.

26. Ji, X.; Kang, Y.; Fan, T.; Xiong, Q.; Zhang, S.; Tao, W.; Zhang, H., An antimonene/Cp*Rh(phen)Cl/black phosphorus hybrid nanosheet-based Z-scheme artificial photosynthesis for enhanced photo/bio-catalytic CO_2 reduction. *Journal of Materials Chemistry A* **2020,** *8* (1), 323-333.

27. Tian, Y.; Wang, H.; Li, H.; Guo, Z.; Tian, B.; Cui, Y.; Li, Z.; Li, G.; Zhang, H.; Wu, Y., Recent advances in black phosphorus/carbon hybrid composites: from improved stability to applications. *Journal of Materials Chemistry A* **2020,** *8* (9), 4647-4676.

28. Kong, L.; Ji, Y.; Dang, Z.; Yan, J.; Li, P.; Li, Y.; Liu, S., g-C_3N_4 loading black phosphorus quantum dot for efficient and stable photocatalytic H_2 generation under visible light. *Advanced Functional Materials* **2018,** *28* (22), 1800668.

29. Shi, F.; Geng, Z.; Huang, K.; Liang, Q.; Zhang, Y.; Sun, Y.; Cao, J.; Feng, S., Cobalt Nanoparticles/Black Phosphorus Nanosheets: An Efficient Catalyst for Electrochemical Oxygen Evolution. *Advanced Science* **2018,** *5* (8), 1800575.

30. Bai, L.; Wang, X.; Tang, S.; Kang, Y.; Wang, J.; Yu, Y.; Zhou, Z. K.; Ma, C.; Zhang, X.; Jiang, J.; Chu, P. K.; Yu, X.-F., Black Phosphorus/Platinum Heterostructure: A Highly Efficient Photocatalyst for Solar-Driven Chemical Reactions. *Advanced Materials* **2018,** *30* (40), 1803641.

31. Yuan, Y.-J.; Shen, Z.-K.; Song, S.; Guan, J.; Bao, L.; Pei, L.; Su, Y.; Wu, S.; Bai, W.; Yu, Z.-T.; Ji, Z.; Zou, Z., Co-P bonds as atomic-level charge transfer channel to boost photocatalytic H_2 production of Co_2P/black phosphorus nanosheets photocatalyst. *ACS Catalysis* **2019,** *9* (9), 7801-7807.

32. Zhu, M.; Kim, S.; Mao, L.; Fujitsuka, M.; Zhang, J.; Wang, X.; Majima, T., Metal-free photocatalyst for H_2 evolution in visible to near-infrared region: black phosphorus/graphitic carbon nitride. *Journal of the American Chemical Society* **2017,** *139* (37), 13234-13242.

33. Zhu, M.; Osakada, Y.; Kim, S.; Fujitsuka, M.; Majima, T., Black phosphorus: A promising two dimensional visible and near-infrared-activated photocatalyst for hydrogen evolution. *Applied Catalysis B: Environmental* **2017,** *217*, 285-292.

34. Late, D. J., Temperature Dependent Phonon Shifts in Few-Layer Black Phosphorus. *ACS Applied Materials & Interfaces* **2015,** *7* (10), 5857-5862.

35. Ren, X.; Li, Z.; Huang, Z.; Sang, D.; Qiao, H.; Qi, X.; Li, J.; Zhong, J.; Zhang, H., Environmentally Robust Black Phosphorus Nanosheets in Solution: Application for Self-Powered Photodetector. *Advanced Functional Materials* **2017,** *27* (18), 1606834.

36. Tao, W.; Zhu, X.; Yu, X.; Zeng, X.; Xiao, Q.; Zhang, X.; Ji, X.; Wang, X.; Shi, J.; Zhang, H.; Mei, L., Black phosphorus nanosheets as a robust delivery platform for cancer theranostics. *Advanced Materials* **2017,** *29* (1), 1603276.

37. Liu, W.; Cao, L.; Cheng, W.; Cao, Y.; Liu, X.; Zhang, W.; Mou, X.; Jin, L.; Zheng, X.; Che, W., Single-site active cobalt-based photocatalyst with a long carrier lifetime for spontaneous overall water splitting. *Angewandte Chemie International Edition* **2017,** *56* (32), 9312-9317.

38. Mao, L.; Cai, X.; Yang, S.; Han, K.; Zhang, J., Black phosphorus-CdS-$La_2Ti_2O_7$ ternary composite: Effective noble metal-free photocatalyst for full solar spectrum activated H_2 production. *Applied Catalysis B: Environmental* **2019,** *242*, 441-448.

39. Liang, Q.; Shi, F.; Xiao, X.; Wu, X.; Huang, K.; Feng, S., In Situ Growth of CoP Nanoparticles Anchored on Black Phosphorus Nanosheets for Enhanced Photocatalytic Hydrogen Production. *ChemCatChem* **2018,** *10* (10), 2179-2183.

40. Mizuno, J., An X-ray study on the structure of cobalt dichloride hexahydrate. *Journal of the Physical Society of Japan***1960,** *15* (8), 1412-1420.

41. Ha, D.-H.; Moreau, L. M.; Bealing, C. R.; Zhang, H.; Hennig, R. G.; Robinson, R. D., The structural evolution and diffusion during the chemical transformation from cobalt to cobalt phosphide nanoparticles. *Journal of Materials Chemistry* **2011,** *21* (31), 11498-11510.

42. Saadi, F. H.; Carim, A. I.; Drisdell, W. S.; Gul, S.; Baricuatro, J. H.; Yano, J.; Soriaga, M. P.; Lewis, N. S., Operando spectroscopic analysis of CoP films electrocatalyzing the hydrogen-evolution reaction. *Journal of the American Chemical Society* **2017,** *139* (37), 12927-12930.

43. Ran, J.; Zhu, B.; Qiao, S. Z., Phosphorene Co-catalyst Advancing Highly Efficient Visible-Light Photocatalytic Hydrogen Production. *Angewandte Chemie International Edition* **2017,** *56* (35), 10373-10377.

44. Simon, T.; Carlson, M. T.; Stolarczyk, J. K.; Feldmann, J., Electron transfer rate vs recombination losses in photocatalytic H_2 generation on Pt-decorated CdS nanorods. *ACS Energy Letter* **2016,** *1* (6), 1137-1142.

45. Ma, L.; Chen, K.; Nan, F.; Wang, J.-H.; Yang, D.-J.; Zhou, L.; Wang, Q. Q., Improved Hydrogen Production of Au-Pt-CdS Hetero-Nanostructures by Efficient

Plasmon-Induced Multipathway Electron Transfer. *Advanced Functional Materials* **2016,** *26* (33), 6076-6083.

46. Li, Q.; Zhao, F.; Qu, C.; Shang, Q.; Xu, Z.; Yu, L.; McBride, J. R.; Lian, T., Two-dimensional morphology enhances light-driven H_2 generation efficiency in CdS nanoplatelet-Pt heterostructures. *Journal of the American Chemical Society* **2018,** *140* (37), 11726-11734.

47. Yuan, Y.-J.; Wang, P.; Li, Z.; Wu, Y.; Bai, W.; Su, Y.; Guan, J.; Wu, S.; Zhong, J.; Yu, Z.-T.; Zou, Z., The role of bandgap and interface in enhancing photocatalytic H_2 generation activity of 2D-2D black phosphorus/MoS_2 photocatalyst. *Applied Catalysis B: Environmental* **2019,** *242*, 1-8.

48. Edmonds, M. T.; Tadich, A.; Carvalho, A.; Ziletti, A.; O'Donnell, K. M.; Koenig, S. P.; Coker, D. F.; Özyilmaz, B.; Neto, A. C.; Fuhrer, M., Creating a stable oxide at the surface of black phosphorus. *ACS Applied Materials & Interfaces* **2015,** *7* (27), 14557-14562.

49. Wood, J. D.; Wells, S. A.; Jariwala, D.; Chen, K.-S.; Cho, E.; Sangwan, V. K.; Liu, X.; Lauhon, L. J.; Marks, T. J.; Hersam, M. C., Effective passivation of exfoliated black phosphorus transistors against ambient degradation. *Nano Letter* **2014,** *14* (12), 6964-6970.

50. Wang, S.; Yao, W.; Lin, J.; Ding, Z.; Wang, X., Cobalt imidazolate metal-organic frameworks photosplit CO_2 under mild reaction conditions. *Angewandte Chemie International Edition* **2014,** *53* (4), 1034-1038.

51. Gao, C.; Meng, Q.; Zhao, K.; Yin, H.; Wang, D.; Guo, J.; Zhao, S.; Chang, L.; He, M.; Li, Q.; Zhao, H.; Huang, X.; Gao, Y.; Tang, Z., Co_3O_4 Hexagonal Platelets with Controllable Facets Enabling Highly Efficient Visible-Light Photocatalytic Reduction of CO_2. *Advanced Materials* **2016,** *28* (30), 6485-6490.

52. Zhao, K.; Zhao, S.; Gao, C.; Qi, J.; Yin, H.; Wei, D.; Mideksa, M. F.; Wang, X.; Gao, Y.; Tang, Z.; Yu, R., Metallic Cobalt-Carbon Composite as Recyclable and Robust Magnetic Photocatalyst for Efficient CO_2 Reduction. *Small* **2018,** *14* (33), 1800762.

53. Li, Y.; Ren, J.; Ouyang, S.; Hou, W.; Petit, T.; Song, H.; Chen, H.; Philo, D.; Kako, T.; Ye, J., Atomic carbon chains-mediated carriers transfer over polymeric carbon nitride for efficient photocatalysis. *Applied Catalysis B: Environmental* **2019,** *259*, 118027.

54. Wang, Y.; Wang, S.; Lou, X. W., Dispersed nickel cobalt oxyphosphide nanoparticles confined in multichannel hollow carbon fibers for photocatalytic CO_2 reduction. *Angewandte Chemie International Edition* **2019,** *58* (48), 17236-17240.

55. Zhang, H. X.; Hong, Q. L.; Li, J.; Wang, F.; Huang, X.; Chen, S.; Tu, W.; Yu, D.; Xu, R.; Zhou, T.; Zhang, J., Isolated Square-Planar Copper Center in Boron Imidazolate Nanocages for Photocatalytic Reduction of CO_2 to CO. *Angewandte Chemie* **2019,** *131* (34), 11878-11882.

56. Zhou, P.; Zhang, Q.; Xu, Z.; Shang, Q.; Wang, L.; Chao, Y.; Li, Y.; Chen, H.; Lv, F.; Zhang, Q.; Gu, L.; Guo, S., Atomically Dispersed Co-P_3 on CdS Nanorods with Electron-Rich Feature Boosts Photocatalysis. *Advanced Materials* **2020,** *32* (7), 1904249.

57. Fu, J.; Jiang, K.; Qiu, X.; Yu, J.; Liu, M., Product selectivity of photocatalytic CO_2 reduction reactions. *Materials Today* **2020,** *32*, 222-243.

Chapter 3 Metal dopants mediated interfacial engineering of ultrafine CoP nanoparticles for promoting photocatalytic H_2 evolution

3.1 Introduction

Hydrogen (H_2) is known as a clean and sustainable energy carrier that plays an essential role in the low-carbon economic system. In the past decades, the developments of hydrogen energy system as well as applications of hydrogen in different fields have attracted worldwide interests.[1-3] Until now, a variety of photocatalysts have been exploited in the H_2 evolution reaction. However, semiconductor-based photocatalysts usually suffer from rapid electron-hole recombination, lack of reaction sites, and low efficiency in solar to chemical energy conversion. To overcome the aforementioned difficulties, a cocatalyst is usually required to enhance the separation of photogenerated electron-hole pair and to provide sufficient active sites for surface chemical reactions.[4-10] Generally, most highly efficient photocatalytic systems are realized by utilizing noble-metal-based cocatalysts such as Pt, Pd, Ag, etc.[11] Unfortunately, noble metals are too scarce and expensive to be used for large-scale energy production. Therefore, the explorations and developments of cost-effective cocatalysts are highly desired.

Of particular interest, cobalt-based transition metal phosphides have attracted worldwide attention as promising noble metal-free alternatives for noble-metal-based cocatalysts in photocatalytic H_2 production.[12] Amongst various cobalt-based materials, cobalt phosphides (CoP_x) including Co_2P, CoP, CoP_2, CoP_3, etc. have become the hot topic in catalytic H_2 production owing to the metal-like characteristics of Co-P bond.[13-15] With lower Fermi energy level, it was anticipated that CoP can play a significant role in promoting both electrocatalytic and photocatalytic H_2 evolution.[16] Previous studies indicated that rational construction of Schottky junction between CoP and semiconductor CdS can enable promising improvements on photocatalytic H_2 evolution performance.[17-21] Meanwhile, the efficient electron transfer property with long-lived charge carriers endows great capability to photogenerated electrons for reducing adsorbed H^+ into H_2.

Moreover, it has been reported that metal cations can be employed to tailor the electronic structure of CdS for further enhancing the photocatalytic performance.[22] By doping with a donor impurity, the impurity levels below the conduction band may induce the generation of electron trap sites on the surface of CdS, which is believed to hinder photogenerated electron-hole recombination and increase the lifetime of photogenerated electrons.[23, 24] Common alkaline-earth metal ions like (Mg^{2+}, Ca^{2+}, Sr^{2+}, Ba^{2+}) with good stability and charge transition properties have been applied in modifying semiconductor.[25] Benefitted from the good electron-donating feature and stability of alkaline-earth metal ions, significant enhancement on the photocatalytic activities have been realized after doping with alkaline-earth metal ions.[26] However, it has rarely been applied in modifying CdS-based photocatalysts.

Herein, we proposed a convenient preparation strategy to fabricate ultrafine CoP nanoparticles and applied it into photocatalytic H_2 evolution. By utilizing organophosphorus compound triphenylphosphine (PPh_3) as phosphorous source, the as-fabricated CoP nanoparticles are intrinsically encapsulated by carbon layer and applied as the cocatalyst for photocatalytic H_2 evolution. To our notice, this is the first report about the design of carbon assisted CoP@CdS interfacial structure through the pyrolysis of PPh_3, which does not require additional hybrid carbon source via multi-step reactions. The relation between metal dopants and the catalytic performance has been investigated. Benefitted from the interfacial engineering, the charge transfer behavior between CdS and CoP has been modified through Ca^{2+} dopant. Specially, the photocatalytic H_2 generation over Ca-modified CoP@CdS can reach up to 2441.5 μmol h^{-1} with the apparent quantum efficiency of 35.4% at 420 nm. Finally, the mechanism was explored to reveal the effect of Ca^{2+} dopant on the underlying mechanism of the excellent photocatalytic H_2 generation performance.

3.2 Experimental section

3.2.1 Material preparation

Materials and reagents. Commercial CdS power (98%) was provided by Strem Chemicals, Inc. Chemicals were purchased from FUJIFILM Wako Pure Chemical Corporation, including Triphenylphosphine (PPh_3, Practical Grade), ethanol (95 %, Extra Pure), and $CoCl_2 \cdot 6H_2O$ (Guaranteed Reagent). All chemicals were used directly

without further purification. The deionized water supplied by a Millipore System (Millipore Q) with a resistivity of 18.2 MΩ cm^{-1} was used in all experiments.

Fabrication of CoP@CdS. In order to prepare CoP@CdS, a certain amount of PPh_3 was first mixing and grinding with commercial CdS. After the self-assembling process of PPh_3 molecules, $CoCl_2$ with mole ratio of 0.5% were added and annealed at 300 °C, 400 °C, 450 °C, 500 °C, 550 °C, and 600 °C under argon atmosphere. The resulting samples were applied as photocatalysts for hydrogen generation.

Fabrication of Ca-modified CoP@CdS. The Ca-modified CoP@CdS photocatalyst was prepared through the pyrolysis of organophosphorus compound triphenylphosphine (PPh_3). In detail, the commercial CdS was first mixed with 0.5% mole proportions of Co^{2+} and Ca^{2+} in ethanol solution. After that, the dried mixture was annealed at temperatures at 500 °C under argon atmosphere. The resulting sample was denoted as Ca-modified CoP@CdS and applied as photocatalyst for hydrogen generation. For comparison, Ca-modified CdS and CdS-P were prepared by respectively annealing the mixture of CdS/$CaCl_2$ and CdS/PPh_3 under same conditions. The annealing CdS refers to the CdS annealed directly at temperatures at 500 °C under argon atmosphere without any other modification. In addition to Ca^{2+}, CdS has been modified with other metals dopants (Mg^{2+}, Sr^{2+}, Ba^{2+}, Cr^{3+}, Al^{3+}, V^{3+}, Nd^{3+}, and Mo^{5+}) in equal amounts. All the resulting samples were applied as photocatalysts for hydrogen generation.

3.2.2 Material characterization

Characterizations. Elemental contents have been determined by inductively coupled plasma optical emission spectrometry (ICP-OES, Agilent5800). The atomic structural information of the sample was determined by X-ray diffraction (XRD, PANalytical X'Pert PRO). The surface morphologies of the samples were performed on the field emission scanning electron microscopy (FE-SEM, JSM-6701F). High resolution Transmission electron microscopy (TEM) images and energy dispersive X-ray spectroscopy (EDX) images were obtained using a JEOL-2100F operated at 200 kV. The diffuse reflectance spectroscopy in the range of 400-800 nm were recorded by UV-vis spectroscopy (UV-2600 Shimadzu Corp., Japan), the bandgap can be calculated according to transformed Kubelka-Munk function. Raman spectra were collected by engaging the Raman microscope (NRS-1000, Japan) with 532 nm excitation at room temperature. The core-level photoelectron spectra were recorded by X-ray

photoelectron spectroscopy (XPS, ThermoFisher, Thermo Scientific K-Alpha) equipped with a mono Al Kα X-ray radiation (1486.6 eV) source. The charge effect was calibrated using the binding energy of the C-C bond in C 1s (284.8 eV). The decay time measurements were performed on a Hamamatsu instrument (Hamamatsu C5680, Japan). After the sample was irradiated by 420 nm excitation light, 150 W Xe lamp (Osram XBO; 150 W) was applied as the probe light source for analyzing the absorption of transient species. The transient absorption intensity decay curves at 520 nm were fitted and investigated.

ICP-OES measurements. 2 mg of sample was weighed and transferred into PFA beaker. 10 mL of NNO_3 (1+1) was added into the beaker and decomposed by heating. After cooling, the solution was poured into 100 mL of PP volumetric flask and then 10 mL of 20 mg/L Y standard solution was added into the flask as internal standard. This solution was diluted to marked line with Milli-Q water. And the concentrations of Cd, P, Co and Ca in the prepared solution were measured by ICP-OES.

3.2.3 Photochemical measurements

Measurement of H_2 evolution performance. Photocatalytic H_2 evolution activities were evaluated under visible-light irradiation. The 300 W xenon arc lamp equipped with a 420 nm cut-off filter was used as the light source. In a typical measurement, 100 mg of as-prepared sample was dissolved into 260 mL of 0.25 M/0.35 M Na_2S/Na_2SO_3 solution, after that the solution was transferred into a quartz glass reaction cell and connect to a gas-closed system with a gas-circulated pump. Before the irradiation, the reaction cell was evacuated to remove the air completely. The produced H_2 was recorded and analyzed by an online gas chromatograph (GC-8A, Shimadzu Corp., Ar carrier, TCD, Japan) with argon as the carrier gas.

Measurement of quantum efficiencies. The apparent quantum efficiency (AQE) was measured under similar conditions as described above except for the light intensity and the wavelength regions of the irradiation light. A series of band-pass filters with central wavelengths of 420 nm, 440 nm, 460 nm, 480 nm, 500 nm, 520 nm, 540 nm, 560 nm, 580 nm, and 600 nm were adopted to control the wavelength regions of monochromatic light. A water filer was also used together with the band-pass filter to avoid the possible damage caused by heating effect of Xe lamp. The average intensity of irradiation was

determined by using a spectroradiometer (Ushio, USR-40, Japan). The AQE at each monochromatic wavelength was estimated by following the equation below:

$$\text{AQE for } H_2 \text{ evolution} = \frac{2 \times number\ of\ evolved\ H_2\ molecules}{number\ of\ incident\ photons} \times 100\%$$

The first-principles calculations are performed using the Vienna ab-initio simulation package (VASP)[27, 28] within spin-polarized density functional theory (DFT).The generalized gradient approximation (GGA) with the Perdew–Burke–Ernzerhof functional (PBE)[29] is used to describe the electronic exchange-correlation interaction. A plane-wave basis set with a kinetic cutoff energy of 400 eV is employed. A 3 × 3 × 1 gamma centered Monkhorst-Pack grids in the Brillouin zone (BZ) is used in the geometry optimization and static electronic structure computation. The criteria for energy and atom force convergence are set to 10^{-4} eV per unit cell and 0.05 eV $Å^{-1}$, respectively.

In order to evaluate the hydrogen evolution reaction electrocatalytic activity, the Gibbs free energy of the strained phosphorene adsorbed H atoms are calculated by the following :

$$\Delta G_{H^*} = E_{H^*} + \Delta E_{ZPE} - T\Delta S \quad (1)$$

Where E_{H^*}, ΔE_{ZPE} and $T\Delta S$ stand for the hydrogen adsorption energy, zero-point energy and entropy contributions between H absorbed and H_2 gas molecule, respectively.

To gain insight into the charge transfer between CdS and CoP, we calculated the difference charge density as:

$$\Delta\rho = \rho_{A+B} - \rho_A - \rho_B \quad (2)$$

where ρ_A, ρ_B and ρ_{A+B} represent total charge densities of CdS supercell, CoP supercell and CoP@CdS system, respectively.

3.3 Results and discussion

3.3.1 Synthesis and structural characterizations of Ca-modified CoP@CdS

The Ca-modified CoP@CdS photocatalyst was prepared through the pyrolysis of organophosphorus compound triphenylphosphine (PPh_3), and the detail synthetic routes have been demonstrated in Figure 3.1. In order to prepare Ca-modified CoP@CdS, a certain amount of PPh_3 was first mixing and grinding with commercial CdS. After the

self-assembling process of PPh_3 molecules, $CoCl_2$ and $CaCl_2$ with mole ratio of 0.5% were added and annealed at 500 °C under argon atmosphere. Different from previous reported phosphatizing protocols for synthesize TMP-based hybrids, the developed strategy does not require flammable compounds (e.g. PH_3 or H_2, etc.) and corrosive conditions and it is much safer and easier to manifest comparing to conventional methods. This finding also simplifies the fabrication procedure to create carbon layer without the needs of additional hybrid carbon source via multi-step reactions.

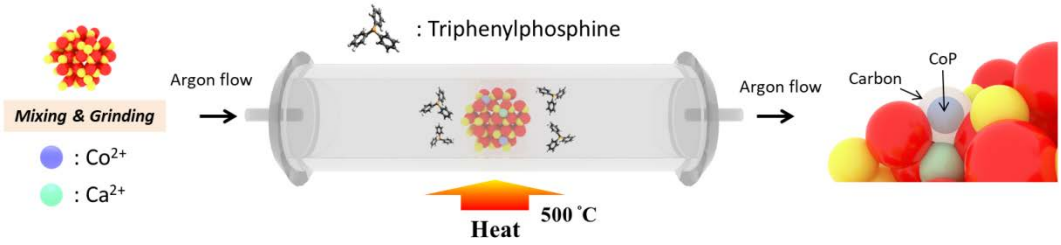

Figure 3.1 Schematically illustration on the synthesize processes of Ca-modified CoP@CdS.

3.3.2 Structural characterizations of Ca-modified CoP@CdS

To unveil the morphology of Ca-modified CoP@CdS structure, characterizations including transmission electron microscopy (TEM) images, high-resolution TEM (HRTEM) and energy dispersive X-ray spectroscopy (EDX) were investigated. The morphology of CoP@CdS before the modification of Ca^{2+} has been demonstrated. As shown in Figure 3.2, the amorphous carbon cages can be observed on the surface of CdS after annealing, where small Co-based nanoparticles are separately anchored in the carbon cages.

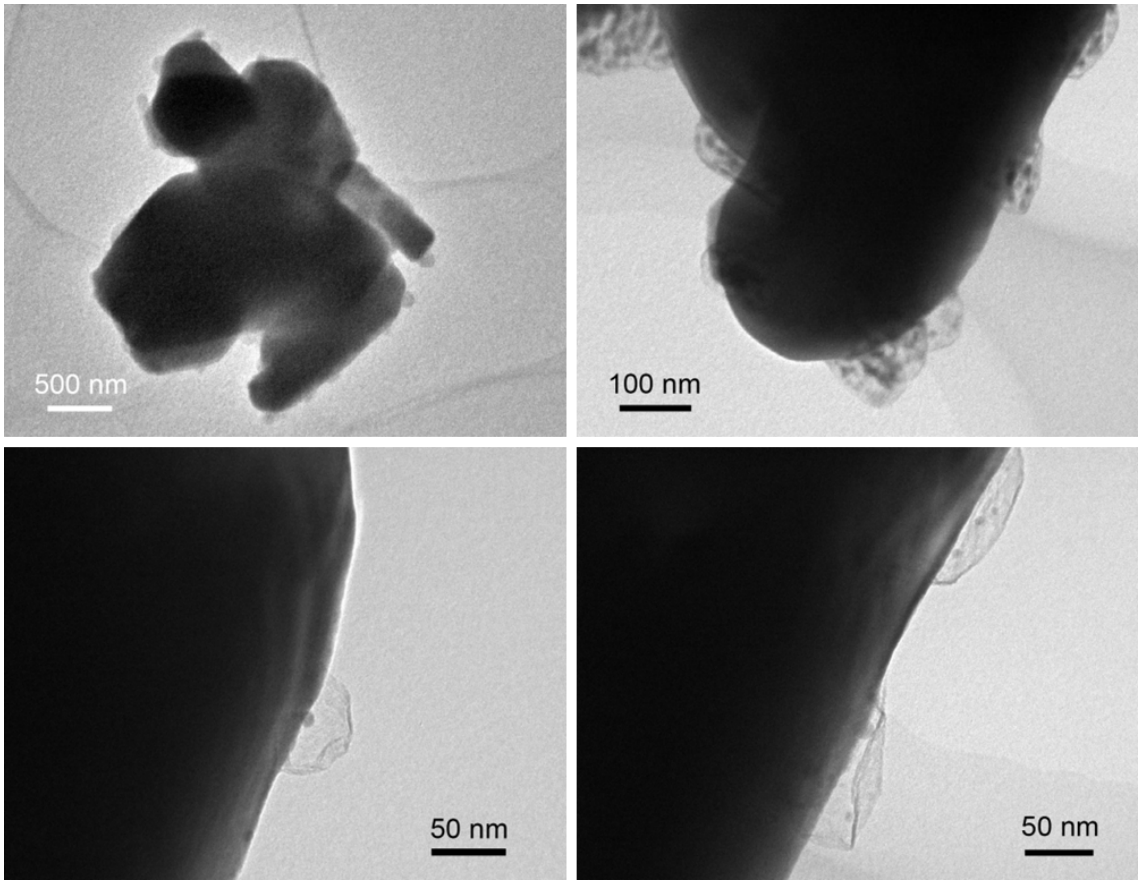

Figure 3.2 TEM images of CoP@CdS.

The elemental mapping displays that C and Co elements uniformly distribute on the surface of CdS, while P element concentrates at interface region between CdS and carbon cages (Figure 3.3). In this situation, the amorphous carbon cages act as the substrate for the growth of Co active sites (Figure 3.4). However, the long distance between CdS and Co active sites usually leads to negative effect on electron transport which is undesired for photocatalytic reactions.

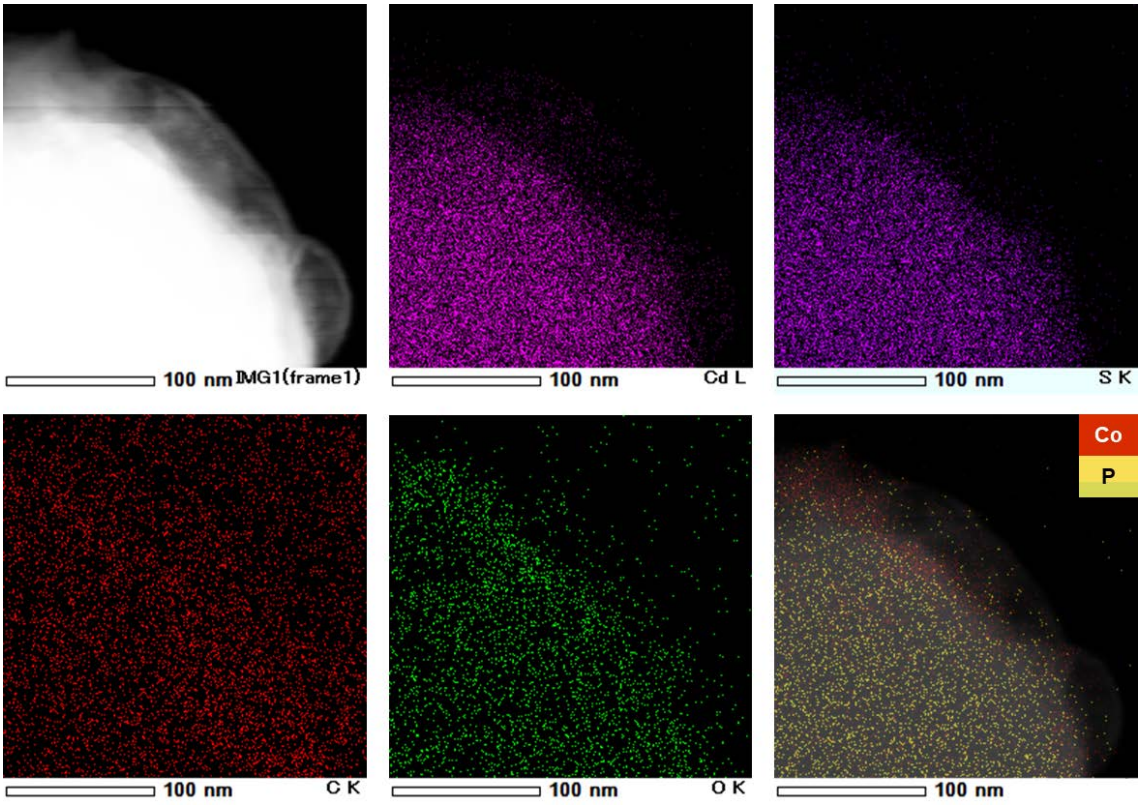

Figure 3.3 EDS mapping of CoP@CdS.

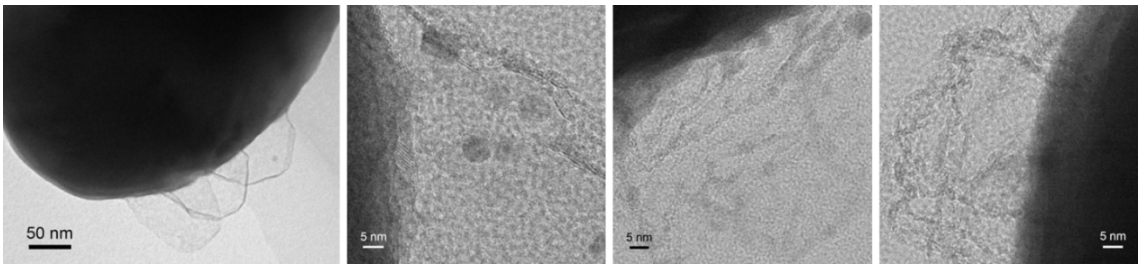

Figure 3.4 High-resolution TEM images of CoP@CdS.

After Ca^{2+} modification, the carbon layer was wrapped on the surface of CdS tightly (Figure 3.5a), which may be attributed to ascending reducibility of Ca-modified CdS together with strong interaction between PPh_3 and Ca^{2+} dopant.[30] The SAED of CdS can be observed in Figure 3.5b, which indicates the typical single crystal structure of CdS.[31] HRTEM images in Figure 3.5c and Figure 3.5d depict that the ultrathin CoP nanoparticles are anchored on the surface of CdS and wrapped by thin carbon layer (approximate thickness < 4 nm, Figure 3.6). The inter-planar spacing≈0.242 nm agrees with the (102) plane of hexagonal crystalline structure of CdS, while the d-spacing of 0.28 nm corresponded to the (002) plane of CoP (Figure 3.5d). Besides that, EDX mappings (Figure 3.7) also indicate the uniformly distribution of C, Co, P, and Ca elements on CdS. The chemical compositions of the samples (Table 3.1) were

quantitatively determined using inductively coupled plasma-optical emission spectrometry (ICP-OES), and the mass ratio of Ca has been determined to be 0.1 wt.%.

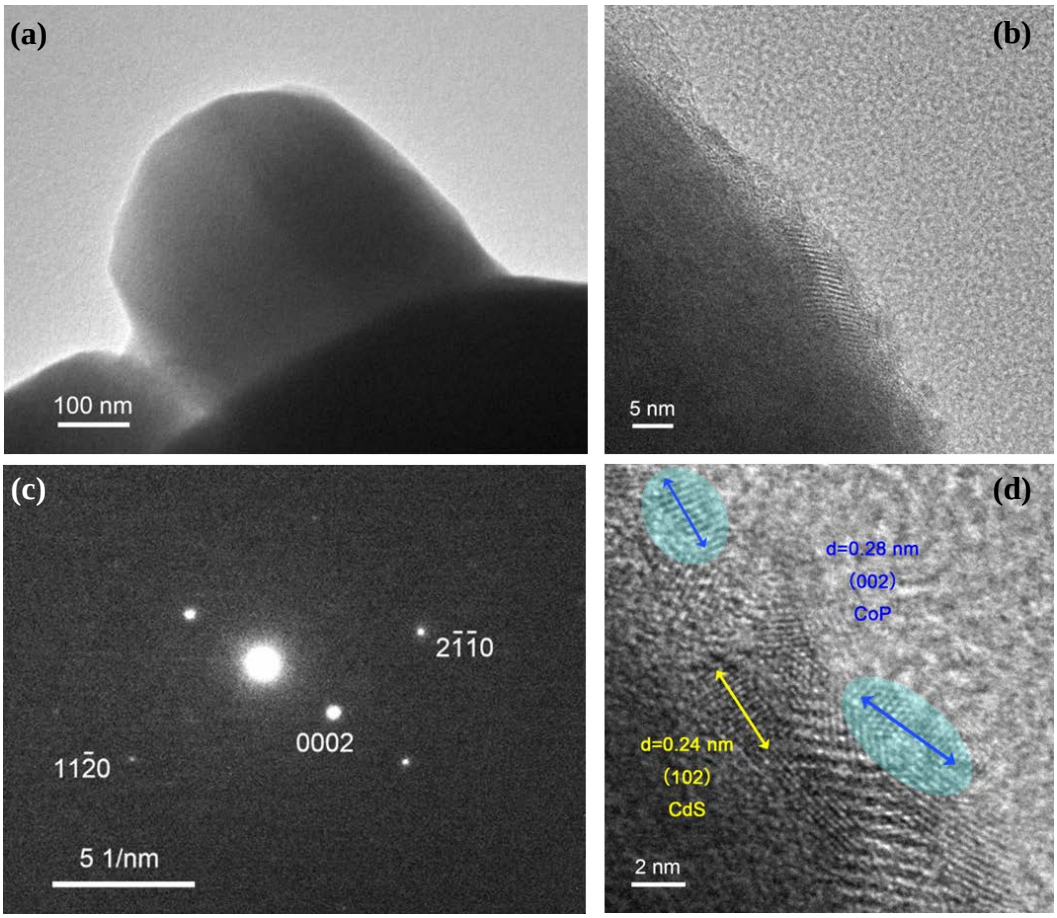

Figure 3.5 (a) TEM image and (b) SAED pattern of Ca-modified CoP@CdS. (c) and (d) HRTEM image on the interface between carbon, CoP and CdS.

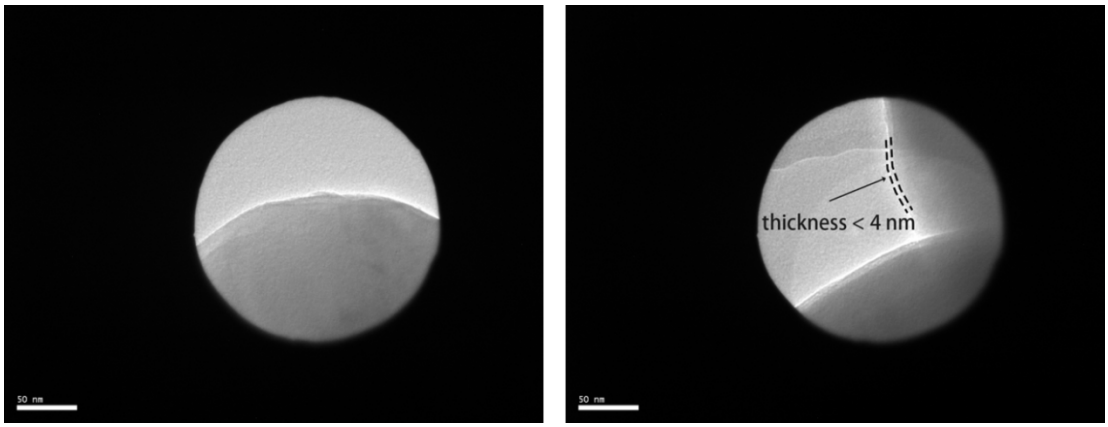

Figure 3.6 TEM image to reveal the thickness of carbon layer.

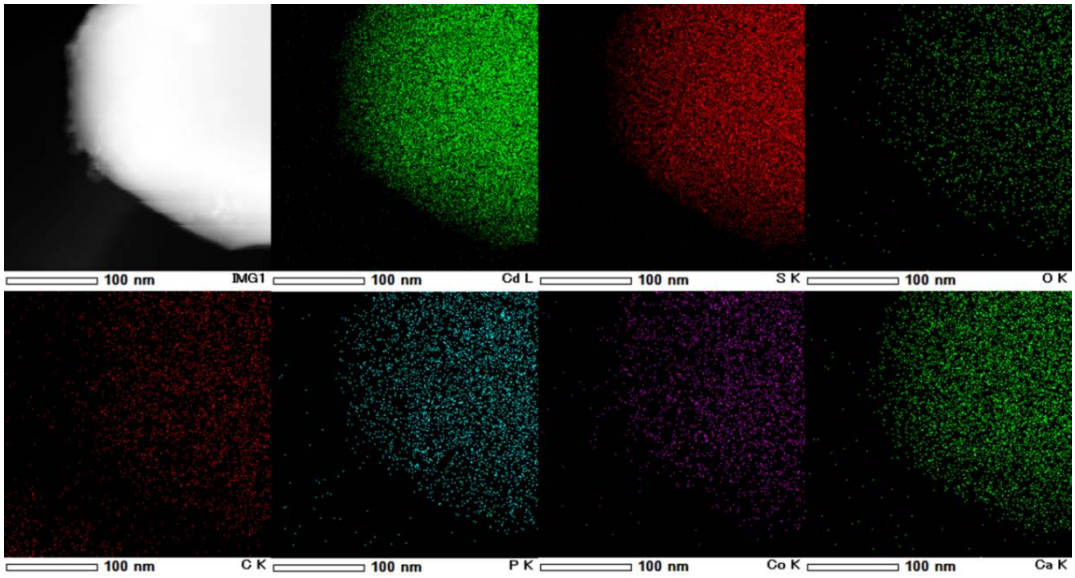

Figure 3.7 HADDF and overlapping EDX mappings of Cd, S, O, C, P, Co and Ca elements on the Ca-modified CoP@CdS.

Table 3.1 ICP-OES results.

Samples	Elements (mass %)			
	Cd	P	Co	Ca
CoP@CdS	76.0	<0.1	0.2	-
Ca-modified CoP@CdS	76.2	<0.1	0.2	0.1

Due to it is the first time to apply PPh_3 as phosphorus source in CdS system, X-ray diffraction (XRD) measurements confirmed the structure of the Ca-modified CoP@CdS and related samples. The XRD results of CdS and Ca-modified CoP@CdS after calcination under 500 °C show no distinct difference, and the patterns which are demonstrated in Figure 3.8a can be indexed into standard hexagonal crystalline structure of CdS (P63mc space group, JCPDS No. 06-0314) for the peaks at 24.9°, 26.6°, 28.2° corresponding to (100), (002), and (101) planes of wurtzite CdS. No obvious shift of the XRD peaks (Figure 3.8b) can be observed since the ionic radii of Ca^{2+} (0.099 nm) is similar to that of Cd^{2+} (0.097 nm).[32]

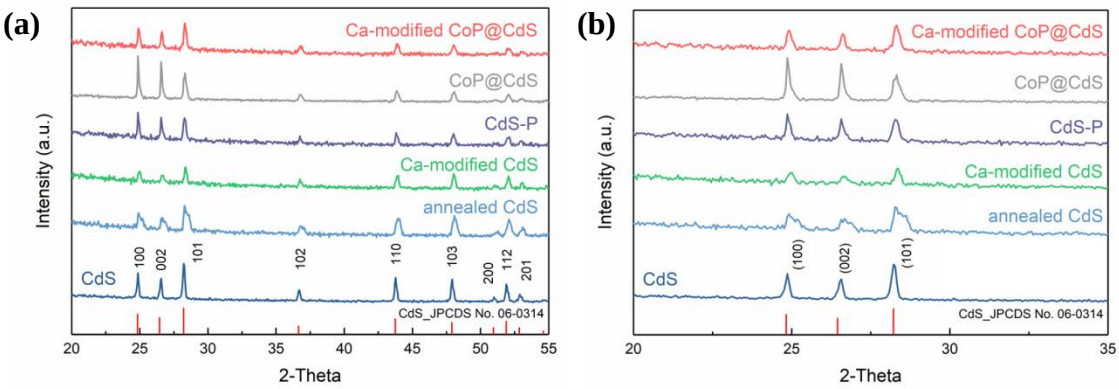

Figure 3.8 (a) XRD analysis of CdS, annealed CdS, Ca-modified CdS, CdS-P, CoP@CdS, and Ca-modified CoP@CdS. (b) Enlarged XRD results.

Meanwhile, I have conducted X-ray photoelectron spectroscopy (XPS) to study the characteristics of Ca-modified CoP@CdS. The full-survey spectrum demonstrates the existence of Cd, S, C, O, Co, P, and Ca elements in the hybrid (Figures 3.9). The peak centered at 347.3 eV corresponds to Ca2$p_{3/2}$ indicating that calcium mainly exists as Ca^{2+}. In the high-resolution spectrum of Co 2p (Figure 3.10), the binding energy 779.6 eV is very close to that of Co $2p_{3/2}$ in CoP, which may suggest a new electron transfer channel has formed due to the interaction between Co and P as previous reported.[23, 33, 34] Other peaks that belong to Co $2p_{1/2}$ and Co $2p_{3/2}$ of Co^{2+} components can be attributed into unavoidable surface oxidation. Comparing to the results of EDX (Figure 3.11) and ICP-OES, the atomic percentage of Ca^{2+} is much higher when analyzed by XPS (Table 3.2). Therefore, it can be expected that most of Ca^{2+} ions are existed mainly on the surface of CdS

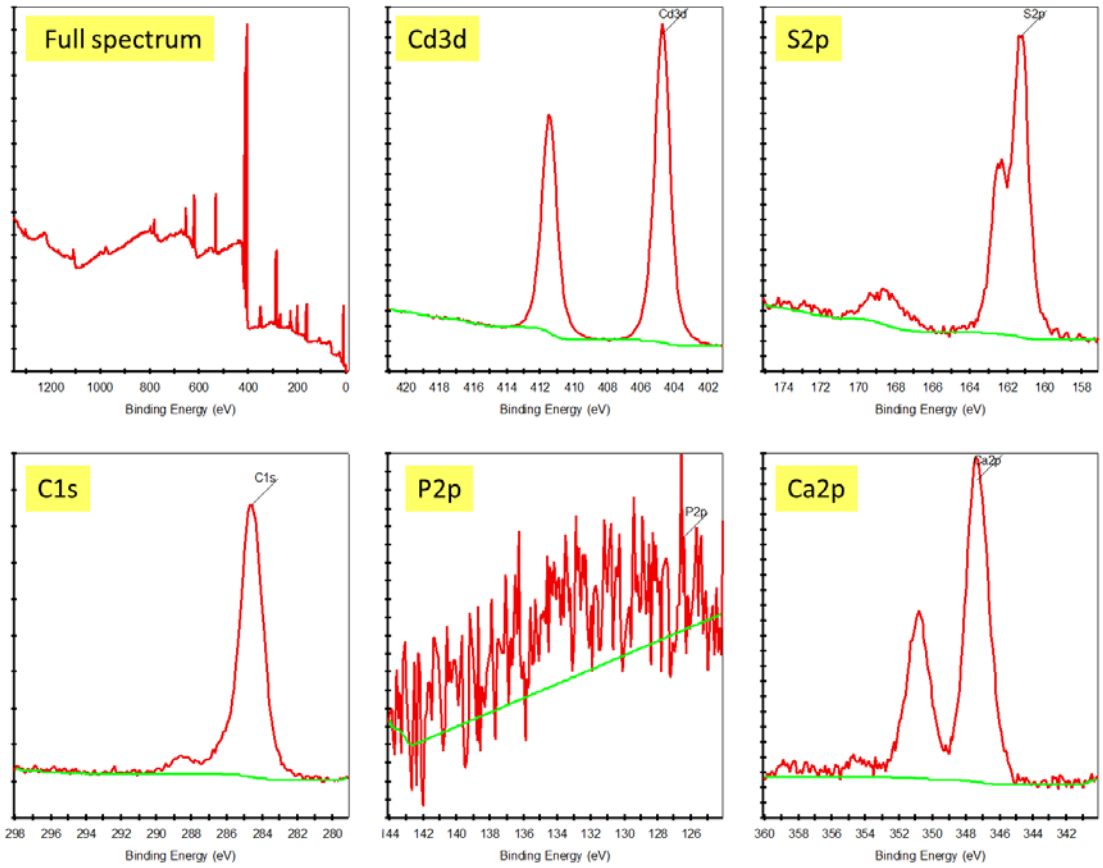

Figure 3.9 Full-survey spectrum and high-resolution XPS spectrum of Cd 3d, S 2p, C 1s, O 1s, Co 2p, P 2p, and Ca 2p for Ca-modified CoP@CdS.

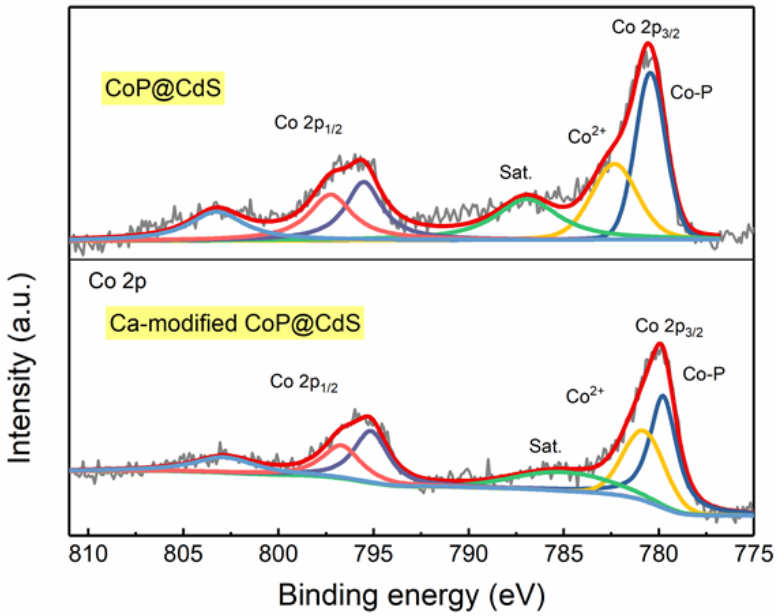

Figure 3.10 High-resolution XPS spectrum of Co 2p for Ca-modified CoP@CdS.

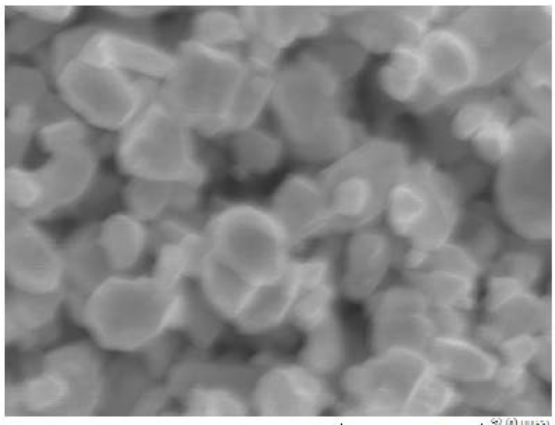

ZAF法 簡易定量分析
フィッティング係数 : 0.0259

元素	(keV)	質量%	σ	原子数%	化合物	質量%	カチオン数	K
P K	2.013	0.14	0.03	0.33				0.1484
S K	2.307	19.12	0.10	45.01				23.1059
Ca K*	3.690	0.18	0.06	0.34				0.2045
Co K	6.924	0.36	0.08	0.47				0.4082
Cd L*	3.132	80.19	0.35	53.85				76.1330
合計		100.00		100.00				

Figure 3.11 EDX result of Ca-modified CoP@CdS.

Table 3.2 XPS experiments of Ca-modified CoP@CdS: weight and atomic percentage of the elemental analyses.

Peaks	Start BE	Peak BE	End BE	Height CPS	FWHM eV	**wt. %/at. %**	PP Height CPS
C1s	297.98	284.59	279.18	37339.44	1.5	19.83/48.04	38012.75
Ca2p	359.98	347.33	340.18	10619.85	1.58	4.91/3.57	10976.76
Cd3d	420.98	404.7	401.18	208148.2	1.06	41.87/10.83	212548.26
Co2p	811.98	780.07	771.18	8071.05	2.83	6.5/3.2	8839.23
P2p	143.98	126.52	124.18	315.14	-	1.26/1.18	590.33
O1s	544.98	531.35	525.18	23958.4	2.24	10.89/19.78	25654.69
S2p	174.98	161.26	157.18	20035.64	1.17	14.74/13.4	20182.33

The electron transfer process has been elucidated by photoluminescence and time-resolved photoluminescence spectra under room-temperature. In general, the recombination of electron-hole pairs in CdS leads to photoluminescence phenomenon, and the intensity suggest the recombination rate of photogenerated charge carriers (Figure 3.12). In our experiments, a sharp emission band centered at 520 nm and a broad emission band centered at 650 nm can be observed when the photocatalysts were excited at a wavelength of 420 nm. The two characteristic peaks can be assigned to band-to-band transition and surface radiative transition resulting from band-gap emission and trap-state emission, respectively. After Ca doping, the band-gap emission of CdS are dramatically quenched which indicate a low recombination rate of carriers. In contrast, the trap-state emission becomes stronger and broader after Ca doping, this phenomenon reveals that photon-induced carriers can be extracted out to reach the electron trapping sites centered on the surface owing to the increase of Ca-related defects located on the surface.[25] We also notice that the intensities of both band-gap emission and trap-state emission were remarkably quenched upon loading CoP. This photoluminescence quench behavior indicates fast charge transfer of electrons from CdS to CoP, attributing to more effective electron-hole separation ability in Ca-modified CoP@CdS than that in pure CdS.

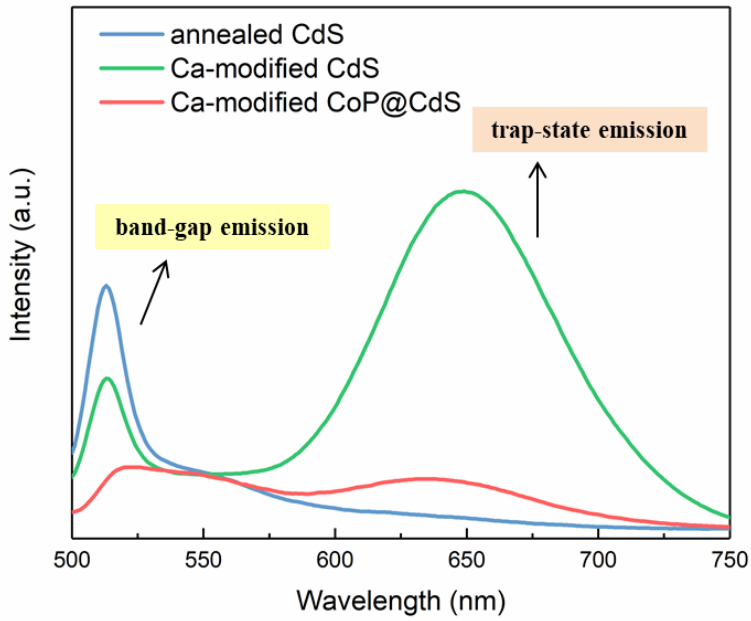

Figure 3.12 Steady-state photoluminescence spectra of annealed CdS, Ca-modified CdS, and Ca-modified CoP@CdS. (excitation 420 nm)

The light absorption spectra are used to acquire optical property of as-prepared photocatalysts (Figure 3.13a). Both unmodified and Ca-modified CdS can only absorb light with wavelength less than ~550 nm. An increment on light absorption properties over the visible wavelength range has been discovered benefitted from the incorporation of CoP.[35] The optical absorption spectra demonstrate the slightly decreased bandgap of Ca-modified CdS comparing to annealed CdS (Figure 3.13b).

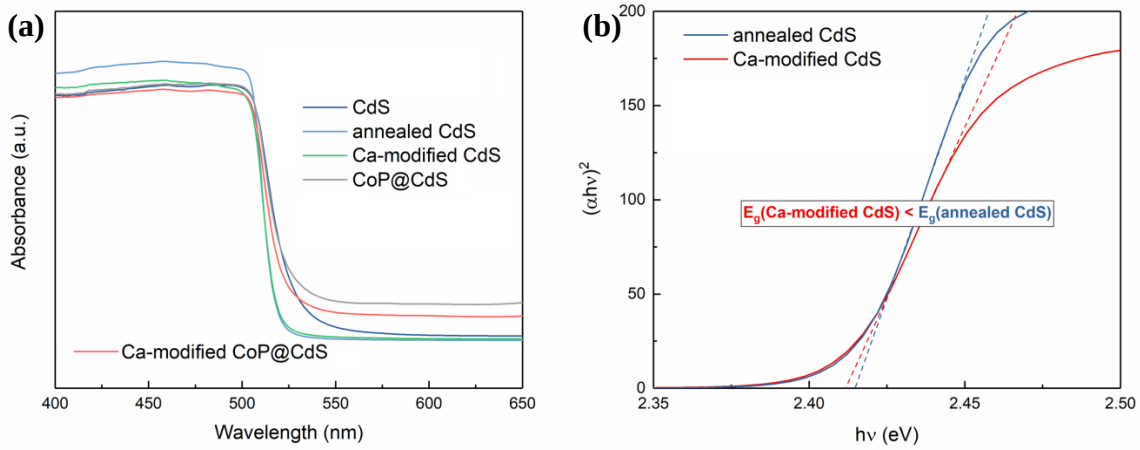

Figure 3.13 (a) Light absorption spectra and (b) corresponding apparent optical bandgap of CdS and Ca-modified CoP@CdS.

In order to gain in-depth understanding on the transfer dynamics of photogenerated electron in the conduction band of CdS, I have investigated the time-resolved photoluminescence spectra over obtained systems together with the average lifetime of excitons. The charge transfer dynamics between CdS before and after heat treatment has been compared at first. As shown in Figure 3.14, the decay time for CdS (band-gap emission, monitored at 520 nm) has been greatly prolonged from 0.072 ns to 0.161 ns after annealing process. This phenomenon can be explained as that the photogenerated electrons are surprisingly long lived in the presence of effective trapping states, and endowed with the capability to reach the surface for redox reaction in consequence.

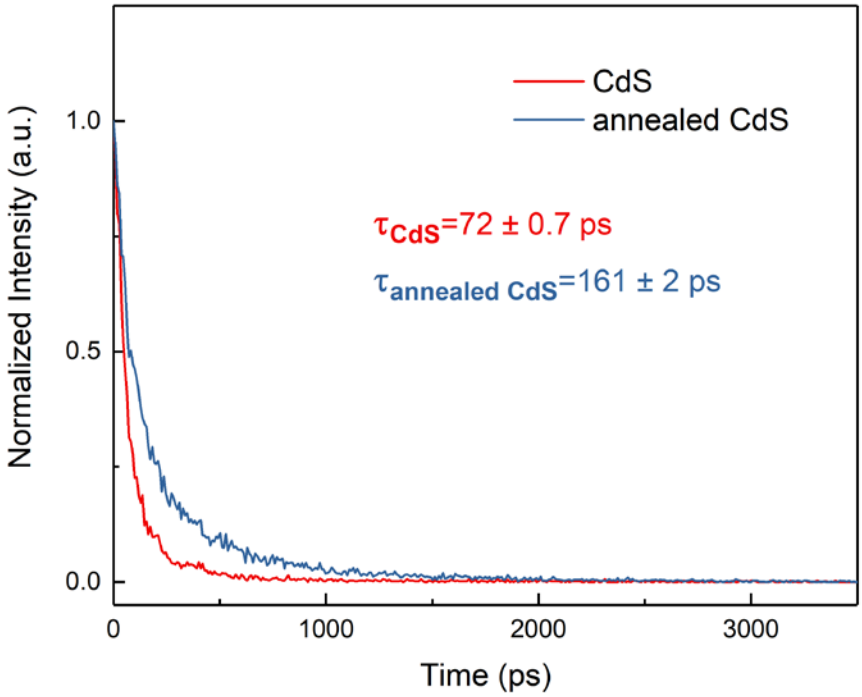

Figure 3.14 Time-resolved photoluminescence spectra of CdS and annealed CdS. (excitation 420 nm)

In addition, a much shorter carrier lifetime of Ca-modified CdS (τ = 81± 1 ps) compared to annealed CdS (τ = 161 ± 2 ps) may indicate that Ca dopants are likely to trigger efficient electron extraction from CdS to defect sites (Figure 3.15). Besides that, a shorter and dominant time constant has been achieved by CoP@CdS (τ = 37 ± 1.5 ps), which features smooth carrier transfer channel with intimate interfacial contact between CdS and CoP active species (Figure 3.16). The acceleration of decay kinetics for Ca-modified CoP@CdS further decreases the lifetime from 37 ± 1.5 ps to 29 ± 1.2 ps. It is believed that fast charge injection from CdS to CoP active sites has been realized after Ca^{2+} modification. In this regards, the Ca^{2+} would act as the interfacial mediator for accelerate the electron transfer, attributing to effective electron-hole separation ability.

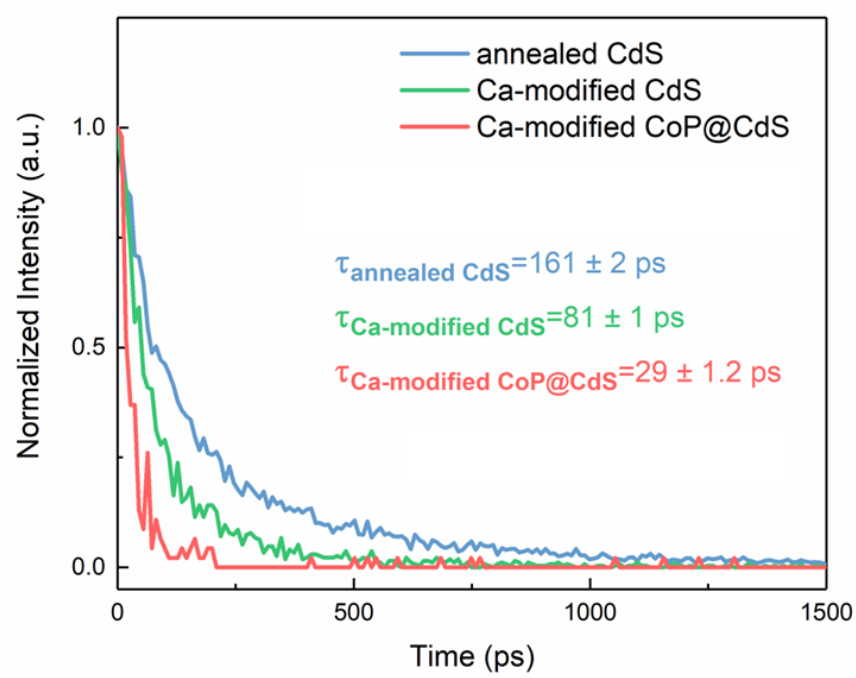

Figure 3.15 Time-resolved photoluminescence spectra of annealed CdS, Ca-modified CdS, and Ca-modified CoP@CdS. (excitation 420 nm)

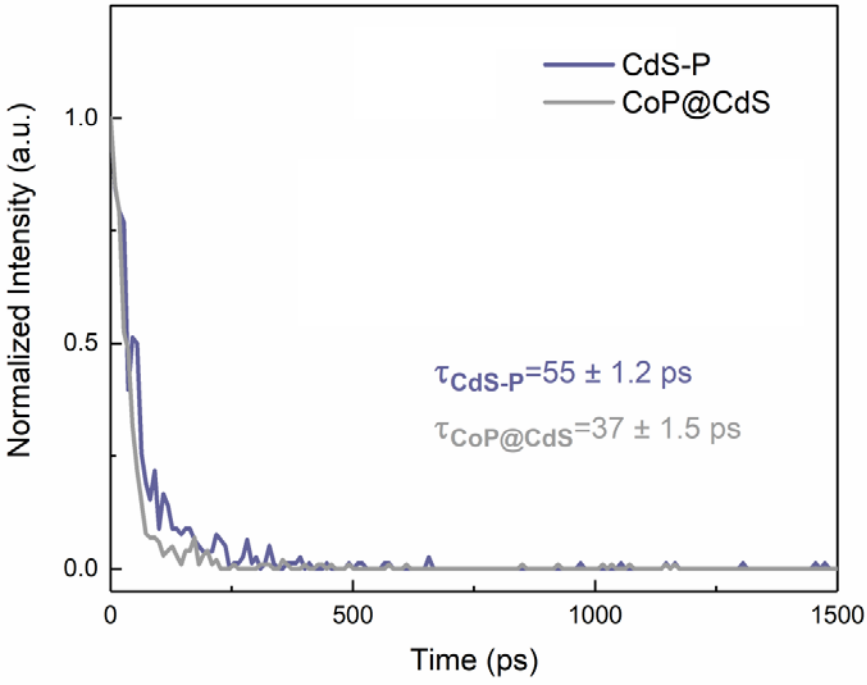

Figure 3.16 Time-resolved photoluminescence spectra of CdS-P and CoP@CdS. (excitation 420 nm)

3.3.3 Photocatalytic H_2 generation performance

The photocatalytic H_2 evolution performance was evaluated at room temperature under visible light ($\lambda > 420$ nm) illumination. Notably, pristine CdS contains different deep defect states and is not active for H_2 evolution. Due to the lack of active sites and high recombination rate of carriers, CdS alone can only demonstrate a poor H_2 production rate of 284.5 μmol h^{-1} (Figure 3.17).

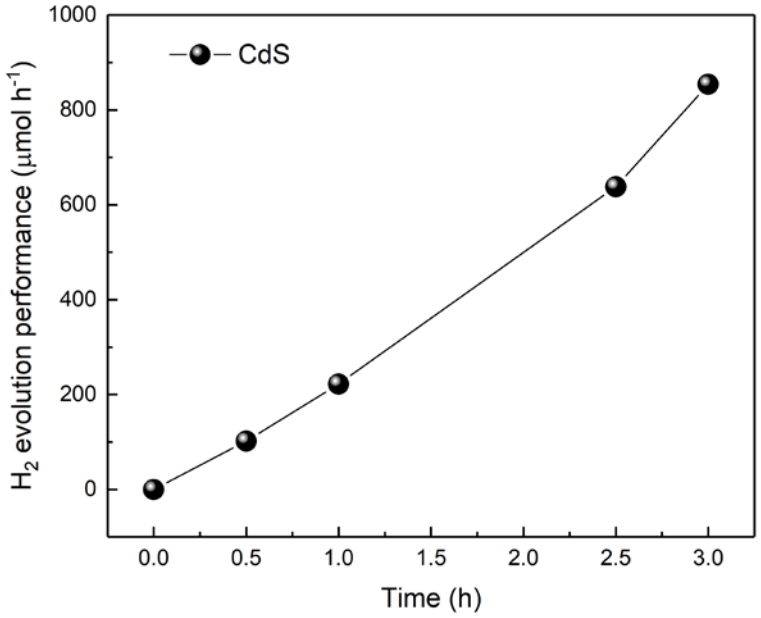

Figure 3.17 Photocatalytic H_2 evolution performance of CdS.

After annealing, the H_2 production efficiency over CdS can be promoted to 639.0 μmol h^{-1} (Figure 3.18a). Compared with CdS-P (937.2 μmol h^{-1}) and CoP@CdS (1425.2 μmol h^{-1}), the photocatalytic H_2 generation rate of Ca-modified CoP@CdS has reached the highest value about 2441.5 μmol h^{-1}. The turnover frequency (TOF) can be calculated as the number of moles of H_2 divided by the number of moles of active sites, which is as high as 703.2 h^{-1}.[42] To verify the important role of Ca^{2+} for improving the H_2 generation activity over CoP@CdS, a comprehensive overview on the photocatalytic H_2 generation performance of CoP@CdS which modified by Ca^{2+} and other metal dopants (Mg^{2+}, Sr^{2+}, Ba^{2+}, Cr^{2+}, Ni^{2+}, Al^{3+}, V^{3+}, Nd^{3+}, and Mo^{5+}) has been demonstrated in Fig. 3.18b. The enhancement on H_2 production performance follows in the order of Ca>Mo>Ba>Mg>Nd>Sr>Al>V>Cr.

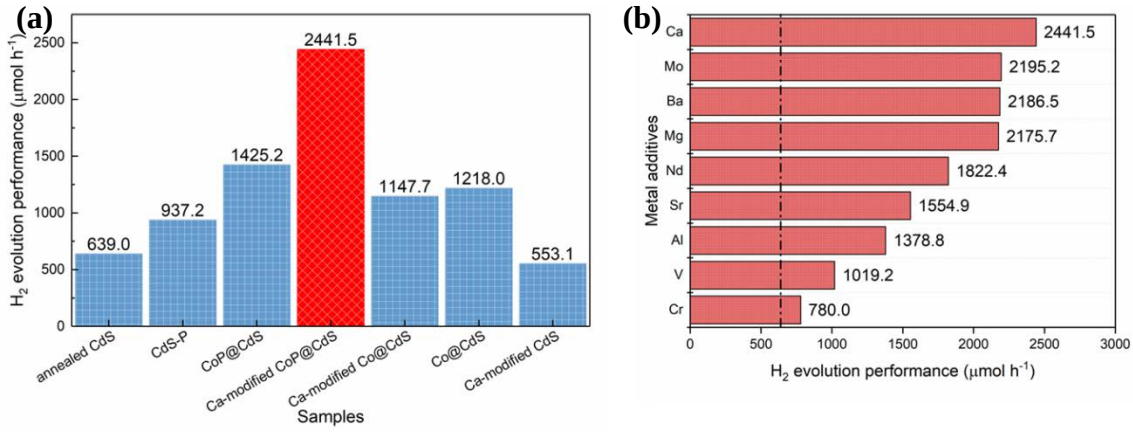

Figure 3.18 (a) Comparison on the photocatalytic H_2 evolution performance between annealed CdS, CdS-P, CoP@CdS, Ca-modified CoP@CdS, Ca-modified Co@CdS, Co@CdS and Ca-modified CdS. (b) The photocatalytic H_2 evolution performance of CoP@CdS modified by different metal dopants.

Apparent quantum efficiency (AQE) is used to determine the actual driving force of photocatalysis over Ca-modified CoP@CdS (Figure 3.19). The curve of AQE of Ca-modified CoP@CdS shows wavelength-dependent feature with strong relevance to the optical absorbance. In addition, the AQE can reach to 35.4% at 420 nm which is comparable or even higher than those of reported CdS-based photocatalyst system that use CoP as cocatalyst (Table 3.3). The cycling stability over Ca-modified CoP@CdS has been investigated as shown in Figure 3.20. Notably, Ca-modified CoP@CdS exhibited outstanding stability in Na_2S/Na_2SO_3 solution, and the H_2 evolution performance can retain after five cycling tests without significant decrease.

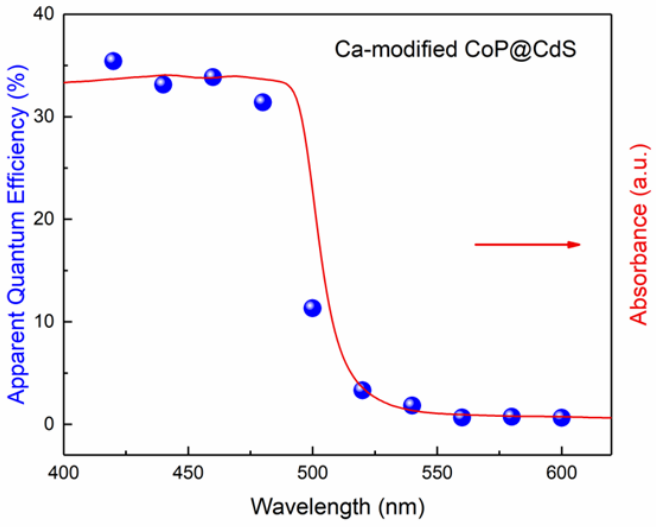

Figure 3.19 AQE curve of Ca-modified CoP@CdS.

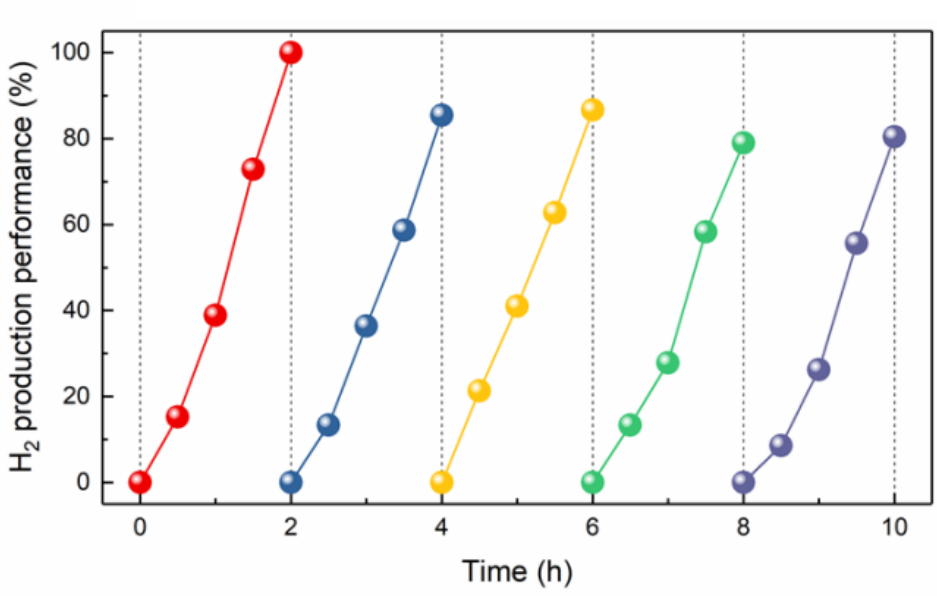

Figure 3.20 Cycling stability measurement over Ca-modified CoP@CdS.

Table 3.3 Comparison of Ca-modified CoP@CdS with other CdS-based photocatalyst systems in which CoP was used as the cocatalyst for photocatalytic H_2 generation.

Material	Application	Activity	Ref
Ca-modified CoP@CdS	Hydrogen evolution (0.35 M Na_2S/0.25 M Na_2SO_3)	2441.5 μmol h^{-1} AQE = 35.4% (420 nm)	**This work**
Co_2P-CdS	Hydrogen evolution (10 vol% K_2HPO_4 solution)	356 μmol h^{-1} AQE = 13.88% (420 nm)	36
o-Co_2P/CdS	Hydrogen evolution (13.2 vol% lactic acid solution)	920 μmol h^{-1} AQE = 22.17% (420 nm)	37
CoP@CdS/RGO-MoS_2	Hydrogen evolution (20 vol% lactic acid solution)	839.07 μmol h^{-1} AQE = 22.5% (425 nm)	38
CoP/CdS NRs	Hydrogen evolution (0.35 M Na_2S/0.25 M Na_2SO_3)	69.375 μmol h^{-1} AQE = 11.6% (420 nm)	17
CdS@C-CoP	> 400 nm (0.25 M Na_2S/0.35 M Na_2SO_3)	50.445 μmol h^{-1}	18
CoP_x-CdS	> 420 nm 1.5 M Na_2S/2.1 M Na_2SO_3	500 μmol h^{-1} AQE = 35% (450 nm)	19
Co_xP/CdS NRs	> 420 nm 1.25 M Na_2S/1.75 M Na_2SO_3	504 μmol h^{-1}	39
CdS/CoP@RGO	6.6 M formic acid solution	182 μmol h^{-1} AQE = 32% (420 nm)	21

Moreover, the H_2 production of Ca-modified CoP@CdS depicted linear increasing without apparent decay (Figure 3.21) and sustained for 24 hours under appropriate conditions (20 mg Ca-modified CoP@CdS photocatalyst, dispersed into 260 mL of 0.25/0.35 Na_2S/Na_2SO_3 solution, irradiated by 420 nm monochromatic light). A total

amount of 289 μmol H_2 has been produced with a steady rate of 12 μmol h^{-1} during the course of 24 hours long-term stability test. All these results prove that Ca-modified CoP@CdS is a robust H_2 production photocatalyst.

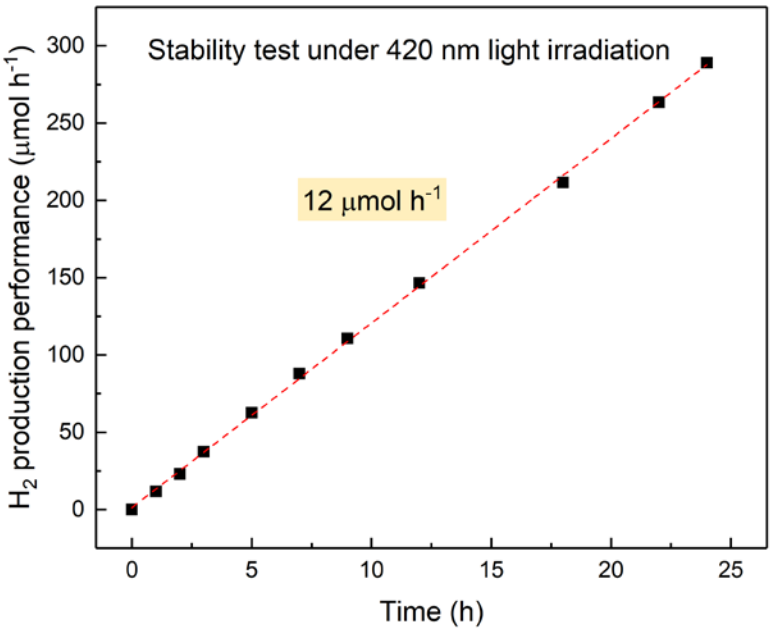

Figure 3.21 The long-term stability test irradiated by 420 nm monochromatic light.

3.3.4 DFT calculation and mechanism analysis

The DFT calculation has been carried out to gain in-depth understanding on the intrinsic properties of Ca-modified CoP@CdS as well as the underlying mechanism of the excellent photocatalytic H_2 generation performance. First of all, the Gibbs free energy for H* adsorption (ΔG_{H^*}) values of CoP@CdS before and after Ca^{2+} modification have been investigated. The Gibbs free energy change of the adsorbed H* ($|\Delta G_{H^*}|$) is an essential indicator to measure the H_2 evolution activity. Usually, a moderate $|\Delta G_{H^*}|$ close to 0 signifies the materials possess neither too strongly nor too weakly bonding with hydrogen, which can realize favorable adsorption and desorption of hydrogen during reactions. As shown in Figure 3.22, the obtained ΔG_{H^*} of pristine CoP@CdS is 0.17 eV, and the ΔG_{H^*} of the system decreases to -0.06 eV when a Cd atom in CdS has been replaced by Ca atom. It can be found that Ca^{2+} doping can greatly reduce the $|\Delta G_{H^*}|$ of CoP@CdS, which is in agreement with the improved H_2 generation performance comparing to that of CoP@CdS.

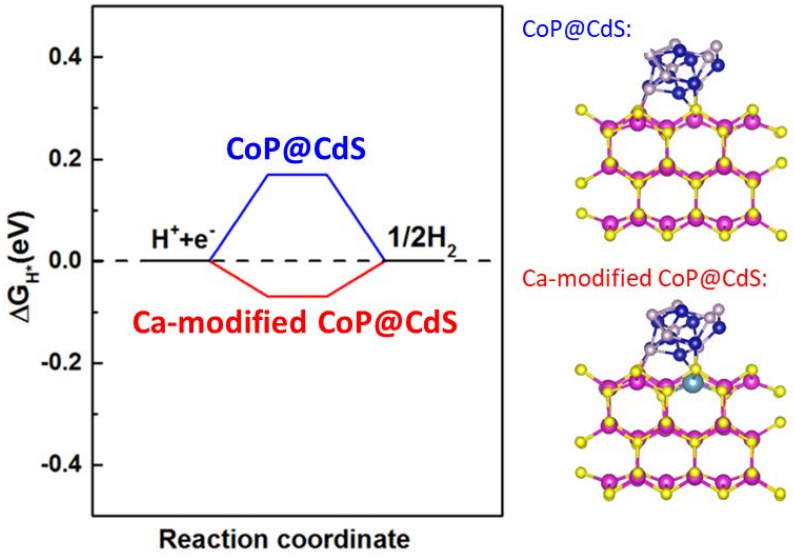

Figure 3.22 The calculated Gibbs free energy of H adsorbed CoP@CdS and Ca-modified CoP@CdS.

In addition, charge-density difference between the interface region of CdS and CoP layer has been investigated to explore the charge transferring mechanism. As shown in Figure 3.23, the side views of the difference charge density for CoP@CdS and Ca-modified CoP@CdS indicate that the charge redistribution mainly occurs at the interface region between CdS and CoP layer (the cyan region represents charge depletion, and the yellow region indicates charge accumulation), and almost no charge change has been observed in the area away from the interface. Different from CoP@CdS, the electron densities on the surface of CoP are redistributed after Ca^{2+} doping, which suggest much more favorable charge transfer between CdS and CoP and accumulation of charge on the interface owing to the existence of Ca^{2+} dopant. Moreover, the electron density accumulation in CdS and depletion in CoP will result in a built-in electric field with the direction from CdS to adjacent CoP (charge gain and loss of each atom have been demonstrated in Figure 3.24 and Table 3.4).

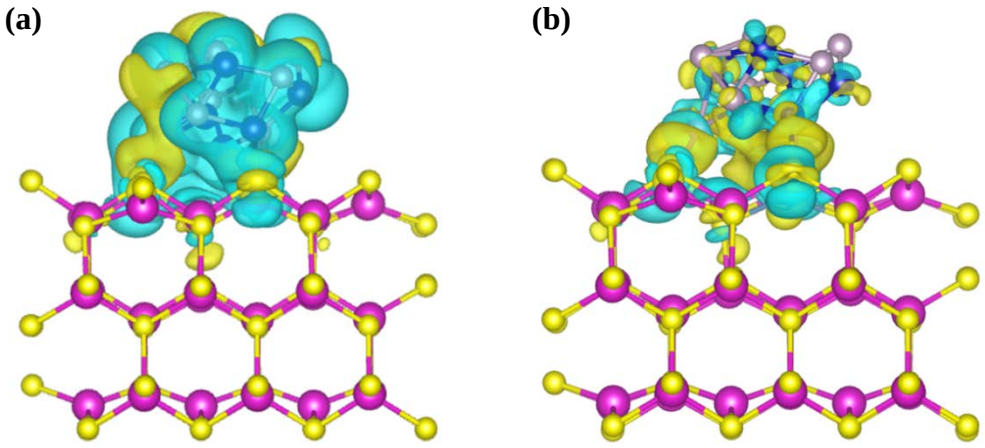

Figure 3.23 The side view of the difference charge density for (a) CoP@CdS and (b) Ca-modified CoP@CdS system. (Yellow balls: S; Magenta balls: Cd; Gray balls: P; Blue balls: Co; Wathet balls: Ca, the cyan region represents charge depletion, and the yellow region indicates charge accumulation). The isosurface value is 0.001 e $Å^{-3}$.

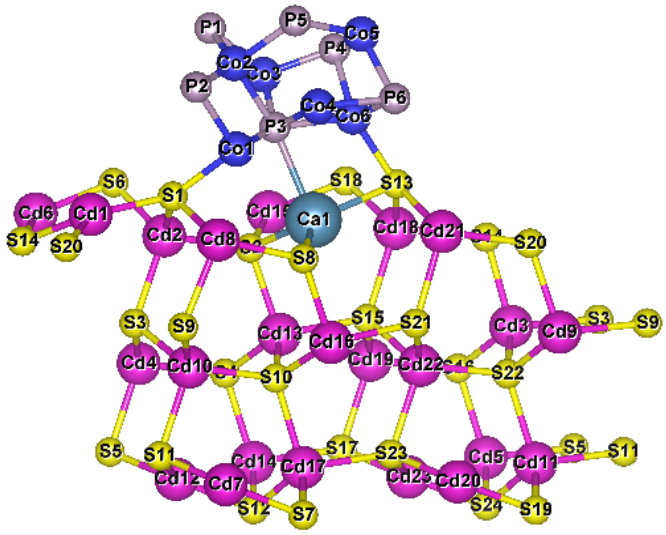

Figure 3.24 Bader charge analysis of Ca-modified CoP@CdS.

Table 3.4 Bader charge analysis about charge transfer on the theoretical structure.

Atom	Charge	Atom	Charge	Atom	Charge
Cd1	11.1886	Cd21	11.18288	S17	6.83996
Cd2	11.1672	Cd22	11.16729	S18	6.76466
Cd3	11.17073	Cd23	11.18673	S19	6.77088
Cd4	11.16434	Ca1	8.55308	S20	6.82546
Cd5	11.16231	S1	6.78448	S21	6.87207

Cd6	11.18456	S2	6.97324	S22	6.86193
Cd7	11.18395	S3	6.85345	S23	6.84244
Cd8	11.17581	S4	6.86381	S24	6.77124
Cd9	11.16089	S5	6.84048	Co1	8.79766
Cd10	11.15598	S6	6.75512	Co2	8.8305
Cd11	11.16006	S7	6.77352	Co3	8.91072
Cd12	11.18461	S8	6.99297	Co4	8.89672
Cd13	11.16801	S9	6.86082	Co5	8.83363
Cd14	11.16323	S10	6.87461	Co6	8.7936
Cd15	11.19622	S10	6.84171	P1	5.08596
Cd16	11.17053	S12	6.77019	P2	5.20743
Cd17	11.16548	S13	6.94897	P3	5.40325
Cd18	11.16957	S14	6.83759	P4	5.14672
Cd19	11.16873	S15	6.87713	P5	5.09558
Cd20	11.18815	S16	6.86178	P6	5.08822

Similarly, the electron localization functions (Figure 3.25) show that the electron locality of the Co atoms is very weak, while that of the P and Ca atoms is strong. This fact is attributed to the Co can inject electrons into the P atoms and Ca dopant. In addition, the total density of states (TDOS) of CoP@CdS before and after Ca^{2+} doping have been performed in Figure 3.26, pronounced peak changes can be observed in the close vicinity of Fermi level when comparing the DOS between CoP@CdS and Ca-modified CoP@CdS systems. The results indicate that electron density near the Fermi level becomes more localized, and an enhancement of local electrical conductivity can be realized owing to the dopant effect of Ca. Meanwhile, to further clarify the effect of Ca doping on the electronic structure, the partial density of states (PDOS) for the orbitals of Cd atoms, Co atoms and Ca atom are shown in Figure 3.27. The overlapping of Cd, Co, and Ca orbitals suggest the formation of new electron transport channels between Co and Ca which may be the results from orbital hybridization.[40, 41]

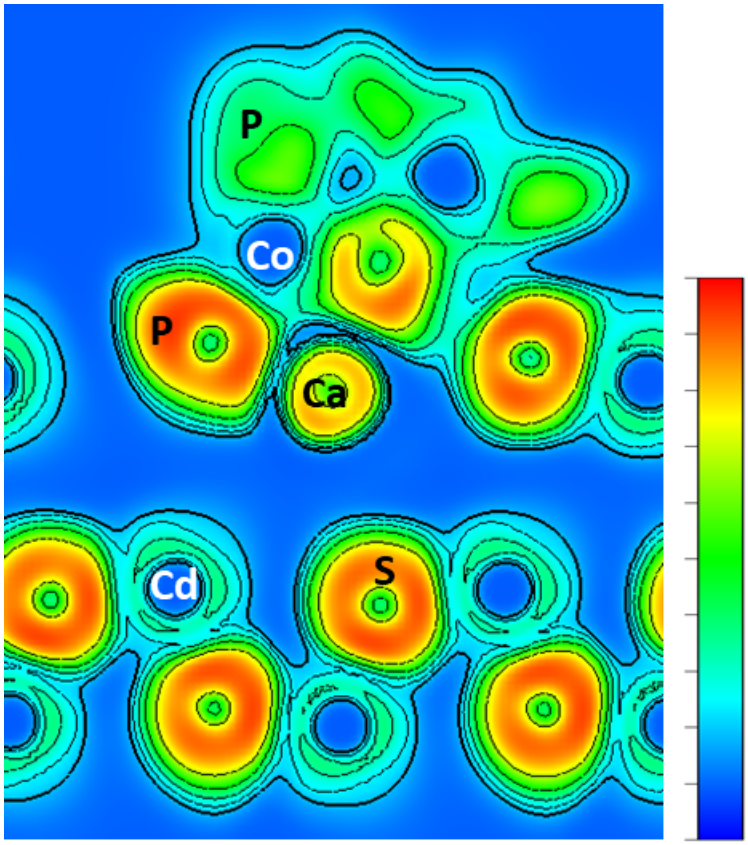

Figure 3.25 The side views of the electron localization functions from the (010) section of the Ca-modified CoP@CdS. The concentration of electrons increases from blue to red.

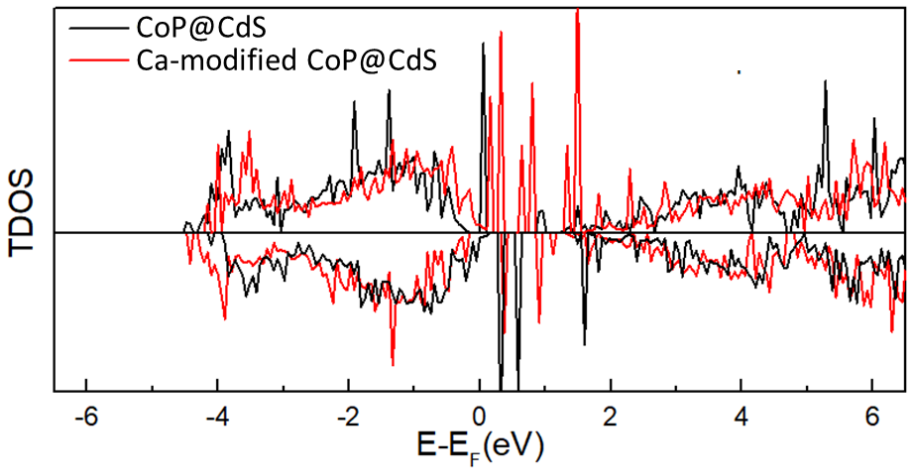

Figure 3.26 The total density of states (TDOS) of (a) CoP@CdS and (b) Ca-modified CoP@CdS.

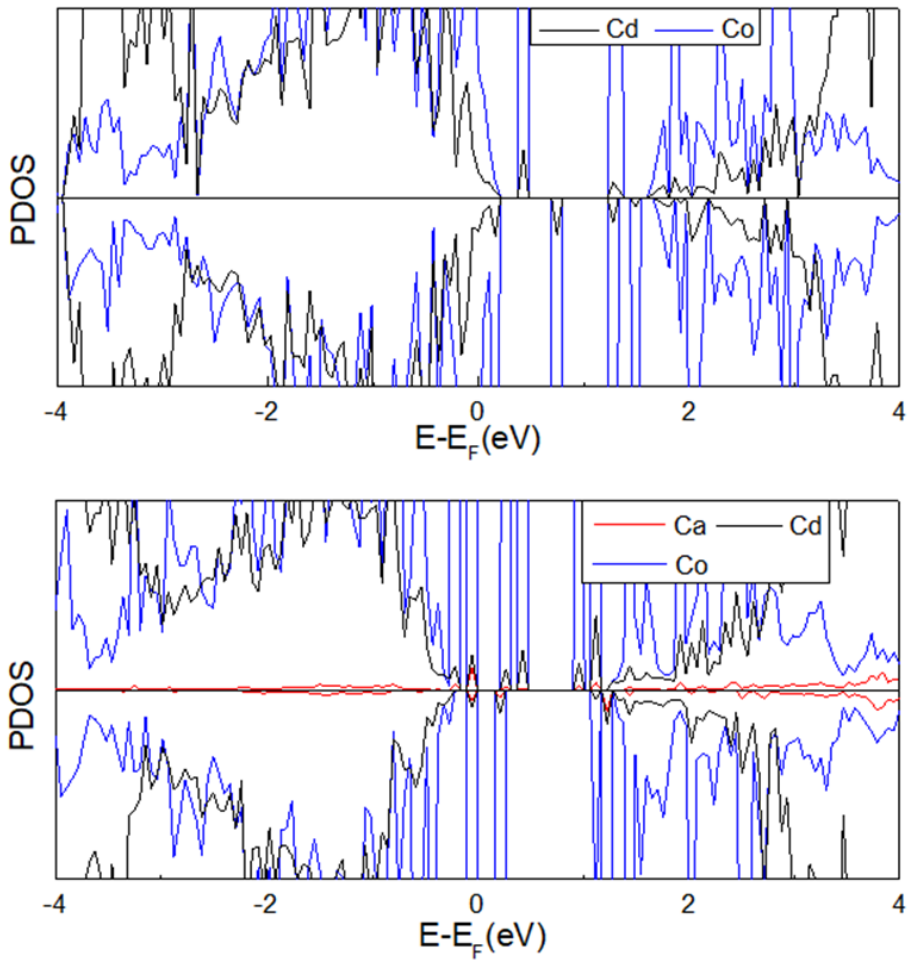

Figure 3.27 The partial density of states (PDOS) of Cd atoms, Co atoms, and Ca atom for (a) CoP@CdS and (b) Ca-modified CoP@CdS system.

To summarize the aforementioned results, both PL measurements and DFT calculations elucidate that the electron transfer behavior and efficient photogenerated electron-hole separation in the hetero-interface of CdS and CoP should be the critical factor, while the adsorption performance and surface affinity of cocatalysts also contribute to the improved photocatalytic H_2 performance (Figure 3.28). Under light illumination, the newly formed chemical bonds mediated by Ca^{2+} dopant can overcome the undesired charge carrier recombination at the interface between semiconductor and cocatalyst. Thus, photogenerated electrons would be transfer through the interlayer between CdS and CoP more efficiently for enhancing H_2 generation.

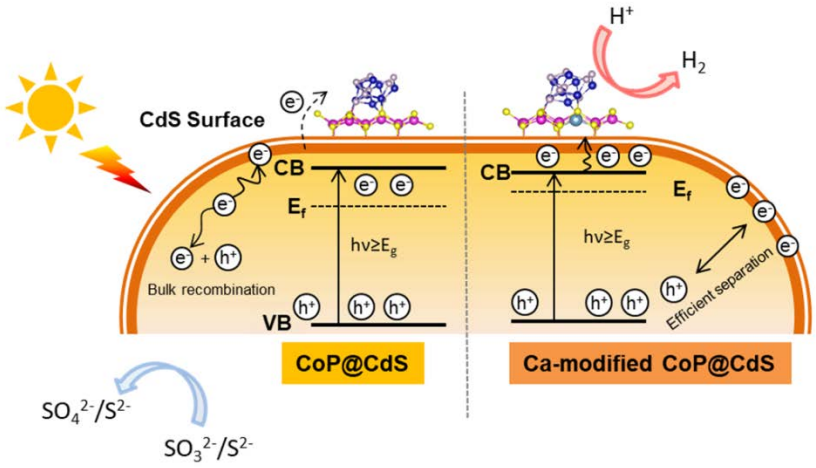

Figuer 3.28 Schematic illustration on charge carriers transfer and separation in Ca-modified CoP@CdS.

3.4 Conclusions

In summary, PPh_3 has been successfully applied to fabricate carbon encapsulated ultrafine CoP nanoparticles on the surface of CdS. Meanwhile, Ca^{2+} as an alkaline earth metal ion may easily substitute the Cd^{2+} lattice sites of CdS, which has induced strong trap-state emission together with long-lived charge carriers. In-depth investigations on the transfer dynamics of photogenerated electron demonstrated fast charge transfer behavior in Ca-modified CoP@CdS, indicating the more effective electron-hole separation ability than that of unmodified CdS. The surface Ca^{2+} may act as the interfacial mediator for accelerating the electron transfer from CdS towards CoP to participate in the H_2 generation reaction. As the result, Ca-modified CoP@CdS can achieve 2441.5 μmol h^{-1} H_2 generation rate with apparent quantum efficiency of 35.4% at 420 nm. Therefore, we hope this investigation would offer new opportunities and be beneficial for future modification on photocatalysts through metal dopants.

References

1. Abe, J. O.; Popoola, A. P. I.; Ajenifuja, E.; Popoola, O. M., Hydrogen energy, economy and storage: Review and recommendation. *International Journal of Hydrogen Energy* **2019,** *44* (29), 15072-15086.

2. Quarton, C. J.; Tlili, O.; Welder, L.; Mansilla, C.; Blanco, H.; Heinrichs, H.; Leaver, J.; Samsatli, N. J.; Lucchese, P.; Robinius, M.; Samsatli, S., The curious case of the conflicting roles of hydrogen in global energy scenarios. *Sustainable Energy & Fuels* **2020,** *4* (1), 80-95.

3. Staffell, I.; Scamman, D.; Velazquez Abad, A.; Balcombe, P.; Dodds, P. E.; Ekins, P.; Shah, N.; Ward, K. R., The role of hydrogen and fuel cells in the global energy system. *Energy & Environmental Science* **2019,** *12* (2), 463-491.

4. Fujishima, A.; Honda, K., Electrochemical Photolysis of Water at a Semiconductor Electrode. *Nature* **1972,** *238* (5358), 37-38.

5. Nakata, K.; Fujishima, A., TiO_2 photocatalysis: Design and applications. *J. Photochem. Photobiol. C* **2012,** *13* (3), 169-189.

6. Yu, B.; Zhou, Y.; Li, P.; Tu, W.; Li, P.; Tang, L.; Ye, J.; Zou, Z., Photocatalytic reduction of CO_2 over Ag/TiO_2 nanocomposites prepared with a simple and rapid silver mirror method. *Nanoscale* **2016,** *8* (23), 11870-11874.

7. Qi, K.; Cheng, B.; Yu, J.; Ho, W., A review on TiO_2-based Z-scheme photocatalysts. *Chinese Journal of Catalysis* **2017,** *38* (12), 1936-1955.

8. Liu, G.; Sheng, Y.; Ager, J. W.; Kraft, M.; Xu, R., Research advances towards large-scale solar hydrogen production from water. *EnergyChem* **2019,** *1* (2), 100014.

9. Chen, X.; Shen, S.; Guo, L.; Mao, S. S., Semiconductor-based Photocatalytic Hydrogen Generation. *Chemical Reviews* **2010,** *110* (11), 6503-6570.

10. Luo, C.; Ren, X.; Dai, Z.; Zhang, Y.; Qi, X.; Pan, C., Present perspectives of advanced characterization techniques in TiO_2-based photocatalysts. *ACS Applied Materials & Interfaces* **2017,** *9* (28), 23265-23286.

11. Ran, J.; Zhang, J.; Yu, J.; Jaroniec, M.; Qiao, S. Z., Earth-abundant cocatalysts for semiconductor-based photocatalytic water splitting. *Chemical Society Reviews* **2014,** *43* (22), 7787-7812.

12. Fei, H.; Dong, J.; Arellano-Jiménez, M. J.; Ye, G.; Kim, N. D.; Samuel, E. L. G.; Peng, Z.; Zhu, Z.; Qin, F.; Bao, J.; Yacaman, M. J.; Ajayan, P. M.; Chen, D.; Tour, J. M., Atomic cobalt on nitrogen-doped graphene for hydrogen generation. *Nature Communications* **2015,** *6*, 8668.

13. Cao, S.; Chen, Y.; Hou, C.-C.; Lv, X.-J.; Fu, W.-F., Cobalt phosphide as a highly active non-precious metal cocatalyst for photocatalytic hydrogen production under visible light irradiation. *Journal of Materials Chemistry A* **2015,** *3* (11), 6096-6101.

14. Tian, B.; Li, Z.; Zhen, W.; Lu, G., Uniformly sized (112) facet Co_2P on graphene for highly effective photocatalytic hydrogen evolution. *The Journal of Physical Chemistry C* **2016,** *120* (12), 6409-6415.

15. Pan, Z.; Zheng, Y.; Guo, F.; Niu, P.; Wang, X., Decorating CoP and Pt Nanoparticles on Graphitic Carbon Nitride Nanosheets to Promote Overall Water Splitting by Conjugated Polymers. *ChemSusChem* **2017,** *10* (1), 87-90.

16. Yang, H.; Zhang, Y.; Hu, F.; Wang, Q., Urchin-like CoP Nanocrystals as Hydrogen Evolution Reaction and Oxygen Reduction Reaction Dual-Electrocatalyst with Superior Stability. *Nano Letters* **2015,** *15* (11), 7616-7620.

17. Wang, J.; Wang, P.; Wang, C.; Ao, Y., In-situ synthesis of well dispersed CoP nanoparticles modified CdS nanorods composite with boosted performance for photocatalytic hydrogen evolution. *International Journal of Hydrogen Energy* **2018,** *43* (32), 14934-14943.

18. Wang, P.; Wu, T.; Ao, Y.; Wang, C., Fabrication of noble-metal-free CdS nanorods-carbon layer-cobalt phosphide multiple heterojunctions for efficient and robust photocatalyst hydrogen evolution under visible light irradiation. *Renewable Energy* **2019,** *131,* 180-186.

19. Sun, Z.; Lv, B.; Li, J.; Xiao, M.; Wang, X.; Du, P., Core–shell amorphous cobalt phosphide/cadmium sulfide semiconductor nanorods for exceptional photocatalytic hydrogen production under visible light. *Journal of Materials Chemistry A* **2016,** *4* (5), 1598-1602.

20. Wang, X.-j.; Tian, X.; Sun, Y.-j.; Zhu, J.-y.; Li, F.-t.; Mu, H.-y.; Zhao, J., Enhanced Schottky effect of a 2D–2D CoP/g-C_3N_4 interface for boosting photocatalytic H_2 evolution. *Nanoscale* **2018,** *10* (26), 12315-12321.

21. Cao, S.; Chen, Y.; Wang, H.; Chen, J.; Shi, X.; Li, H.; Cheng, P.; Liu, X.; Liu, M.; Piao, L., Ultrasmall CoP Nanoparticles as Efficient Cocatalysts for Photocatalytic Formic Acid Dehydrogenation. *Joule* **2018,** *2* (3), 549-557.

22. Wu, J.-C.; Zheng, J.; Wu, P.; Xu, R., Study of Native Defects and Transition-Metal (Mn, Fe, Co, and Ni) Doping in a Zinc-Blende CdS Photocatalyst by DFT and Hybrid DFT Calculations. *The Journal of Physical Chemistry C* **2011,** *115* (13), 5675-5682.

23. Shi, R.; Ye, H.-F.; Liang, F.; Wang, Z.; Li, K.; Weng, Y.; Lin, Z.; Fu, W.-F.; Che, C.-M.; Chen, Y., Interstitial P-Doped CdS with Long-Lived Photogenerated Electrons for Photocatalytic Water Splitting without Sacrificial Agents. *Advanced Materials* **2018,** *30* (6), 1705941.

24. Huang, H.; Dai, B.; Wang, W.; Lu, C.; Kou, J.; Ni, Y.; Wang, L.; Xu, Z., Oriented Built-in Electric Field Introduced by Surface Gradient Diffusion Doping for Enhanced Photocatalytic H_2 Evolution in CdS Nanorods. *Nano Letters* **2017,** *17* (6), 3803-3808.

25. Zhang, K.; Zhou, Z.; Guo, L., Alkaline earth metal as a novel dopant for chalcogenide solid solution: Improvement of photocatalytic efficiency of $Cd_{1-x}Zn_xS$ by barium surface doping. *International Journal of Hydrogen Energy* **2011,** *36* (16), 9469-9478.

26. Zhou, M.; Han, D.; Liu, X.; Ma, C.; Wang, H.; Tang, Y.; Huo, P.; Shi, W.; Yan, Y.; Yang, J., Enhanced visible light photocatalytic activity of alkaline earth metal ions-doped CdSe/rGO photocatalysts synthesized by hydrothermal method. *Applied Catalysis B: Environmental* **2015,** *172-173*, 174-184.

27. Gk, A.; Jf, B., Efficiency of ab-initio total energy calculations for metals and semiconductors using a plane-wave basis set. *Computational Materials Science* **1996,** *6* (1), 15-50.

28. Kresse, G. G.; Furthmüller, J. J., Efficient Iterative Schemes for Ab Initio Total-Energy Calculations Using a Plane-Wave Basis Set. *Physical Review B* **1996,** *54*, 11169.

29. Blochl, P.; Blöchl, E.; Blöchl, P. E., Projected augmented-wave method. *Physical Review B* **1994,** *50* (24): 17953.

30. Linganiso, L. Z.; Jacobs, G.; Azzam, K. G.; Graham, U. M.; Davis, B. H.; Cronauer, D. C.; Kropf, A. J.; Marshall, C. L., Low-temperature water–gas shift: Strategy to lower Pt loading by doping ceria with Ca^{2+} improves formate mobility/WGS rate by increasing surface O-mobility. *Applied Catalysis A: General* **2011,** *394* (1), 105-116.

31. An, Q.; Meng, X.; Sun, P., High-Performance Fully Nanostructured Photodetector with Single-Crystalline CdS Nanotubes as Active Layer and Very Long Ag Nanowires as Transparent Electrodes. *ACS Applied Materials & Interfaces* **2015,** *7* (41), 22941-22952.

32. Yılmaz, S.; Polat, İ.; Tomakin, M.; Bacaksız, E., Transparent and conductive CdS:Ca thin films for optoelectronic applications. *Applied Physics A* **2020,** *126* (7), 555.

33. Guo, W.; Liang, Z.; Zhao, J.; Zhu, B.; Cai, K.; Zou, R.; Xu, Q., Hierarchical Cobalt Phosphide Hollow Nanocages toward Electrocatalytic Ammonia Synthesis under Ambient Pressure and Room Temperature. *Small Methods* **2018,** *2* (12), 1800204.

34. Liang, Q.; Shi, F.; Xiao, X.; Wu, X.; Huang, K.; Feng, S., In Situ Growth of CoP Nanoparticles Anchored on Black Phosphorus Nanosheets for Enhanced Photocatalytic Hydrogen Production. *ChemCatChem* **2018,** *10* (10), 2179-2183.

35. Yi, S.-S.; Yan, J.-M.; Wulan, B.-R.; Li, S.-J.; Liu, K.-H.; Jiang, Q., Noble-metal-free cobalt phosphide modified carbon nitride: An efficient photocatalyst for hydrogen generation. *Applied Catalysis B: Environmental* **2017,** *200*, 477-483.

36. Li, S.; Wang, L.; Liu, S.; Xu, B.; Xiao, N.; Gao, Y.; Song, W.; Ge, L.; Liu, J., In situ synthesis of strongly coupled Co_2P-CdS nanohybrids: an effective strategy to regulate photocatalytic hydrogen evolution activity. *ACS Sustainable Chemistry & Engineering* **2018,** *6* (8), 9940-9950.

37. Chao, Y.; Zheng, J.; Zhang, H.; Li, F.; Yan, F.; Tan, Y.; Zhu, Z., Oxygen-incorporation in Co_2P as a non-noble metal cocatalyst to enhance photocatalysis for reducing water to H_2 under visible light. *Chemical Engineering Journal* **2018,** *346*, 281-288.

38. Reddy, D. A.; Choi, J.; Lee, S.; Kim, Y.; Hong, S.; Kumar, D. P.; Kim, T. K., Hierarchical dandelion-flower-like cobalt-phosphide modified CdS/reduced graphene oxide-MoS_2 nanocomposites as a noble-metal-free catalyst for efficient hydrogen evolution from water. *Catalysis Science & Technology* **2016,** *6* (16), 6197-6206.

39. Dong, Y.; Kong, L.; Wang, G.; Jiang, P.; Zhao, N.; Zhang, H., Photochemical synthesis of Co_xP as cocatalyst for boosting photocatalytic H_2 production via spatial charge separation. *Applied Catalysis B: Environmental* **2017,** *211*, 245-251.

40. Fernández, I.; Holzmann, N.; Frenking, G., The Valence Orbitals of the Alkaline-Earth Atoms. *Chemistry – A European Journal* **2020,** *26* (62), 14194-14210.

41. Rösch, B.; Gentner, T. X.; Langer, J.; Färber, C.; Eyselein, J.; Zhao, L.; Ding, C.; Frenking, G.; Harder, S., Dinitrogen complexation and reduction at low-valent calcium. *Science* **2021,** *371* (6534), 1125-1128.

Chapter 4 Rational construction of dual cobalt active species encapsulated by ultrathin carbon matrix from MOF for boosting photocatalytic H_2 generation

4.1 Introduction

The Semiconductor-based photocatalysis which directly generates hydrogen (H_2) from water by consuming solar energy as the sole driving force has been recognized as an essential technology in "Green Chemistry".[1, 2] Although many attempts have been devoted to developing high efficient semiconductor-based photocatalytic system, the low light conversion efficiency and fast recombination rate of photo-induced carriers still become the main obstacles.[3, 4] The concept of dual cocatalyst which integrates the merits of metal and metal oxide can realize great improvement on the photocatalytic efficiency over semiconductor.[5] In addition to the built-in electrical field which is formed within metal-semiconductor junction and beneficial for charge carrier separation, metal-based cocatalysts may form specific bonding with semiconductors, thus providing effective active sites to enhance the photocatalytic performance. As for metal oxide cocatalysts, the main functionality is to trap charge carriers for realizing effective electron-hole separation.[6] With contributions from different functional cocatalyst, photocatalysts that are modified by dual cocatalyst are regarded as appealing building blocks for high performance photocatalysis.

With the growing abilities on the atomic designation of metal nanostructure, earth-abundant transition metals and its clusters have been endowed with competitive advantages over noble metals for achieving efficient H_2 evolution.[7, 8] Of particular interest, cobalt (Co) with less 3d-orbital occupancy has already demonstrated its promising advantages in energy conversion and storage, especially for H_2 evolution.[9] However, metal-based nanostructures with high surface energy are prone to aggregate or deform during catalytic reactions.[10-13] In this consideration, carbon materials as the most utilized conductive and stable platforms would not only protect catalytic sites from agglomeration in harsh environment but also provide robust charge transfer channels for improving catalytic efficiency.[14-16] Early investigations in our group reported that ultrathin carbon-layers encapsulated metal nanoparticles or species can achieve excellent catalytic H_2 generation performance.[17-19] Besides, Liu et al. reported N-doped

carbon nanotube encapsulating Co nanoparticle with expanded spatial scale and enriched reaction sites can afford 172-fold enhancement on H_2 evolution activity compared with pristine g-C_3N_4.[20] All these previous investigations showed potential of using carbon materials to construct high efficient and low-cost photocatalysts, however, most studies known to date were paused on single cocatalyst-based photocatalysts. Recent advances have reported the ability of CoO_x (CoO and Co_3O_4) for capturing hole in a time frame of few picoseconds and also actively partaking in the photocatalytic reaction as oxidation cocatalyst.[21-23] In this case, developing spatially separated Co and CoO_x dual cocatalyst in carbon substrate with more efficient charge extraction and separation would be beneficial for further enhancing the photocatalytic activity. Nevertheless, up until now a controllable preparation of such carbon encapsulated dual cocatalyst is still lacking of investigation and good understanding.

Metal-organic framework (MOF) with identical network-like skeleton can afford sufficient vacancy to the coordinated metal atoms.[24] Similar to other carbon materials, MOF structures are easy to undergo pyrolysis to form metal-encapsulated carbon hybrid materials.[25-27] Owing to the intrinsic strong structure binding relation with metal ions, MOF structure would be able to immobilize metal and metal oxides without the use of structure controlling templates.[28-30] Herein, ultrathin two-dimensional (2D) Co-based MOF (Co-MOF) nanosheets have been attempted as specific precursors for preparing carbon matrix encapsulated dual cobalt active species. To the best of our knowledge, this is the first comprehensive study on manipulating MOF structure through pyrolysis to fabricate dual metal species for photocatalytic applications. In contrast to previous works, I found that the 2D skeleton of MOF was remained after moderate calcination, providing an ideal carbon matrix for locating and separating dual cobalt active species (Co and CoO_x species). The cooperation between Co (reduction cocatalyst) and CoO_x (oxidation cocatalyst and hole acceptor) in carbon matrix is vital for the enhanced overall photocatalytic performance. After confining Co and CoO_x species into different spatial location of carbon sections, highly active metal sites and optimized electron transfer structure can be obtained. In addition, the H_2 generation performance map as a function of annealing temperatures and Co-MOF contents has been provided. By disclosing the critical roles of dual cobalt active species in ultrathin carbon towards photocatalytic performance enhancement, I hope our results can provide a meaningful way for controllable designing 2D-MOF derived nanostructure towards efficient photocatalysis.

4.2 Experimental section

4.2.1 Materials preparation

Preparation of ultrathin Co-MOF nanosheets. Ultrathin Co-MOF nanosheets were prepared in accordance with the previous literature.[24] First, 32 ml DMF, 2 ml ethanol (99.5%) and 2 ml water were mixed in a 50 ml polytetrafluoroethylene (PE) tube. Next, 0.124 g BDC was dissolved into the mixed solution under ultrasonication. Subsequently, 0.75 mmol $CoCl_2 \cdot 6H_2O$ was added. After Co^{2+} salts were dissolved, 0.8 ml TEA was quickly injected into the solution. Then, the solution was stirred for 5 minutes to obtain a uniform colloidal suspension. Then, the colloidal solution was continuously ultrasonicated for 8 h (40 kHz) under airtight conditions. Finally, the products were obtained via centrifugation, washed with ethanol for 5 times to remove the residual reagents and store in 35 ml ethanol for further experiments. The light pink Co-MOF precipitates can be easily obtained after dying in vacuum chamber under 60 °C for 12 hours.

Fabrication of CdS-Co-MOF precursors and CdS-Co-CoO_x@C materials. In a typical experiment, a certain amount of obtained MOF nanosheets were mixed with CdS directly to reach different Co/CdS mole ratios of 0.1%, 0.5%, 1%, 5%, 10%, and 20% under continuous sonication. After sonication for 15 minutes, the CdS-Co-MOF precursors will be collected and dying in vacuum chamber overnight. After that, the self-assembled CdS-Co-MOF precursors were transferred into a porcelain boat and located at the heating center of the quartz tube furnace. Before heating, the sealed quartz tube was pumped with argon gas for approximately 30 minutes to evacuate oxygen and air as much as possible. After the argon gas washing was finished, the furnace was heated to 400, 450, 500, 550 and 600 °C with heat speed 5 °C min^{-1} and maintain at this temperature for 3 hours.

4.2.2 Material characterization

The atomic structural information of the sample was determined by X-ray diffraction (XRD, PANalytical X'Pert PRO). Thermogravimetric (TG) measurements were conducted on a Seiko Instrument thermogravimetry/differential thermal analyzer (TG-DTA 6200) under argon. The in-situ Fourier transform infrared spectroscopy (FTIR) experiments were carried out on a FT/IR-6300 (JASCO, Japan). The surface morphologies of the samples were performed on the field emission scanning electron

microscopy (FE-SEM, JSM-6701F). High resolution Transmission electron microscopy (TEM) images and energy dispersive X-ray spectroscopy (EDX) images were obtained using a JEOL-2100F operated at 200 kV. Raman spectra were collected by engaging the Raman microscope (NRS-1000, Japan) with 532 nm excitation at room temperature. Ultraviolet-visible (UV-Vis) absorption spectra were recorded by UV-vis spectroscopy (UV-2600 Shimadzu Corp., Japan), the bandgap can be calculated according to transformed Kubelka-Munk function. The surface chemical analysis was conducted on X-ray photoelectron spectroscopy (XPS, VG-ESCA Mark II). The decay time measurements were performed on a Hamamatsu instrument (Hamamatsu C5680, Japan).

4.2.3 Photocatalytic performance measurement

Measurement of H_2 evolution performance. Photocatalytic H_2 evolution activities were evaluated under visible-light irradiation. The 300 W xenon arc lamp equipped with a 420 nm cut-off filter was used as the light source. In a typical measurement, 100 mg of as-prepared sample was dissolved into 260 mL of 0.25 M/0.35 M Na_2S/Na_2SO_3 solution, after that the solution was transferred into a quartz glass reaction cell and connect to a gas-closed system with a gas-circulated pump. Before the irradiation, the reaction cell was evacuated to remove the air completely. The produced H_2 was recorded and analyzed by an online gas chromatograph (GC-8A, Shimadzu Corp., Ar carrier, TCD, Japan) with argon as the carrier gas.

Measurement of quantum efficiencies. The apparent quantum efficiency (AQE) was measured under similar conditions as described above except for the light intensity and the wavelength regions of the irradiation light. A series of band-pass filters with central wavelengths of 420 nm, 440 nm, 460 nm, 480 nm, 520 nm, 540 nm, 560 nm, 580 nm, and 600 nm were adopted to control the wavelength regions of monochromatic light. A water filer was also used together with the band-pass filter to avoid the possible damage caused by heating effect of Xe lamp. The average intensity of irradiation was determined by using a spectroradiometer (Ushio, USR-40, Japan). The AQE at each monochromatic wavelength was estimated by following the equation below:

$$\text{AQE for } H_2 \text{ evolution} = \frac{2 \times number\ of\ evolved\ H_2\ molecules}{number\ of\ incident\ photons} \times 100\%$$

4.2.4 Calculation methods.

The calculation of adsorption energy and redistribution of electrons are carried out by density functional theory (DFT) as implemented in the Vienna ab initio simulation package(VASP).[31] The electron-ion interactions are displayed by projector augmented-wave (PAW) method,[32] while the exchange-correlation interactions are visualized by generalized-gradient approximation of Perdew-Burke-Ernzerhof (PBE) approach.[33] A 400 eV cutoff energy is used for plane wave basis and k-mesh grids of 8*8*1 are used in the self-consistent Calculations and more than 15 Å vacuum perpendicular to the 2D plane is adopted to avoid the interaction between repeated images. The self-consistent calculations were performed until the energy of two neighboring steps is within 10^{-6} eV per atom.

4.3 Results and discussion

4.3.1 Synthesis of CdS-Co-CoO_x@C

Ultrathin sheet-like morphology of 2D Co-MOF structures with lateral size of 1-2 μm has been observed from scanning electron microscopy (SEM) as shown in Figure 4.1. The XRD diffraction peaks in Figure 4.2 are well-matched with the identical crystalline structure of 2D Co-MOF nanosheets according to previous report.[26] Subsequently, the pyrolysis of Co-MOF at 400 °C-600 °C under argon atmosphere can produce Co and CoO_x species on the surface of CdS.

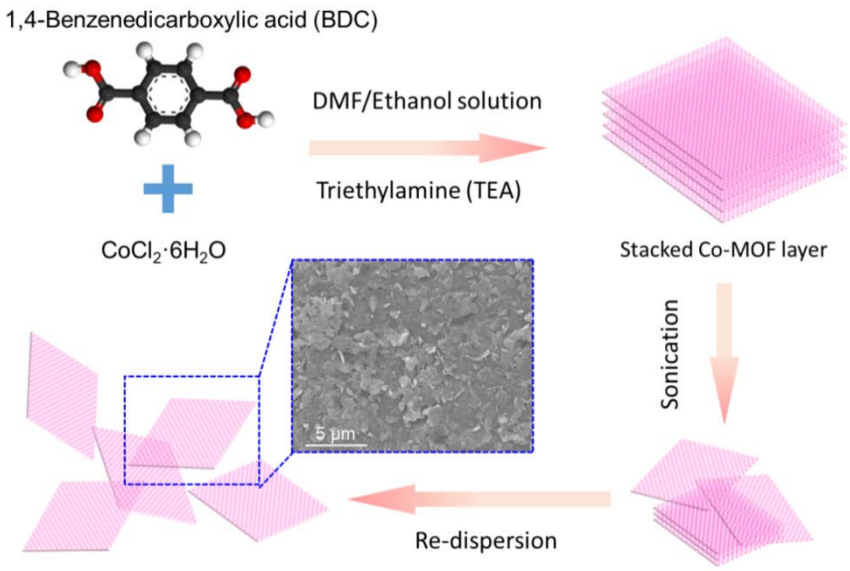

Figure 4.1 Schematic illustrations about the preparation of 2D ultrathin Co-MOF nanosheets.

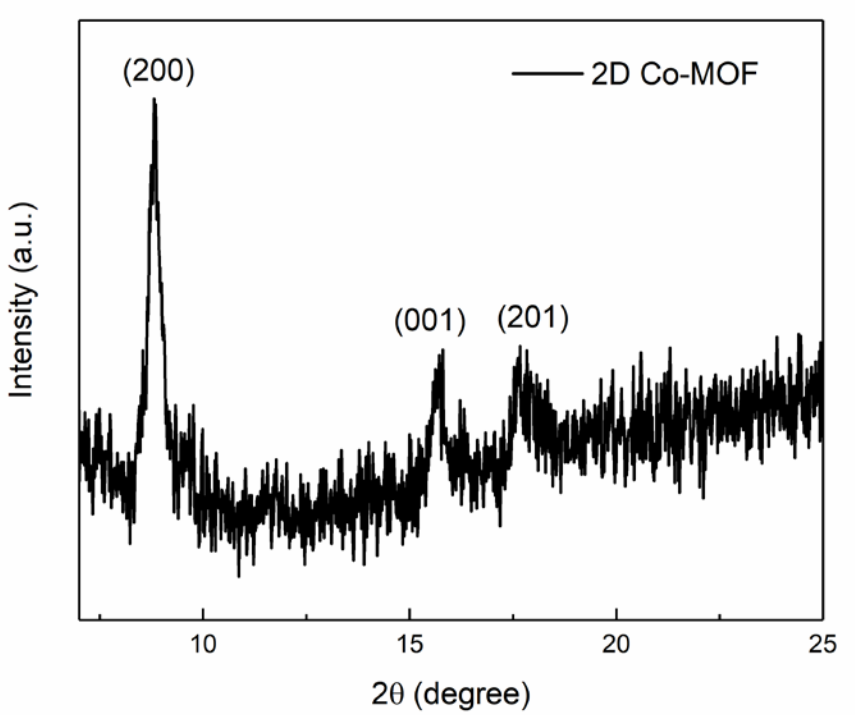

Figure 4.2 XRD of as-prepared 2D ultrathin Co-MOF nanosheets.

In order to visualize the pyrolysis behaviors of 2D Co-MOF nanosheets, the investigation which combines Thermogravimetric (TG) with in-situ Fourier transform infrared spectroscopy (FTIR) analysis has been performed. The TG measurement in Figure 4.3 indicates the thermal decomposition temperature of as-prepared Co-MOF nanosheets is near 438 °C. The first weight loss of 3% between 30 °C and 100 °C can be ascribed into water desorption, while a further drastic weight loss (44%) corresponds well to the decomposition of organic linker (C, O and H) from Co-MOF nanosheets.

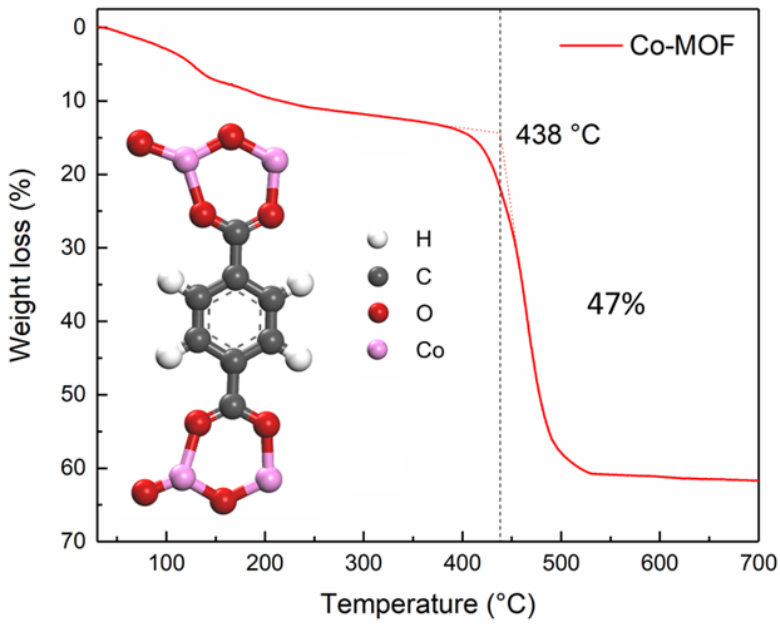

Figure 4.3 The TG analysis of CdS-Co-MOF in argon atmosphere.

The three-step synthetic route of CdS-Co-CoO_x@C has been schematically illustrated in Figure 4.4a. In FTIR analysis, the intensity of Co^{2+} coordinated C=O stretch (≈ 1600 cm^{-1}) and C-O stretch (≈ 1010 cm^{-1}) in carboxylate increases after the temperature is raised from 200 °C to 400 °C, suggesting the decomposition of 2D Co-MOF structure starts from the isolation of BDC ligands and metal nodes Figure 4.4b. The calcination-time dependent infrared spectra Figure 4.4c measured at 400 °C demonstrate that the C=O stretch intensity has nearly no changes, whereas the C-O absorbance becomes weaker when compared to its pristine stage. Meanwhile, a broad gaseous phase CO_2 signal appears at around 2320 cm^{-1}, while C-H bending vibrations at 830-860 cm^{-1} are gradually increased along with time. Those time-resolved chemical bond variation results further prove the decarboxylation of the carboxylate groups. Based on these results, MOF structure is suspected to degrade through disconnection of Co^{2+} coordinated C=O bonds (metal-ligand bonds) as well as C-O bonds in carboxylate during the calcination.[34] Eventually, 2D Co-MOF nanosheets will be converted into CoO_x (CoO and Co_3O_4) and metallic Co as confirmed from the SEM and X-ray diffraction (XRD) results in Figure 4.5. The bulk form of Co-MOF skeleton which contains CoO_x (CoO and Co_3O_4) and metallic Co can be observed in the situation of Co@C-400. Besides that, metallic Co nanoparticles gradually appear when raising the annealing temperature from 400 ^oC to 600 ^oC, while the XRD peaks of CoO_x disappear for Co@C prepared under temperature above 450 ^oC. Thus, I suggest that the

decomposition of 2D Co-MOF structure starts from the formation of CoO_x and ends in aggregated metallic Co.

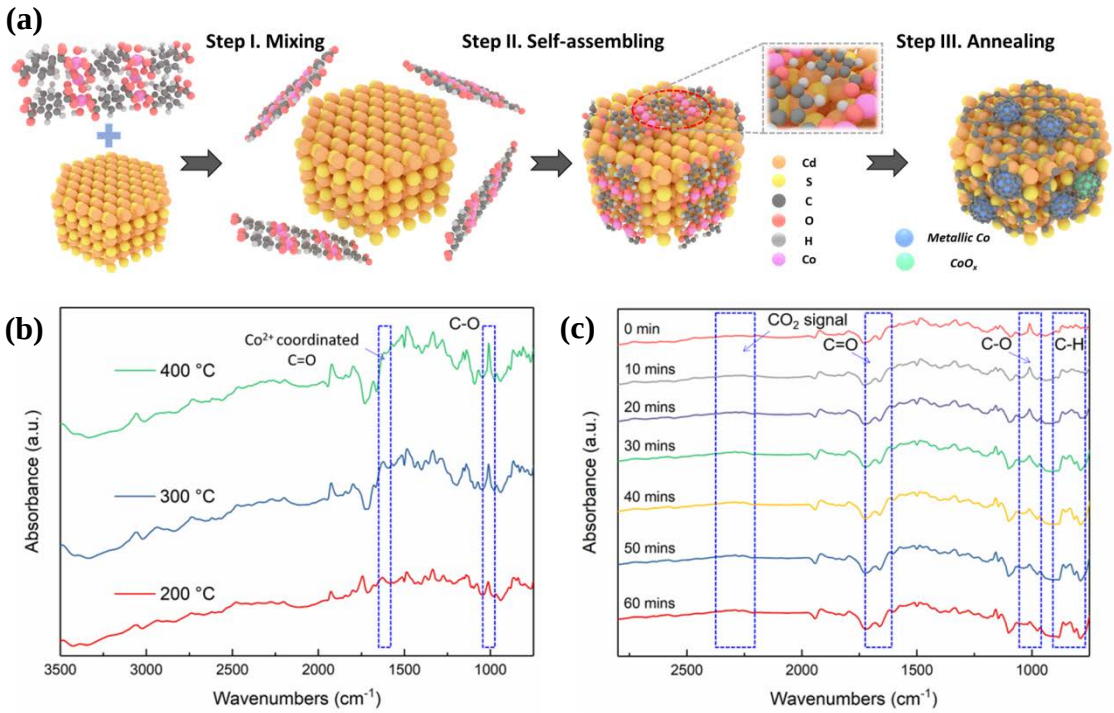

Figure 4.4. (a) Schematically illustration of preparing CdS-Co-CoO_x@C from self-assembly CdS-Co-MOF precursor. In-situ FTIR spectra measured (b) under various temperatures and (c) maintain at 400 °C for 60 minutes.

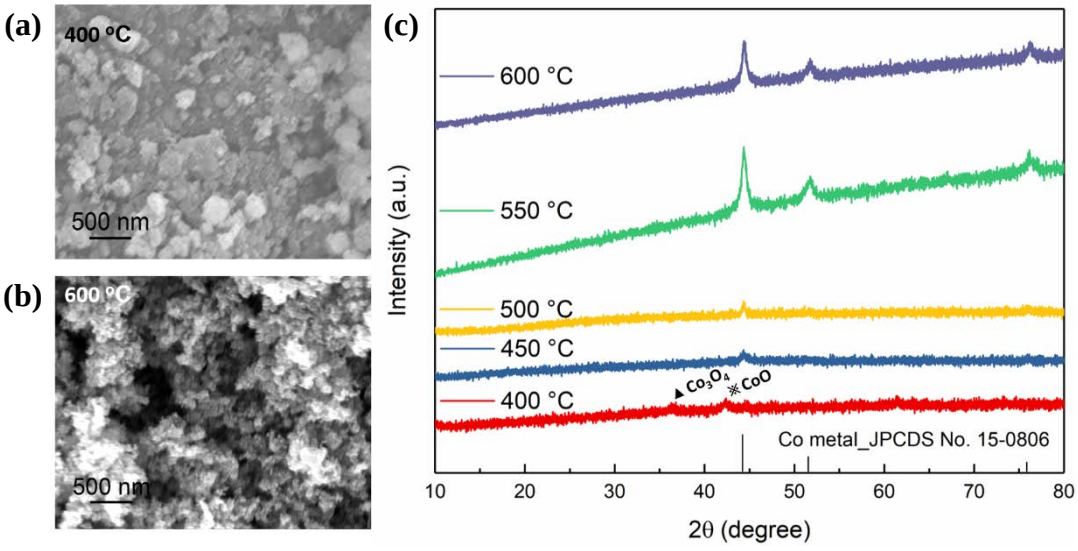

Figure 4.5. SEM images of (a) Co@C-400 and (b) Co@C-600. (c) XRD analysis of Co@C prepared under different annealing temperatures.

To our notice, 2D Co-MOF nanosheets can retain its pristine morphology and skeleton on the surface of CdS (Figure 4.6) after heat treatment.

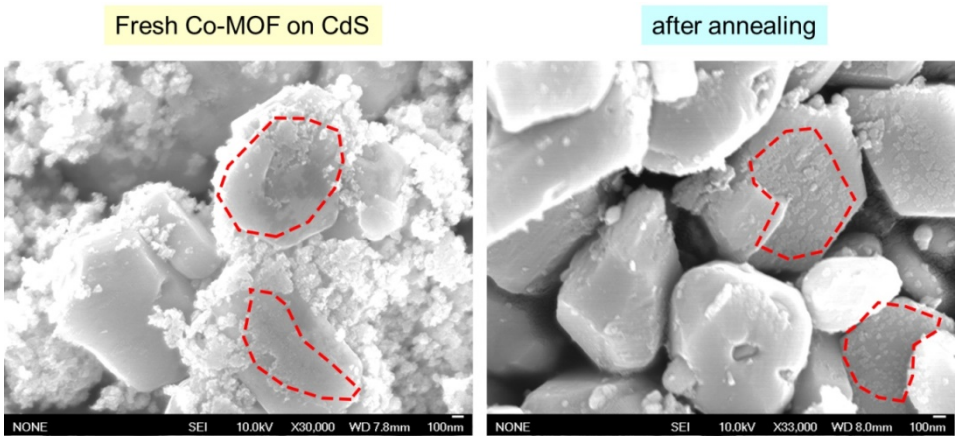

Figure 4.6 SEM images of 2D Co-MOF on CdS before and after annealing.

Meanwhile, the transformation temperature is slightly decreased (Figure 4.7) when compared with free-stranding 2D Co-MOF due to surface contact.[35] Compared to bare 2D Co-MOF, the transformation temperature decreased from 438 °C to 427 °C after 2D Co-MOF nanosheets were loaded on CdS.

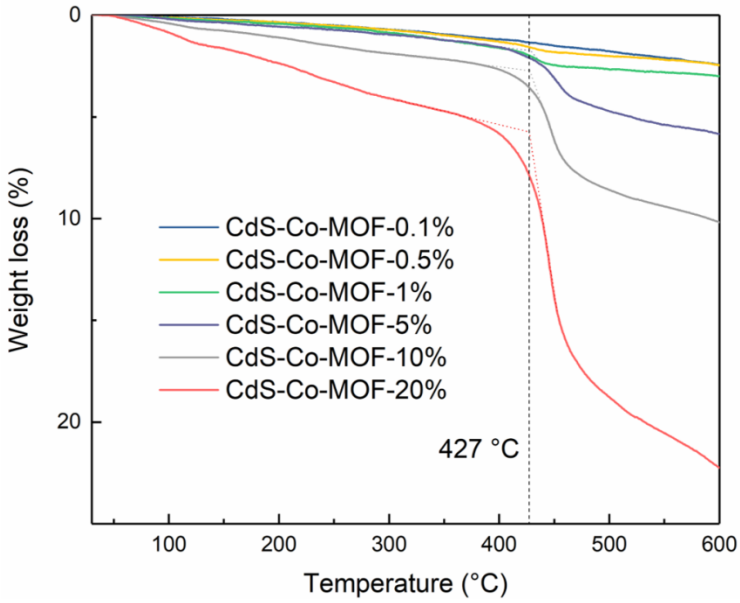

Figure 4.7. TG of CdS-Co-MOF with different Co-MOF contents.

The XRD results (Figure 4.8) of CdS-Co-MOF after calcination under temperature varying from 400 °C to 600 °C show no distinct difference, and the patterns which are demonstrated in can be indexed into standard hexagonal crystalline structure of CdS (JCPDS No. 06-0314).[36]

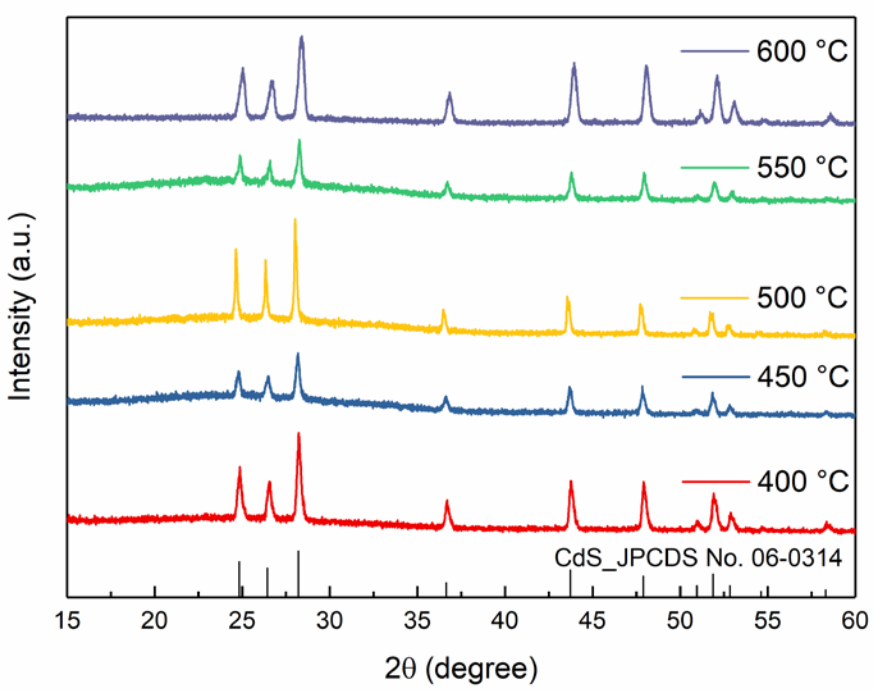

Figure 4.8 XRD of CdS-Co-CoO_x@C with Co-MOF content of 0.5% prepared under different annealing temperatures.

The nanostructure of CdS-Co-CoO_x@C has analyzed by Raman spectroscopy as shown in Figure 4.9. Two characteristic peaks corresponding to the first and second longitudinal optical phonon modes (1LO and 2LO) of CdS can be observed.[37] For CdS-Co-CoO_x@C prepared under different annealing temperatures, no obvious peak shift has been observed. The UV-Vis absorption spectra (Figure 4.10) of CdS and CdS-Co-CoO_x@C-450 demonstrate the threshold values of absorption edge 523.2 nm for CdS and 514.5 nm for CdS-Co-CoO_x@C-450 are corresponding to the optical bandgaps of 2.37 eV and 2.41 eV, respectively.

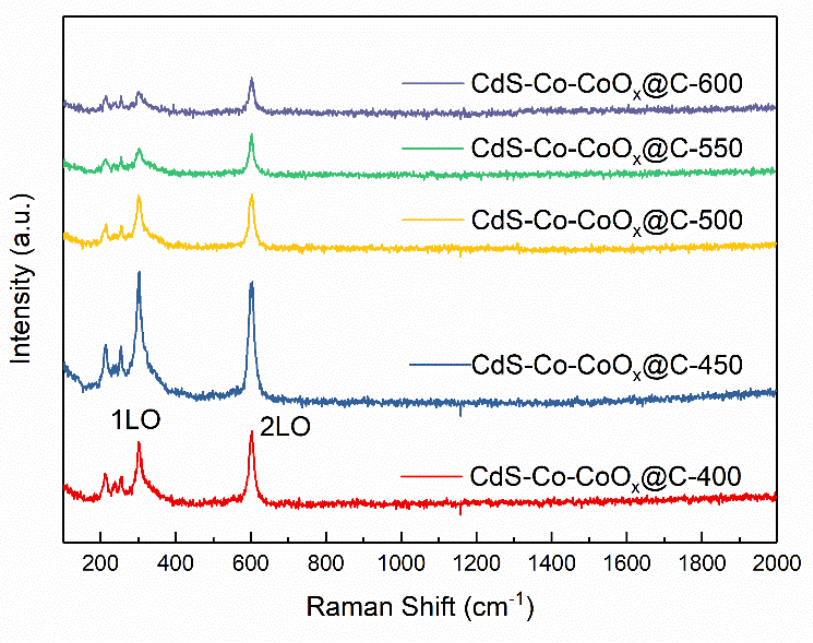

Figure 4.9 Raman spectra of CdS-Co-CoO$_x$@C with Co-MOF content of 0.5% prepared under different annealing temperatures.

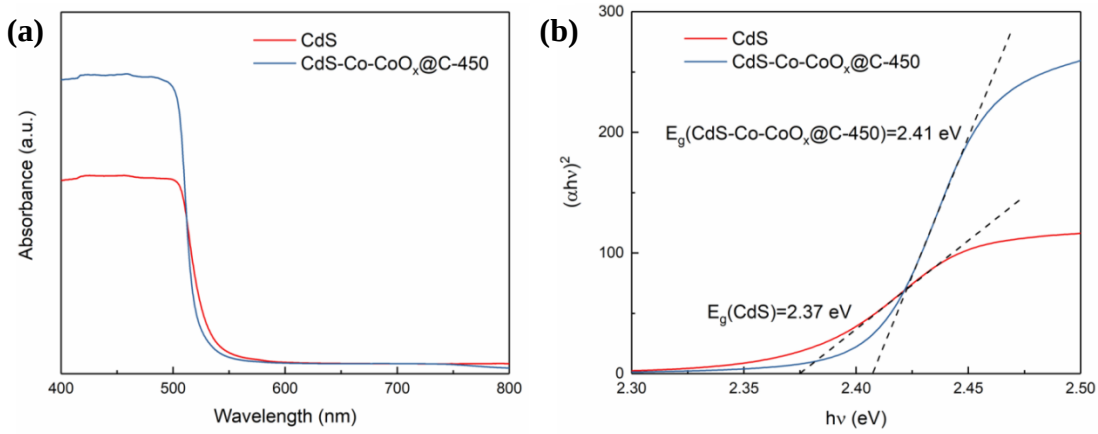

Figure 4.10 (a) UV-vis spectra and (b) corresponding apparent optical bandgap of CdS and CdS-Co-CoO$_x$@C-450.

2.3.2 Characterization of Co-MOF decomposed Co@C

To further verify the CdS-Co-CoO$_x$@C structure, characterizations including transmission electron microscopy (TEM) images, high-resolution TEM (HRTEM) and energy dispersive X-ray spectroscopy (EDX) are investigated (detail descriptions are available in **supporting information**). The low-resolution TEM image in Figure 4.11a demonstrates the CdS particles with size of ~0.4 μm. In Figure 4.11b, the ultrathin Co-CoO$_x$@C layer wraps CdS continuously. HRTEM images in Figure 4.11c and Figure 4.11d depict that the ultrafine Co nanoparticles are separately located on the surface of

CdS and wrapped by thin carbon layer. The inter-planar spacing of (102) is ≈0.242 nm, which agrees with the hexagonal crystalline structure of CdS. To our notice, a small quantity of isolated CoO_x (CoO and Co_3O_4) has also been confirmed (Figure 4.11c and Figure 4.13). Besides that, EDX mappings (Figure 4.12 and Figure 4.14) also indicate the uniformly distribution of Co, O, and C elements on CdS, indicating the important role of carbon matrix for preventing Co from aggregation. With the assistance of carbon matrix, the spatially separated Co and CoO_x dual cocatalyst could be functionally integrated together, thus promoting the efficacy of each species.

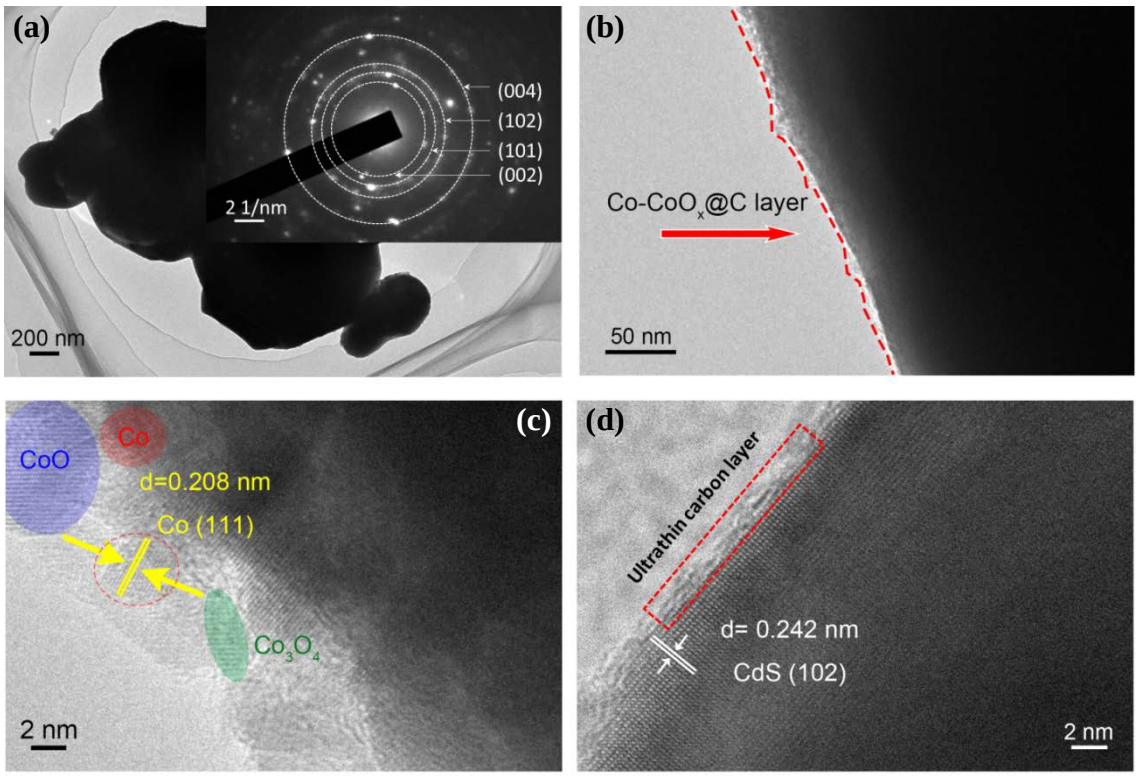

Figure 4.11 (a) TEM image of CdS-Co-CoO_x@C-450. (Inset image: SAED pattern obtained from corresponding area) (b) TEM image on the interface between Co-CoO_x@C layer and CdS nanoparticles. (c) HRTEM image of CdS-Co-CoO_x@C-450 indicates the existence of Co, CoO, and Co_3O_4. (d) HRTEM image of the ultrathin carbon layer in CdS-Co-CoO_x@C-450.

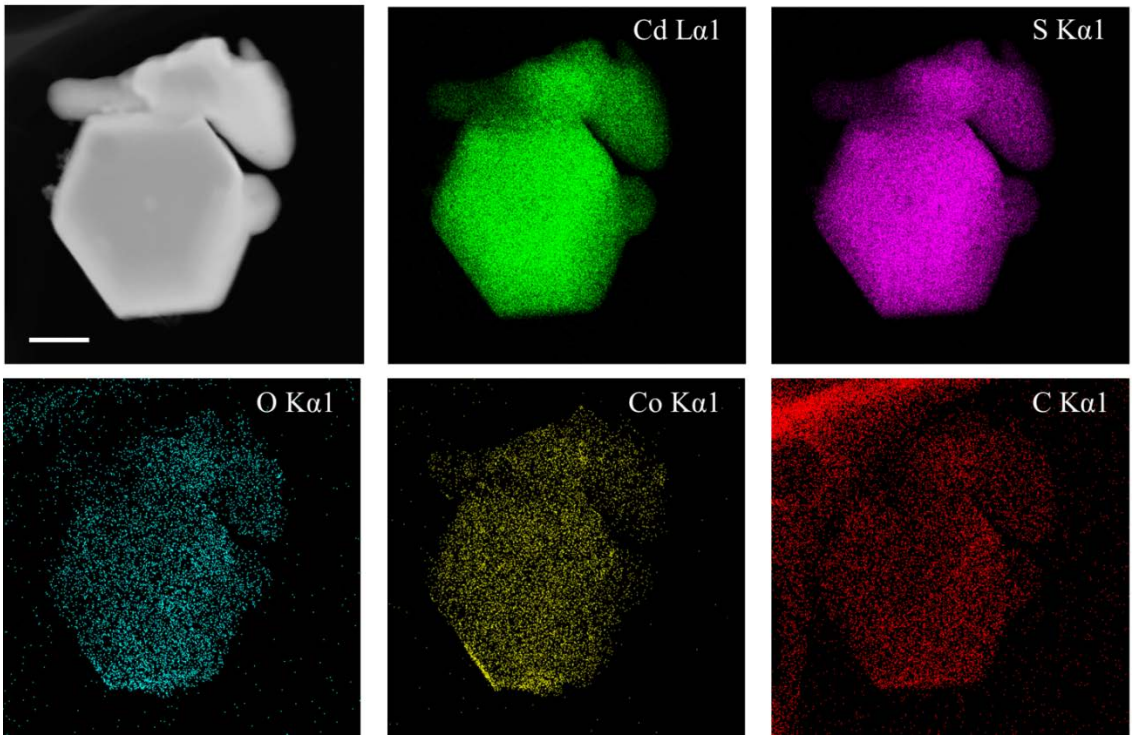

Figure 4.12 EDS analysis of CdS-Co-CoO_x@C-450 with on signals of Cd, S, O, Co, and C elements.

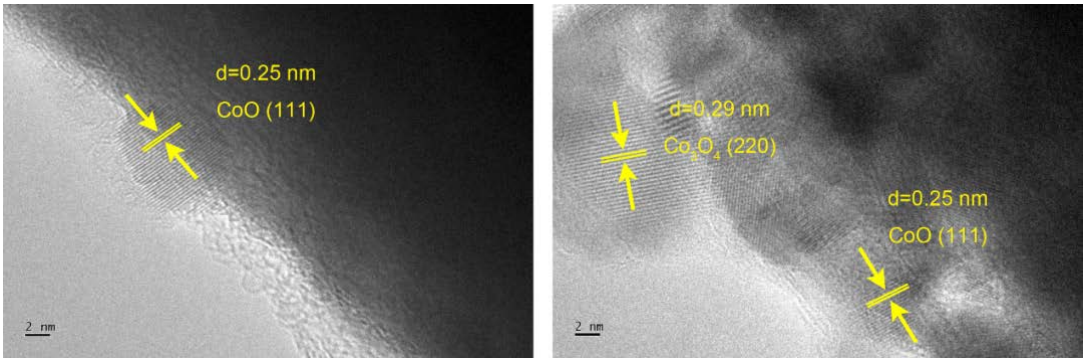

Figure 4.13 SEM images of CdS-Co-CoO_x@C-450 with identical CoO_x (CoO and Co_3O_4) lattice space d values.

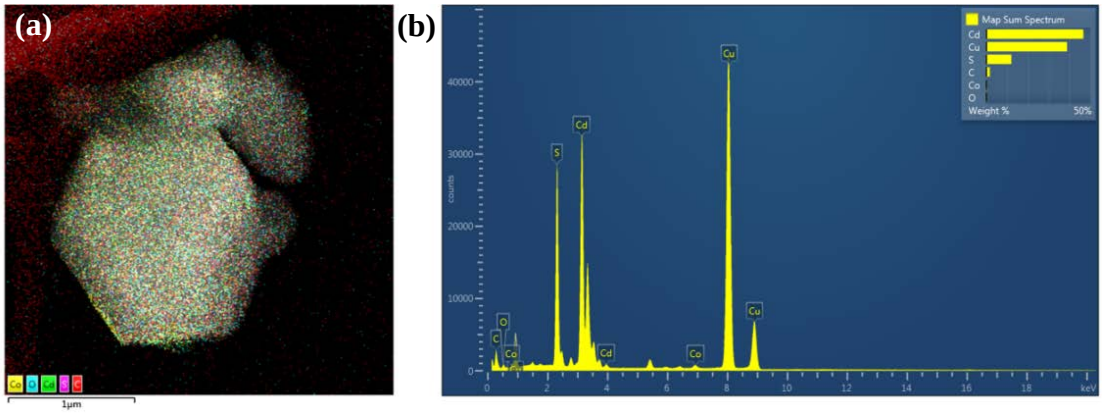

Figure 4.14 (a) EDS layered image of CdS-Co-CoO_x@C-450 with overlapped signals of Co, O, Cd, S, and C elements. (b) Corresponding EDS analysis on Co, O, Cd, S, and C elements.

In-depth understanding on the rational design of MOF-derived dual cobalt active species has been provided from XPS analysis. For Co-MOF decomposed Co@C materials, Co^{2+} and Co^{3+} components as well as metallic Co^0 can be detected. As shown in Figure 4.15a, both the $2p_{3/2}(Co^0)$ peak position as well as peak intensity ratio between $2p_{3/2}(Co^0)$ and $2p_{3/2}(CoO_x)$ in Table 4.1 are varying along with annealing temperature. Such results may indicate the gradually evolution of metallic Co nanoparticles and strong interaction between Co species and carbon matrix when improving the annealing temperature.[38-40] Similarly, the Co 2p core-level peaks of Co@C-600 shift to higher binding energy compared to CdS-Co-CoO_x@C-400 (Figure 4.15b).

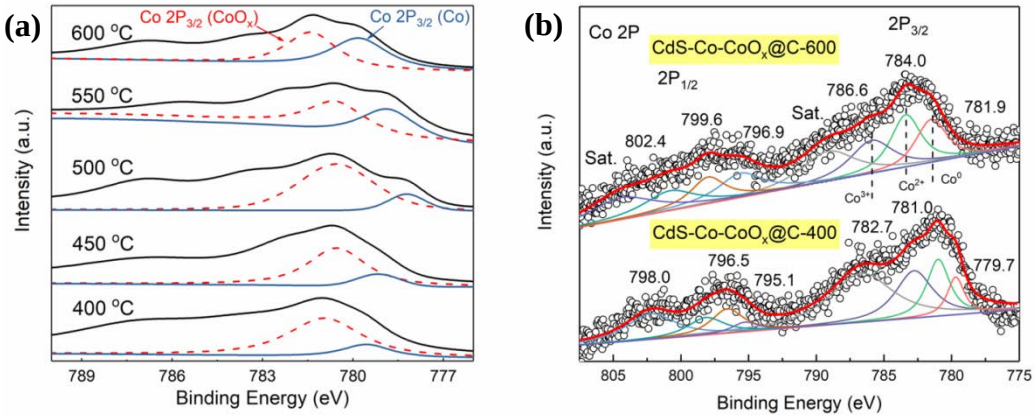

Figure 4.15 (a) Temperature-dependent XPS analysis on Co 2p binding energy spectra of Co@C. (b) XPS spectra of Co 2p of CdS-Co-CoO_x@C-400 and CdS-Co-CoO_x@C-600.

Table 4.1 The ratios of peak intensity between $2p_{3/2}(Co^0)$ and $2p_{3/2}(CoO_x)$.

Sample	Co@C-400	Co@C-450	Co@C-500	Co@C-550	Co@C-600
I_{Co}/I_{CoOx}	**0.225**	**0.186**	**0.18**	**0.874**	**1**

Raman spectra of Co@C prepared under different annealing temperatures shown in Figure 4.16 indicate the intensity and position of identical peaks of CoO_x (CoO and Co_3O_4) are highly related to to annealing temperature.[41] The intensity of CoO_x peak increases with annealing temperature from 400 °C to 450 °C but decreases when further improving the temperature to 600 °C, indicating the generation of CoO_x has reached the maximum value near 450 °C. Meanwhile, the CoO_x peak shifts to a higher wavenumber

with increasing the annealing temperature from 400 °C to 450 °C and then backwards to a lower wavenumber when further increasing the temperature, suggesting the CoO content in CoO_x is increasing from 400 °C to 450 °C until CoO_x component has been reduced under higher temperature. Based on these results, I suspect that MOF-derived carbon species with moderate reduction ability can reduce CoO_x during annealing process. Moreover, carbon layer would be gradually consumed by CoO_x and give to the evolution of Co nanoparticles encapsulated in ultrathin carbon layer and release CO_2 gas.

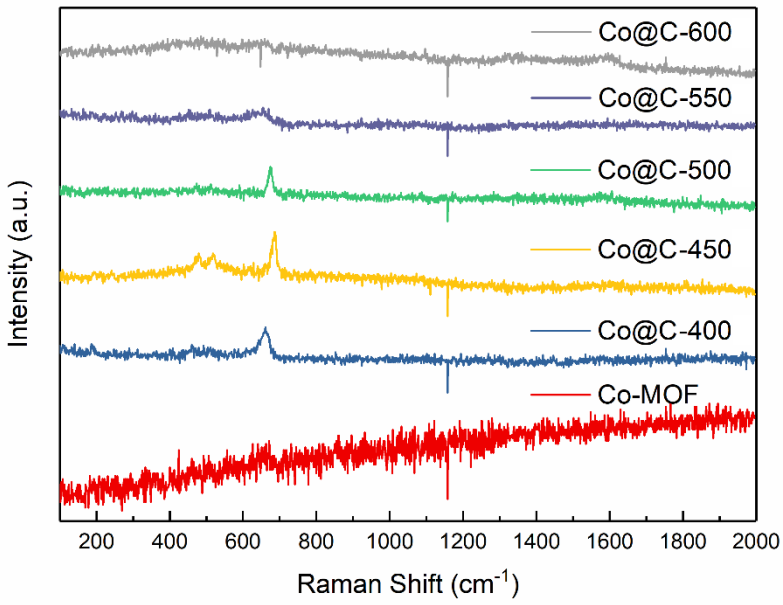

Figure 4.16 Raman spectra of pristine Co-MOF and Co-MOF annealed under different temperatures.

In the meantime, S 2p core-level peaks shift to opposite direction compared to CdS-Co-CoO_x@C-400 (Figure 4.17). The shifts of binding energy also reveal that metallic Co can donate electrons to S sites in CdS. On the other hand, no signals of N 1s have been detected (Figure 4.18), which suggests that TEA which have used for synthesis only serves as the environment controller rather than the reactant. As shown in Figure 4.19, the XPS analysis also demonstrates the existence of C-O and C=O species, which can be attributed into the remaining MOF structure after moderate decomposition on CdS surface. Based on these results, it has been supposed that MOF-derived carbon species with moderate reduction ability can reduce CoO_x into Co nanoparticle during annealing process, which realizing controllable evolution of Co and CoO_x specie encapsulated in ultrathin carbon matrix in consequence.

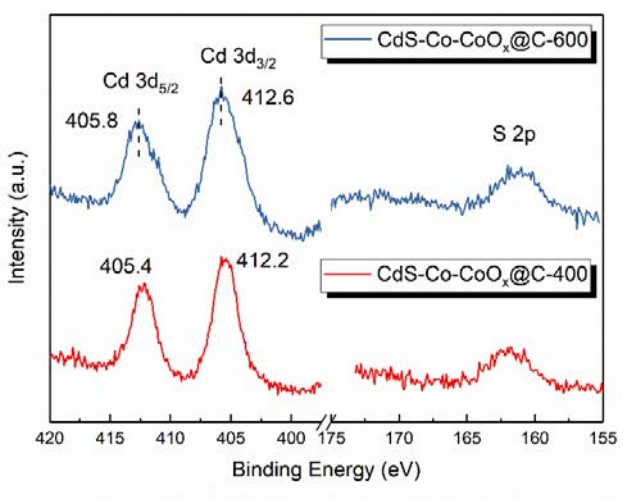

Figure 4.17 Comparison of Cd 3d and S 2p between CdS-Co-CoO$_x$@C-400 and CdS-Co-CoO$_x$@C-600.

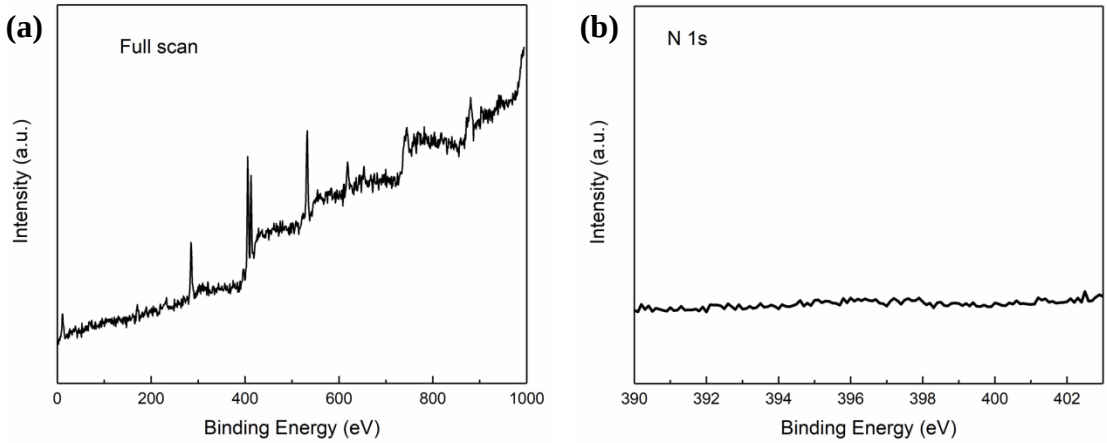

Figure 4.18 (a) Full scan and (b) N 1s of CdS-Co-CoO$_x$@C-450.

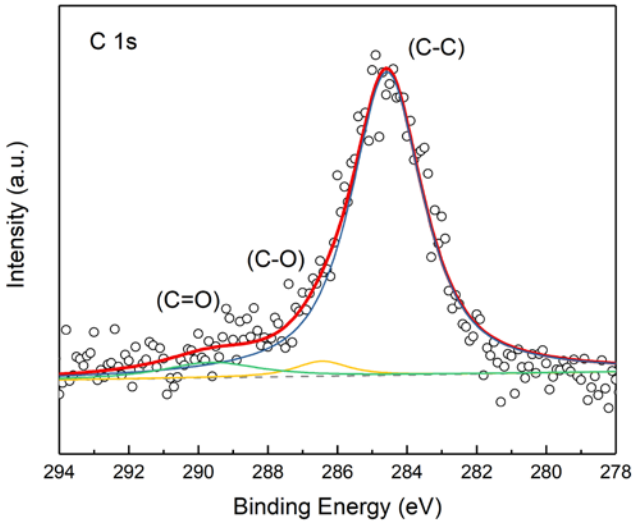

Figure 4.19 C 1s of typical CdS-Co-CoO$_x$@C.

4.3.3 Photocatalytic H_2 generation performance

The photocatalytic H_2 evolution performance over CdS-Co-CoO_x@C materials (with 0.1%, 0.5%, 1%, 5%, and 10% Co-MOF contents) prepared under different annealing temperature has been evaluated. Figure 4.20a indicates the optimal H_2 evolution performance has been achieved by CdS-Co-CoO_x@C-450 with a rate of 1.997 mmol h^{-1}, which suggesting that the optimized annealing temperature is 450 °C. Further investigation on the effect of loaded Co-MOF ratio on CdS on the H_2 generation performance of CdS-Co-CoO_x@C-450 has also been gained. As shown in Figure 4.20b, the H_2 generation performance increases from 0.161 mmol h^{-1} for annealed CdS to 0.88 mmol h^{-1} for CdS-Co-CoO_x@C-450 with 0.1% Co-MOF loading amount. Continuous improvement of the Co-MOF percentage from 0.1% to 0.5% can result in additional 2.3-fold enhancement, whereas further increasing the content from 0.5% to 20% will lead to performance dropping from 1.997 mmol h^{-1} to 0.719 mmol h^{-1}. The turnover frequency (TOF) of CdS-Co-CoO_x@C-450 with Co mole proportion 0.1% and 0.5% can reach up to 1271 h^{-1} and 577 h^{-1}, respectively. The H_2 generation performance map that considering annealing temperature and Co-MOF contents as two main factors for photocatalytic activity has been investigated as shown in Figure 4.21.

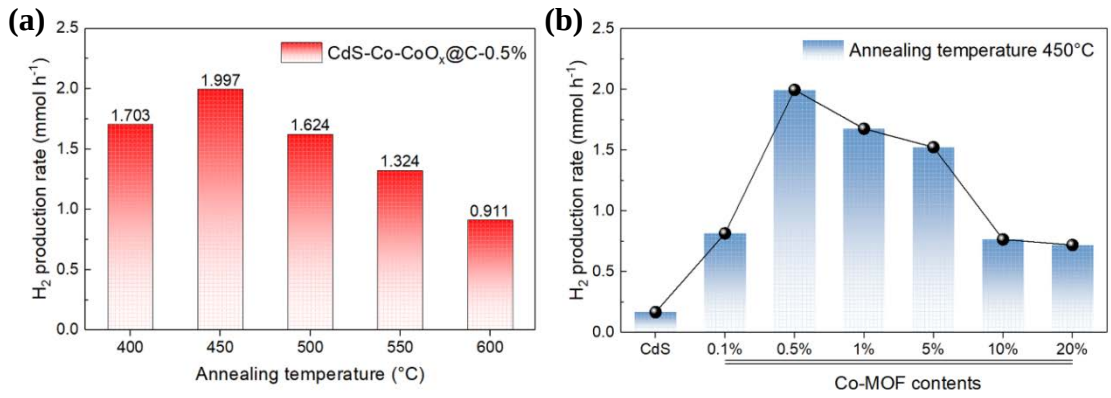

Figure 4.20 (a) H_2 production rate of CdS-Co-CoO_x@C (Co content is 0.5%) annealed under 400 °C, 450 °C, 500 °C, 550 °C, and 600 °C. (b) H_2 production rate of CdS-Co-CoO_x@C-450 with various Co contents from 0 % to 20 %.

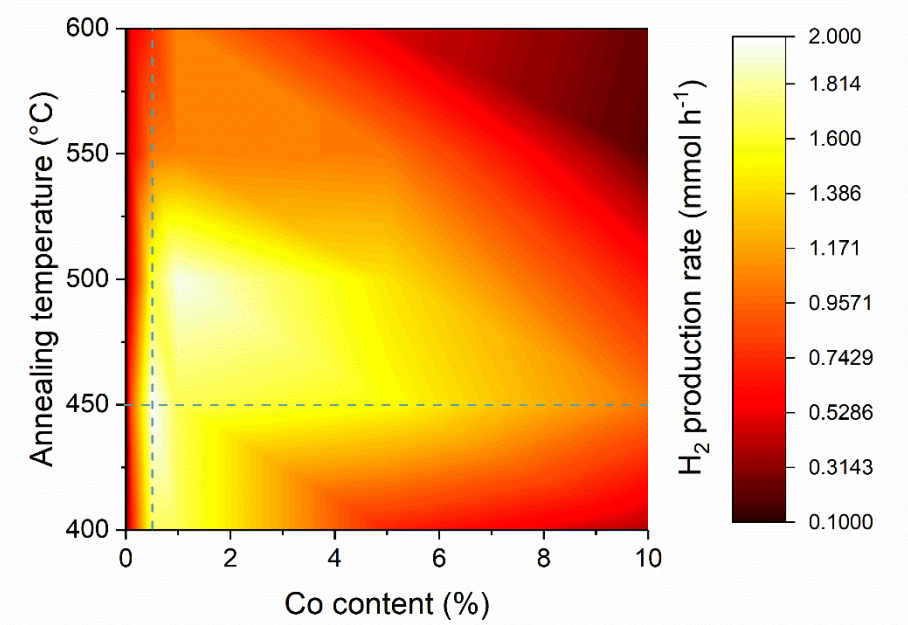

Figure 4.21 H_2 production rate map as a function of annealing temperature and Co content.

The results indicate that annealing temperature of 450 °C and Co-MOF content of 0.5% are the optimal conditions in our experiment. Upon further rise in temperature above 450 °C, the Co-MOF tends to be over decomposed due to C=O and C-C bonds breaking in MOF may no longer support the structure of carbon matrix, and CoO_x will be fully reduced into aggregated Co nanoparticles which would result in lower activity. In addition, introducing higher content of Co-MOF means thicker carbon layer under the same annealing temperature. Co-MOF can be identified from XRD analysis (Figure 4.22) when introducing 20% under the same condition, thus shielding effect from carbon may happen when surface Co-MOF cannot be totally decomposed (Figure 4.23) and most of the light is absorbed by carbon instead of CdS for producing photogenerated electrons.

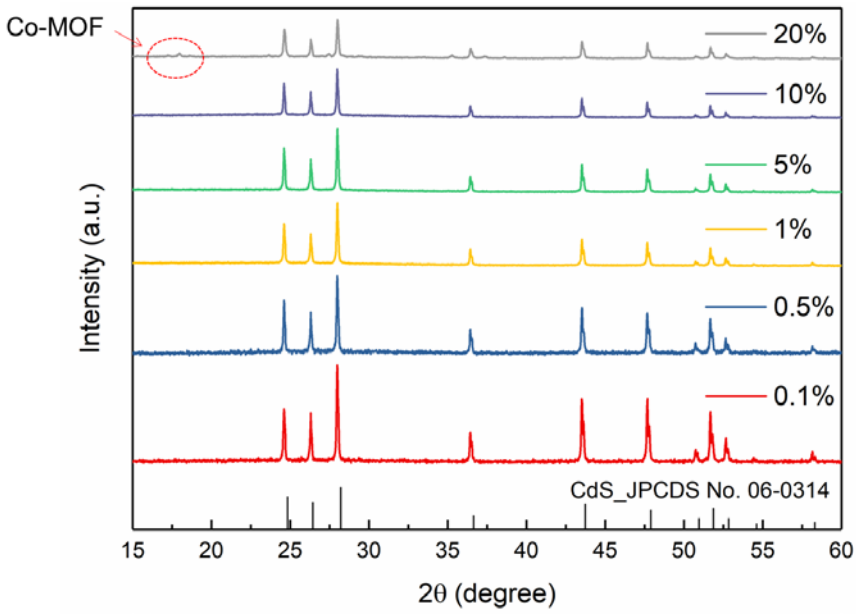

Figure 4.22 XRD analysis of CdS-Co-CoO_x@C-450 prepared with different Co-MOF contents.

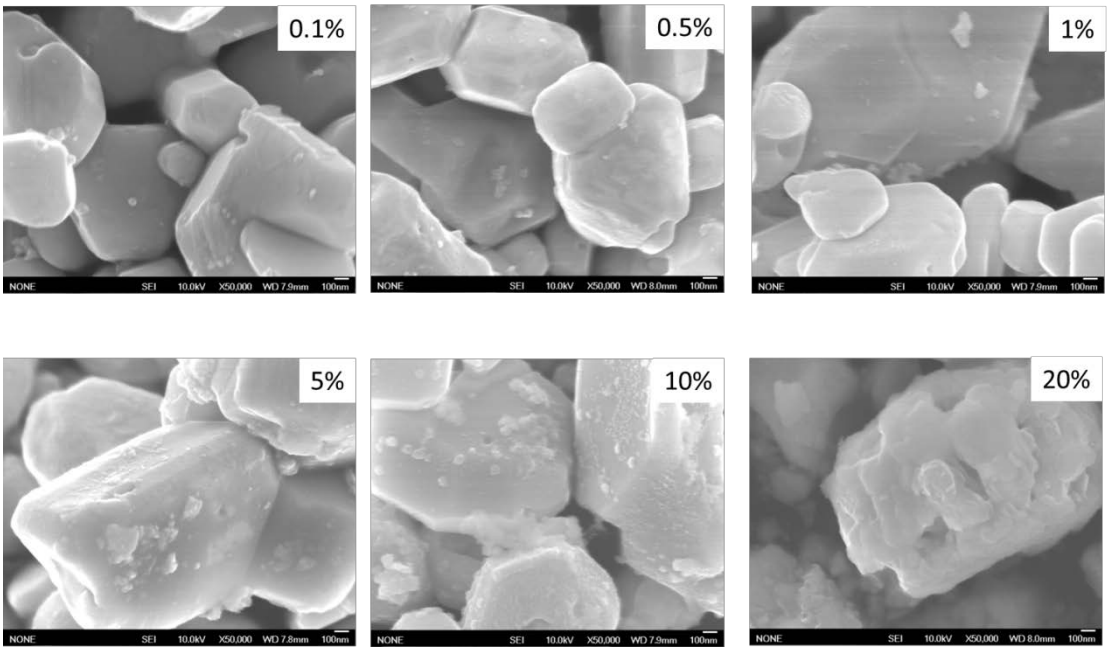

Figure 4.23 SEM images of CdS-Co-CoO_x@C-450 prepared with different Co-MOF contents.

To verify the important role of carbon matrix for supporting Co as cocatalyst on improving the H_2 generation activity, I compare the activity of CdS modified by different Co and carbon benchmarks. As shown in Figure 4.24, photo-deposition of $CoCl_2$ could only gave ~1.3 times enhancement. Meanwhile, 5-fold enhancement can be

achieved by physical mixing of CdS and Co-MOF, and further 2-times improvement can be gained after annealing.

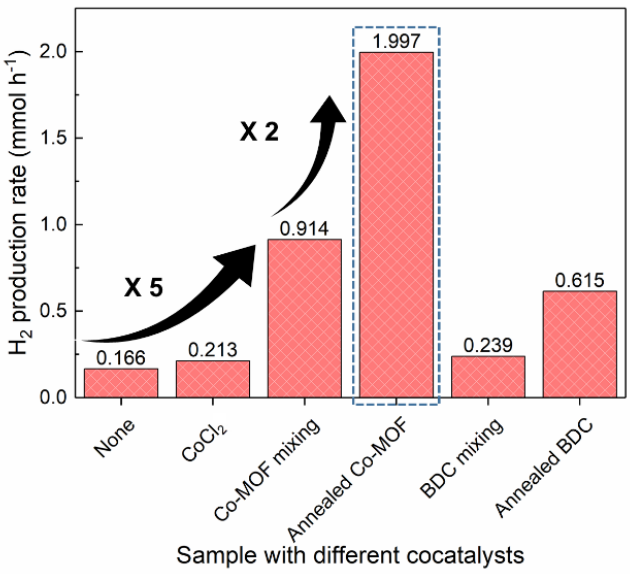

Figure 4.24 Comparison of the cocatalytic performance of different materials.

Comparing to CdS-Co-CoO_x, the performance of CdS-Co-CoO_x@C has been greatly enhanced from 1.275 mmol h^{-1} to 1.997 mmol h^{-1} (Figure 4.25), suggesting that MOF and MOF-derived carbon matrix can help to isolate Co species for achieving high activity. Apart from that, mixing CdS with BDC will slightly increase the H_2 generation rate from 0.166 mmol h^{-1} to 0.239 mmol h^{-1}, while limited improvement can be found after annealing, suggesting that ultrathin carbon layer may facilitate photogenerated electron-hole separation.

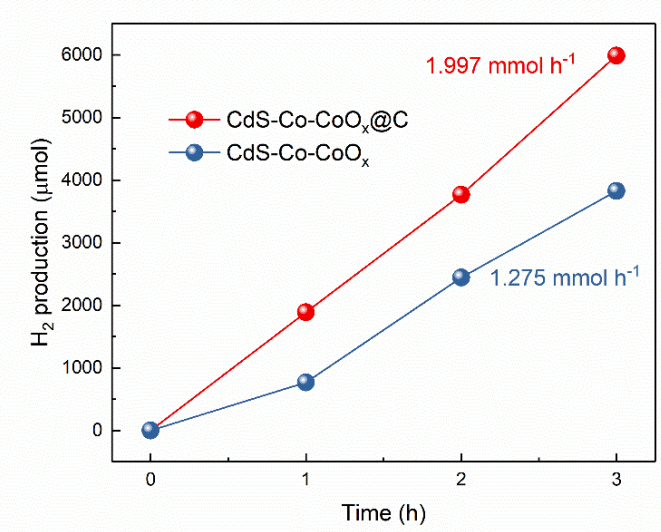

Figure 4.25 Comparing the H_2 production performance between CdS-Co-CoO_x@C and CdS-Co-CoO_x.

Apparent quantum efficiency (AQE) is used to determine the actual driving force of photocatalysis over CdS-Co-CoO_x@C-450 (Figure 4.26a). The curve of AQE of CdS-Co-CoO_x@C-450 shows wavelength-dependent feature which shows strong relevance with the optical absorbance. In addition, the AQE of 43.7% at 420 nm is comparable or even higher than that amongst CdS-based photocatalyst which use Co or Co-species as cocatalyst measured under similar conditions. The optimal activity has been compared with the performance of other cocatalysts over CdS semiconductor in Table 2.2. The stability over CdS-Co-CoO_x@C-450 has been investigated as shown in Figure 4.26b. The H_2 production performance of CdS-Co-CoO_x@C-450 depicts linear increasing without apparent decay during four cycling tests.

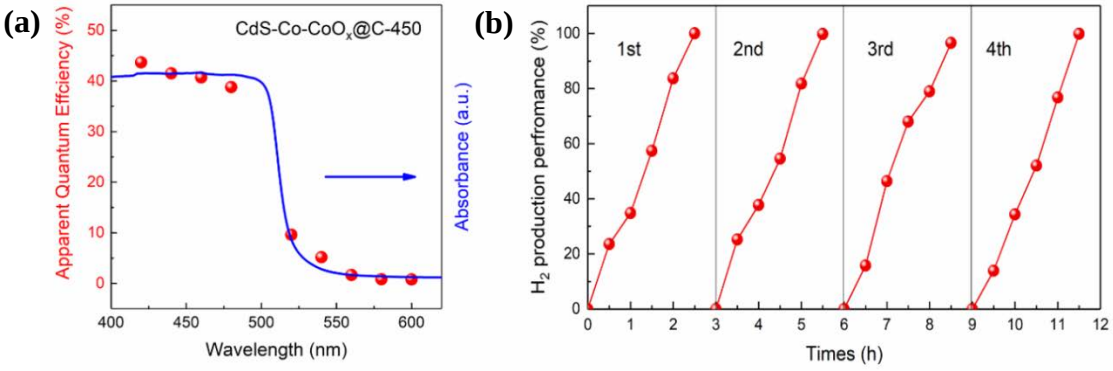

Figure 4.26 (a) Calculated AQE of photocatalytic H_2 evolution dependent with the wavelength and (b) Stability test of H_2 evolution performance over CdS-Co-CoO_x@C-450 with 0.5% Co mole proportion.

Table 4.2 Comparison of the photocatalytic H_2 production performance between the present CdS-based photocatalysts with rivaling performance in literatures.

Materials	**Measurement condition**	**H_2 production** (mmol h^{-1})	AQE at 420 nm	**Reference**
CdS-Co-CoO_x@C-450	> 420 nm Na_2S-Na_2SO_3	1.997	43.7%	**This work**
CdS-MoS_2-graphene	> 420 nm Na_2S-Na_2SO_3	1.2	20.6%	ACS Nano, 2014[42]
CdS-MoS_2	> 420 nm Na_2S-Na_2SO_3	2.0	30.2%	Advanced Energy Materials, 2015[43]
CdS-Ni_3C	> 420 nm Na_2S-Na_2SO_3	0.357	7.58%	Applied Catalysis B: Environmental, 2018[44]
CdS-CoO_x	> 420 nm Na_2S-Na_2SO_3	0.14	-	Applied Catalysis B: Environmental, 2018[22]
CdS-Pt	> 420 nm Na_2S-Na_2SO_3	3.89	50.5%	Advanced Energy Materials, 2015[43]
CdS-α-Fe_2O_3	> 420 nm Na_2S-Na_2SO_3	2.25	46.9	Applied Catalysis B: Environmental, 2020[45]

CdS-Cu_7S_4	> 420 nm Na_2S-Na_2SO_3	0.139	14.7	Chinese Journal of Catalysis, 2020[46]
CdS-hexacoordinated Co(II)	> 420 nm Na_2S-Na_2SO_3	3.1	56.2	Advanced Materials, 2017[47]
CdS-Ni_2S	λ > 420 nm 20 vol.% lactic acid	0.1795	4.2	Catalysis Science & Technology, 2019[48]
CdS-Co_3O_4	λ > 420 nm 10 vol.% lactic acid	0.15	9.7%	Catalysis Science & Technology, 2016[49]
CdS-MoO_2-C	λ > 420 nm 10 vol.% lactic acid	0.402	-	Applied Catalysis B: Environmental, 2020[50]
CdS-cobalt lactate complex	λ > 420 nm 15 vol.% lactic acid	0.77	12.1%	Catalysis Science & Technology, 2018[51]
CdS-VN	λ > 420 nm 10 vol.% lactic acid	0.249	5.3	The Journal of Physical Chemistry C, 2019[52]
CdS-single atom Co	λ > 400 nm 20 vol.% lactic acid	4.34	63.0 %	Nano Energy, 2020[53]

To investigate the behavior of photogenarated charge transfer and recombination behaviors, photoluminescence (PL) measurements were performed on CdS, CdS-Co-CoO_x@C-450 under 420 nm light excitation (Figure 4.27). The emission band is observed at ≈539 nm (2.3 eV) which can be attributed to a band to band transition of hexagonal phase CdS. The PL intensity of CdS-Co-CoO_x@C-450 is weakened compared to that of pure CdS. The PL quench behavior indicates that the charge carrier separation in CdS-Co-CoO_x@C-450 is more efficient than that in pure CdS.

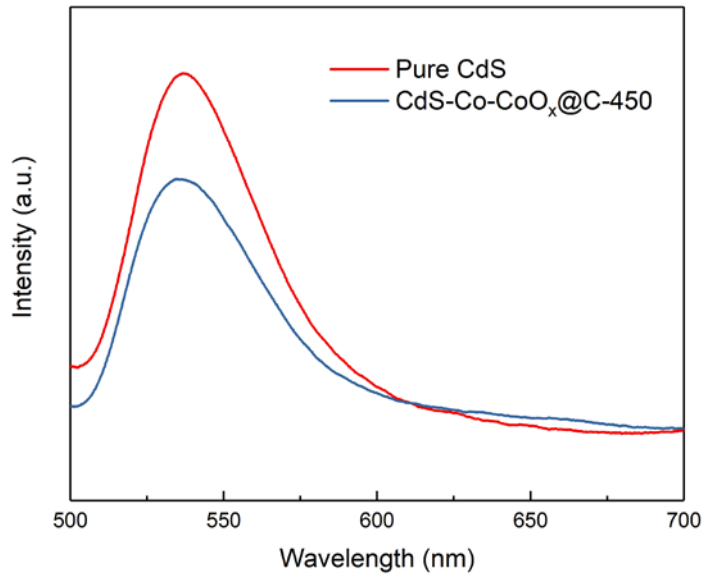

Figure 4.27 PL spectra of CdS and CdS-Co-CoO_x@C-450 under 420 nm excitation.

In addition, time resolved photoluminescence (TRPL) decay spectra (Figure 4.28) were applied to study the carrier dynamics in CdS and CdS-Co-CoO_x@C after 400 nm excitation. A longer carrier lifetime of CdS-BDC (0.197 ns) compared to CdS (0.101 ns) has been found, which is derived from efficient electron transfer from CdS to carbon

due to ultrathin carbon matrix has good conductivity that can facilitate electron-hole separation. As to CdS-Co@C, the loading of metallic Co incorporate with carbon matrix can slightly decrease the lifetime from 0.101 ns to 0.093 ns, revealing charge injection from CdS to Co active sites through newly formed charge transfer channel. More importantly, CdS-Co-CoO_x@C-450 exhibits an obvious acceleration of the decay kinetics, featuring a shorter and dominant time constant τ = 0.065 ns owing to the smooth carrier channel with intimate interfacial contact between CdS and Co active species in carbon matrix. Therefore, the incorporation of dual metal cocatalyst indeed realizes the spatial separation of photogenerated charge carriers, suppressing the electron-hole combination together with providing additional electron-transfer channels.

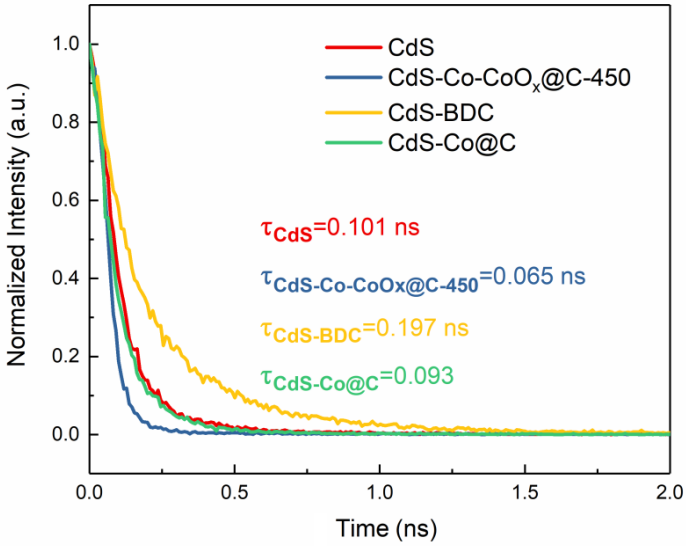

Figure 4.28 PL decay spectra of CdS, CdS-Co-CoO_x@C, CdS-BDC, and CdS-Co@C.

4.3.4 Research on catalytic mechanism

To understand the underlying mechanism of photocatalytic H_2 generation, I have adopted DFT studies to calculate the Gibbs free energy for H* adsorption (ΔG_{H^*}) values of different cocatalysts on the surface of CdS. The Gibbs free energy change of the adsorbed H* ($|\Delta G_{H^*}|$) is an essential indicator to measure the H_2 evolution activity. Usually, a moderate $|\Delta G_{H^*}|$ close to 0 signifies the materials possess neither too strongly nor too weakly bonding with hydrogen, which can realize favorable adsorption and desorption of hydrogen during reactions. As shown in Figure 4.29a, the carbon matrix confining cobalt active species exhibit much lower $|\Delta G_{H^*}|$ comparing to that of Co@C and graphene, which is in agreement with the cocatalytic H_2 generation performance as shown in Figure 4.29b.

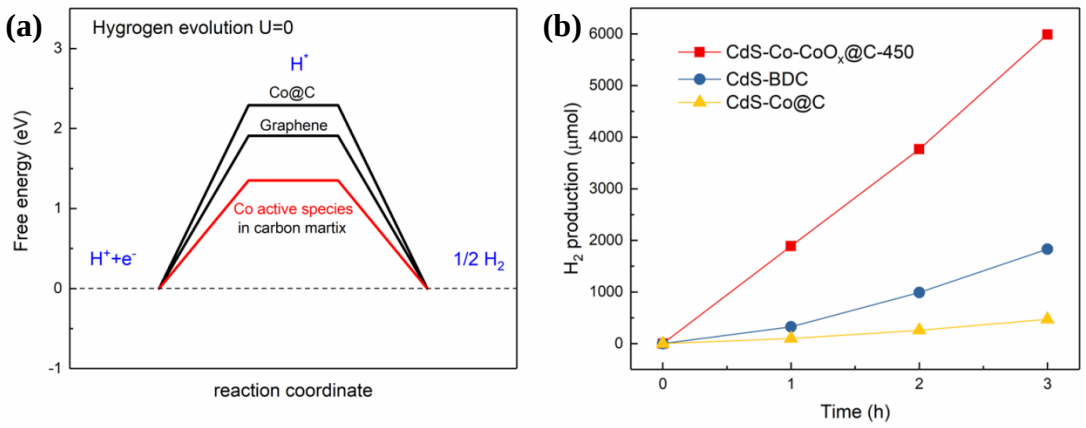

Figure 4.29 (a) The calculated free energy diagram for hydrogen evolution. (b) Comparison of H_2 evolution performance between CdS-Co-CoO_x@C, CdS-BDC and CdS-Co@C.

In addition to the thermodynamically superiority, an intimate contact between CdS and cobalt active species in carbon matrix that formed after calcination could also enable fast charge transfer for efficient catalytic reactions.[53] To explore the charge transferring mechanism in CdS-Co-CoO_x@C heterojunction, charge-density difference between the interface region of cobalt and carbon layer has been provided in Figure 4.30a. The charge redistribution mainly occurs at charge density difference the interface region between cobalt and carbon layer, whereas almost no charge change has been observed in the area away from the interface. The electron densities on the surface of Co are redistributed after encapsulating in carbon matrix, and the electron density accumulation in carbon matrix and depletion in Co will result in a built-in electric field with direction from adjacent cobalt species to carbon (charge gain and loss of each atom have been demonstrated in Table 4.3 and Figure 4.30b).[54] Under light illumination, photogenerated electrons would be confined in the interlayer between Co and carbon matrix for enhanced H_2 generation. In the meantime, holes can be dragged through CoO_x into carbon layer and participate in the oxidation reactions.[22] The accumulation of photogenerated electrons and holes in different section can endow remarkably enhanced photocatalytic performance.

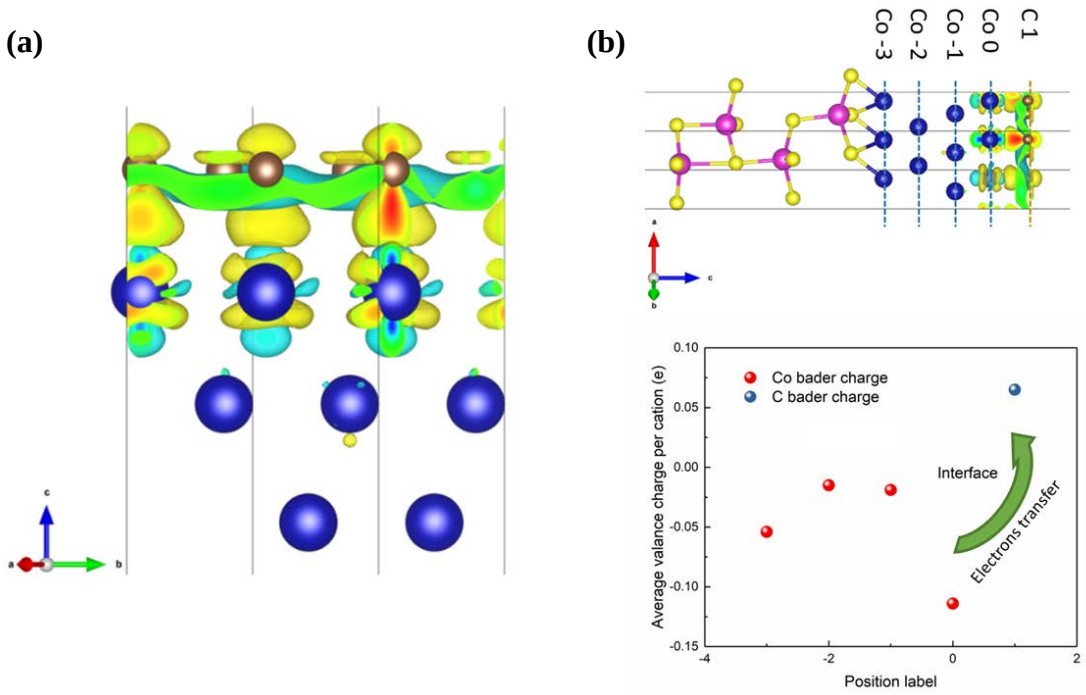

Figure 4.30 (a) The side view of the charge-density difference (Brown balls: C; Blue balls: Co, the cyan region represents charge depletion, and the yellow region indicates charge accumulation). (b) Bader charge analysis of CdS-Co-CoO_x@C.

Table 4.3 Bader charge analysis about charge transfer on the theoretical structure.

Atom	Charge	Atom	Charge
Co1	8.921442	Co10	8.984166
Co2	8.980097	Co11	9.019446
Co3	8.937969	Co12	8.950648
Co4	8.851472	C1	4.043997
Co5	8.922593	C2	4.055057
Co6	8.884054	C3	4.049575
Co7	9.014217	C4	4.065936
Co8	8.977978	C5	4.066437
Co9	8.950883	C6	4.108386

To summarize the aforementioned results, both PL measurements and DFT calculations elucidate that the electron transfer behavior and efficient photogenerated electron-hole separation in the hetero-interface should be the critical factor in our reaction system (Figure 4.31), while the adsorption performance and surface affinity of cocatalysts to H_2 also contribute to the improved photocatalytic performance.

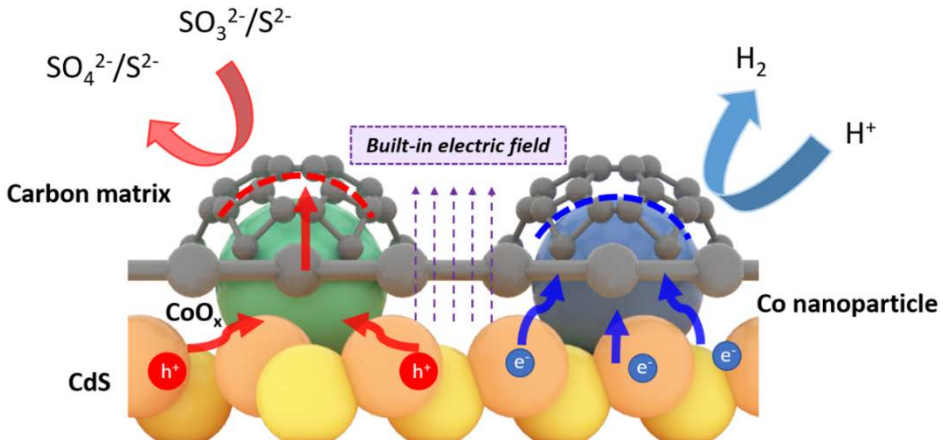

Figurre 4.31 Schematic illustration on charge carriers transfer and separation in CdS-Co-CoO_x@C.

4.4 Conclusions

In summary, the photocatalytic H_2 generation performance of CdS-Co-CoO_x@C has been systematically investigated. The cooperation between Co and CoO_x in carbon matrix has been proven to be vital for achieving 1.997 mmol h^{-1} H_2 production rate with apparent quantum efficiency of 43.7% at 420 nm. After elucidate the mechanism on rational construction of dual cobalt active species (Co and CoO_x species), the enhanced H_2 generation ability can be attributed into 1) The carbon matrix can confine dual cobalt active species in spatial locations with good stability; 2) Carbon layer could effectively suppress photogenerated electron-hole recombination by enhancing metal-semiconductor built-in electrical field; 3) The ultrafine metallic Co active sites and co-existed CoO_x hole acceptors can boost photogenerated electron-hole separation for enhanced H_2 evolution reaction. It is therefore envisaged the present work can contribute to extendable understanding on the manipulation of dual cobalt active species within 2D-MOF derived carbon matrix towards enhanced photocatalytic performance.

References

1. Tu, W.; Zhou, Y.; Zou, Z., Photocatalytic Conversion of CO_2 into Renewable Hydrocarbon Fuels: State-of-the-Art Accomplishment, Challenges, and Prospects. *Advanced Materials* **2014,** *26* (27), 4607-4626.

2. Song, H.; Meng, X.; Wang, Z.-j.; Liu, H.; Ye, J., Solar-Energy-Mediated Methane Conversion. *Joule* **2019,** *3* (7), 1606-1636.

3. Pelaez, M.; Nolan, N. T.; Pillai, S. C.; Seery, M. K.; Falaras, P.; Kontos, A. G.; Dunlop, P. S. M.; Hamilton, J. W. J.; Byrne, J. A.; O'Shea, K.; Entezari, M. H.; Dionysiou, D. D., A review on the visible light active titanium dioxide photocatalysts for environmental applications. *Applied Catalysis B: Environmental* **2012,** *125*, 331-349.

4. Moniz, S. J. A.; Shevlin, S. A.; Martin, D. J.; Guo, Z.-X.; Tang, J., Visible-light driven heterojunction photocatalysts for water splitting – a critical review. *Energy & Environmental Science* **2015,** *8* (3), 731-759.

5. Yang, J.; Wang, D.; Han, H.; Li, C., Roles of Cocatalysts in Photocatalysis and Photoelectrocatalysis. *Accounts of Chemical Research* **2013,** *46* (8), 1900-1909.

6. Meng, A.; Zhang, L.; Cheng, B.; Yu, J., Dual Cocatalysts in TiO_2 Photocatalysis. *Advanced Materials* **2019,** *31* (30), 1807660.

7. Ran, J.; Zhang, J.; Yu, J.; Jaroniec, M.; Qiao, S. Z., Earth-abundant cocatalysts for semiconductor-based photocatalytic water splitting. *Chemical Society Reviews* **2014,** *43* (22), 7787-7812.

8. Twilton, J.; Le, C. C.; Zhang, P.; Shaw, M. H.; Evans, R. W.; MacMillan, D. W. C., The merger of transition metal and photocatalysis. *Nature Reviews Chemistry* **2017,** *1* (7), 0052.

9. Fei, H.; Dong, J.; Arellano-Jiménez, M. J.; Ye, G.; Kim, N. D.; Samuel, E. L. G.; Peng, Z.; Zhu, Z.; Qin, F.; Bao, J.; Yacaman, M. J.; Ajayan, P. M.; Chen, D.; Tour, J. M., Atomic cobalt on nitrogen-doped graphene for hydrogen generation. *Nature Communications* **2015,** *6*, 8668.

10. Meier, J. C.; Galeano, C.; Katsounaros, I.; Topalov, A. A.; Kostka, A.; Schüth, F.; Mayrhofer, K. J. J., Degradation Mechanisms of Pt/C Fuel Cell Catalysts under Simulated Start–Stop Conditions. *ACS Catalysis* **2012,** *2* (5), 832-843.

11. Cao, S.; Chang, J.; Fang, L.; Wu, L., Metal Nanoparticles Confined in the Nanospace of Double-Shelled Hollow Silica Spheres for Highly Efficient and Selective Catalysis. *Chemistry of Materials* **2016,** *28* (16), 5596-5600.

12. Xu, Y.; Tu, W.; Zhang, B.; Yin, S.; Huang, Y.; Kraft, M.; Xu, R., Nickel Nanoparticles Encapsulated in Few-Layer Nitrogen-Doped Graphene Derived from Metal–Organic Frameworks as Efficient Bifunctional Electrocatalysts for Overall Water Splitting. *Advanced Materials* **2017,** *29* (11), 1605957.

13. Wang, X.; Li, Z.; Qu, Y.; Yuan, T.; Wang, W.; Wu, Y.; Li, Y., Review of Metal Catalysts for Oxygen Reduction Reaction: From Nanoscale Engineering to Atomic Design. *Chem* **2019,** *5* (6), 1486-1511.

14. Deng, J.; Ren, P.; Deng, D.; Bao, X., Enhanced Electron Penetration through an Ultrathin Graphene Layer for Highly Efficient Catalysis of the Hydrogen Evolution Reaction. *Angewandte Chemie International Edition* **2015,** *54* (7), 2100-2104.

15. Cui, X.; Ren, P.; Deng, D.; Deng, J.; Bao, X., Single layer graphene encapsulating non-precious metals as high-performance electrocatalysts for water oxidation. *Energy & Environmental Science* **2016,** *9* (1), 123-129.

16. Jin, Z.; Zhang, Q.; Chen, J.; Huang, S.; Hu, L.; Zeng, Y.-J.; Zhang, H.; Ruan, S.; Ohno, T., Hydrogen bonds in heterojunction photocatalysts for efficient charge transfer. *Applied Catalysis B: Environmental* **2018,** *234*, 198-205.

17. Zhang, H.; Ma, Z.; Duan, J.; Liu, H.; Liu, G.; Wang, T.; Chang, K.; Li, M.; Shi, L.; Meng, X.; Wu, K.; Ye, J., Active Sites Implanted Carbon Cages in Core–Shell Architecture: Highly Active and Durable Electrocatalyst for Hydrogen Evolution Reaction. *ACS Nano* **2016,** *10* (1), 684-694.

18. Zhao, G.; Sun, Y.; Zhou, W.; Wang, X.; Chang, K.; Liu, G.; Liu, H.; Kako, T.; Ye, J., Superior Photocatalytic H_2 Production with Cocatalytic Co/Ni Species Anchored on Sulfide Semiconductor. *Advanced Materials* **2017,** *29* (40), 1703258.

19. Tong, L.; Ren, L.; Fu, A.; Wang, D.; Liu, L.; Ye, J., Copper nanoparticles selectively encapsulated in an ultrathin carbon cage loaded on $SrTiO_3$ as stable photocatalysts for visible-light H2 evolution via water splitting. *Chemical Communications* **2019,** *55* (86), 12900-12903.

20. Liu, Q.; Zeng, C.; Xie, Z.; Ai, L.; Liu, Y.; Zhou, Q.; Jiang, J.; Sun, H.; Wang, S., Cobalt@nitrogen-doped bamboo-structured carbon nanotube to boost photocatalytic hydrogen evolution on carbon nitride. *Applied Catalysis B: Environmental* **2019,** *254*, 443-451.

21. Zhu, Y.; Wan, T.; Wen, X.; Chu, D.; Jiang, Y., Tunable Type I and II heterojunction of CoO_x nanoparticles confined in g-C_3N_4 nanotubes for photocatalytic hydrogen production. *Applied Catalysis B: Environmental* **2019,** *244*, 814-822.

22. Liu, Y.; Ding, S.; Shi, Y.; Liu, X.; Wu, Z.; Jiang, Q.; Zhou, T.; Liu, N.; Hu, J., Construction of CdS/CoO_x core-shell nanorods for efficient photocatalytic H_2 evolution. *Applied Catalysis B: Environmental* **2018,** *234*, 109-116.

23. Zhang, J.; Yu, Z.; Gao, Z.; Ge, H.; Zhao, S.; Chen, C.; Chen, S.; Tong, X.; Wang, M.; Zheng, Z.; Qin, Y., Porous TiO_2 Nanotubes with Spatially Separated Platinum and CoO_x Cocatalysts Produced by Atomic Layer Deposition for

Photocatalytic Hydrogen Production. *Angewandte Chemie International Edition* **2017,** *56* (3), 816-820.

24. Zhao, S.; Wang, Y.; Dong, J.; He, C.-T.; Yin, H.; An, P.; Zhao, K.; Zhang, X.; Gao, C.; Zhang, L.; Lv, J.; Wang, J.; Zhang, J.; Khattak, A. M.; Khan, N. A.; Wei, Z.; Zhang, J.; Liu, S.; Zhao, H.; Tang, Z., Ultrathin metal–organic framework nanosheets for electrocatalytic oxygen evolution. *Nature Energy* **2016,** *1* (12), 16184.

25. Cao, F.; Zhao, M.; Yu, Y.; Chen, B.; Huang, Y.; Yang, J.; Cao, X.; Lu, Q.; Zhang, X.; Zhang, Z.; Tan, C.; Zhang, H., Synthesis of Two-Dimensional $CoS_{1.097}$/Nitrogen-Doped Carbon Nanocomposites Using Metal–Organic Framework Nanosheets as Precursors for Supercapacitor Application. *Journal of the American Chemical Society* **2016,** *138* (22), 6924-6927.

26. Han, B.; Ou, X.; Deng, Z.; Song, Y.; Tian, C.; Deng, H.; Xu, Y.-J.; Lin, Z., Nickel Metal–Organic Framework Monolayers for Photoreduction of Diluted CO_2: Metal-Node-Dependent Activity and Selectivity. *Angewandte Chemie International Edition* **2018,** *57* (51), 16811-16815.

27. Cheng, N.; Wang, N.; Ren, L.; Casillas-Garcia, G.; Liu, N.; Liu, Y.; Xu, X.; Hao, W.; Dou, S. X.; Du, Y., In-situ grafting of N-doped carbon nanotubes with Ni encapsulation onto MOF-derived hierarchical hybrids for efficient electrocatalytic hydrogen evolution. *Carbon* **2020,** *163*, 178-185.

28. Jagadeesh, R. V.; Murugesan, K.; Alshammari, A. S.; Neumann, H.; Pohl, M.-M.; Radnik, J.; Beller, M., MOF-derived cobalt nanoparticles catalyze a general synthesis of amines. *Science* **2017,** *358* (6361), 326.

29. Ren, L.; Tong, L.; Yi, X.; Zhou, W.; Wang, D.; Liu, L.; Ye, J., Ultrathin graphene encapsulated Cu nanoparticles: A highly stable and efficient catalyst for photocatalytic H2 evolution and degradation of isopropanol. *Chemical Engineering Journal* **2020,** *390*, 124558.

30. Ren, L.; Yi, X.; Tong, L.; Zhou, W.; Wang, D.; Liu, L.; Ye, J., Nitrogen-doped ultrathin graphene encapsulated Cu nanoparticles decorated on $SrTiO_3$ as an efficient water oxidation photocatalyst with activity comparable to $BiVO_4$ under visible-light irradiation. *Applied Catalysis B: Environmental* **2020,** *279*, 119352.

31. Kresse, G.; Furthmüller, J., Efficient iterative schemes for ab initio total-energy calculations using a plane-wave basis set. *Physical Review B* **1996,** *54* (16), 11169-11186.

32. Blöchl, P. E., Projector augmented-wave method. *Physical Review B* **1994,** *50* (24), 17953-17979.

33. Perdew, J. P.; Burke, K.; Ernzerhof, M., Generalized Gradient Approximation Made Simple. *Physical Review Letters* **1996,** *77* (18), 3865-3868.

34. Elmas Kimyonok, A. B.; Ulutürk, M., Determination of the Thermal Decomposition Products of Terephthalic Acid by Using Curie-Point Pyrolyzer. *Journal of Energetic Materials* **2016,** *34* (2), 113-122.

35. Liu, Y.; Meng, X.; Liu, Z.; Meng, M.; Jiang, F.; Luo, M.; Ni, L.; Qiu, J.; Liu, F.; Zhong, G., Preparation of a Two-Dimensional Ion-Imprinted Polymer Based on a Graphene Oxide/SiO2 Composite for the Selective Adsorption of Nickel Ions. *Langmuir* **2015,** *31* (32), 8841-8851.

36. Di, T.; Zhu, B.; Zhang, J.; Cheng, B.; Yu, J., Enhanced photocatalytic H_2 production on CdS nanorod using cobalt-phosphate as oxidation cocatalyst. *Applied Surface Science* **2016,** *389*, 775-782.

37. Saleem, M. F.; Zhang, H.; Deng, Y.; Wang, D., Resonant Raman scattering in nanocrystalline thin CdS film. *Journal of Raman Spectroscopy* **2017,** *48* (2), 224-229.

38. Liu, L.; Concepción, P.; Corma, A., Non-noble metal catalysts for hydrogenation: A facile method for preparing Co nanoparticles covered with thin layered carbon. *Journal of Catalysis* **2016,** *340*, 1-9.

39. Zhong, H.; Luo, Y.; He, S.; Tang, P.; Li, D.; Alonso-Vante, N.; Feng, Y., Electrocatalytic Cobalt Nanoparticles Interacting with Nitrogen-Doped Carbon Nanotube in Situ Generated from a Metal–Organic Framework for the Oxygen Reduction Reaction. *ACS Applied Materials & Interfaces* **2017,** *9* (3), 2541-2549.

40. Cai, J.; Chen, Y.; Song, H.; Hou, L.; Li, Z., MOF derived C/Co@C with a “one-way-valve”-like graphitic carbon layer for selective semi-hydrogenation of aromatic alkynes. *Carbon* **2020,** *160*, 64-70.

41. Rivas-Murias, B.; Salgueiriño, V., Thermodynamic CoO–Co_3O_4 crossover using Raman spectroscopy in magnetic octahedron-shaped nanocrystals. *Journal of Raman Spectroscopy* **2017,** *48* (6), 837-841.

42. Chang, K.; Mei, Z.; Wang, T.; Kang, Q.; Ouyang, S.; Ye, J., MoS_2/Graphene Cocatalyst for Efficient Photocatalytic H_2 Evolution under Visible Light Irradiation. *ACS Nano* **2014,** *8* (7), 7078-7087.

43. Chang, K.; Li, M.; Wang, T.; Ouyang, S.; Li, P.; Liu, L.; Ye, J., Drastic Layer-Number-Dependent Activity Enhancement in Photocatalytic H_2 Evolution over

nMoS2/CdS (n ≥ 1) Under Visible Light. *Advanced Energy Materials* **2015,** *5* (10), 1402279.

44. Ma, S.; Deng, Y.; Xie, J.; He, K.; Liu, W.; Chen, X.; Li, X., Noble-metal-free Ni3C cocatalysts decorated CdS nanosheets for high-efficiency visible-light-driven photocatalytic H2 evolution. *Applied Catalysis B: Environmental* **2018,** *227*, 218-228.

45. Shen, R.; Zhang, L.; Chen, X.; Jaroniec, M.; Li, N.; Li, X., Integrating 2D/2D CdS/α-Fe_2O_3 ultrathin bilayer Z-scheme heterojunction with metallic β-NiS nanosheet-based ohmic-junction for efficient photocatalytic H_2 evolution. *Applied Catalysis B: Environmental* **2020,** *266*, 118619.

46. Ren, D.; Shen, R.; Jiang, Z.; Lu, X.; Li, X., Highly efficient visible-light photocatalytic H_2 evolution over 2D–2D CdS/Cu_7S_4 layered heterojunctions. *Chinese Journal of Catalysis* **2020,** *41* (1), 31-40.

47. Zhao, G.; Sun, Y.; Zhou, W.; Wang, X.; Chang, K.; Liu, G.; Liu, H.; Kako, T.; Ye, J., Superior photocatalytic H_2 production with cocatalytic Co/Ni species anchored on sulfide semiconductor. *Advanced Materials* **2017,** *29* (40), 1703258.

48. Liu, C.; Xiong, M.; Chai, B.; Yan, J.; Fan, G.; Song, G., Construction of 2D/2D Ni2P/CdS heterojunctions with significantly enhanced photocatalytic H_2 evolution performance. *Catalysis Science & Technology* **2019,** *9* (24), 6929-6937.

49. Lang, D.; Cheng, F.; Xiang, Q., Enhancement of photocatalytic H_2 production activity of CdS nanorods by cobalt-based cocatalyst modification. *Catalysis Science & Technology* **2016,** *6* (16), 6207-6216.

50. Wei, W.; Tian, Q.; Sun, H.; Liu, P.; Zheng, Y.; Fan, M.; Zhuang, J., Efficient visible-light-driven photocatalytic H2 evolution over MoO_2-C/CdS ternary heterojunction with unique interfacial microstructures. *Applied Catalysis B: Environmental* **2020,** *260*, 118153.

51. Wang, L.; Xu, N.; Pan, X.; He, Y.; Wang, X.; Su, W., Cobalt lactate complex as a hole cocatalyst for significantly enhanced photocatalytic H_2 production activity over CdS nanorods. *Catalysis Science & Technology* **2018,** *8* (6), 1599-1605.

52. Tian, L.; Min, S.; Wang, F.; Zhang, Z., Metallic Vanadium Nitride as a Noble-Metal-Free Cocatalyst Efficiently Catalyzes Photocatalytic Hydrogen Production with CdS Nanoparticles under Visible Light Irradiation. *The Journal of Physical Chemistry C* **2019,** *123* (47), 28640-28650.

53. Li, Y.; Wang, S.; Wang, P.; He, Y.; Wang, X.; Chang, K.; Lin, H.; Ding, X.; Chen, H.; Zhang, H.; Izumi, Y.; Kako, T.; Ye, J., Targeted removal of interfacial

adventitious carbon towards directional charge delivery to isolated metal sites for efficient photocatalytic H_2 production. *Nano Energy* **2020,** *76*, 105077.

54. Zhang, J.; Chen, X.; Bai, Y.; Li, C.; Gao, Y.; Li, R.; Li, C., Boosting photocatalytic water splitting by tuning built-in electric field at phase junction. *Journal of Materials Chemistry A* **2019,** *7* (17), 10264-10272.

Chapter 5 Conclusions and future prospects

5.1 General conclusions

In this thesis, the main objective is to realize controllable growth and distribution of cobalt-based cocatalysts as well as modify the cobalt active sites with improved efficiency and stability for photocatalytic H_2 generation. Size modulation and coordination environment modification are two important strategies for improving the catalytic performance of cobalt-based cocatalysts. By taking CdS as benchmark semiconductor, the relations between interfacial charge transfer behavior and coordination environment of cobalt active sites have been studied. I found the surface chemistry and electronic properties of cobalt-based cocatalysts are two vital factors for interfacial charge transfer to realize efficient H_2 generation. Based on the investigation, those strategies would be beneficial in future: 1) Utilize carbon materials to support isolated metal sites with stable dispersion; 2) Introduce electronegative elements to restrict the electron delocalization and decrease the energy barrier of H_2 generation on metal active sites; 3) Construct dual cocatalyst to enable efficient charge transfer and separation.

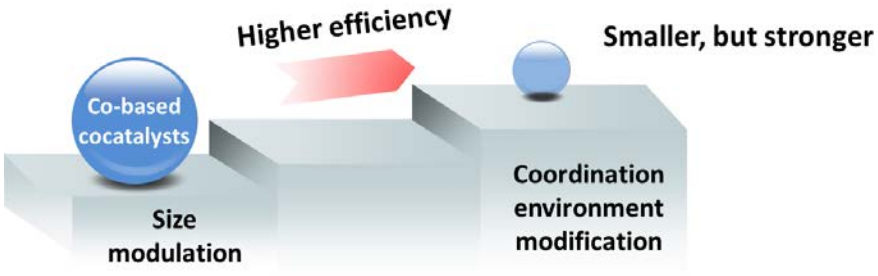

The detailed study could be concluded in the following parts.

1. Single cobalt atom anchored black phosphorous nanosheets as an effective cocatalyst promotes photocatalysis

In this part, two-dimensional black phosphorous (BP) has been chosen as the substrate for dispersing single-atom cobalt active sites, which maximizing the size effect and enlarging surface exposed area of cobalt-based active sites. The as-prepared BP-Co can be used as cocatalyst to enhance photocatalytic ability for both H_2 production and CO_2 reduction. I find that BP-Co loaded CdS can deliver much higher H_2 production performance than that of Pt loaded CdS, indicating great potential of BP-

Co as substitute for Pt cocatalyst for photocatalytic H_2 evolution. On the other hand, the CO evolution rate as high as 88.6 μmol h^{-1} has been realized from photocatalytic CO2 reduction over BP-Co in the presence of [Ru], superior to those obtained from the state-of-the-art noble-metal-free cocatalysts. Based on the results of photocatalytic and photoresponse measurements, I attribute the enhancement of photocatalytic reduction to additional charge transfer channel and active sites derived from Co-P(O) bonding which can benefit photocatalytic conversion kinetics for boosting performance. In our work, the Co-P(O) interaction assist stable dispersion of single atom cobalt on the surface of BP, leading BP-Co nano-materials with good activity as well as promising future in many photo-related applications including hydrogen generation, CO_2 reduction, pollutant degradation and photo-thermal reactions.

2. Metal dopants mediated formation of carbon confined ultrafine CoP nanoparticles promotes catalytic H_2 evolution under visible light

In this part, a novel and facile preparation strategy has been developed to fabricate ultrafine CoP nanoparticles on the surface of CdS. By utilizing organophosphorus compound triphenylphosphine (PPh_3) as phosphorous source, the as-fabricated CoP nanoparticles were intrinsically encapsulated by carbon layer and applied as cocatalyst into photocatalytic H_2 evolution. Meanwhile, Ca^{2+} as an alkaline earth metal ion may easily substitute the Cd^{2+} lattice sites of CdS, which has induced strong trap-state emission together with long-lived charge carriers. In-depth investigations on the transfer dynamics of photogenerated electron demonstrated fast charge transfer behavior in Ca-modified CdS-CoP, indicating the more effective electron-hole separation ability than that of unmodified CdS. The doped Ca^{2+} may act as the interfacial mediator for accelerate the electron transfer from CdS towards CoP to participation in the H_2 generation reaction. As the result, Ca-modified CdS-CoP can achieve 2441.5 μmol h^{-1} H_2 generation rate with apparent quantum efficiency of 35.4% at 420 nm. This finding simplifies the fabrication procedure for constructing and modifying cobalt active sites with efficient photocatalytic H_2 generation performance.

3. Rational construction of dual cobalt active species encapsulated by ultrathin carbon matrix from MOF for boosting photocatalytic H_2 generation

In this part, the spatially separated Co and CoO_x dual cocatalyst encapsulated in carbon substrate was constructed by annealing ultrathin two-dimensional (2D) Co-based MOF (Co-MOF) nanosheets on the surface of CdS. The photocatalytic H_2 generation

performance of CdS-Co-CoO_x@C has been systematically investigated. The cooperation between Co and CoO_x in carbon matrix has been proven to be vital for achieving 1.997 mmol h^{-1} H_2 production rate with apparent quantum efficiency of 43.7% at 420 nm. After elucidate the mechanism on rational construction of dual cobalt active species (Co and CoO_x species), I attribute the enhanced H_2 generation ability into 1) The carbon matrix can confine dual cobalt active species in spatial locations with good stability; 2) Carbon layer could effectively suppress photogenerated electron-hole recombination by enhancing metal-semiconductor built-in electrical field; 3) The ultrafine metallic Co active sites and co-existed CoO_x hole acceptors can boost photogenerated electron-hole separation for enhanced H_2 evolution reaction. It is therefore envisaged the present work can contribute to extendable understanding on the manipulation of dual cobalt active species within 2D-MOF derived carbon matrix towards enhanced photocatalytic performance.

5.2 Future prospects

For a long time, the exploration of efficient catalysts with sufficient active sites and electron-hole separation ability is deemed to be an important step towards the practical application of photocatalysis. Previous and ongoing reports indicate the great potential of applying cobalt-based materials as co-catalysts for photocatalysis, while attempts on construction as well as modification of the cobalt active sites effectively improve the photocatalytic ability. However, many challenges still exist which should be mentioned for better development of efficient cobalt-based cocatalysts:

(1) Single-atom metals have demonstrated remarkable catalytic activity owing to the strong size effect and enlarged surface exposed area. Despite numerous merits of single-atom metals, the tendency of aggregation is usually unavoidable during fabrication processes. It was suggested that the single-atom metals can be stabilized by the lattice or the coordination environment strong covalent bonds. However, the maximum loading amount of single atoms in this method is still far from expectation, which has become the major obstacle to achieve high efficient photocatalytic activity. More efforts are required to explore new strategies for achieving stable dispersion of isolated metal sites together with high photocatalytic performance.

(2) Owing to different functions granted by various cocatalysts, dual-cocatalysts have demonstrated remarkable capability on promoting photocatalytic hydrogen evolution.

Depending on the components and architectures, the synergy effect of dual-cocatalysts needs to be further explored and elaborated to adequately exert the functions including adsorption capacity and charge transfer efficiency. Despite encouraging achievements on the rational construction and modification of dual-cocatalysts have achieved, the controllable growth and distribution of dual-cocatalysts still remains a great challenge.

(3) The activity of photocatalytic system is highly dependent on the physicochemical properties of cocatalysts (such as chemical composition, phase structure, morphology, size distribution, and surface area) as well as interfacial interaction between cocatalyst and photocatalyst. However, no direct evidence on the actual active sites and migration pathway of photogenerated electrons and holes is available. Thus, the in-depth photocatalytic mechanism related to the photocatalytic reaction active site and the migration pathway of photogenerated charge carriers require comprehensive studies.

(4) The fabrication and modification of the cocatalyst can be expected to substantially enhanced photocatalytic activity. Especially, it is very important to find the relation between interfacial charge transfer behavior and coordination environment of cobalt active sites. Further investigations which focused on chemical environment manipulation including ligand design, analytical and physicochemical characterization, and multi-scale modeling can help to gain deep understanding on the mechanism of cocatalytic behaviors.

(5) Photocatalytic overall water splitting is a dream reaction for the conversion of abundant solar energy into clean and renewable H_2 energy on a large scale. In an ideal photocatalytic overall water splitting system, all of the photogenerated electrons and holes will participate into catalytic reactions on the surface of photocatalyst. Up to now, the highest solar to hydrogen conversion efficiency value is 1.1%, which should be increased up to 10% in regarding to the basic requirement of industrializing solar hydrogen production. Therefore, further exploration of visible light absorbing semiconductors and application of aforementioned construction and modification approaches for photocatalytic overall water splitting are still the core issues in this field.

Acknowledgement

At first, I would like to express my deep and sincere gratitude to my supervisor Prof. Jinhua Ye for her valuable guidance, kind help and constant encouragement throughout my Ph.D. studies and personal life. Her proficiency, intelligence, and unparalleled instruction ensure the progress of my Ph.D. research project, and these impacts will benefit me through my whole life. I would also like to extend my sincere appreciation of the academic freedom and great platform that Prof. Ye offered. I am so appreciative and lucky to meet such a nice supervisor.

I am also grateful to my supervisors, Prof. Naoto Shirahata and Prof. Tadanaga Kiyoharu. Thank you for all your suggestions and kind help during my PhD study.

Then, I would like to thank Dr. Li Shi, who gave me a lot of advice for my research. I also want to thank all the members in the Photocatalytic Materials Group in NIMS and the persons who have helped me. I would like to express my thanks to Prof. Kun Chang, Dr. Yunxiang Li, Dr. Gaoliang Yang, Dr. Huiwen Lin, Dr. Hui Song, Dr. Shengyao Wang, Dr. Hong Pang, Dr. Fumihiko Ichihara, Dr. Tetsuya Kako, Mr. Shunqin Luo, Mr. Qi Wang, Mr. Bowen Deng, Ms. Sijie Li, Ms. Lan Li, Mr. Davin Philo, Ms. Kanae Hasegawa, and Ms. Haruna Kaunang for their kind helps in both experiments and daily life.

Thanks to the China Scholarship Council for the financial support during my PhD study.

At last, I would like to thank my parents, other family members and friends for their support and belief in me.